IMPRINTS OF NON-THERMAL PARTICLES ON SPECTRAL AND TEMPORAL PROPERTIES OF ACCRETING BLACK HOLES

ALEXANDRA VELEDINA

Division of Astronomy
Department of Physics
University of Oulu
Finland

Academic Dissertation to be presented with the assent of the
Graduate School, University of Oulu, for public discussion
in the Auditorium of Tuorla Observatory
on 2014 October 10, at 12 o'clock.

TURKU 2014

Veledina, Alexandra: The doctoral thesis at the Division of Astronomy

Department of Physics
P.O. Box 3000
FIN-90014 University of Oulu
FINLAND

Supervisors
Prof. Juri Poutanen, University of Turku, Finland
Prof. Dmitrij I. Nagirner, St. Petersburg State University, Russia

Reviewers
Prof. Christine Done, Durham University, Durham, UK
Prof. Andrzej A. Zdziarski, N. Copernicus Astronomical Centre, Warsaw, Poland

Opponent
Prof. James M. Stone, Princeton University, USA

Custos
Prof. Ilya G. Usoskin, University of Oulu, Finland

ISBN 978-951-29-5839-9
ISBN 978-951-29-5840-5 (PDF)

JUVENES PRINT
Turku 2014

Abstract

This thesis investigates the spectral and temporal properties of accreting black holes, with the main emphasis on optical and X-ray wavelengths. The topic is interesting thanks to the recent discovery of the complex interconnection of the light-curves in these two far-separated energy bands. Advances in optical instruments, which now can resolve light-curve fluctuations on sub-second time-scales, were not followed by the progress of understanding the principle mechanisms responsible for this connection. Motivated by these exciting findings, we investigate possible origins of the optical/X-ray relation. We suggest that the information contained at optical and infrared wavelengths can be used to probe the accretion flow physics.

We propose that the vicinity of the hard-state black holes is occupied by some type of hot geometrically thick, optically thin accretion flow with hybrid (thermal/non-thermal) electrons. In the presence of various acceleration mechanisms, the particle distribution tends to become a power-law. However, the electrons at lower energies efficiently thermalise. The overall steady-state distribution, which we call hybrid, generally resembles a Maxwellian at lower electron energies plus a high-energy power-law-like tail.

What are the advantages of the proposed hot flow scenario compared to the entirely thermal case? It was realized already a decade ago that even a tiny non-thermal tail results in a dramatic increase of the lower-energy synchrotron emission. We show that this emission can quantitatively explain observational characteristics of the optical/infrared wavelengths and their complex relation to the X-rays.

What are the disadvantages of considering hybrid particles? In the purely thermal case, the emergent spectra can be easily calculated once the electron temperature is known. In our studies, the spectra have to be obtained self-consistently with the electron distribution, which in turn is not known in advance. For this, the system of coupled kinetic equations for photons and electrons (and positrons) is being solved until the steady-state solution is found. Whilst the spectral calculations are rather complex, the results are quite promising. We show that a little twist to the well-established hot flow scenario allows the understanding of the whole set of observational data, like in no other model.

Acknowledgments

My deepest gratitude goes to Prof. Juri Poutanen for guiding my way in science throughout these years and for the endless enthusiasm reminding me there is always light at the end of the tunnel. I am thankful to my adviser Prof. Dmitrij Nagirner, who initiated this way back in Saint Petersburg State University. I am highly grateful to Prof. Andrzej Zdziarski and Prof. Christine Done for their careful reading of this manuscript and for the useful comments during the work and at its final stages. I also wish to thank Prof. James Stone for agreeing to become my opponent and Prof. Ilya Usoskin for chairing the PhD defence.

The completion of this thesis is due to efforts of a number of people. My dear collaborators, Dr. Indrek Vurm, Dr. Jari Kajava, Dr. Adam Ingram, Dr. Vitaly Neustroev, Dr. Sergey Tsygankov, Dr. Mike Revnivtsev and Dr. Piergiorgio Casella, I am sincerely thankful for your participation in our projects. I am grateful to my office mates Alexander Mushtukov, Joonas Nättilä, Tuulia Pennanen and Marja Annala for brightening my work hours (usually not very sunny otherwise) and to the previous members of the high energy astrophysics group, Dr. Valery Suleimanov, Dr. Askar Ibragimov and Dr. Aleksei Medvedev, for the entertaining weekend activities. Many thanks to my friends Olesya Yakovchouk and Diana Bulavetova for bringing me back to the real life after work. I highly appreciate nice and friendly atmosphere I encountered during the PhD studies, especially the coffee-break company at the University of Oulu and the lunch-time company of Tuorla observatory. Thanks to all who is responsible for that. I also wish to thank Sarah Bird for her attempts to fix my non-English sentences in the thesis.

The completion of this work would not have been possible without insightful and stimulating discussions during various meetings. I acknowledge all the people whom I had a pleasure to talk to for their interest in my work, and especially for the critical comments, as they led to my comprehension of the overall physical picture. I am particularly grateful to Dr. Marion Cadolle Bel (ESAC), Prof. Anatoly Spitkovsky (Princeton University), Dr. Lorenzo Sironi and Prof. Ramesh Narayan (CfA), and Prof. Axel Brandenburg and Dr. Andrey Beresnyak (NORDITA) for their hospitality during my visits.

I acknowledge the Finnish Graduate School in Astronomy and Space Physics, Magnus Ehrnrooth foundation, Space Institute of the University of

Oulu for funding. I would like to thank Prof. Matti Weckström for introducing the stipend for publications, which was quite motivating.

I am grateful to my family for the continuous support and faith in me. Thanks to my dad for the encouragement during these years. Thanks to my mum for the frequent visits which gave me strength and time.

List of the original publications

Paper I: Veledina A., Poutanen J., Vurm I.: Hot accretion flow in black hole binaries: a link connecting X-rays to the infrared. 2013, MNRAS, 430, 3196

Paper II: Veledina A., Poutanen J., Vurm I.: A synchrotron self-Compton-disk reprocessing model for optical/X-Ray correlation in black hole X-ray binaries. 2011, ApJ, 737, L17

Paper III: Veledina A., Poutanen J., Ingram A.: A unified Lense-Thirring precession model for optical and X-ray quasi-periodic oscillations in black hole binaries. 2013, ApJ, 778, 165

Paper IV: Veledina A., Poutanen J.: Reprocessing model for the optical quasi-periodic oscillations in black hole binaries. MNRAS, to be submitted

Paper V: Poutanen J., Veledina A., Revnivtsev M. G.: Colours of black holes: infrared flares from the hot accretion disc in XTE J1550–564. MNRAS, submitted

Paper VI: Veledina A., Vurm I., Poutanen J.: A self-consistent hybrid Comptonization model for broad-band spectra of accreting supermassive black holes. 2011, MNRAS, 414, 3330

Paper VII: Poutanen J., Veledina A.: Modelling spectral and timing properties of accreting black holes: the hybrid hot flow paradigm. 2014, Space Science Reviews, in press, arXiv:1312.2761

Paper VIII: Neustroev V. V., Veledina A., Poutanen J., Zharikov S. V., Tsygankov S. S., Sjoberg G., Kajava J. J. E.: Spectroscopic evidence for a low-mass black hole in SWIFT J1753.5–0127. MNRAS, submitted

Contents

Chapter 1

Accreting black holes

1.1 Subject of study

The present dissertation is devoted to the observational signatures and theoretical interpretation of probably the most exotic objects in the Universe, the black holes (BHs hereafter). These objects come in at least two different flavours: stellar-mass BHs in binary systems and supermassive BHs in the innermost regions of active galaxies. Whether there exists the intermediate-mass BH class, which fills the mass gap between the two major classes, is currently debated.

BHs are observable due to accretion of the surrounding matter. They are among the brightest X-ray emitters on the sky. In radio, the objects are seen due to outflowing material, the jet. The first extragalactic BHs – the quasars – were noticed thanks to these outflows. Stellar-mass BHs are predominantly discovered by the X-ray satellites. Support monitoring is also performed in the ultraviolet (UV), optical, infrared and radio bands. It has lately become evident that the information contained in these longer wavelengths is of principal importance when trying to judge the nature of radiation from BHs. The present thesis investigates mechanisms of the broadband spectral formation, covering the infrared to X-ray/γ-ray energies. We find that the multiwavelength and temporal properties require the presence of non-thermal particles close to the compact object. They constrain the global accretion picture, limiting its possible geometry, heating mechanisms and physical conditions in the vicinity of the BH.

1.2 Some history

The first documented suggestion of the existence of stars so massive that the escape velocity from their surface is equal to the speed of light belongs to John Mitchell (see Pounds, 2014, and references therein) and is dated back to year 1783. However, the idea did not excite any interest in the scientific

community at that time since the fundamental significance of light speed was understood only more than a century later. The fact that such objects are very different from normal stars was emphasised by John Wheeler (1968), who proposed to call them "black holes". In the nowadays understanding, the BHs are specific solutions (Schwarzschild 1916; English translation by S. Antoci and A. Loinger of the original work can be found as Schwarzschild 1999; Kerr 1963) of the equations of General Relativity (Einstein, 1915, 1916). A characteristic feature of BHs is the event horizon – an imaginary surface beyond which events cannot affect an outside observer. The search of BHs began only after their precise mathematical formulation. An object is classified as a BH if the measured size is close to its Schwarzschild radius $R_{\rm S} = 2GM_{\rm BH}/c^2$. Two independent estimates are therefore required: mass and radius. The size estimations of compact objects in binary systems are based on the observations of rapid irregular flickering. The lower limit on the mass of the compact object can be obtained from the velocity curve of the companion star. It provides two independent parameters: the orbital period P and the semi-amplitude of the companion velocity K. They define the mass function as

$$f(M) = \frac{PK^3}{2\pi G} = \frac{M_{\rm BH}\sin^3 i}{(1+q)^2}, \tag{1.1}$$

where q is the ratio of the companion star mass to the BH mass and i is the binary inclination. As can be seen from the formula, the mass function gives an absolute minimum value for the mass of the compact object. If its inferred mass is too high for a neutron star, i.e. $f(M) \gtrsim 3M_\odot$, it is conventionally considered to be a BH. This does not mean, however, that an object with $M < 3M_\odot$ cannot be a BH.

As the material is captured by the gravitational field of the BH, it starts to orbit around the compact object and soon forms an accretion disc (Frank et al., 2002). As the matter approaches the compact object, it looses gravitational energy due to the viscous forces, which heat the material giving rise to the observed radiation. The Eddington limit is an upper limit on its luminosity, above which the accretion will be stopped by radiation pressure. If the accreting matter is composed of pure hydrogen and the radiation pressure is due to Thomson scattering, the Eddington luminosity is $L_{\rm Edd} \simeq 1.3 \times 10^{38}(M/M_\odot)$ erg s^{-1}. This limit can be used to estimate the spectral range of major energy release. A lower limit can be set on the frequency of the observed emission by assuming that the infalling matter is optically thick and is in thermal equilibrium with the radiation. In this case the characteristic temperature is set by the blackbody temperature of a sphere of a few $R_{\rm S}$ emitting at luminosity $L_{\rm Edd}$, from which we derive $T_{\rm bb} \sim 1$ keV. An upper limit can be obtained from the concept of the virial temperature which gives $T_{\rm vir} \sim 20$ MeV. Thus, the BH binaries are expected to be X-ray and, possibly, γ-ray emitters. Indeed, these are well-known to be powerful X-ray sources.

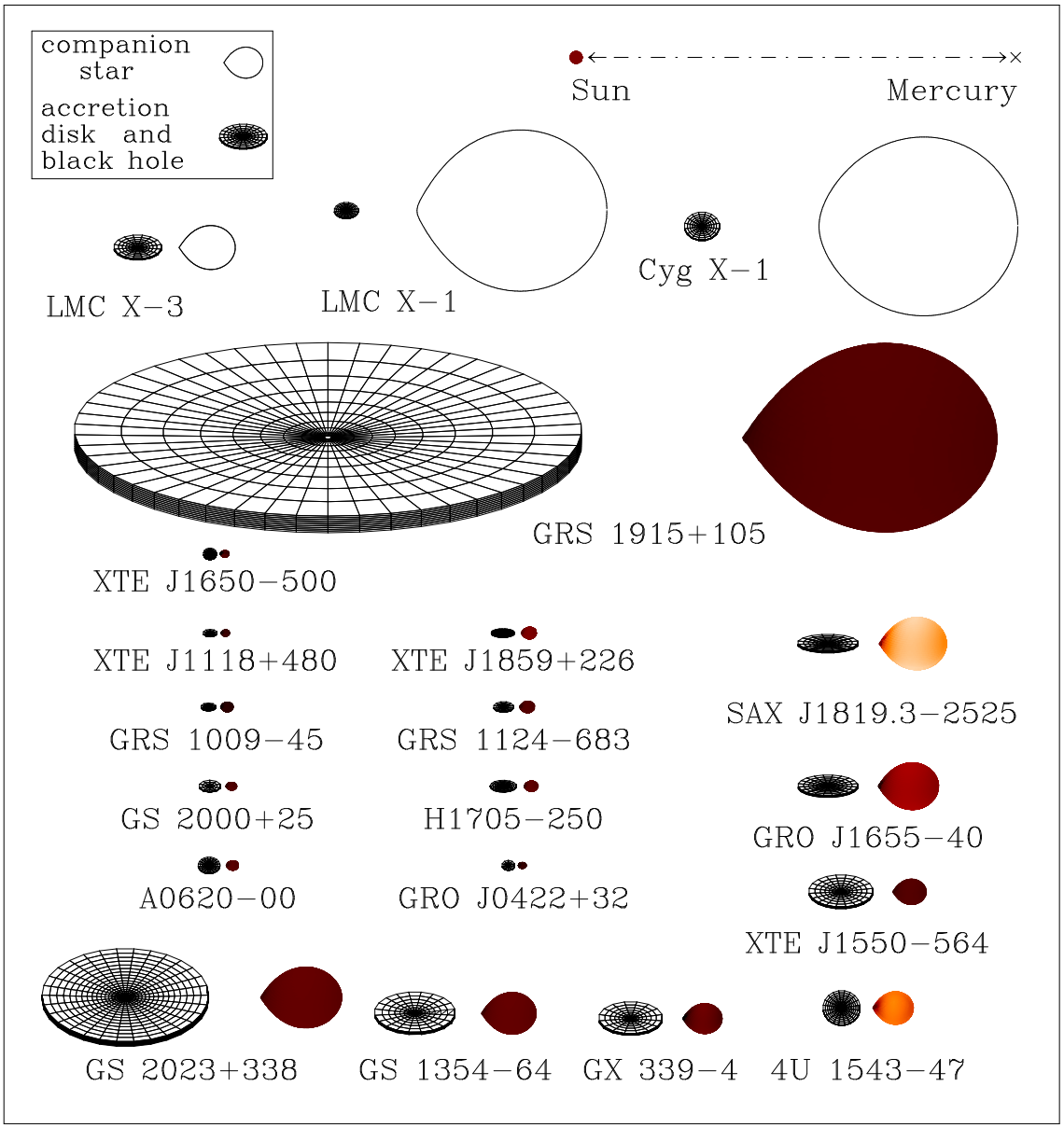

Figure 1.1. Schematic diagram of 20 dynamically confirmed black hole binaries. By J. Orosz, http://mintaka.sdsu.edu/faculty/orosz/web.

Altogether 25 confirmed BH binaries have been discovered since the beginning of the X-ray era (see reviews by Narayan and McClintock 2014; Casares and Jonker 2014 and recent measurements in Casares et al. 2014; Corral-Santana et al. 2013). Some of them are sketched in Figure 1.1. In addition, there are about 40 BH candidates, which show spectral and temporal properties typical for BH binaries, but their masses have not been dynamically measured. Masses of BHs used to be comfortably above the conventional limit $3M_\odot$; however, recent measurements suggest there exists a population of BHs very close to or even below this limit. Two sources are currently not included into the "confirmed BH list", yet their X-ray properties leave no doubts in their origin: the compact object in the binary Cyg X-3 has $M = 2.4^{+2.1}_{-1.1}M_\odot$ (Zdziarski et al., 2013), and in the SWIFT J1753.5–0127 with $M < 4.5M_\odot$ (Neustroev et al., MNRAS submitted, Paper VIII hereafter). It becomes evident that the firm classification based on the compact object mass estimate alone is becoming less and less reliable, and other diagnostic methods should be agreed on to serve as a criterion to distinguish between BHs and neutron stars. Such a technique will likely be based on observational appearances of objects with and without a solid surface. The most promising methods are based on the X-ray colour evolution as a function of flux (Done and Gierliński, 2003) and on the properties of the broadband noise (Sunyaev and Revnivtsev, 2000).

Half a century after the discovery, BHs are still fascinating for a number of reasons. First, BHs are unique objects for testing predictions of one of the most fundamental theories, General Relativity. Second, the compactness of the object along with its high mass result in high efficiency of energy extraction, much higher than in nuclear reactions, which allows us to explore the physical properties of matter at extreme conditions. Finally, probing the presence of BH's event horizon remains a challenge.

1.3 Main observables and their interpretation

This section briefly describes our current knowledge about observational properties and physical mechanisms operating in BH binaries and supermassive BHs, with the main stress on their X-ray and optical radiation. A somewhat more detailed discussion is presented in the review by Poutanen and Veledina (2014, hereafter Paper VII) and the comprehensive reviews by Zdziarski and Gierliński (2004); Remillard and McClintock (2006); McClintock and Remillard (2006); Charles and Coe (2006); Done et al. (2007); Done (2010); Gilfanov (2010); Yuan and Narayan (2014).

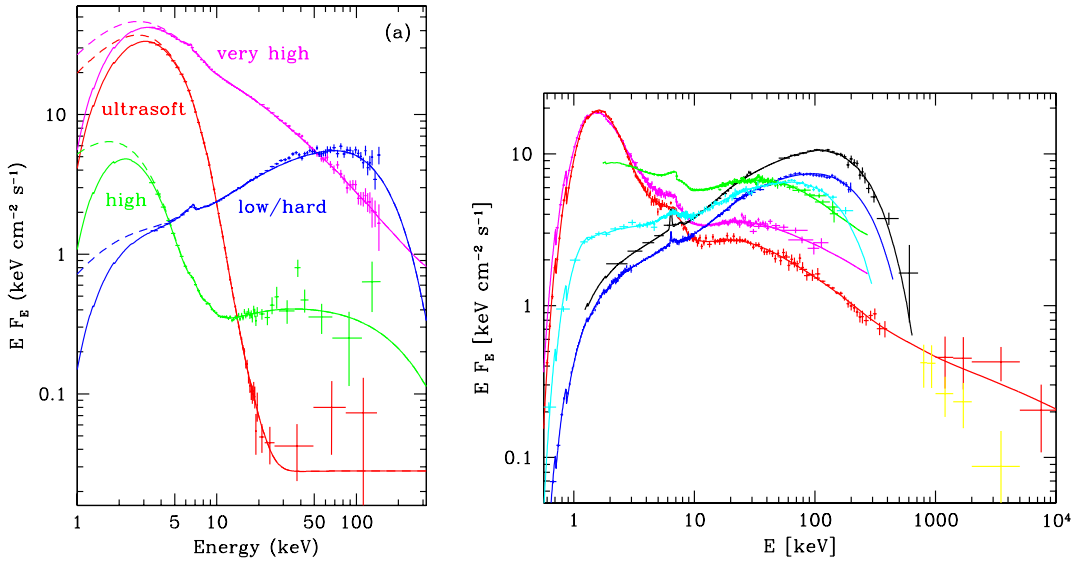

Figure 1.2. Left: examples of X-ray spectral states observed in LMXB XTE J1550–564 (from Zdziarski and Gierliński, 2004). The high state (green) corresponds to the soft state introduced in the text. Right: states of the HMXB Cyg X-1 (from Zdziarski et al., 2002). Soft state (red and magenta), hard state (black and blue) and intermediate states (cyan and green) are observed in this object.

1.3.1 Galactic black hole binaries

There are two major classes of Galactic BH binaries: high-mass and low-mass X-ray binaries (HMXBs and LMXBs), determined on the basis of the mass of the companion (Charles and Coe, 2006). In HMXBs, the secondary star is $\gtrsim 3 M_\odot$. Accretion here proceeds through the capture of material from the companion wind. There are 7 such objects known to date, all of them except for one are persistent X-ray sources. The well-studied X-ray binary Cyg X-1 is a prototype for this class. LMXBs are transient sources, which are typically active for several months and then become quiescent for years to decades. The companions are stars with masses up to a few solar masses, normally below one solar mass, but the key property here is that the accretion proceeds through the Roche lobe overflow. There are 18 such sources, including the prototype 1A 0620–00 which underwent an outburst in 1975. The thesis mainly concerns LMXBs, where the companion is typically so small that the observed optical, infrared and UV radiation is due to the proceeding accretion processes.

Though the structure of the binary along with optical emission mechanisms are completely different in these two classes of sources, they possess common X-ray properties. Both classes exhibit two major states defined according to the shape of their X-ray spectrum (Zdziarski and Gierliński, 2004). The soft state is characterized by the presence of the thermal component in the soft X-rays, which is commonly accepted to be coming from the stan-

dard geometrically thin, optically thick accretion disc (Shakura and Sunyaev, 1973). More often the objects are found in the hard state, characterized by a power-law spectral shape in the 2–10 keV band of typical index $\alpha = -0.6$ to -0.8 ($F_\nu \propto \nu^\alpha$). A Compton reflection feature is often detected atop of the power-law continuum. The underlying continuum is found to peak at energies $\sim$50–200 keV whenever the high-energy data are available (the reflection feature can shift the overall peak towards lower energies). In addition, a γ-ray tail going up to MeV energies was detected in several objects. This tail is due to emission of non-thermal particles (Poutanen and Vurm, 2009; Malzac and Belmont, 2009; Zdziarski et al., 2012; Malyshev et al., 2013). In addition to these canonical states, the nowadays phenomenology introduces the quiescent state (when the object is very dim/undetectable in the X-rays), the intermediate states (effectively, these states are characterized by the spectral indexes between those of the hard and the soft states), the ultrasoft state (when the soft X-rays can be fully described by the blackbody-like component) and the very high state (resembles the soft state, but with a more prominent hard X-ray power-law). Characteristic spectra for different states are presented in Figure 1.2.

Most BH binaries show transitions between these states. Generally, the hard state is found at lower X-ray luminosity than the soft state, however, as the outburst proceeds, the object makes a hysteresis loop, commonly known as the "q-track" (hard-soft-hard) as seen in the colour-luminosity diagram (Homan et al., 2001). It is also worth noticing that if the binary demonstrates several outbursts, the transition occurs at different X-ray luminosities (see the compilation of a number of outbursts in Muñoz-Darias et al., 2013, and Figure 1.3). From Figure 1.3, one can notice spectral softening at luminosities below about $10^{-2} L_{\rm Edd}$ (see also Sobolewska et al., 2011). This property became crucial for understanding the mechanisms responsible for the state transition. Unlike the soft state, the hard state is characterized by high-amplitude broadband variability and the presence of different classes of low-frequency quasi-periodic oscillations (QPOs hereafter, classification can be found in Casella et al., 2005, see Figure 1.4). These features became defining properties, allowing the new X-ray transient to be considered as a BH candidate.

Though BHs in the hard state are broader studied, geometry and emission mechanisms in this state are more debated. Probable geometries include a truncated cold disc with a hot inner flow and a hot corona above the cold disc, which is not truncated (Done et al., 2007). The truncated disc scenario is, perhaps, the most promising nowadays. It involves evaporation of the inner part of the standard accretion disc into some hot geometrically thick, optically thin (Thomson optical depth $\tau \sim 1$) flow as the object makes a soft-to-hard state transition (Meyer et al., 2000). Dynamical and spectral properties of such flows are well studied with numerical experiments (e.g., reviews by Blaes, 2014; Yuan and Narayan, 2014). Due to its complexity,

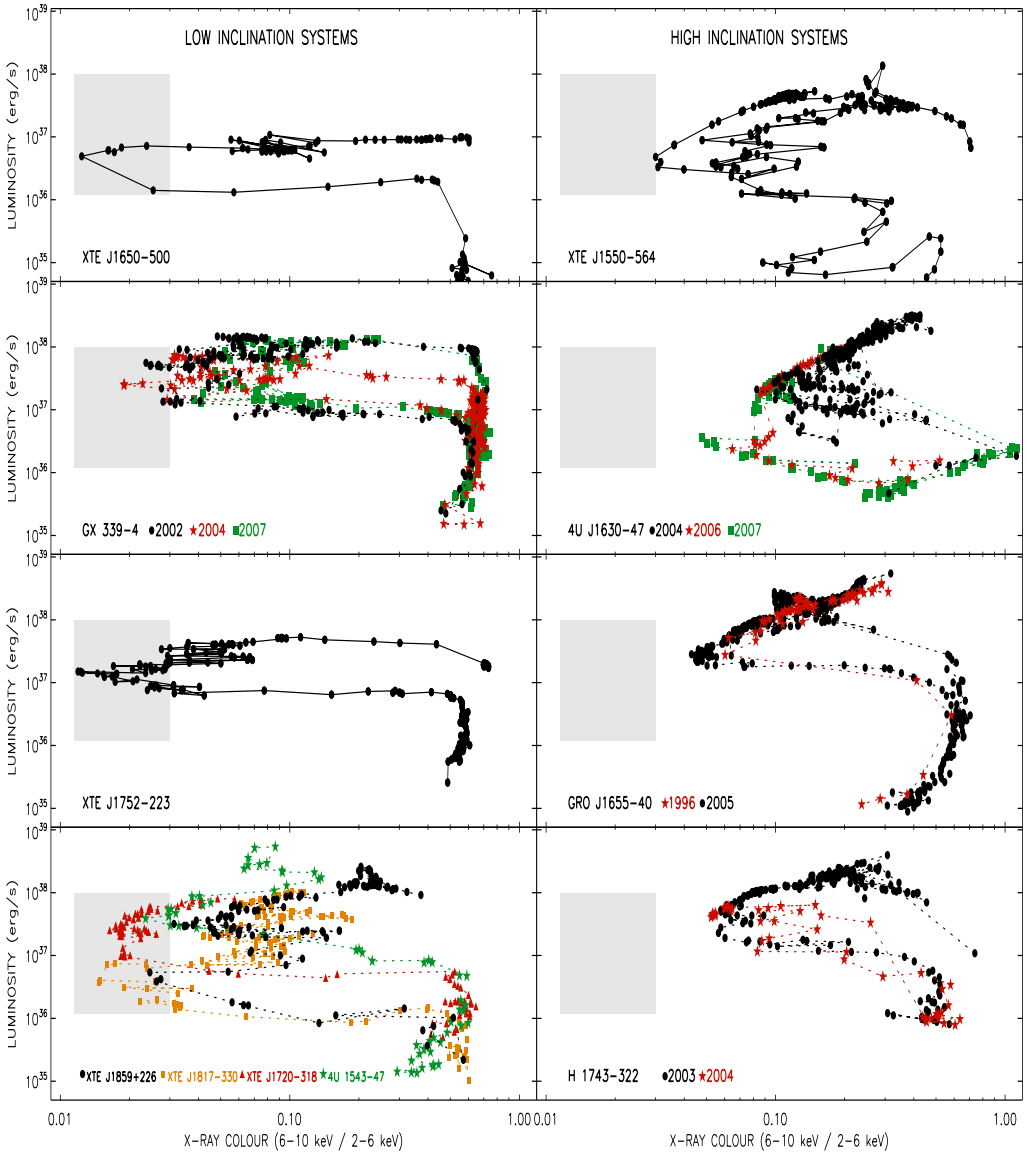

Figure 1.3. Hardness (colour) – luminosity diagrams plotted for eight BH binaries. The objects make the famous "q-loop" as the outbursts proceed. If the observations happen to catch the very beginning of the outburst, the loop starts with the hard spectrum at low luminosity (lower right parts of each panel). Then the luminosity grows, but the hardness stays (almost) the same, until the highest luminosity for such hardness is reached. At this point the state transition occurs: as the object goes through the intermediate states, the spectra soften at roughly constant luminosity, until the softest spectrum is reached. Then the luminosity decreases with the soft spectra, until the reverse transition takes place. Slight softening is again seen at luminosities below $\sim 10^{-2} L_{\rm Edd}$. From Muñoz-Darias et al. (2013).

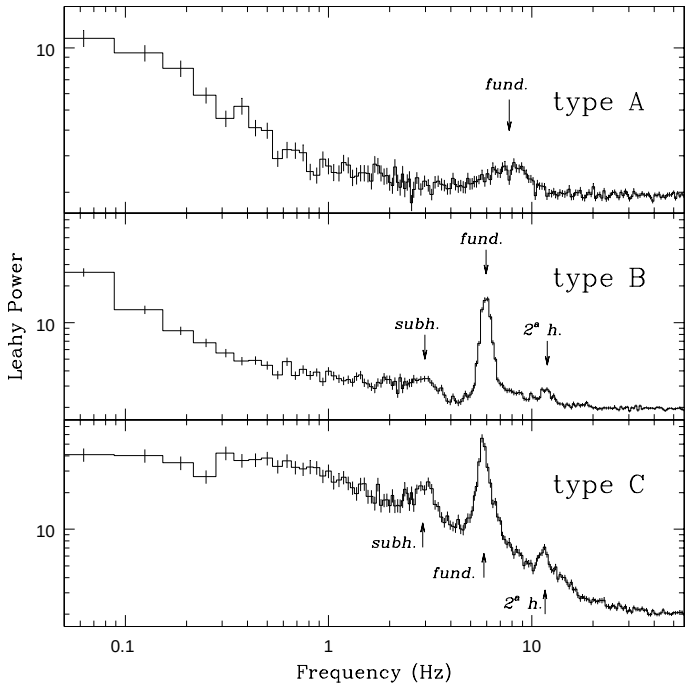

Figure 1.4. Appearance of different classes of QPOs, type A–C, in the X-ray power spectral density of BH binary XTE J1859+226. From Casella et al. (2004).

the task is usually simplified to consider purely thermal particles. However a small fraction of non-thermal electrons should be present in the medium as suggested by the observed MeV tails. Under the conditions relevant to the BH vicinity (electron number density and temperature) and with reasonable assumptions of the magnetic field energy density (of the order of or below that of radiation energy density), these non-thermal electrons can play a fundamental role in spectral formation (Wardziński and Zdziarski, 2001; Poutanen and Vurm, 2009; Malzac and Belmont, 2009). Not only do they contribute to the γ-ray energies, but also can produce radiation which dominates the low-energy part of the spectrum (UV, optical and even infrared). The primary aim of the thesis is to investigate how these electrons manifest themselves in the temporal and broadband spectral data. We propose a phenomenological model of the hot accretion flow with hybrid (thermal/non-thermal) electrons (Veledina et al., 2013, Paper I hereafter). In this model, the hot flow dominates in X-rays and also significantly contributes to longer wavelengths.

Observations of many sources, including XTE J1118+480 (Hannikainen et al., 2000; Esin et al., 2001), XTE J1859+226 (Hynes et al., 2002), A0620–00 (Gallo et al., 2007), V404 Cyg (Hynes et al., 2009), GX 339–4 (e.g., Gandhi et al., 2011; Shidatsu et al., 2011) and SWIFT J1753.5–0127 (Durant et al., 2009; Chiang et al., 2010), in the UV, optical and infrared wave-

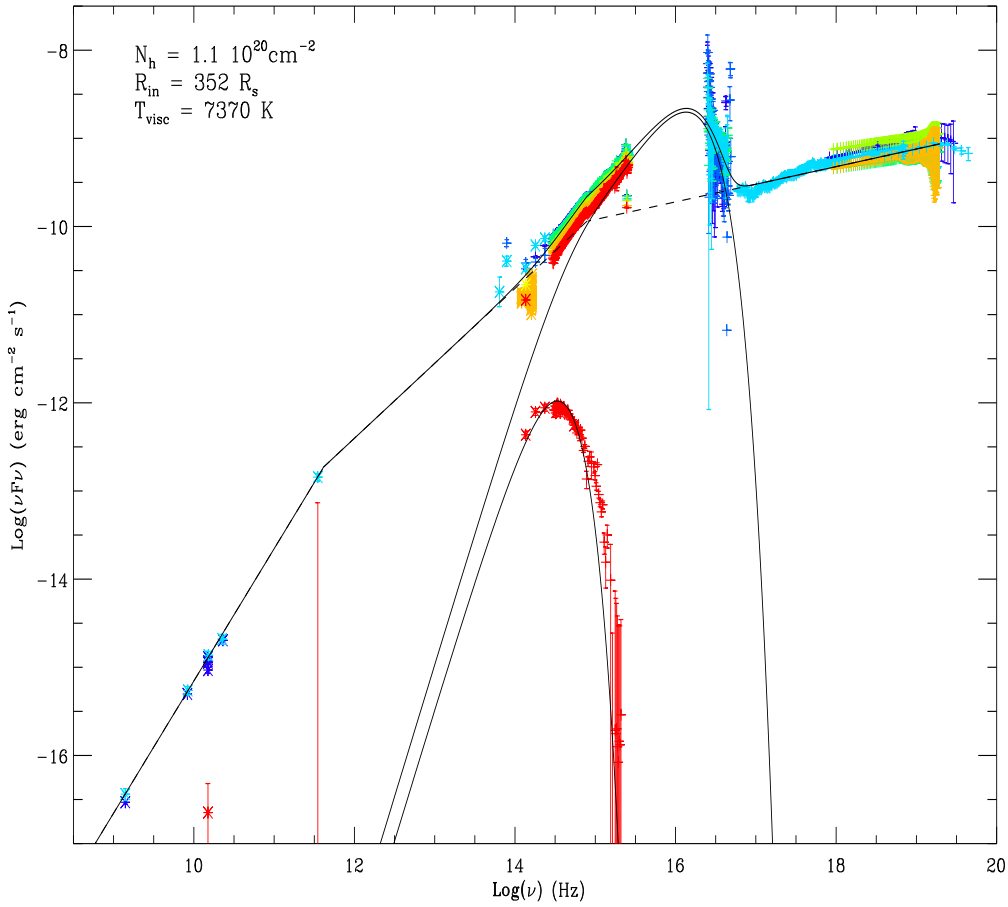

Figure 1.5. Spectral energy distribution of BH binary XTE J1118+480. Different colours correspond to different epochs of observations. Solid lines represent the accretion disc and the double-broken power-law model. The lower curve corresponds to blackbody emission, likely from the companion star. The infrared data cannot be described by thermal emission from the accretion disc. An additional non-thermal component is required. From Chaty et al. (2003).

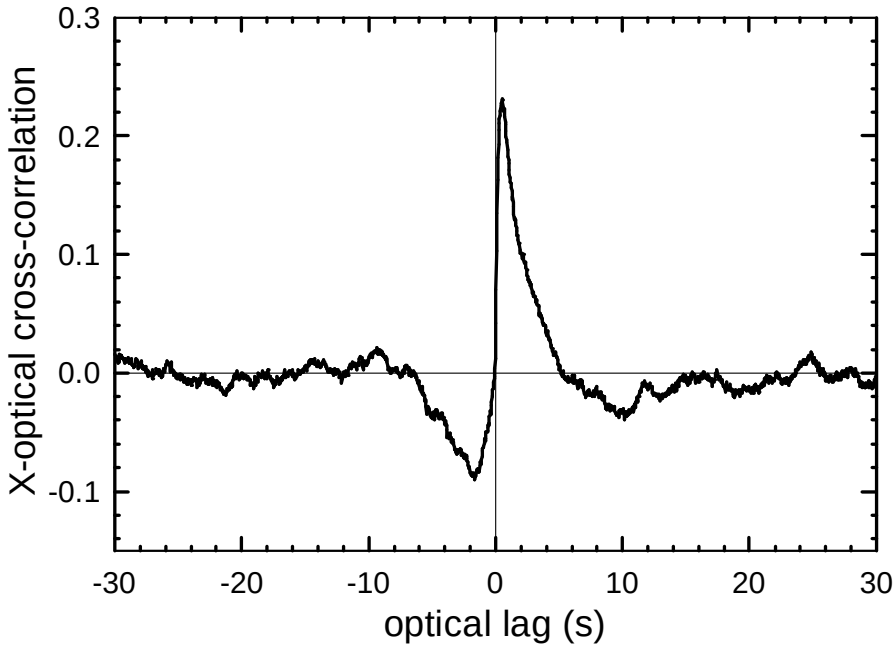

Figure 1.6. Optical/X-ray cross-correlation function observed in XTE J1118+480. The so-called precognition dip (anti-correlation at negative lags) can be noticed. From Kanbach et al. (2001).

lengths revealed emission in excess of that expected from the standard accretion disc. The observations of continuous outburst state in GX 339–4 (Buxton et al., 2012) and SWIFT J1753.5–0127 (Chiang et al., 2010) and of the repeated mini-outburst of XTE J1118+480 (Hynes et al., 2000) confirm that the excess is a permanent attribute of the hard state. Two possible sources of this excess were considered. The first is the irradiated accretion disc (Cunningham, 1976; Gierliński et al., 2009), which was shown to successfully work in a number of BH binaries. But sometimes the inferred optical luminosity is too high to originate from thermal emission for any reasonable size of the emitter (e.g., in BH binary XTE J1118+480, see Figure 1.5 and Chaty et al., 2003). In these cases the emission was routinely attributed to a jet.

The distinctive signature of the jet is non-thermal radio emission. In order to trace its formation and evolution, the BH binaries are actively monitored in radio bands during the outbursts. When the contemporaneous radio/optical data are obtained, the optical points appear to be lying on the continuation of the rather flat ($\alpha = 0$) radio continuum (e.g., Gallo et al., 2007). However, the large error bars in radio lead to the large uncertainty of the extrapolated continuum, thus it is possible to explain optical points anywhere within a couple of orders of magnitude. Whenever the additional contemporaneous sub-mm data is available, a significantly harder radio spectrum (with spectral index $\alpha \sim 0.5$) is required in order to fit the overall spectrum. The optical/infrared excess, though, remained rather flat, even after

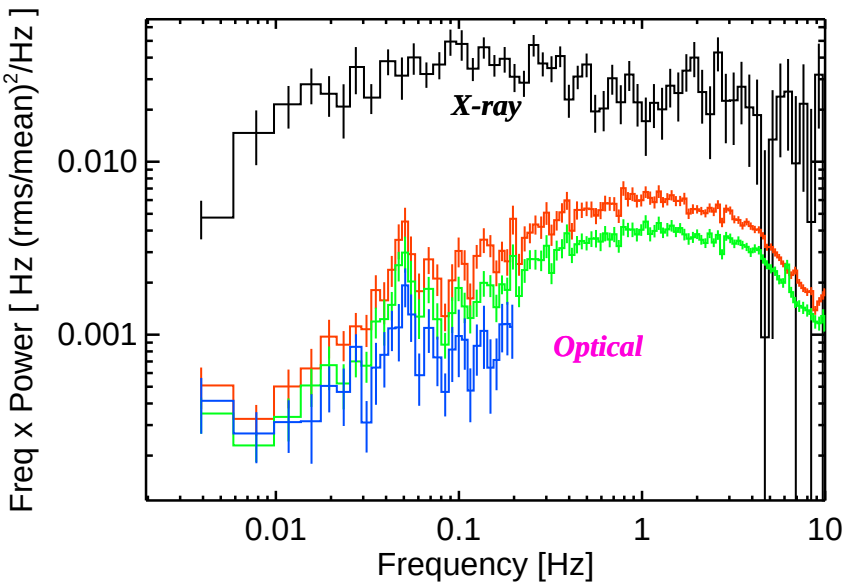

Figure 1.7. X-ray (black line) and optical (green, red and blue lines correspond to different filters) power spectral densities observed in BH binary GX 339–4. A prominent QPO at frequency ∼0.05 Hz is present in the optical, but not in the X-rays. From Gandhi et al. (2010).

subtraction of possible irradiated disc contribution (Chaty et al., 2003; Corbel et al., 2013), thus questioning the jet contribution at these wavelengths. Moreover, the faint radio fluxes measured from the binary SWIFT J1753–0127 do not allow the jet model to fit the high optical emission in this object. We propose that optical/infrared excess is instead attributed to a hot accretion flow (Paper I).

With the advances of the UV, optical and infrared instruments, it became possible to probe temporal characteristics of the BH binaries at a subsecond time-resolution. This led to a discovery of a number of peculiar temporal properties, which are difficult to explain in terms of either irradiated disc or jet scenario. A complex optical/X-ray correlation was reported for three sources, GX 339–4, XTE J1118+480 and SWIFT J1753.5–0127 (Motch et al., 1983; Kanbach et al., 2001; Durant et al., 2008; Gandhi et al., 2010, Figure 1.6). These studies revealed that optical leads the X-rays with negative correlation together with positive correlation lagging the X-rays. In addition, the variability power at optical wavelengths seemed to be peaking at higher Fourier frequencies, compared to the X-rays, suggesting optical photons are coming from a more compact region. A number of models were proposed to explain these complex properties, most of them, however, did not address the problem quantitatively. Detailed calculations were made in the so-called reservoir model (Malzac et al., 2004), which attributes the op-

tical emission to jet. Their comparison with the data from XTE J1118+480 showed an overall quantitative agreement. This model, however, fails to explain the new data from SWIFT J1753.5–0127 showing very faint jet (radio) emission, but at the same time demonstrating the most pronounced anti-correlation dip. On the other hand, the hot flow scenario can easily account for the dip by the overall spectral pivoting (Veledina et al., 2011, hereafter Paper II). The irradiated disc adds the correlation at positive lags. Joint contribution of these two components to the optical emission reproduces the observed complex cross-correlation. The interplay of the two optical components also naturally explains the optical power spectral density peaking at frequencies higher than the X-rays (for details see Paper I).

Another intriguing discovery, the low-frequency optical QPOs (see Figure 1.7), further constrains possible models. The QPOs were detected in the same three objects where the complex cross-correlation behaviour was found (Motch et al., 1983, 1985; Imamura et al., 1990; Steiman-Cameron et al., 1997; Hynes et al., 2003; Durant et al., 2009; Gandhi et al., 2010). When both optical(/UV) and X-ray QPOs were observed, they shared a common characteristic frequency, which evolved with time (Hynes et al., 2003). Apart from this property, little is known about the optical QPOs. We propose two scenarios explaining them. The irradiated accretion disc is the first natural candidate to produce the optical QPOs. Following the model of Ingram et al. (2009) and Fragile et al. (2007), we assumed that the X-ray QPOs are produced by the hot flow, which is subject to Lense-Thirring (solid-body) precession. The oscillations in our model are produced because the X-ray emissivity function depends on the hot flow viewing angle, which, in turn, depends on the precession phase. This quasi-periodic X-ray signal is intercepted by the disc and is reprocessed into optical emission to produce the QPOs. This scenario predicts that the oscillation variability amplitude is a specific function of the QPO frequency and wavelength (see Paper IV). Alternatively, the optical QPOs could be produced by the outer parts of the hot flow itself (Veledina et al., 2013, Paper III hereafter). In this case, we find a certain phase shift between optical and X-rays, either 0 or π, depending on the observer's position relative to the BH spin. Optical QPOs could, in principle, be produced in the jet as well. In general, all three components (irradiated disc, hot flow and jet) can contribute to the optical spectrum, making it very difficult to distinguish between them.

Interestingly, the contributions of thermal and non-thermal spectral components can be separated using the outburst light-curves in several optical/infrared filters. The whole outburst of the BH binary XTE J1550–564 in 2000 was monitored by the Yale 1 m telescope at CTIO in V, I and H filters (Jain et al., 2001). The light-curves cannot be simply described by the fast-rise exponential-decay pattern, which is expected if the optical wavelengths are dominated by the irradiated disc. An additional component, manifesting itself as flares at times of the X-ray spectral transition, is required. By

fitting the exponential-decay profile to the soft-state optical data and extrapolating it further to the hard state, it is feasible to obtain the thermal (disc) component during the flare and thus to extract the contribution of the non-thermal component. We find that the spectrum of the non-thermal component changes during the flare, starting with hard, $\alpha \sim 1$, then softening down to $\alpha \sim 0$ and then hardening again to $\alpha \sim 1$ (see Paper V). We argue that the behaviour is inconsistent with the jet, but can be explained in terms of the hot flow scenario.

Numerous evidence show the accretion disc contribution is insufficient to explain the data in the optical. Non-thermal processes have been suggested to shape the spectrum at these wavelengths for long ago. The major efforts, however, aimed to attribute these processes to the outflow. Our findings suggest that they are rather originating from the inflow, instead. We show that the broadband spectral shape, both short-term and long-timescale variability can be explained in terms of the hybrid hot flow scenario.

1.3.2 Supermassive black holes

The accretion onto a supermassive BH (10^6 to $10^{10} M_\odot$) was proposed to be the engine powering active galactic nuclei independently by Zel'dovich (1964) and Salpeter (1964). Similarities in the X-ray spectral properties indeed suggest these objects are larger analogues of BH binaries. Our studies mainly concern a subclass of Seyfert 1 galaxies, which demonstrate the power-law spectrum of typical index $\alpha = -0.9$ to -1.0 in the X-ray band, somewhat softer than a typical spectrum of an X-ray binary. The γ-ray data of these objects are substantially poorer compared to the Galactic sources, however, the existing upper limits on the average flux above 100 keV are compatible with the presence of weak non-thermal tails (Gondek et al., 1996; Johnson et al., 1997; Lubiński et al., 2010). The non-detection of high-energy tails can be interpreted in terms of purely thermal Comptonization models, but it then becomes difficult to explain why the objects demonstrate a preferential slope. We investigated whether the spectra of supermassive BHs can be explained by the synchrotron self-Compton mechanism (Veledina et al., 2011, Paper VI hereafter), previously shown to give stable slopes in the case of X-ray binaries (Poutanen and Vurm, 2009). We find that the mechanism not only successfully explains the commonly-observed X-ray spectra of Seyfert 1s, but also accounts for the somewhat softer spectra of low-luminosity active galactic nuclei (which resemble BH binaries at luminosities below $10^{-2} L_{\rm Edd}$, see review Ho 2008) and can easily be extended to explain spectra of narrow-line Seyfert 1s. This implies that the same hybrid hot accretion flow is present both in the vicinity of stellar-mass BHs and of their supermassive analogs.

Chapter 2

Summary of the original publications

2.1 Paper I – Hot accretion flow in black hole binaries: a link connecting X-rays to the infrared

Here we propose the original idea of the extended hot accretion flow with hybrid electrons. We first consider an analytical model of an extended inhomogeneous synchrotron source with purely non-thermal (power-law) electrons. Under the conditions relevant to the BH vicinity such a source radiates in the optical/infrared wavelengths. On the other hand, Compton up-scattering of these low-energy photons results in an X-ray continuum. The cooling processes and interactions with the locally emitted photons lead to deviations of the electron distribution from the power-law shape. To obtain the resulting spectrum we compute the photon and electron distributions of such a source self-consistently, accounting for all relevant radiative and cooling/heating processes. We attribute such source to the earlier-studied hot geometrically thick flow (previously, only with thermal electrons). We investigate its temporal properties under changing mass accretion rate. We find that, unlike in the purely thermal case, the model can quantitatively account for the observed optical/infrared emission, its behaviour at state transition and complex relation to the X-rays. We discuss that the model is also consistent with a number of other X-ray spectral and temporal properties, explained earlier.

2.2 Paper II – A synchrotron self-Compton-disk reprocessing model for optical/X-ray correlation in black hole X-ray binaries

Physical picture of the emission mechanisms operating in the X-ray binaries was put under question by the simultaneous optical/X-ray observations with high time resolution. The light curves of the two energy bands appeared to be connected and the cross-correlation functions observed in three black hole binaries exhibited a complicated shape. The optical emission leads the X-rays and anti-correlated with them, together with a positive correlation lagging the X-rays. This behaviour could not be explained in terms of standard optical emission candidates (e.g., emission from the cold accretion disk or a jet). We presented a novel model, which explains the broadband optical to the X-ray spectra and the variability properties. We suggested that the optical emission consists of two components: synchrotron radiation from the non-thermal electrons in the hot accretion flow and the emission produced by reprocessing of the X-rays in the outer part of the accretion disk. The first component is anti-correlated with the X-rays, while the second one is correlated, but delayed and smeared relative to the X-rays. The interplay of the components explains the complex shape of the cross-correlation function, the features in the optical power spectral density as well as the time lags.

2.3 Paper III – A unified Lense-Thirring precession model for optical and X-ray quasi-periodic oscillations in black hole binaries

Recent observations of accreting black holes reveal the presence of the QPOs both in the optical and X-ray power density spectra at the same frequencies. Among the numerous suggested X-ray QPO mechanisms some may also work in the optical. However, their relevance to the broadband – optical through X-ray – spectral properties have not been investigated. For the first time, we discuss the QPO mechanism in the context of the self-consistent spectral model. We proposed that the QPOs are produced by Lense-Thirring (solid body) precession of the whole hot accretion flow, whose outer parts radiate in the optical wavelengths. At the same time, its innermost parts are emitting the X-rays, explaining the observed connection of QPO periods. We predicted that the X-ray and optical QPOs should be either in phase or shifted by half a period, depending on the observer position. We investigated the QPO harmonic content and found that the variability amplitudes at the fundamental frequency are larger in the optical, while the X-rays are expected to have strong harmonics. We then discuss the QPO spectral dependence and compare the expectations to the existing data.

2.4 Paper IV – Reprocessing model for the optical quasi-periodic oscillations in black hole binaries

In this paper we develop an alternative model for the optical QPOs, which are arising from the modulation by the oscillating X-ray flux. Similarly to the previous paper, we assume that the X-ray QPOs are due to the precessing hot flow. This precession results in varying irradiation condition at the outer parts of the accretion disc. We find that the X-ray and optical profiles cannot be connected through the disc transfer function as the observer sees different X-ray signal from those seen from the disc. We propose two ways of recognising this type of QPOs from others: by the dependence of the QPO rms on the Fourier frequency and by its dependence on the wavelength of the observed radiation.

2.5 Paper V – Colours of black holes: infrared flares from the hot accretion disc in XTE J1550–564

Outbursts of the BH binaries are detected by the X-ray telescopes and often monitored at longer wavelengths. In the optical/infrared, a typical fast rise exponential decay profile is usually accompanied by two strong flares. They likely originate from non-thermal processes. We accurately analysed the X-ray and optical/infrared light-curves and colour-magnitude diagrams of the BH binary XTE J1550–564 during its 2000 outburst. We put strong constraints on the extinction towards the source from the extreme colours observed and from the characteristic decay timescales at different energies. This allowed us to relate the observed colours to the slopes of the intrinsic spectrum. We further extracted the non-thermal component and showed that its spectral shape and evolution during the outburst are naturally explained in terms of the hot flow scenario.

2.6 Paper VI – A self-consistent hybrid Comptonization model for broad-band spectra of accreting supermassive black holes

In this work we investigate the broadband spectral properties of accreting supermassive BHs produced by the synchrotron-self Compton mechanism from hybrid particles. Such a mechanism can operate in the hot accretion flow close to the compact object. We find that, similarly to the hard-state BH binaries, it well reproduces the spectra of AGNs. Under a very broad range of parameters the model predicts a rather narrow distribution of spec-

tral indexes consistent with that observed from Seyferts. The softer X-ray spectra observed in narrow-line Seyfert galaxies may correspond to non-thermal Comptonization of the disc photons, predicting that no cutoff should be observed up to MeV energies in these sources, similarly to the soft-state X-ray binaries. The model predicts a slight spectral softening towards low-luminosity (in Eddington units) AGNs, consistent with the data. This feature cannot be accounted for in the standard disc-corona scenario. Finally, we show that the entire infrared to X-ray spectrum of these objects can be described in terms of synchrotron self-Compton mechanism from the hot flow, suggesting a tight correlation between these two energy bands.

2.7 Paper VII – Modelling spectral and timing properties of accreting black holes: the hybrid hot flow paradigm

The review covers current observational properties of accreting BH binaries in the infrared, optical, UV and X-ray/γ-ray energies and their interpretation in terms of the developed hot flow model with hybrid electrons. The following observational facts are naturally accounted for by the model:

1. presence of the MeV tail in the hard state,
2. stability of the hard-state spectra and the cutoff at $\sim$100 keV,
3. concave X-ray spectrum,
4. X-ray spectral softening with decreasing luminosity below $\sim 10^{-2} L_{\rm Edd}$,
5. weakness of the cold accretion disc component in the hard state,
6. correlation between the spectral index, the reflection amplitude, the width of the iron line and the frequency of the quasi-periodic oscillations,
7. hard X-ray lags with logarithmic energy dependence,
8. low level of the X-ray and OIR polarization,
9. non-thermal excesses and flat spectra at the optical/infrared wavelengths,
10. strong correlation between optical/infrared and X-ray emission and a complicated shape of the cross-correlation function,
11. optical/infrared flares and fast colour changes near the times of X-ray state transitions,

12. quasi-periodic oscillations at the same frequency in the X-ray and optical bands.

We argue that only the hot flow model is capable of explaining the whole set of these observational properties.

2.8 Paper VIII – Spectroscopic evidence for a low-mass black hole in SWIFT J1753.5–0127

We report the results of the spectroscopic observations of the BH binary SWIFT J1753.5–0127, supported by the photometric monitoring. We use these data to determine the system parameters. Our main conclusion concerns the mass of the primary in this system, which appears to be a low-mass BH, with an upper limit for the mass of about $4M_{\odot}$. This result supports the possibility of existence of compact objects with mass in the range 2–5$M_{\odot}$, the so-called mass gap, strongly limiting the formation scenarios. We also performed time-series analysis of our photometric and spectroscopic data and confirm that SWIFT J1753.5-0127 is one of the shortest-period X-ray binaries. We find the orbital period of 2.85 h, in contrast to the 3.24 h, suggested earlier.

2.9 The author's contribution to the thesis

The idea of the extended hot disc discussed in Paper I appeared in the discussion of J. Poutanen and the author of the thesis. Simulations, most of the formulae, figures (except for figure 2) and the applications to the data were made by the author of the thesis, who also wrote the main body of the manuscript.

The original idea of Paper II belongs to the author of the thesis, who also made the simulations, figures and wrote most of the text. The formalism was proposed by J. Poutanen and developed by the author of the thesis.

In Paper III, the original idea belongs to the author of the thesis, who also wrote most of the text and described applications of the model.

In Paper IV, the author of the thesis adapted the formalism, previously developed by J. Poutanen, to the case of reprocessed quasi-periodic signals from the accretion disc. All figures and the main body of the manuscript were prepared by the author of the thesis.

In Paper V, the author of the thesis proposed the idea to explain the fast change of the observed colours during the state transitions and wrote Section 4.

In Paper VI the author of the thesis included the description of bremsstrahlung processes into the spectral code, made the simulations and wrote

the main body of the manuscript.

The text for Paper VII was jointly written by J. Poutanen and the author of the thesis. Figures 3, 5 and 12 were plotted using the simulations made by the author of the thesis.

In Paper VIII, the author of the thesis wrote the Discussion section and significantly contributed to the rest of the text. The author of the thesis was the proposal PI of the *HST* data, used in the article.

Chapter 3

Main results and outlook

Black hole accretion discs are among the most efficient energy converters. Transformation of the gravitational energy into radiation proceeds here via sheer viscosity, which arises from the differential rotation. Interestingly, it is relatively easier to put plausible limits on the magnitude of the viscosity, than to understand its origin. A substantial progress in accretion disc modelling was achieved after the work of Shakura and Sunyaev (1973), which connected the angular momentum transporting stress to the disc properties through the famous α-parameter. This is, however, only a prescription, which does not address the question about the nature of viscosity. A number of physical mechanisms responsible for the extraction of the angular momentum were proposed afterwords (see review in Blaes, 2014), but only the magnetorotational turbulence (Balbus and Hawley, 1991) might be described by the α prescription. The value of α-parameter can be obtained with numerical simulations (Brandenburg et al., 1996; Stone et al., 1996).

The accretion picture in BH X-ray binaries was lately advanced by consideration of radiatively inefficient accretion regimes, beginning with pioneering works by Shapiro et al. (1976) and Ichimaru (1977), later being developed and improved by Narayan and Yi (1994, 1995). An extensive review on the more recent advances and the inclusion of relativistic outflow/jet models (the modern jet simulations are mostly based on the mechanism originally proposed by Blandford and Znajek 1977) is given by Yuan and Narayan (2014). Similar mechanisms operate in active galactic nuclei, in the vicinity of supermassive black holes (Zdziarski et al., 1997). The properties of radiatively inefficient flows are mainly probed by the magnetohydrodynamic simulations, but the main difficulty here is that the gas densities are often so low that the plasma becomes collisionless. The (more sophisticated) kinetic treatment is then required to check that the relevant physics is captured.

Another class of problems concerns the radiation processes in BH binaries. Despite of our knowledge about principle emission components, the details of their manifestation and possible interaction are still being actively debated. Current challenges include the hard-state accretion/ejection geometry, the physics of state transitions and the nature of MeV emission. The

wide span of related problems can be reduced to the following questions:

- What are the processes shaping the broadband spectrum from radio to γ-rays? What is the relative role of the jet versus the hot accretion flow at these energies?
- What is the nature of variability in BH binaries? How are the variability spectra formed at different wavelengths?
- How is the gravitational energy transformed to relativistic electrons and what is the efficiency of this process? What are the resulting particle distributions? How do relativistic particles affect the dynamical structure of the inner flow?
- Which processes trigger state transitions? How do the transitions proceed and why do some BH binaries show the transitions, while others do not?

In the framework of this list, the present thesis deals with the following sub-problems: the origin of the UV/optical/infrared emission, broadband noise and QPOs at these wavelengths and their relation to the X-ray temporal properties. We considered them through the prism of the hot accretion flow scenario. The key ingredient which distinguishes our model from other radiatively inefficient accretion flows, is presence of a small amount of non-thermal particles. These particles give rise to the MeV radiation, but at the same time substantially contribute to the emission at longer wavelengths (optical, infrared), complementing here the disc/jet radiation. We investigated the temporal properties of such a flow with the main stress on the multiwavelength interconnection, specifically the optical/X-ray cross-correlation and common QPO mechanisms. We found that they can adequately describe the observed characteristics. The proposed model, however, is not constructed from the first principles and thus cannot be claimed to be a unique solution for the aforementioned questions. Its main weakness is the phenomenological prescription of the acceleration mechanism. It is not clear whether a high efficiency of this mechanism can be maintained in a physically realistic situation. Another important issue is how much the hot flow structure will change under the influence of non-thermal particles, which trigger faster cooling, thus likely changing the geometrical thickness of the flow.

My future research will be devoted to development of the first-principle accretion flow model with a fraction of non-thermal electrons. The first step in this direction will be to include the description of dynamical quantities (such as electron density, ion temperature and velocity) by performing magnetohydrodynamic simulations with hybrid particles. The equations describing the system are the same as in other radiatively inefficient accretion flows, with the main difference being that the electrons are not thermal

anymore. The electron distribution will be computed self-consistently with the emitted spectrum at each radius accounting for all relevant processes: acceleration, heating, cooling (by Compton scattering, synchrotron emission and bremsstrahlung) and thermalization (by Coulomb collisions, synchrotron self-absorption, and Compton scattering). The emitted spectra will be computed by solving two-dimensional radiation transport equations in a realistic flow geometry using electron distributions computed at a previous step. The solution for equations for electrons and photons will be iterated until a self-consistent solution is found. The next step will be to accurately calculate the electron acceleration. An important role here can be played by the cross-scale phenomena (such as magnetic field reconnection) and collisionless plasma effects, which cannot be probed by fluid simulations. Using the knowledge of the macroscopic hot flow structure obtained from the previous step, we can then check its microscopic conditions using particle-in-cell simulations.

The development of such a model will allow us to address the questions uncovered in the PhD studies, such as, how the non-thermal particles in BH binaries are accelerated and what is the geometry of the inner part of the accretion flow and how it evolves during state transitions. I also plan to organize a systematic study of the optical, infrared, UV and X-ray variability of BH binaries, which seems to be a clue to the accretion/ejection enigma.

Bibliography

S.A. Balbus, J.F. Hawley, A powerful local shear instability in weakly magnetized disks. I - Linear analysis. II - Nonlinear evolution. ApJ **376**, 214–233 (1991). doi:10.1086/170270

O. Blaes, General Overview of Black Hole Accretion Theory. SSRv, in press (2014). doi:10.1007/s11214-013-9985-6

R.D. Blandford, R.L. Znajek, Electromagnetic extraction of energy from Kerr black holes. MNRAS **179**, 433–456 (1977)

A. Brandenburg, A. Nordlund, R.F. Stein, U. Torkelsson, The Disk Accretion Rate for Dynamo-generated Turbulence. ApJ **458**, 45 (1996). doi:10.1086/309913

M.M. Buxton, C.D. Bailyn, H.L. Capelo, R. Chatterjee, T. Dinçer, E. Kalemci, J.A. Tomsick, Optical and Near-infrared Monitoring of the Black Hole X-ray Binary GX 339–4 during 2002-2010. AJ **143**, 130 (2012). doi:10.1088/0004-6256/143/6/130

J. Casares, P.G. Jonker, Mass Measurements of Stellar and Intermediate-Mass Black Holes. SSRv, in press (2014). doi:10.1007/s11214-013-0030-6

J. Casares, I. Negueruela, M. Ribó, I. Ribas, J.M. Paredes, A. Herrero, S. Simón-Díaz, A Be-type star with a black-hole companion. Nature **505**, 378–381 (2014). doi:10.1038/nature12916

P. Casella, T. Belloni, L. Stella, The ABC of Low-Frequency Quasi-periodic Oscillations in Black Hole Candidates: Analogies with Z Sources. ApJ **629**, 403–407 (2005). doi:10.1086/431174

P. Casella, T. Belloni, J. Homan, L. Stella, A study of the low-frequency quasi-periodic oscillations in the X-ray light curves of the black hole candidate XTE J1859+226. A&A **426**, 587–600 (2004). doi:10.1051/0004-6361:20041231

P.A. Charles, M.J. Coe, Optical, Ultraviolet and Infrared Observations of X-ray Binaries, in *Compact stellar X-ray sources, Cambridge Astrophysics Series, No. 39*, ed. by W.H.G. Lewin, M. van der Klis (Cambridge University Press, Cambridge, 2006), pp. 215–265

S. Chaty, C.A. Haswell, J. Malzac, R.I. Hynes, C.R. Shrader, W. Cui, Multi-wavelength observations revealing the evolution of the outburst of the black hole XTE J1118+480. MNRAS **346**, 689–703 (2003). doi:10.1111/j.1365-2966.2003.07115.x

C.Y. Chiang, C. Done, M. Still, O. Godet, An additional soft X-ray component in the dim low/hard state of black hole binaries. MNRAS **403**, 1102–1112 (2010). doi:10.1111/j.1365-2966.2009.16129.x

S. Corbel, H. Aussel, J.W. Broderick, P. Chanial, M. Coriat, et al., Formation of the compact jets in the black hole GX 339–4. MNRAS **431**, 107–111 (2013).

doi:10.1093/mnrasl/slt018

J.M. Corral-Santana, J. Casares, T. Muñoz-Darias, P. Rodríguez-Gil, T. Shahbaz, M.A.P. Torres, C. Zurita, A.A. Tyndall, A Black Hole Nova Obscured by an Inner Disk Torus. Science **339**, 1048–1051 (2013). doi:10.1126/science.1228222

C. Cunningham, Returning radiation in accretion disks around black holes. ApJ **208**, 534–549 (1976). doi:10.1086/154636

C. Done, Observational Characteristics of Accretion Onto Black Holes, in *XXI Canary Islands Winter School of Astrophysics*, ed. by T. Shahbaz (Cambridge University Press, Cambridge, 2010), pp. 184–226

C. Done, M. Gierliński, Observing the effects of the event horizon in black holes. MNRAS **342**, 1041–1055 (2003). doi:10.1046/j.1365-8711.2003.06614.x

C. Done, M. Gierliński, A. Kubota, Modelling the behaviour of accretion flows in X-ray binaries. Everything you always wanted to know about accretion but were afraid to ask. A&ARv **15**, 1–66 (2007). doi:10.1007/s00159-007-0006-1

M. Durant, P. Gandhi, T. Shahbaz, A.P. Fabian, J. Miller, V.S. Dhillon, T.R. Marsh, SWIFT J1753.5–0127: A Surprising Optical/X-ray Cross-Correlation Function. ApJ **682**, 45–48 (2008). doi:10.1086/590906

M. Durant, P. Gandhi, T. Shahbaz, H.H. Peralta, V.S. Dhillon, Multiwavelength spectral and high time resolution observations of SWIFTJ1753.5–0127: new activity? MNRAS **392**, 309–324 (2009). doi:10.1111/j.1365-2966.2008.14044.x

A. Einstein, Die Feldgleichungen der Gravitation. Sitzungsberichte der Königlich Preußischen Akademie der Wissenschaften (Berlin), Seite 844-847 (1915)

A. Einstein, Die Grundlage der allgemeinen Relativitätstheorie. Annalen der Physik **354**, 769–822 (1916). doi:10.1002/andp.19163540702

A.A. Esin, J.E. McClintock, J.J. Drake, M.R. Garcia, C.A. Haswell, R.I. Hynes, M.P. Muno, Modeling the Low-State Spectrum of the X-ray Nova XTE J1118+480. ApJ **555**, 483–488 (2001). doi:10.1086/321450

P.C. Fragile, O.M. Blaes, P. Anninos, J.D. Salmonson, Global General Relativistic Magnetohydrodynamic Simulation of a Tilted Black Hole Accretion Disk. ApJ **668**, 417–429 (2007). doi:10.1086/521092

J. Frank, A. King, D.J. Raine, *Accretion Power in Astrophysics* (Cambridge University Press, Cambridge, 2002)

E. Gallo, S. Migliari, S. Markoff, J.A. Tomsick, C.D. Bailyn, S. Berta, R. Fender, J.C.A. Miller-Jones, The Spectral Energy Distribution of Quiescent Black Hole X-ray Binaries: New Constraints from Spitzer. ApJ **670**, 600–609 (2007). doi:10.1086/521524

P. Gandhi, V.S. Dhillon, M. Durant, A.C. Fabian, A. Kubota, et al., Rapid optical and X-ray timing observations of GX339–4: multicomponent optical variability in the low/hard state. MNRAS **407**, 2166–2192 (2010). doi:10.1111/j.1365-2966.2010.17083.x

P. Gandhi, A.W. Blain, D.M. Russell, P. Casella, J. Malzac, et al., A Variable Mid-infrared Synchrotron Break Associated with the Compact Jet in GX 339–4. ApJ **740**, 13 (2011). doi:10.1088/2041-8205/740/1/L13

M. Gierliński, C. Done, K. Page, Reprocessing of X-rays in the outer accretion disc of the black hole binary XTE J1817–330. MNRAS **392**, 1106–1114 (2009). doi:10.1111/j.1365-2966.2008.14166.x

M. Gilfanov, X-ray Emission from Black-hole Binaries, in *The Jet Paradigm, Lecture*

Notes in Physics, vol. 794, ed. by T. Belloni (Springer, Berlin, 2010), pp. 17–51

D. Gondek, A.A. Zdziarski, W.N. Johnson, I.M. George, K. McNaron-Brown, P. Magdziarz, D. Smith, D.E. Gruber, The average X-ray/gamma-ray spectrum of radio-quiet Seyfert 1s. MNRAS **282**, 646–652 (1996)

D.C. Hannikainen, R.W. Hunstead, D. Campbell-Wilson, K. Wu, D.J. McKay, D.P. Smits, R.J. Sault, Radio Emission from GRO J1655–40 during the 1994 Jet Ejection Episodes. ApJ **540**, 521–534 (2000). doi:10.1086/309294

L.C. Ho, Nuclear Activity in Nearby Galaxies. ARA&A **46**, 475–539 (2008). doi:10.1146/annurev.astro.45.051806.110546

J. Homan, R. Wijnands, M. van der Klis, T. Belloni, J. van Paradijs, M. Klein-Wolt, R. Fender, M. Méndez, Correlated X-ray Spectral and Timing Behavior of the Black Hole Candidate XTE J1550–564: A New Interpretation of Black Hole States. ApJS **132**, 377–402 (2001). doi:10.1086/318954

R.I. Hynes, C.W. Mauche, C.A. Haswell, C.R. Shrader, W. Cui, S. Chaty, The X-ray Transient XTE J1118+480: Multiwavelength Observations of a Low-State Minioutburst. ApJ **539**, 37–40 (2000). doi:10.1086/312836

R.I. Hynes, C.A. Haswell, S. Chaty, C.R. Shrader, W. Cui, The evolving accretion disc in the black hole X-ray transient XTE J1859+226. MNRAS **331**, 169–179 (2002). doi:10.1046/j.1365-8711.2002.05175.x

R.I. Hynes, C.A. Haswell, W. Cui, C.R. Shrader, K. O'Brien, S. Chaty, D.R. Skillman, J. Patterson, K. Horne, The remarkable rapid X-ray, ultraviolet, optical and infrared variability in the black hole XTE J1118+480. MNRAS **345**, 292–310 (2003). doi:10.1046/j.1365-8711.2003.06938.x

R.I. Hynes, C.K. Bradley, M. Rupen, E. Gallo, R.P. Fender, J. Casares, C. Zurita, The quiescent spectral energy distribution of V404 Cyg. MNRAS **399**, 2239–2248 (2009). doi:10.1111/j.1365-2966.2009.15419.x

S. Ichimaru, Bimodal behavior of accretion disks - Theory and application to Cygnus X-1 transitions. ApJ **214**, 840–855 (1977). doi:10.1086/155314

J.N. Imamura, J. Kristian, J. Middleditch, T.Y. Steiman-Cameron, The 8 second optical quasi-periodic oscillations in GX 339–4. ApJ **365**, 312–316 (1990). doi:10.1086/169484

A. Ingram, C. Done, P.C. Fragile, Low-frequency quasi-periodic oscillations spectra and Lense-Thirring precession. MNRAS **397**, 101–105 (2009). doi:10.1111/j.1745-3933.2009.00693.x

R.K. Jain, C.D. Bailyn, J.A. Orosz, J.E. McClintock, R.A. Remillard, Multiwavelength Observations of the Black Hole Candidate XTE J1550–564 during the 2000 Outburst. ApJ **554**, 181–184 (2001). doi:10.1086/321700

W.N. Johnson, K. McNaron-Brown, J.D. Kurfess, A.A. Zdziarski, P. Magdziarz, N. Gehrels, Long-Term Monitoring of NGC 4151 by OSSE. ApJ **482**, 173 (1997). doi:10.1086/304148

G. Kanbach, C. Straubmeier, H.C. Spruit, T. Belloni, Correlated fast X-ray and optical variability in the black-hole candidate XTE J1118+480. Nature **414**, 180–182 (2001)

R.P. Kerr, Gravitational field of a spinning mass as an example of algebraically special metrics. Phys. Rev. Lett. **11**, 237–238 (1963). doi:10.1103/PhysRevLett.11.237

P. Lubiński, A.A. Zdziarski, R. Walter, S. Paltani, V. Beckmann, S. Soldi, C. Ferrigno,

T. Courvoisier, Extreme flux states of NGC 4151 observed with INTEGRAL. MNRAS **408**, 1851–1865 (2010). doi:10.1111/j.1365-2966.2010.17251.x

D. Malyshev, A.A. Zdziarski, M. Chernyakova, High-energy gamma-ray emission from Cyg X-1 measured by Fermi and its theoretical implications. MNRAS **434**, 2380–2389 (2013). doi:10.1093/mnras/stt1184

J. Malzac, R. Belmont, The synchrotron boiler and the spectral states of black hole binaries. MNRAS **392**, 570–589 (2009). doi:10.1111/j.1365-2966.2008.14142.x

J. Malzac, A. Merloni, A.C. Fabian, Jet-disc coupling through a common energy reservoir in the black hole XTE J1118+480. MNRAS **351**, 253–264 (2004). doi:10.1111/j.1365-2966.2004.07772.x

J.E. McClintock, R.A. Remillard, Black Hole Binaries, in *Compact stellar X-ray sources, Cambridge Astrophysics Series, No. 39*, ed. by W.H.G. Lewin, M. van der Klis (Cambridge University Press, Cambridge, 2006), pp. 157–213

F. Meyer, B.F. Liu, E. Meyer-Hofmeister, Black hole X-ray binaries: a new view on soft-hard spectral transitions. A&A **354**, 67–70 (2000)

C. Motch, M.J. Ricketts, C.G. Page, S.A. Ilovaisky, C. Chevalier, Simultaneous X-ray/optical observations of GX 339–4 during the May 1981 optically bright state. A&A **119**, 171–176 (1983)

C. Motch, S.A. Ilovaisky, C. Chevalier, P. Angebault, An IR, optical and X-ray study of the two state behaviour of GX 339–4. SSRv **40**, 219–224 (1985). doi:10.1007/BF00212888

T. Muñoz-Darias, M. Coriat, D.S. Plant, G. Ponti, R.P. Fender, R.J.H. Dunn, Inclination and relativistic effects in the outburst evolution of black hole transients. MNRAS **432**, 1330–1337 (2013). doi:10.1093/mnras/stt546

R. Narayan, J.E. McClintock, Observational Evidence for Black Holes, in *General Relativity and Gravitation: A Centennial Perspective*, ed. by A. Ashtekar, J. Berger and M.A.H. MacCallum (Cambridge University Press, Cambridge, 2014), arXiv:1312.6698

R. Narayan, I. Yi, Advection-dominated accretion: A self-similar solution. ApJ **428**, 13–16 (1994). doi:10.1086/187381

R. Narayan, I. Yi, Advection-dominated Accretion: Underfed Black Holes and Neutron Stars. ApJ **452**, 710–735 (1995). doi:10.1086/176343

K. Pounds, Searching for Black Holes in Space. SSRv, in press (2014). doi:10.1007/s11214-013-0011-9

J. Poutanen, A. Veledina, Modelling Spectral and Timing Properties of Accreting Black Holes: The Hybrid Hot Flow Paradigm. SSRv, in press (2014). doi:10.1007/s11214-013-0033-3

J. Poutanen, I. Vurm, On the Origin of Spectral States in Accreting Black Holes. ApJ **690**, 97–100 (2009). doi:10.1088/0004-637X/690/2/L97

R.A. Remillard, J.E. McClintock, X-ray Properties of Black-Hole Binaries. ARA&A **44**, 49–92 (2006). doi:10.1146/annurev.astro.44.051905.092532

E.E. Salpeter, Accretion of Interstellar Matter by Massive Objects. ApJ **140**, 796–800 (1964). doi:10.1086/147973

K. Schwarzschild, On the Gravitational Field of a Mass Point According to Einstein's Theory. Abh. Konigl. Preuss. Akad. Wissenschaften zu Berlin, Phys.-Math. Klasse, 189–196 (1916)

K. Schwarzschild, On the gravitational field of a mass point according to Einstein's

theory. arxiv: physics/9905030 (1999)
N.I. Shakura, R.A. Sunyaev, Black holes in binary systems. Observational appearance. A&A **24**, 337–355 (1973)
S.L. Shapiro, A.P. Lightman, D.M. Eardley, A two-temperature accretion disk model for Cygnus X-1 - Structure and spectrum. ApJ **204**, 187–199 (1976)
M. Shidatsu, Y. Ueda, F. Tazaki, T. Yoshikawa, T. Nagayama, et al., X-ray and Near-Infrared Observations of GX 339–4 in the Low/Hard State with Suzaku and IRSF. PASJ **63**, 785 (2011)
M.A. Sobolewska, I.E. Papadakis, C. Done, J. Malzac, Evidence for a change in the X-ray radiation mechanism in the hard state of Galactic black holes. MNRAS **417**, 280–288 (2011). doi:10.1111/j.1365-2966.2011.19209.x
T.Y. Steiman-Cameron, J.D. Scargle, J.N. Imamura, J. Middleditch, 16 Second Optical Quasi-periodic Oscillations in GX 339–4. ApJ **487**, 396–401 (1997). doi:10.1086/304601
J.M. Stone, J.F. Hawley, C.F. Gammie, S.A. Balbus, Three-dimensional Magnetohydrodynamical Simulations of Vertically Stratified Accretion Disks. ApJ **463**, 656 (1996). doi:10.1086/177280
R. Sunyaev, M. Revnivtsev, Fourier power spectra at high frequencies: a way to distinguish a neutron star from a black hole. A&A **358**, 617–623 (2000)
A. Veledina, J. Poutanen, A. Ingram, A Unified Lense-Thirring Precession Model for Optical and X-ray Quasi-periodic Oscillations in Black Hole Binaries. ApJ **778**, 165 (2013). doi:10.1088/0004-637X/778/2/165
A. Veledina, J. Poutanen, I. Vurm, A Synchrotron Self-Compton-Disk Reprocessing Model for Optical/X-ray Correlation in Black Hole X-ray Binaries. ApJ **737**, 17 (2011). doi:10.1088/2041-8205/737/1/L17
A. Veledina, J. Poutanen, I. Vurm, Hot accretion flow in black hole binaries: a link connecting X-rays to the infrared. MNRAS **430**, 3196–3212 (2013). doi:10.1093/mnras/stt124
A. Veledina, I. Vurm, J. Poutanen, A self-consistent hybrid Comptonization model for broad-band spectra of accreting supermassive black holes. MNRAS **414**, 3330–3343 (2011). doi:10.1111/j.1365-2966.2011.18635.x
G. Wardziński, A.A. Zdziarski, Effects of non-thermal tails in Maxwellian electron distributions on synchrotron and Compton processes. MNRAS **325**, 963–971 (2001). doi:10.1046/j.1365-8711.2001.04387.x
J.A. Wheeler, Our universe: the known and the unknown. American Scientist **56**, 1–20 (1968)
F. Yuan, R. Narayan, Hot Accretion Flows Around Black Holes. ARA&A **52**, 529–588 (2014)
A.A. Zdziarski, M. Gierliński, Radiative Processes, Spectral States and Variability of Black-Hole Binaries. Progress of Theoretical Physics Supplement **155**, 99–119 (2004). doi:10.1143/PTPS.155.99
A.A. Zdziarski, P. Lubiński, M. Sikora, The MeV spectral tail in Cyg X-1 and optically thin emission of jets. MNRAS **423**, 663–675 (2012). doi:10.1111/j.1365-2966.2012.20903.x
A.A. Zdziarski, J. Mikołajewska, K. Belczyński, Cyg X-3: a low-mass black hole or a neutron star. MNRAS **429**, 104–108 (2013). doi:10.1093/mnrasl/sls035
A.A. Zdziarski, W.N. Johnson, J. Poutanen, P. Magdziarz, M. Gierlinski, X-rays and

Gamma-rays from Accretion Flows Onto Black Holes in Seyferts and X-ray Binaries, in *ESA SP-382: The Transparent Universe*, ed. by C. Winkler, T.J.-L. Courvoisier, P. Durouchoux (ESA, Noordwijk, 1997), pp. 373–380

A.A. Zdziarski, J. Poutanen, W.S. Paciesas, L. Wen, Understanding the Long-Term Spectral Variability of Cygnus X-1 with Burst and Transient Source Experiment and All-Sky Monitor Observations. ApJ **578**, 357–373 (2002). doi:10.1086/342402

Y.B. Zel'dovich, The Fate of a Star and the Evolution of Gravitational Energy Upon Accretion. Soviet Physics Doklady **9**, 195 (1964)

Original publications

Monthly Notices
of the
ROYAL ASTRONOMICAL SOCIETY

MNRAS **430,** 3196–3212 (2013) doi:10.1093/mnras/stt124

Hot accretion flow in black hole binaries: a link connecting X-rays to the infrared

Alexandra Veledina,[1]⋆ Juri Poutanen[1] and Indrek Vurm[2,3]

[1]*Astronomy Division, Department of Physics, PO Box 3000, FIN-90014 University of Oulu, Finland*
[2]*Racah Institute of Physics, Hebrew University of Jerusalem, 91904 Jerusalem, Israel*
[3]*Tartu Observatory, 61602 Tõravere, Tartumaa, Estonia*

Accepted 2013 January 18. Received 2013 January 18; in original form 2012 September 30

ABSTRACT

Multiwavelength observations of Galactic black hole transients have opened a new path to understanding the physics of the innermost parts of the accretion flows. While the processes giving rise to their X-ray continuum have been studied extensively, the emission in the optical and infrared (OIR) energy bands was less investigated and remains poorly understood. The standard accretion disc, which may contribute to the flux at these wavelengths, is not capable of explaining a number of observables: the infrared excesses, fast OIR variability and a complicated correlation with the X-rays. It was suggested that these energy bands are dominated by the jet emission; however, this scenario does not work in a number of cases. We propose here an alternative, namely that most of the OIR emission is produced by the extended hot accretion flow. In this scenario, the OIR bands are dominated by the synchrotron radiation from the non-thermal electrons. An additional contribution is expected from the outer irradiated part of the accretion disc heated by the X-rays. We discuss the properties of the model and compare them to the data. We show that the hot-flow scenario is consistent with many of the observed spectral data, at the same time naturally explaining X-ray timing properties, fast OIR variability and its correlation with the X-rays.

Key words: accretion, accretion discs – black hole physics – radiation mechanisms: non-thermal – X-rays: binaries.

1 INTRODUCTION

Although the black hole X-ray binaries (BHBs) have been intensively studied for over four decades, many problems remain unsolved. Among the most debated topics are the physics of state transitions, the interplay between the cold accretion disc and the hot medium, the role of the jet, the source of rapid variability, radiative processes shaping the broad-band spectrum and, specifically, the nature of various components contributing to its different parts. When addressing the latter problem, three distinct components are usually considered: the standard (or irradiated) cool accretion disc, the hot inner flow (or corona) and the jet. Their relative contribution depends on the spectral energy range and varies with time and can be assessed by performing (quasi-) simultaneous multiwavelength observations.

Over the past decade, numerous multiwavelength campaigns have resulted in a significant progress in the field. Broad-band radio-to-X-ray spectral energy distributions for many black hole (BH) low-mass X-ray binaries (LMXBs) were constructed (e.g. Hynes et al. 2000; McClintock et al. 2001; Chaty et al. 2003; Cadolle Bel et al. 2007, 2011; Durant et al. 2009). In addition to the spectral information, data on the fast variability are now available in the X-rays as well as at lower energies. The light curves in the optical/infrared (OIR) and ultraviolet (UV) bands are significantly correlated with the X-rays (Kanbach et al. 2001; Hynes et al. 2003, 2006, 2009b; Durant et al. 2008, 2011; Gandhi et al. 2010) showing a complex shape of the cross-correlation function (CCF). It provides an important information on the interrelation between various components and gives clues to their physical origin.

The radio emission in BHBs is likely dominated by the jet as supported by the observed linear polarization at a 1–3 per cent level in the hard state (Corbel et al. 2000) and up to 10 per cent in spatially resolved components during the transient events (Fender et al. 1999; Hannikainen et al. 2000). In addition, a relatively high luminosity, requiring the size exceeding the typical binary separation (Fender 2006), as well as the detection of superluminal motion (Mirabel & Rodríguez 1994) leans towards this interpretation. The power-law-like radio spectrum is often attributed to synchrotron emission of an inhomogeneous source in analogy with the extragalactic jets (Blandford & Königl 1979). In blazars, the jet is also responsible for the X-ray and γ-ray production (Königl 1981;

⋆ E-mail: alexandra.veledina@oulu.fi

Dermer & Schlickeiser 1993; Sikora, Begelman & Rees 1994; Stern & Poutanen 2006). On the contrary, the jets in BHBs are unlikely to be responsible for bulk of the X-ray photons (for comprehensive discussion, see Poutanen & Zdziarski 2003; Zdziarski et al. 2003). Furthermore, the medium producing the X-ray radiation can neither form the base of the jet (Malzac, Belmont & Fabian 2009) nor be a jet-dominated accretion flow (Maccarone 2005).

The spectra of hard-state BHBs constitute a power law in the X-ray band with a stable spectral slope and ubiquitous sharp cutoff at $\sim$100 keV (Gierlinski et al. 1997; Zdziarski et al. 1998; Ibragimov et al. 2005). It is broadly accepted to be produced by thermal Comptonization (e.g. Poutanen 1998; Zdziarski & Gierliński 2004). Additionally, a Compton reflection feature originating from cool opaque matter (likely the cool accretion disc) is often detected. Its strength is correlated with the X-ray slope (Zdziarski, Lubinski & Smith 1999; Zdziarski et al. 2003), with the width of the iron line as well as with the quasi-periodic oscillation (QPO) frequency (Gilfanov, Churazov & Revnivtsev 1999; Revnivtsev, Gilfanov & Churazov 2001; Gilfanov 2010). These observations support a view that the X-rays are produced in the very vicinity of the BH, in a hot flow surrounded by the cold disc. In this scenario, variations in the mass accretion rate are correlated with the cool disc truncation radius (Esin, McClintock & Narayan 1997; Poutanen, Krolik & Ryde 1997), with the flux of soft seed photons that determines the spectral slope and with the reflection amplitude that scales with the solid angle at which the cold disc is seen from the hot flow. Correlations with the QPO frequency are also naturally explained if the oscillations are produced in the innermost part of the accretion flow by Lense–Thirring precession (Ingram & Done 2011). Such a scenario would favour models where seed photons for Comptonization are provided by the standard Shakura & Sunyaev (1973) accretion disc. However, the hot flow itself also produces synchrotron radiation that can contribute or even dominate the seed photon flux to the Comptonizing medium (Ghisellini, Haardt & Svensson 1998; Wardziński & Zdziarski 2000, 2001; Malzac & Belmont 2009; Poutanen & Vurm 2009; Sobolewska et al. 2011; Veledina, Vurm & Poutanen 2011b).

Discovery of the high-energy (MeV) tails in the hard-state accreting BHBs (McConnell et al. 1994, 2002; Ling et al. 1997; Droulans et al. 2010; Jourdain, Roques & Malzac 2012b) suggests the presence of non-thermal particles in these systems. Such particles may be produced in a hot inner flow or a jet. Their association with the jet, however, is inconsistent with detections of even more prominent high-energy non-thermal tails in the soft state of BHBs (Grove et al. 1998; Gierliński et al. 1999; Zdziarski et al. 2001; McConnell et al. 2002; Gierliński & Done 2003), when the jet is quenched (Fender, Belloni & Gallo 2004). In this state the inner flow is likely to be replaced by a corona, which remains here the only alternative. In the hard state, the entire X/γ-ray spectra can be produced by hybrid (thermal plus non-thermal) electrons via the synchrotron self-Compton (SSC) mechanism (Malzac & Belmont 2009; Poutanen & Vurm 2009). The thermal part of the particle distribution is responsible for the power-law-like Comptonization continuum with the sharp cutoff, while the non-thermal particles both produce seed synchrotron photons for Comptonization and contribute to the MeV energies via inverse Compton process. Transition to the soft state can then be associated with the rising role of the disc as a source of seed photons, which increases Compton cooling and causes changes in the electron distribution from mostly thermal to nearly non-thermal (Poutanen & Coppi 1998; Poutanen & Vurm 2009; Veledina et al. 2011b). The SSC mechanism was also shown to be consistent with the peculiar optical variability, which in a number of BHBs is partially anticorrelated with the X-ray emission (Kanbach et al. 2001; Durant et al. 2008; Gandhi et al. 2008). Namely, the increasing mass accretion rate results in a higher X-ray and a lower synchrotron OIR emission, because of an increasing role of synchrotron self-absorption within the source (Veledina, Poutanen & Vurm 2011a).

The OIR spectra of LMXBs often show an excess above the standard accretion disc (e.g. Hynes et al. 2000, 2002; Gelino, Gelino & Harrison 2010). In some cases, the spectrum can be described by a power law of index close to zero (i.e. $F_\nu \propto \nu^0$). Such data were previously explained by additional contribution from the irradiated disc (Gierliński, Done & Page 2009), dust heated by the secondary star (Muno & Mauerhan 2006) or the jet (Hynes et al. 2002; Gallo et al. 2007). We show that they can also be explained by the synchrotron radiation from the non-thermal particles in the hot flow. However, in some cases the OIR fluxes are higher than expected from any candidate alone (Chaty et al. 2003; Gandhi et al. 2010), suggesting contribution of at least two components simultaneously. This can be a reason for the complex shape of the optical/X-ray CCF (Veledina et al. 2011a).

The general shape of the time-averaged X/γ-ray spectrum of BHB can be well explained in terms of a one-zone hybrid Comptonization model. However, the short-term spectral variability, reflected in hard X-ray time-lags (Miyamoto & Kitamoto 1989; Nowak et al. 1999a), and asymmetries of the CCF between hard and soft X-ray energy bands (Priedhorsky et al. 1979; Nolan et al. 1981; Maccarone, Coppi & Poutanen 2000) suggest that a number of regions simultaneously contribute to the total spectrum. The observed logarithmic dependence of the time-lags on photon energy can be phenomenologically explained by spectral pivoting (Poutanen & Fabian 1999). Theoretical model capable of explaining the observed timing properties was proposed by Kotov, Churazov & Gilfanov (2001) and further developed in Arévalo & Uttley (2006). It assumes that the X-ray spectrum is produced in the hot flow/corona, present in a range of radii, by Comptonization of the disc photons. The power-law slope of the locally emitted spectrum depends on the distance from the BH: the hardest spectra are produced in the innermost region due to the lack of photons from the cold disc. The main source of the short-term variability in BHs is believed to be fluctuations in the mass accretion rate, propagating through the hot accretion flow (Lyubarskii 1997). The hard time-lags thus naturally appear from the perturbations propagating from the larger distances to the vicinity of the BH. The model of Kotov et al. (2001) considers thermal Comptonization of the disc photons, but as we show below the results hold in the framework of hybrid Comptonization, with the synchrotron mechanism as the major seed photon supplier.

It is clear that the complete description of the timing and spectral properties of BHBs requires a multizone model. In this paper, we construct such a model for the extended hot accretion flow. This model is somewhat analogous to the inhomogeneous synchrotron models developed for extragalactic jets (Marscher 1977; Blandford & Königl 1979). The difference is that in our model the emission originates from an inflow, not an outflow. The advantage of the hot-flow model is that the energy input can be estimated from the available gravitational energy transferred to particles via some mechanism, while in the jet scenario the energy release is an arbitrary function.

Similarly to the previously studied one-zone models (Malzac & Belmont 2009; Poutanen & Vurm 2009; Veledina et al. 2011b), we assume that gravitational energy is dissipated in the flow and injected in the form of electrons having a power-law distribution (while the steady-state electron distribution is mostly thermal).

We compute the steady-state particle and photon distributions self-consistently by solving corresponding kinetic equations. Our aim is to understand the broad-band spectral properties of such a flow and compare them to the BHB data.

In Section 2, we give constraints on the size of the hot accretion flow that can be derived from the observed level of the OIR emission. We first construct an analytical model for the hot flow assuming power-law radial dependences of the main parameters. We then proceed to the numerical model where the electron distributions and the emitted spectra are computed self-consistently. In Section 3, we present the results of simulations for the model corresponding to the hard state of BHBs. We show that the multizone hot disc model produces flat OIR spectra resulting from synchrotron emission of non-thermal electrons at different radii. We then model the state transitions by decreasing the truncation radius of the hot flow. In Section 4, we provide a detailed analysis of the observational data and compare them to our model and to the jet scenario. We summarize our finding in Section 5.

2 ANALYTICAL MODEL

2.1 Geometry

Many observational properties suggest that the standard disc in the hard state is truncated far away from the central object (for a detailed description and challenges to the truncated disc scenario, see the review by Done, Gierliński & Kubota 2007). The inner part is probably occupied by some type of geometrically thick, optically thin, hot accretion flow, which is responsible for the X-ray Comptonization continuum, but also contributes to the longer wavelengths.

One can roughly estimate the minimum size of the source that is required to produce the observed OIR luminosity. Let us first assume that OIR emission is produced by synchrotron radiation from thermal particles (as for example was discussed earlier by Fabian et al. 1982). The typical temperature of the electron gas determined from the Comptonization cutoff is $kT_e \sim 100$ keV and the typical infrared (IR) luminosity at 1 eV can reach $\nu L_{\nu,1\ \mathrm{eV}} = 10^{36}$ erg s^{-1}. Thus, we get the minimum size from the Rayleigh–Jeans formula

$$R = \left(\frac{\nu L_\nu}{8\pi^2 \nu (\nu/c)^2 k T_e} \right)^{1/2} \approx 2.3 \times 10^9 \text{ cm}. \quad (1)$$

For a 10 $M_\odot$ BH, assumed in all calculations hereafter, this corresponds to 750 R_S (here $R_S = 2GM/c^2$ is the Schwarzschild radius). However, many observed properties [e.g. iron line width, amplitude of Compton reflection, drop of the iron line equivalent width with the Fourier frequency, see Gilfanov (2010), as well as dependence of the X-ray time-lags on energy below ∼1 keV, Uttley et al. (2011)] suggest that the cold disc in the hard state is truncated at a smaller radius. Moreover, in order to produce sufficient amount of seed photons for Comptonization, an extremely high magnetic field is required in addition to the large source size (see Appendix B1 and also, e.g., Di Matteo, Celotti & Fabian 1999; Merloni, Di Matteo & Fabian 2000). Thus, the thermal radiation of the hot flow is unlikely to be a good candidate to produce enough OIR photons (see also Wardziński & Zdziarski 2000).

However, even a weak, energetically unimportant non-thermal tail, in addition to the mostly Maxwellian distribution, gives a significant rise to the synchrotron luminosity (e.g. Wardziński & Zdziarski 2001). For example, a tail containing only 1 per cent of the total particle energy increases it by a factor of 100. Accurate calculations (see below) show that the source size of $R \approx (30\text{–}50)R_S$, an order magnitude smaller than given by equation (1), would in principle be enough to radiate the observed OIR luminosity. Such a size is consistent with the above estimates of the truncation radius and with the typical size of the region of the gravitational energy release. It is worth noticing that a strong synchrotron emission from non-thermal particles makes it a good candidate for seed photons for Comptonization (Malzac & Belmont 2009; Poutanen & Vurm 2009), which implies that the SSC spectrum extends from the X-rays down to the OIR band with the low-energy turnover determined by the maximum extent of the hot flow.

2.2 Hard-state OIR spectra

Spectral properties of the hot flow in the OIR band can be understood from simple analytical considerations. Let us consider the flow with a constant height-to-radius ratio H/R, extending between radii $R_{\rm in}$ and $R_{\rm out}$ (see Fig. 1 for the geometry). In order to estimate the synchrotron luminosity and spectra, we assume that the electrons follow a power-law distribution in Lorentz factor $n_e(\gamma) \equiv \mathrm{d}n_e/\mathrm{d}\gamma = n_0 \gamma^{-p}$, starting from $\gamma_{\rm le} = 1$ to infinity. Deviations from the power law at low energies do not play any role, as the synchrotron emission produced by these electrons is self-absorbed. The Thomson optical depth across the disc is assumed to follow the power law $\tau(R) \propto R^{-\theta}$. For the constant H/R this is equivalent to $n_0(R) \propto \tau/R \propto R^{-\theta-1}$. We further assume that the magnetic field depends on the distance from the BH as $B(R) \propto R^{-\beta}$.

Our analytical model of the hot flow is analogous to the non-uniform synchrotron source models, previously applied to the

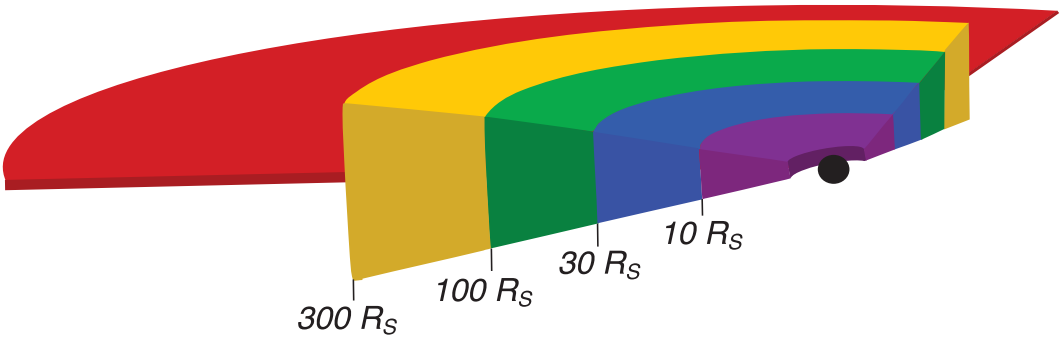

Figure 1. Schematic picture of the accretion flow inner regions. The red outer component represents the multicolour cold accretion disc, truncated at 300 Schwarzschild radii (R_S). The inner parts are occupied by a geometrically thick hot accretion flow. In our numerical model, we split the inner hot flow into four zones with outer radii $10R_S$ (violet), $30R_S$ (blue), $100R_S$ (green) and $300R_S$ (yellow).

emission from extragalactic jets (Condon & Dressel 1973; de Bruyn 1976; Marscher 1977; Blandford & Königl 1979; Königl 1981; Ghisellini, Maraschi & Treves 1985). For the parameters considered here, most of the luminosity is produced in the inner part of the source, so that the OIR spectrum is composed of emission components coming from different radii and is not dominated by the radiation from the outer regions (these two cases are illustrated in figs 2a and b in Ghisellini et al. 1985).

A region of the disc at a given radius emits synchrotron radiation, which is self-absorbed below the turnover frequency $\nu_{\rm t}$. For power-law electrons, this frequency can be calculated as (Rybicki & Lightman 1979; Wardziński & Zdziarski 2001)

$$\nu_{\rm t} = 3^{\frac{p+1}{p+4}} 2^{-\frac{6}{p+4}} \pi^{\frac{1}{p+4}} \nu_{\rm L}^{\frac{p+2}{p+4}} [G_1(p) c R r_{\rm e} n_0]^{\frac{2}{p+4}}, \quad (2)$$

where $\nu_{\rm L} = eB/(2\pi m_{\rm e} c)$ is the Larmor frequency, $G_1(p) \simeq 1$ is a combination of Euler's Gamma functions (due to averaging over electron pitch angles) and $r_{\rm e}$ is the classical electron radius. Substituting the constants, we get

$$\nu_{\rm t} \approx 3 \times 10^{15} B_6^{\frac{p+2}{p+4}} (\sigma_{\rm T} n_0 R)^{\frac{2}{p+4}} \ {\rm Hz}, \quad (3)$$

where $Q = 10^x Q_x$ in cgs units. The term in brackets can also be written as $\sigma_{\rm T} n_0 R = \tau(\gamma_{\rm t}) \gamma_{\rm t}^p$, with $\gamma_{\rm t}$ being the Lorentz factor of the electrons emitting at the turnover frequency and $\tau(\gamma_{\rm t}) = \sigma_{\rm T} R n_{\rm e}(\gamma_{\rm t})$ being the Thomson optical depth per unit Lorentz factor at $\gamma_{\rm t}$. In the latter representation, the equation is also valid for hybrid electrons (e.g. Maxwellian with a power-law tail), as long as the electrons emitting at the turnover frequency are in the power-law tail. The low-frequency cutoff for a synchrotron spectrum from power-law electrons scales as

$$\nu_{\rm t} \propto R^{-[\beta(p+2)+2\theta]/(p+4)}. \quad (4)$$

Again, for a hybrid electron distribution one should consider scaling with radius of the power-law tail (parameter θ), which can be different from scaling of the total optical depth. As immediately follows from equation (3), the turnover frequency may fall to optical and even IR wavelengths for sufficiently low magnetic field and/or Thomson optical depth.

The emission at the turnover frequency is optically thick, so the intensity is equal to the source function for the power-law electrons. For isotropic electrons, the intensity is (averaged over pitch angles)

$$I_{\nu_{\rm t}} = \frac{m_{\rm e} G_2(p)}{2\sqrt{3}} \nu_{\rm L}^{-1/2} \nu_{\rm t}^{5/2}, \quad (5)$$

where $G_2(p) \simeq 1$ (again, coming from the angle averaging). At each wavelength, there is a contribution from the optically thick and optically thin emission from different radii. For simplicity, we assume that emission from each radius contributes only to its own turnover frequency;[1] therefore, the resulting spectrum of an inhomogeneous synchrotron source constitutes a power law

$$\nu L_\nu = 4\pi^2 R^2 \nu I_\nu \approx 2 \times 10^{36} R_8^2 \ B_6^{-1/2} \ \nu_{15}^{7/2} \ {\rm erg\,s^{-1}}. \quad (6)$$

Substituting the appropriate parameter scaling and using equation (4), we get the spectral index

$$\alpha_{\rm OIR} = \frac{5\theta + \beta(2p+3) - 2p - 8}{\beta(p+2) + 2\theta}, \quad (7)$$

[1] Precise calculations of additional contribution from optically thin parts result in a slightly different normalization, while the spectral slope remains the same (see Marscher 1977).

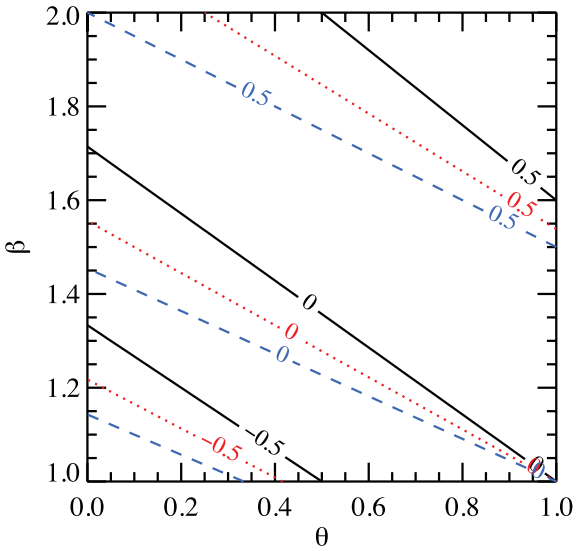

Figure 2. Contour plot of the constant index $\alpha_{\rm OIR}$ as a function of parameters β and θ for three values of electron index $p = 2$ (solid black), 3 (dotted red) and 4 (dashed blue).

where $L_\nu \propto \nu^\alpha$. In a wide range of parameters $\beta \in [1, 2]$ and $\theta \in [0, 1]$ the resulting spectral slope lies between -0.5 and 0.5 (see Fig. 2).

3 NUMERICAL MODEL

The analytical model developed in Section 2.2 describes only the OIR *synchrotron* spectra and is valid for purely power-law electrons. Such distributions may result from various acceleration mechanisms e.g. shock acceleration or magnetic reconnection. In the limit of low optical depth and weak magnetic field, the electrons are unable to cool and the shape of the distribution stays unchanged. These conditions might be satisfied in quiescent state, for which the analytical model can be applied. During the accretion outbursts, the matter density in the hot flow increases and the energy exchange and cooling processes become important; thus, the initial power-law distribution evolves. The most important mechanisms operating in the hot rarefied plasmas of the hot accretion flows are Compton scattering, synchrotron emission and absorption, Coulomb collisions, bremsstrahlung, and possibly photon–photon pair production and annihilation. At high energies, for a continuously operating acceleration, the steady-state distribution remains a power law like, but softens because of cooling by Compton, synchrotron and bremsstrahlung. At lower energies, Coulomb collisions and synchrotron self-absorption efficiently thermalize particles, forming a Maxwellian distribution. The total particle distribution consists of a low-energy Maxwellian plus a high-energy tail. Such a distribution we call hybrid. The shape and energy content of the tail are fully determined by the balance between acceleration and cooling processes. It cannot be calculated analytically; therefore, we treat this problem numerically. The photon spectrum emitted by the hot flow is computed self-consistently with the particle distributions.

The time-scale of equilibration of electron and photon distributions for typical parameters of our model is smaller than the corresponding advection time in the hot flow (see Appendix A). Thus, we can use an assumption that the electron and photon distributions are in a steady state. We obtain them by solving the relevant kinetic equations.

3.1 Model setup

We consider a geometrically thick optically thin inner accretion flow, whose vertical extent is parametrized by the ratio $H/R =$ const. We assume that the hot flow corresponds to some type of radiatively inefficient accretion flow (see the review in Kato, Fukue & Mineshige 2008). In such flow, the radiative loss rate per unit area scales with radius as $Q_{\rm rad} \propto R^{-5/2}$, and the electron number density scales as $n_{\rm e}(R) \propto R^{-3/2}$. The Thomson optical depth along the vertical direction $\tau = \sigma_{\rm T} n_{\rm e}(R) H \propto R^{-1/2}$. The scaling of the magnetic field with radius is model dependent (e.g. Meier 2005; Shadmehri & Khajenabi 2005; Akizuki & Fukue 2006). Here we assume that the magnetic pressure and the radiation pressure are equal throughout the flow, from which we get $B \propto R^{-5/4}$. The latter scaling is the same as in the accretion flow model of Shadmehri & Khajenabi (2005). The hot flow extends from $3R_{\rm S}$ to the truncation radius $R_{\rm tr}$, where the cold disc with luminosity $L_{\rm disc}$ and colour temperature $T_{\rm col}$ starts.

The energy transfer to electrons is simulated as a power-law injection with slope $\Gamma_{\rm inj}$, extending between the Lorentz factors 1 and 10^3.[2] The model has seven parameters: (i) the total luminosity L, (ii) the index of the electron power-law injection spectrum $\Gamma_{\rm inj}$ (constant throughout the flow), (iii) the electron Thomson optical depth τ_1 and (iv) the magnetic field B_1 in the innermost regions, (v,vi) indices of their power-law radial dependences θ and β, and (vii) the hot-flow size $R_{\rm tr}$.

The energy given to electrons is redistributed between the particles (electrons and positrons) and photons in processes of synchrotron emission and self-absorption, Compton scattering, Coulomb collisions, pair production and annihilation and bremsstrahlung emission. The dominating cooling regime for a specific electron Lorentz factor depends on the luminosity, magnetic field and the optical depth (relevant scaling is given in Appendix A). In addition to the internally produced radiation, we also consider soft photons from the cold outer accretion disc in the form of the blackbody radiation injected homogeneously into the system. The kinetic equations for electrons and photons describing relevant radiative processes are solved using the code developed by Vurm & Poutanen (2009).

To compute the radiative transfer in the hot flow, we divide it into a number of separate regions/zones (Fig. 1). Each zone i has size (in the radial direction) $\Delta R_i = R_{i+1} - R_i$ equal to its full height at the zone centre $2H_i = 2R_{i,{\rm c}}(H/R)$ (where $R_{i,{\rm c}} = (R_i + R_{i+1})/2$ is the distance to the centre of ith zone), implying

$$R_{i+1} = R_i \frac{1 + H/R}{1 - H/R}. \tag{8}$$

The net energy input into the ith zone equals its luminosity:

$$L_i = 2\pi \int_{R_i}^{R_{i+1}} Q_{\rm rad}(R) R {\rm d}R \propto \frac{1}{\sqrt{R_i}} - \frac{1}{\sqrt{R_{i+1}}}. \tag{9}$$

The characteristic Thomson optical depth of the ith zone is associated with that in the vertical extension

$$\tau_i = \sigma_{\rm T} n_{\rm e}(R_{i,{\rm c}}) H_i. \tag{10}$$

[2] By using such an approximation, we implicitly assume that 100 per cent of the dissipated energy is transported to particles by acceleration processes, while in reality most of the energy is likely to be given to particles in terms of heating by diffusive processes, e.g. Coulomb collisions with protons. In Appendix B1, we discuss the validity of such an approximation and show that the results hold due to efficient electron thermalization at low Lorentz factors.

Additional soft photons from the outer cold disc are described by the colour temperature $T_{\rm col}$ and the disc luminosity coming to the ith zone $(\Omega_i/4\pi)L_{\rm disc}$. Here the factor Ω_i accounts for the fact that only a part of the disc luminosity is entering the hot flow. It is fully determined by the cold disc/hot-flow geometry and in our case can be approximated as

$$\frac{\Omega_i}{4\pi} \approx \frac{1}{4}\left(\frac{R_{i+1}}{R_{\rm tr}}\right)^3, \tag{11}$$

where $\pi(R_{i+1}/R_{\rm tr})^2$ is the solid angle of the ith zone as seen from the cold accretion disc, and another factor of $R_{i+1}/R_{\rm tr}$ accounts for anisotropy of the disc radiation. This formula is accurate for the zone adjacent to the disc. It overestimates the contribution of disc photons to the innermost zones, but in that case Ω_i is very small and the disc contribution is negligible.

Each zone represents a torus-like structure with the major radius $R_{i,{\rm c}}$ and the minor radius H_i. The radiative transfer is handled under the local approximation of homogeneous isotropic distributions in a sphere with radius H_i, using the escape probability method (see Vurm & Poutanen 2009). The power injected into the sphere is scaled proportionally to the ratio of respective volumes of the sphere and the torus:

$$L_{i,{\rm sph}} = \frac{V_{i,{\rm sph}}}{V_i} L_i = \frac{2}{3\pi}\frac{H}{R} L_i, \tag{12}$$

where $V_{i,{\rm sph}} = \frac{4\pi}{3} H_i^3$ is the sphere volume, V_i and L_i are volume and luminosity of the ith zone. This approach keeps the energy density inside the sphere and the torus the same. After the spectrum in a sphere is computed, we multiply it by the same factor $V_i/V_{i,{\rm sph}}$ in order to account for the radiation from the entire torus. The total spectrum of the flow is the sum of the spectra from each zone.

This local approach neglects the interaction between different zones. The influence of the outer zones on the inner zone spectra is negligible because of their lower luminosity as well as very small solid angle occupied by the inner zones as seen from the outside. Although the effect of the inner zones on the outer zone spectra is more significant, the overall spectral properties are practically the same because the X-ray spectrum is dominated by the inner zone and the OIR spectral shape is determined by the parameter scaling rather than their precise values. The radiative transfer effects are considered in Appendix B2.

3.2 Hard state

In the hard state, the hot flow can extend to large radii $\gtrsim 100R_{\rm S}$ and the role of the soft photons from outer cold accretion disc is negligible. Therefore, we neglect them in the simulations and consider only the emission from the hot flow. We take the total luminosity of the flow $L = 10^{-2}L_{\rm Edd}$ ($L_{\rm Edd}$ is the Eddington luminosity), the Thomson optical depth of the innermost zone $i = 1$ $\tau = 1.25$, typically found from the X-ray/γ-ray data (e.g. Zdziarski et al. 1998; Frontera et al. 2001b), the magnetic field in the innermost zone $B = 10^6$ G and the height-to-radius ratio $H/R = 0.5$. The radial dependences of the parameters are given in Section 3.1 and listed for each zone in Table 1 (first five rows). The results of simulations are shown in Fig. 3 for the injection slope $\Gamma_{\rm inj} = 2.5$ and in Fig. 4 for $\Gamma_{\rm inj} = 3.0$.

Simulations show that larger zones generally have softer spectra, with difference in the X-ray spectral indices $\Delta\alpha_{\rm X} \approx 0.05$–$0.08$. The main reason is that the outer zones are more transparent to the synchrotron radiation, which increases the ratio of the synchrotron to the thermal Compton luminosities. At the same time we see that the equilibrium electron temperature grows with radius from

Table 1. Parameters of the multizone hot inner flow model.

Parameter/zone	1	2	3	4
R_i/R_S	3	10	30	100
R_{i+1}/R_S	10	30	100	300
τ_i	1.25	0.65	0.4	0.2
B_i (10^6 G)	1	0.25	0.06	0.015
L_i (10^{36} erg s^{-1})	6	3	2	1
kT_{col}[a] (keV)	0.25	0.12	0.05	–

[a] kT_{col} is the colour temperature of radiation coming into the hot flow from the inner edge of the cold accretion disc extending down to R_{i+1}.

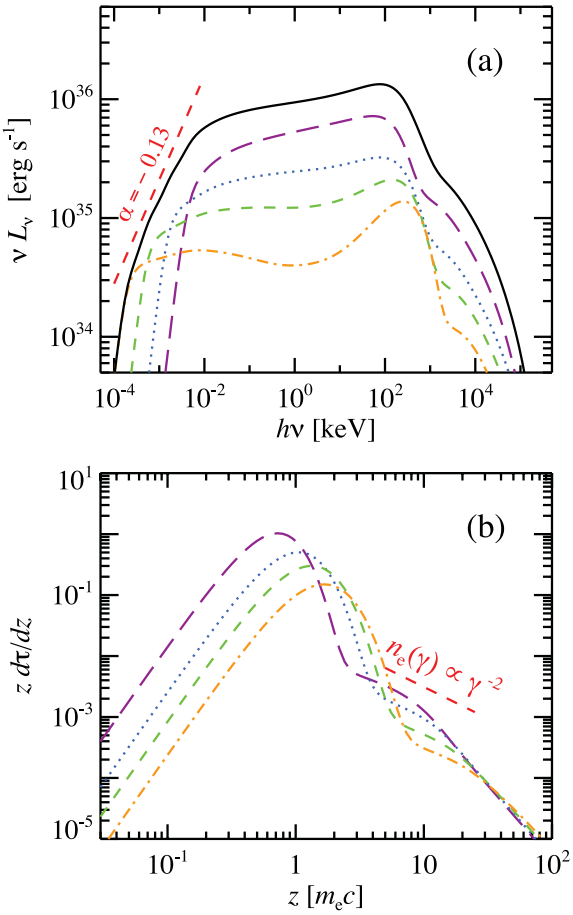

Figure 3. Photon spectra (upper panel) and electron distributions (lower panel) for the hard-state model with initial electron injection index $\Gamma_{inj} = 2.5$. Electron momenta $z = \sqrt{\gamma^2 - 1}$ are measured in units of $m_e c$. Other parameters are listed in Table 1. The lines correspond to zone 1 (long-dashed), zone 2 (dotted), zone 3 (dashed) and zone 4 (dot–dashed). Sum of the components is shown with a solid line. The red short-dashed line shows the slopes from an analytical approximation. For further details, see Section 3.2.

approximately 70 up to 240 keV (Fig. 3). This is caused by a significant drop of the optical depth τ in the outer zones, with a relatively slow change of the Compton y-parameter, defined as $y = 4(kT_e/m_e c^2)\tau$. The X-ray spectrum of the outer zones is dominated by thermal bremsstrahlung, because its role relative to Compton cooling $\propto \tau R/L$ grows linearly with radius (equation 22 in Veledina

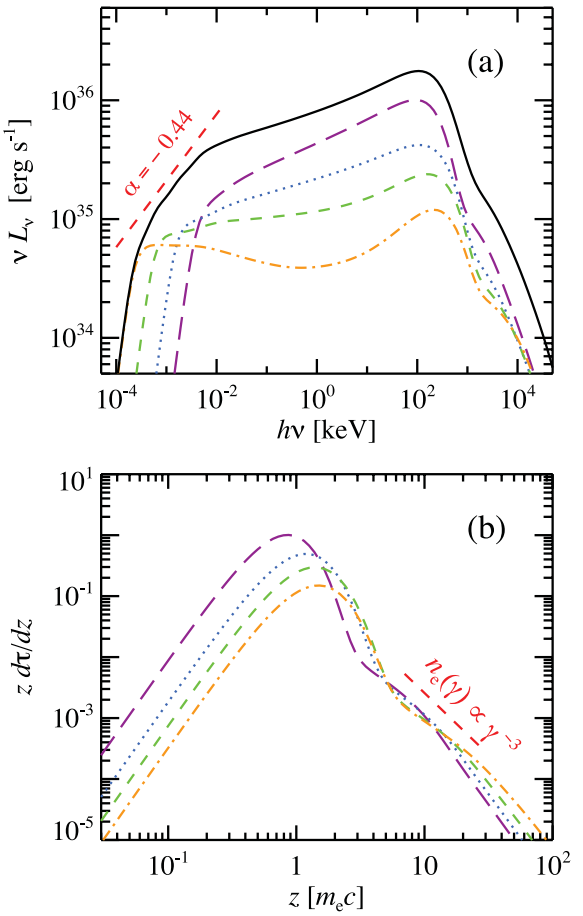

Figure 4. Same as Fig. 3, but for the electron injection index $\Gamma_{inj} = 3.0$. X-ray spectra are harder in this case, while the OIR spectrum is softer.

et al. 2011b). The combined spectrum of all zones has a concave shape, exactly as observed (Ibragimov et al. 2005).

The high-energy tail above a few 100 keV is dominated by Comptonization produced by the non-thermal electron tail. At a Lorentz factor above 20, the tail has a power-law shape corresponding to index $p = \Gamma_{inj} + 1$ due to synchrotron and Compton cooling. At intermediate γ, the distribution is curved, because of the large role of Coulomb collisions which produce an equilibrium distribution with index $p = \Gamma_{inj} - 1$ (equation 12 in Veledina et al. 2011b).

The OIR spectrum is produced by a combination of synchrotron self-absorption peaks from different zones. The outer zones dominate at longer wavelengths. The low-energy cutoff is determined by the size of the largest zone (equation 3), which for $R = 300R_S$ and considered values of the parameters (in particular, the assumed magnetic field in the outermost zone) is at 0.2 eV. At even lower energies, the spectrum is $L_\nu \propto \nu^{5/2}$. Above 10 eV, emission from all zones is optically thin and is dominated by thermal Comptonization of seed non-thermal synchrotron photons.

The X-ray spectra are harder for $\Gamma_{inj} = 3.0$. This is a direct consequence of the softer equilibrium electron distribution, which results in a lower synchrotron luminosity and larger Compton y-parameter. The OIR spectra are, however, softer in this case, because a different slope of the electron non-thermal tail results in a relatively low normalization of the electron distribution and, respectively, in the weaker synchrotron emission from the inner zones.

Many of the numerical results can be understood from the analytical model if one approximates the electron distribution by a

power law in the energy range where electrons emit close to the self-absorption frequency. In our simulations these electrons have Lorentz factors $\gamma_t \approx 10$.

In the case of injection slope $\Gamma_{inj} = 2.5$ the optical depth of the power-law electrons scales the same way as the total optical depth, with index $\theta = 1/2$ (see Fig. 3b). The slope of the electron distribution is approximately $p = 2$. Putting these parameters (with $\beta = 5/4$) into equation (7), we get $\alpha_{OIR} = -0.13$, in good agreement with the numerically computed slope (see Fig. 3a).

For softer electron injection $\Gamma_{inj} = 3.0$, we find that the optical depth at the Lorentz factor $\gamma_t = 10$ is nearly constant for every zone (see Fig. 4b); thus, for an analytical approximation we take $\theta = 0$. The average electron slope at this Lorentz factor is $p \approx 3$. Putting these coefficients into equation (7), we get $\alpha = -0.44$, also in good agreement with the computed spectrum (Fig. 4a).

The turnover frequency of the synchrotron spectrum from each radius is given by equations (3) and (4). For the case with $\Gamma_{inj} = 2.5$ we substitute parameters of zone 1: $R = 10R_S$, $B = 10^6$ G, $\tau = 10^{-2}$ (Thomson optical depth of the high-energy tail), and power-law slopes $\beta = 5/4$, $\theta = 1/2$ and $p = 2$ to obtain the scaling

$$\nu_t \approx 10^{15} \left(\frac{R}{10R_S}\right)^{-1} \text{Hz}. \quad (13)$$

The similar scaling can be obtained for $\Gamma_{inj} = 3.0$. In order to estimate the synchrotron luminosity we substitute the calculated turnover frequency into equation (6)

$$\nu L_\nu \approx 2 \times 10^{35} \left(\frac{R}{10R_S}\right)^{-7/8} \text{erg s}^{-1}, \quad (14)$$

which is consistent (within a factor of 2) with the values obtained in precise numerical calculations.

The main model parameters (see Section 3.1) can be constrained by the data. The first four parameters (L, Γ_{inj}, τ_1 and B_1) can be obtained from the X-ray luminosity and spectral slope, the cutoff temperature and the slope of the γ-ray tail. The other three parameters (θ, β and R_{tr}) can then be extracted from the OIR data: the turnover frequency (equation 3), spectral slope (equation 7) and the luminosity (equation 6).

The precise values of the minimum and maximum Lorentz factors of the injected power-law electrons do not affect much the resulting spectra as far as the electrons emitting at the self-absorption frequency remain in a power law. We note that very similar results can be obtained by assuming that most of the energy goes to heat the thermal distribution and only a small fraction goes to the power-law tail (see Appendix B1). At the same time, the spectra of fully thermal hot flow with the same values of magnetic field are too hard to match the observations in the hard state. Assuming B an order of magnitude larger in every zone would produce the spectra reasonably well describing the observed ones. OIR spectra in this case can also be described by a power law; however, the turnover frequency in every zone is higher compared to the case of hybrid electrons (see Appendix B1 for details). Thus, in order to explain the IR points, a much larger hot-flow size is required. We also note that purely thermal models are not capable of reproducing the observed non-thermal MeV tails.

The considered model qualitatively describes the spectral properties of the hot flow. On the quantitative level, the exact slope of the X-ray spectrum and the relative OIR/X-ray luminosities may vary depending on the details of calculations. For instance, the radiative transfer effects (see Appendix B2) harden a bit the X-ray spectra of the outer zones, while the OIR spectra are nearly unaffected. Also reducing the H/R ratio leads to slightly harder X-ray spectra (see Appendix B2), if other parameters (L, τ and B) are unchanged. Again, the OIR slope remains the same. Thus, the model is rather robust in its predicted spectral properties.

3.3 State transitions

A generally accepted scenario for the hard-to-soft state transition involves the motion of the cold accretion disc towards the compact object (Poutanen et al. 1997; Esin et al. 1997, 1998). In this case, the role of the disc increases and it gradually replaces the synchrotron as a source of seed photons for Comptonization. We simulate this action by replacing the spectrum in the corresponding zone of the hot flow with a multicolour blackbody disc (Shakura & Sunyaev 1973; Frank, King & Raine 2002) of an appropriate inner radius. We take the disc truncation radius R_{tr} equal to the outer radius of the largest zone of the hot flow and we keep the outer disc radius at $R_{d,\,out} = 3 \times 10^4\, R_S$.

The additional seed photons for Comptonization are modelled by the injection of blackbody photons with temperature corresponding to the colour temperature of disc inner radius:

$$kT_{col} = 2.3 \left(\frac{L}{L_{Edd}}\right)^{1/4} \left(\frac{3R_S}{R_{tr}}\right)^{3/4} \left(1 - \sqrt{\frac{3R_S}{R_{tr}}}\right)^{1/4} \text{keV} \quad (15)$$

(see Table 1). Given that the transition occurs at almost constant luminosity (see Done et al. 2007), we assume that the luminosity, magnetic field and Thomson optical depth of each hot-flow zone remain the same as in the hard state (see Table 1). The relative contribution of the cold disc and the hot flow in the observed spectrum depends on the inclination, which we take equal to 60°. The resulting spectra are shown in Fig. 5.

The total spectrum is now composed of synchrotron and bremsstrahlung photons, as well as Comptonized synchrotron and disc radiation. The transition between the Comptonization continua from the disc and synchrotron is reflected in the overall spectral curvature at ∼0.1 keV in the spectra of the largest hot-flow zone (e.g. Fig. 5a, short-dashed line). It is interesting to note that the spectra of the zones closer to the BH remain almost unaffected by the disc Comptonization (e.g. Fig. 5b, long-dashed line) due to a small dilution factor of the disc, while in the outermost hot-flow zone the cold disc is the dominant source of seed photons. The cool disc luminosity grows when it moves towards the BH and its photons are much more energetic than those provided by the synchrotron mechanism; thus, the X-ray spectrum softens as the transition proceeds. Once the truncation radius decreases to $10R_S$, the disc becomes the dominant source of seed photons, resulting in a softer spectrum with $\alpha \approx -1$.[3] As the outburst proceeds, the outer regions of the hot-flow collapse (hours to days before the noticeable X-ray state transition) leading to a dramatic drop in luminosity at ∼0.1 eV. The turnover frequency increases and the OIR spectrum becomes harder (see Fig. 6). Relatively small changes occur around $E \sim 30$ eV.

Hence, one would expect fast change in the luminosity at OIR wavelengths with smaller changes in the UV. For instance, if one observes the collapse of the $100R_S$ zone while the $30R_S$ zone is still present, there will be huge changes at ∼0.5 eV, while not so significant changes at ∼2 eV. The opposite is expected during the

[3] Further softening of the spectrum is expected if the cold disc penetrates into the hot flow forming a corona-like geometry (Poutanen et al. 1997). This results in additional cooling by the disc photons and reduction of the Compton y-parameter.

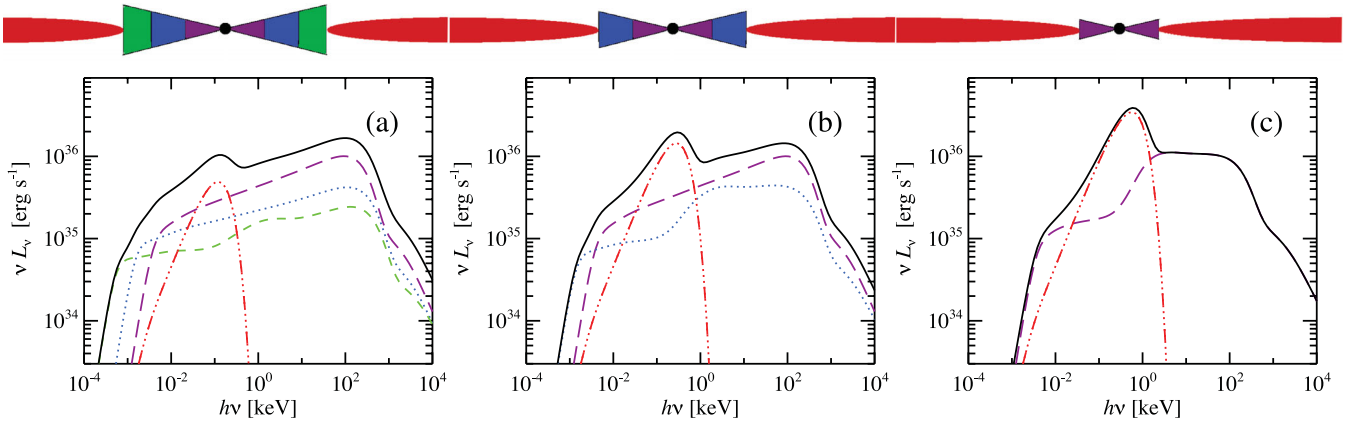

Figure 5. Upper panels: geometrical evolution at state transition. Principal components are standard accretion disc (red) and inner hot flow: zone 1 (within $10R_S$, violet), zone 2 (within $30R_S$, blue) and zone 3 (within $100R_S$, green). Lower panels: spectral evolution at state transition. Contribution of different zones are marked with lines: zone 1 (long-dashed), zone 2 (dotted), zone 3 (short-dashed) and thin accretion disc (three-dot–dashed). Colour coding is the same as in the upper panels. The inner radius of the truncated accretion disc changes from (a) $100R_S$ through (b) $30R_S$ to (c) $10R_S$, replacing the corresponding zones of the hot flow. Spectra are obtained for the case $\Gamma_{inj} = 3.0$.

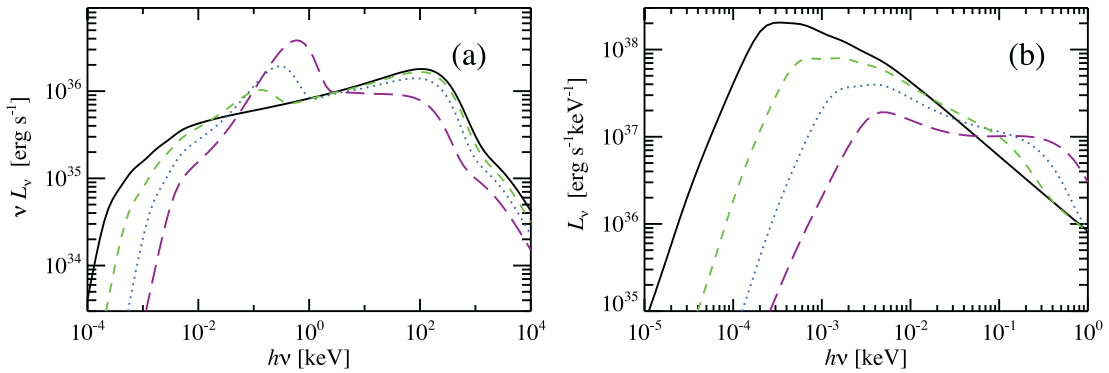

Figure 6. Spectral evolution at state transition: the pure hot-flow spectrum (solid lines), and spectra of the hot flow with the cold disc truncated at $100R_S$ (short-dashed), $30R_S$ (dotted), and $10R_S$ (long-dashed). (a) Spectra in νL_ν units and (b) spectra in L_ν units (note the different photon energy range). Here the outer disc radius is $R_{d,\,out} = 3 \times 10^4\ R_S$.

soft-to-hard state transition: when the disc recedes, the hot flow occupies larger and larger radii and its synchrotron luminosity increases earlier at shorter wavelengths.

Fig. 6(b) shows the L_ν spectra in more detail. Here we see that the pure hot-flow spectrum below the cutoff in the IR band is a power law with index $\alpha = 5/2$ corresponding to the optically thick non-thermal synchrotron. We note that such a hard spectrum is obtained under the assumption of an absence of the hot flow – disc overlap, i.e. that at distances larger than the hot-flow outer radius, the electron density is zero. In reality, a corona may exist atop of the cold disc; thus, a gradual transition from the hot flow to the cold accretion disc is expected leading to the much more gradual turnover of the OIR spectrum.

Fig. 7 illustrates possible spectral features appearing for different sizes of the outer disc radius. We see that the hot flow completely dominates the spectrum below ∼10 eV if its size is larger than $100R_S$. In this case, the exact value of $R_{d,\,out}$ does not play any role (unless reprocessing in the outer disc starts to be important; see Section 4.1.4). The largest changes occur for smaller truncation radius and large $R_{d,\,out} = 10^6 R_S$. For such large discs (see Fig. 7a), radiation in the far-IR is dominated by the Rayleigh–Jeans part of the spectrum from the outer cold disc. The UV radiation is mostly produced at the inner disc edge. Synchrotron from the hot flow is still important in the optical.

4 COMPARISON WITH OBSERVATIONS

In the present work we considered an inhomogeneous hot accretion flow model for the broad-band spectra of the accreting BHs. In the hard state, when the standard cold disc is truncated at a large radius, the central hot region is radiating mostly via thermal Comptonization of the non-thermal synchrotron photons. Hot flow extending over a large range of radii produces a power-law-like flat spectrum in the OIR range.

In the soft state, the cold disc moves in, brightens and takes over as a source of seed soft photons for Comptonization. This effectively reduces the role of synchrotron radiation in electron cooling. At the same time, the reduction of the size of the emitting region results in an increase of the synchrotron self-absorption frequency, making the synchrotron emission in the IR band negligible.

The scenario considered in this work is capable of reproducing the broad-band spectra from the IR to the γ-rays of BHs in all spectral states. However, the spectral data alone are not capable of distinguishing among various models and they have to be

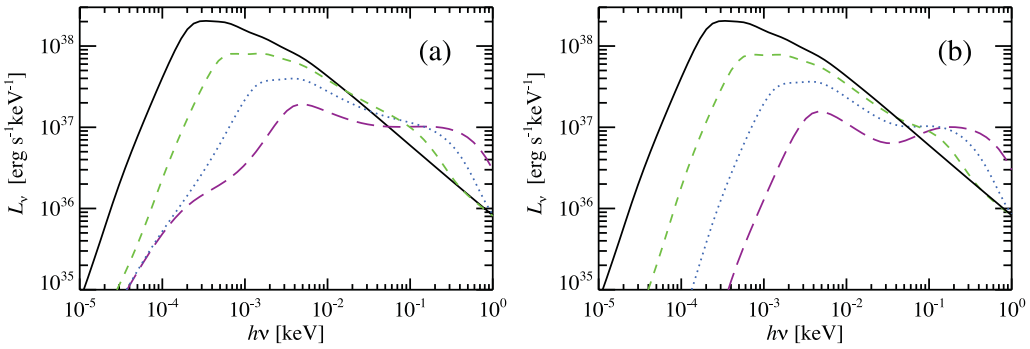

Figure 7. Same as in Fig. 6b, but for outer disc radii (a) $R_{\rm d,\,out} = 10^6 R_{\rm S}$ and (b) $R_{\rm d,\,out} = 300 R_{\rm S}$.

considered together with other sources of information (e.g. timing and polarization). Below we will discuss in details various properties of the developed hot-flow model and compare them to observations. We also compare our model to the popular jet scenario.

4.1 Hard state

4.1.1 X-ray spectrum and variability

In our model the X-ray spectrum is dominated by the Comptonization continuum from the innermost zone where most of the gravitational energy is dissipated. In the X-ray range it can generally be described by a power law. Outer zones of the hot flow have softer spectra, because of a larger role of non-thermal synchrotron and the increasing amount of the cold disc photons. The overall spectrum is thus slightly concave. Such spectra are consistent with those observed from the BHBs. For example, the best studied BH, Cyg X-1, clearly has a concave spectrum (Frontera et al. 2001a) that can be fitted with two Comptonization continua (Ibragimov et al. 2005).

A larger contribution from the outer zones to the soft X-rays should be reflected in the variability properties. Assuming that variability is produced by propagation of fluctuations in the mass accretion rate through the disc (Lyubarskii 1997; Kotov et al. 2001), we expect an increase in the variability amplitude for higher photon energies at higher Fourier frequencies, which is indeed observed (Nowak et al. 1999a). The autocorrelation function of soft X-rays in our model is expected to be wider than that of the hard X-rays, consistent with what is measured in Cyg X-1 (Maccarone et al. 2000). The same effect is more obviously seen in the Fourier-frequency-resolved spectra (Revnivtsev, Gilfanov & Churazov 1999; Gilfanov, Churazov & Revnivtsev 2000), which are softer and have a larger reflection amplitude at low Fourier frequencies. This implies that the outer zones of the hot flow (which are closer to the cold reflecting medium) give a relatively larger contribution to the soft X-ray flux than to the hard X-rays. The reduction of the equivalent width of the 6.4 keV Fe line in the frequency-resolved spectra above 1 Hz suggests that the cold disc truncation radius is of the order of 100 $R_{\rm S}$ (Revnivtsev et al. 1999; Gilfanov et al. 2000), further supporting our scenario. Similarly, even larger inner radii of the cold disc were measured in the low-extinction BH transient XTE J1118+480 (Esin et al. 2001; Chaty et al. 2003).

Another important finding is that the harder X-rays are delayed with respect to the soft X-rays (Nowak et al. 1999a; Nowak, Wilms & Dove 1999b). The large values of these hard time-lags and their frequency dependence f^{-1} can naturally be explained by spectral pivoting of a power-law-like spectrum (Poutanen & Fabian 1999; Poutanen 2001). The spectral evolution can arise when the accretion rate fluctuations propagate towards the BH into the zone with harder spectra (Kotov et al. 2001), again consistent with our multizone hot-flow model.

4.1.2 OIR excesses and flat spectra

The OIR excesses above the standard disc spectrum were reported in a number of sources: XTE J1859+226 (Hynes et al. 2002), XTE J1118+480 (Hannikainen et al. 2000; Esin et al. 2001; Chaty et al. 2003), GX 339−4 (e.g. Gandhi et al. 2011; Shidatsu et al. 2011), A0620–00 (Gallo et al. 2007), SWIFT J1753.5–0127 (Chiang et al. 2010) and V404 Cyg (Hynes et al. 2009a). In our model, the OIR spectrum consists of two components (Fig. 5): one comes from the multicolour accretion disc and another from the hot flow. The relative role of these components varies with the wavelength (Figs 6 and 7). The disc spectrum is hard in the OIR band, while the non-thermal synchrotron from the hot flow is typically softer with $\alpha_{\rm OIR} \sim 0$. The second component thus produces an excess emission.

In many cases the contribution of the non-thermal component is rather small compared to the disc, and it can be seen only as the IR excess. On the other hand, sometimes the synchrotron component dominates, which results in an almost pure power-law OIR spectrum. A good example is XTE J1118+480, where the spectral index $\alpha_{\rm OIR} = -0.15$ was measured (Chaty et al. 2003). This spectral index can be reproduced in our model, for example, with parameters $\theta = 0.5$, $p = 2.0$ and $\beta = 5/4$ (Fig. 3 illustrates this case).

4.1.3 Optical/X-ray cross-correlation

In recent years, a number of simultaneous optical (IR,UV)/X-ray observations with high time resolution were performed (Kanbach et al. 2001; Hynes et al. 2003, 2009b; Gandhi et al. 2008; Durant et al. 2011), all revealing the intrinsic connection of the two light curves on subsecond time-scales. The computed CCF have a complicated shape with a dip in the optical light curve preceding the X-ray peak (the so-called precognition dip), together with an optical peak lagging the X-rays.

The behaviour can be explained if the optical emission consists of two components: one coming from the synchrotron in the hot flow and another from reprocessed X-ray emission (Veledina et al. 2011a). Increase of the mass accretion rate causes an increase in the X-ray luminosity and affects the parameters of the hot flow, leading to a higher synchrotron self-absorption. The latter results in a drop of the optical emission; therefore, these two energy bands appear anticorrelated. This is reflected in the negative CCF with the shape resembling that of the X-ray autocorrelation function. On the other

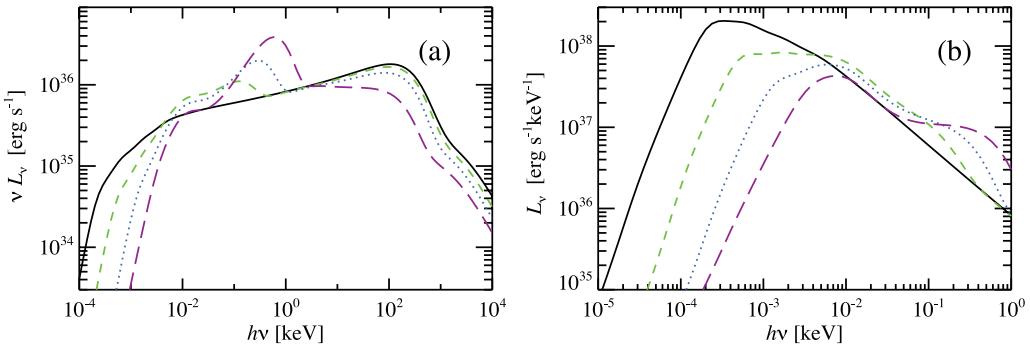

Figure 8. Same as in Fig. 6, but with the additional contribution from the irradiated accretion disc.

hand, the reprocessed radiation is delayed and smeared, giving rise to a CCF peaking at positive lags (optical delay). The combined CCF has a complicated shape consistent with the data. From the point of view of the multizone consideration, with a small increase of the mass accretion rate the cool disc moves inwards and causes the collapse of the hot flow at large radii. Thus, the suppression of the OIR emission with increasing X-ray radiation is also expected in this scenario.

A different, one-peak structure of the IR/X-ray CCF was found in GX 339−4 (Casella et al. 2010), suggesting that the hot flow was not the dominant source of the correlated variability during their observations. However, it might still give significant contribution to the constant flux component, but less to the varying component, and therefore would not be detected in the timing analysis. As it can be seen from Figs 3 and 4, the zones giving major contribution to the IR wavelengths do not contribute much to the X-rays. Therefore, the fraction of the correlated variability coming from these regions is expected to be small, and another source (likely the jet emission, as suggested in Casella et al. 2010) might be responsible for the shape of the CCF. We also note that a large amplitude of fluctuations in the IR light curve suggests that the source of correlated variability is also dominating the constant flux component.

The optical correlation with the X-rays was also detected in the quiescent state of V404 Cyg (Hynes et al. 2009a), while no clear radio/X-ray (nor radio/optical) correlation was found on the time-scales of hours, again suggesting that the radio and optical/X-ray emission are produced by the different components.

4.1.4 Irradiation of the cold disc

The X-ray radiation from the hot flow can be intercepted and reprocessed in the cold disc. The irradiation strongly depends on the disc outer radius and the disc shape. The larger is $R_{\rm d,\,out}$, the cooler can be this emission. The more flared is the disc, the larger is the reprocessed luminosity, which typically is expected to give significant contribution to the OIR band, exceeding the viscous disc luminosity at these energies (Shakura & Sunyaev 1973). Presence of the irradiated disc can also be reflected in the X-ray time-lags (see Poutanen 2002, and reference therein) and in the optical/X-ray CCF (Veledina et al. 2011a). Its signatures are also seen in the spectrum (e.g. Hynes et al. 2002; Gierliński et al. 2009).

For typical parameters of LMXBs with the disc size of 10^{11} cm, the X-ray luminosity of 10^{37} erg s^{-1} and 10 per cent reprocessing efficiency, the temperature of the outer disc is about 1.2 eV. For an illustration, we have added the emission from the irradiated discs to our hot-flow spectra (see Fig. 8). Following Cunningham (1976), we assumed the following dependence of the effective temperature on radius

$$kT_{\rm irr} = 1.2 \left(\frac{R}{R_{\rm d,out}} \right)^{-3/7} \text{eV} \qquad (16)$$

and the outer disc radius of $R_{\rm d,\,out} = 10^{11}$ cm.

As can be seen in Fig. 8, for typical parameters of the BHBs the spectrum of the irradiated disc peaks around 5 eV and has a Rayleigh–Jeans-like tail with $\alpha \sim 2$ in the OIR. If the inner hot-flow size exceeds 30–100 $R_{\rm S}$, its synchrotron emission will dominate the reprocessing below ∼1 eV. We do not expect much of reprocessed emission below 0.5 eV, except for the large-period systems (similar to V404 Cyg and GRS 1915+105). Therefore, at sufficiently long wavelengths in the scenario of Veledina et al. (2011a) we expect the IR/X-ray CCF to have only the dip, with no peak. The overall spectral shape is complex, with a number of bumps corresponding to the standard disc (above ∼100 eV), the irradiated disc and synchrotron from the hot flow (in the 1–10 eV range). A hardening of the spectrum observed in GX 339−4 at ∼2–3 eV (Buxton et al. 2012; Dinçer et al. 2012; Rahoui et al. 2012) can be due to a transition from the hot flow to the irradiated disc spectrum.

4.2 State transition

4.2.1 Broad-band spectral evolution at state transition

During the hard-to-soft state transition the outer zones of the hot flow gradually collapse. This leads to a drop in luminosity at longer wavelengths preceding the subsequent drop at shorter wavelengths. The corresponding time delay between sharp luminosity changes at different wavelengths corresponds to the viscous time-scale of the cold disc between the corresponding radii and, depending on the separation of the wavelengths and accretion parameters, can be as short as hours (e.g. if one observes in different optical filters) and as long as a few days (e.g. IR and UV). The dramatic changes in V, R and I bands were detected, e.g. in GX 339−4 during the rising phase of the 2010 outburst (Cadolle Bel et al. 2011); however, the time resolution of the light curves does not allow us to judge on the exact time of flux quenching at different wavelengths. A much more gradual decrease of the UV flux before the X-ray spectral transition (Yan & Yu 2012) is in principle consistent with our model if one also considers contribution from the irradiated disc (e.g. as in Fig. 8: gradual decrease at ∼10 eV, with sharp drop at ∼1 eV). During the reverse (soft-to-hard) transition, the fast luminosity increase at shorter wavelengths is expected to occur earlier than at longer wavelengths, and the corresponding time delays are expected to be

larger than in the rising phase, as was seen in the 2005 outburst decay of GX 339−4 (Coriat et al. 2009).

Recently, the entire transition of the BH transient XTE J1550−564 from hard to the soft state and back was monitored in the *V*, *I* and *H* filters (Russell et al. 2011). Just before the X-ray spectral transition as well as after the reverse transition, significant colour variations occurred, as indicated by the rapid changes in the *H* band at an almost constant *V* magnitude. In terms of our model, the observed colour change is related to the collapse/recover of a zone in the hot flow that is responsible for the *H*-band emission (see Section 3.3). As is known, the hard–soft and the soft–hard spectral transitions occur at different X-ray luminosities (e.g. Zdziarski et al. 2004). This hysteresis most probably is related to the fact that at the same luminosity the cold disc is further away from the central source on the rising phase of the outburst than on the decline. According to our model, the hysteresis has to be reflected also in the OIR spectra, namely the fast colour change should occur at a higher X-ray luminosity on the rising phase than on the decline. This is indeed observed (Russell et al. 2011).

In the soft state, the accretion disc extends to the last stable orbit, leaving no possibility for the inner hot flow to exist. However, the corona should still be present as supported by the existence of the non-thermal tails (produced by the inverse Compton scattering of the disc photons). It may also produce synchrotron radiation in the OIR band, but at a much lower level.

4.2.2 Change of the X-ray radiation mechanism

At luminosities above a few per cent of Eddington, BHBs show a strong correlation between spectral index and luminosity. At lower luminosities the trend is reversed (Sobolewska et al. 2011). Similarly, an indication of the reverse trend was detected in low-luminosity AGNs (Constantin et al. 2009). This was interpreted as a change of the source of seed photons for Comptonization from the disc photons dominating at higher luminosities to the synchrotron at lower luminosities. The anticorrelation at $L/L_{\rm Edd} \sim 10^{-3}$–$10^{-2}$ can be reproduced within a two-temperature hot accretion flow model (Niedźwiecki, Xie & Zdziarski 2012). The whole spectral index–luminosity dependence is well explained by a one-zone hybrid Comptonization model (see figs 7 and 12 in Veledina et al. 2011b). The multizone consideration presented in the current paper follows the same pattern as the one-zone model, because the X-ray spectrum is dominated by radiation from the inner zone.

4.3 Polarization

The only indication of the X-ray polarization from BHB goes back to the OSO-8 satellite (Weisskopf et al. 1977), which measured 3.1 ± 1.7 per cent linear polarization from Cyg X-1 at 2.6 keV. Such a polarization can be produced by Compton scattering if the geometry of the X-ray emitting region is a flattened disc-like structure ($H/R \sim 0.2$ according to the calculations of Lightman & Shapiro 1976). The number of scatterings the X-ray photons undergo depends on the electron and the seed photon temperatures. For a 100 keV plasma, photons double their energy in each scattering; hence, the disc photons of a typical energy of 0.5 keV would reach 3 keV in only three scatterings, while the synchrotron photons emitted at 10 eV require about eight scatterings. Thus, even if the synchrotron photons are polarized, this information is forgotten, and the X-ray polarization is completely determined by the geometry of the medium. In our model, we considered the case of $H/R = 0.5$; however, the spectral shape remains the same even for the flatter geometry (see Appendix B2). Thus, the polarization measurements are consistent with the hot-flow model.

Recently, strong linear polarization ($\Pi = 67 \pm 30$ per cent) in the soft γ-rays above 400 keV was detected in Cyg X-1 with the IBIS instrument onboard *INTEGRAL* (Laurent et al. 2011). Similar polarization ($\Pi = 76 \pm 15$ per cent) was also observed with the SPI spectrometer (Jourdain et al. 2012a). The polarization angle of 40°–42° is about 60° away from the radio jet axis at ≈−20° (Jourdain et al. 2012a; Zdziarski, Lubiński & Sikora 2012). Such a large polarization degree in the MeV range is extremely difficult to get in any scenario. Synchrotron jet emission from non-thermal electrons in a highly ordered magnetic field can have a large polarization degree (up to ∼70 per cent) in the optically thin part of the spectrum, and indeed a high polarization in the radio and the optical bands reaching 30–50 per cent is observed from extragalactic relativistic jets (Impey, Lawrence & Tapia 1991; Wills et al. 1992; Lister 2001; Marscher et al. 2002; Ikejiri et al. 2011). However, this scenario also needs a very hard electron spectrum as well as an extreme fine-tuning to reproduce the spectral cutoff at a few MeV (Zdziarski et al. 2012). In the hot-flow scenario, the MeV photons are produced by non-thermal Compton scattering of the 100 keV photons by electrons with $\gamma \sim 2$–4. These electrons cannot be isotropic, because no significant polarization is expected in that case (Poutanen 1994). This then implies that they must have nearly one-dimensional motion, e.g. along the large-scale magnetic field lines threading the flow. The 60° offset of the polarization vector relative to the jet axis then implies the inclined field lines. If the measured high polarization degree is indeed real, this would put strong constraints on the physics of particle acceleration in the hot flow and the magnetic field geometry.

The polarization degree of the hot-flow radiation in the OIR band is strongly affected by the Faraday rotation. The rotation angle $\chi_{\rm F} \sim 10^6 \tau B_{||,6} \nu_{15}^{-2}$ exceeds 10^5 rad and the polarization degree is expected to be essentially zero in the optically thin part of the spectrum. In the optically thick regime, the intrinsic flow polarization (parallel to the field lines) is not more than about 10 per cent even for the ordered magnetic field and without Faraday rotation (Pacholczyk & Swihart 1967; Ginzburg & Syrovatskii 1969). Thus, the OIR polarization is expected to be very low.

Optical and UV radiation from the cool accretion disc may also be polarized up to ∼11.7 per cent (parallel to the disc plane) at large inclinations, if the opacity is dominated by the electron scattering (Chandrasekhar 1960; Sobolev 1963). At lower energies, absorption in the atmospheric layers of the disc (Loskutov & Sobolev 1981, 1982) and the Faraday rotation reduce the polarization degree and it can drop down to zero in the IR.

A detection of linear polarization at a few per cent level in the OIR bands in BHBs (Schultz, Hakala & Huovelin 2004; Russell & Fender 2008; Shahbaz et al. 2008; Chaty, Dubus & Raichoor 2011) is consistent with being produced either by the jet synchrotron radiation, extended photosphere of the hot flow, dust/electron scattering in the source vicinity or by the interstellar dust.

4.4 Comparison with the jet paradigm

The simplest jet model has a conical geometry with all parameters distributed as a power law with distance and with electrons having a power-law distribution in Lorentz factor (Marscher 1977; Blandford & Königl 1979). The magnetic field can be assumed ordered or tangled, but this only influences the polarization properties. The mathematical formulation of this model is identical to the analytical model for the hot flow considered in Section 2. Such a simplified

jet model was applied to the broad-band spectra of BHBs (Markoff, Falcke & Fender 2001). In a more realistic situation, the electron distribution would be subject to acceleration mechanisms, as well as cooling processes such as Compton, synchrotron and adiabatic (as e.g. in Pe'er & Casella 2009; Pe'er & Markoff 2012). However, due to complicated physics, the energy input and the acceleration efficiency throughout the jet are generally unknown, and in the spectral models remain ad hoc functions. Thus, the shape of the resulting spectra and its total energetics strongly depend on the assumptions. This disadvantage is avoided in the hot-flow models: the input energy here comes from the liberated gravitational energy, which can be estimated analytically, and the acceleration efficiency (as well as its role compared to other heating mechanisms) does not significantly affect the final spectrum. Both scenarios, however, suffer from a large number of parameters due to an absence of first principle model.

Apart from the different physical assumptions, the jet and the hot-flow models predict different spectral properties. In the simple jet model, the synchrotron spectrum consists of the optically thin part with spectral slope $\alpha = -(p-1)/2$ and the optically thick part (sum of contribution from different zones) with the same slope as given by equation (7). The low-energy cutoff is determined by the jet extension and falls in the radio wavelengths. In contrast, the cutoff of the hot-flow spectrum is related to the truncation radius of the disc and likely falls in the OIR band. The break energy to the optically thin part of the jet is determined by the extension of the injection zone and for X-ray binaries is expected to fall in the IR wavelengths (Heinz & Sunyaev 2003), while in the hot-flow model the break is in the UV/optical band as determined by the size of the inner region. The jet optically thin synchrotron is sometimes claimed to extend to the X-rays, while in the hot-flow model radiation at these energies is produced in the Comptonization processes.

Let us now assess possible contribution of the jet and the hot flow to various wavelengths relying on the observed spectral properties. The X-ray spectra of BHBs have sharp cutoffs at about 100 keV that are impossible to produce by non-thermal synchrotron even if the electron distribution has an abrupt cutoff (Zdziarski et al. 2003). The hard spectra are also difficult to produce by optically thin synchrotron as this requires a very hard injection. Another question is then about the observed low level of the X-ray polarization, which is in contradiction with the theoretical expectations from the optically thin synchrotron, as well as with the levels measured in extragalactic sources. On the other hand, the X-ray spectral properties are well explained by the (nearly) thermal Comptonization in the hot flow (see Section 4.1.1).

Atop of the X-ray power law, the Compton reflection and the iron line are rather often detected features. Their amplitude and its correlation with the underlying spectral shape strongly argue in favour of the small X-ray emission region and against any beamed-away radiation from the jet. The analysis of the hard-state X-ray spectra of the BHB Cyg X-1 revealed that the spectra pivot at energies of 10–50 keV (Zdziarski et al. 2002). If the entire IR-to-X-ray continuum is produced by the same region (as proposed in the jet model), such pivoting would predict two orders of magnitude variations at 1 eV in the hard state, which are not observed. On the contrary, X-ray pivoting can be easily understood in the hot-flow model, where it can be produced by small variations of the cold disc radius and varying injection rate of the disc photons (see Fig. 8).

The observed fast X-ray variability and hard time-lags can naturally be understood in the hot-flow model where the X-ray emitting region is small, and the lags are related to the viscous time-scale of propagating fluctuations (Kotov et al. 2001). At the same time, the lags can occur from Compton scattering delays within the jet (Kylafis et al. 2008); however, this model contradicts the observed narrowing of the autocorrelation function with energy (Maccarone et al. 2000).

The MeV tails detected in the spectra of a number of hard-state BHBs are likely produced by the non-thermal electrons, either by the optically thin synchrotron emission (as in the jet) or by the inverse Compton scattering (as in the hot flow). The detailed investigation of this tail showed that it can be explained by the high-energy end of the jet synchrotron emission; however, in this case one needs to assume a very hard index of the electron power-law distribution $p = 1.3$–1.6, which is in conflict with standard acceleration models and observations (see Zdziarski et al. 2012, and references therein). At the same time, the hot flow easily accounts for the MeV tails in the hard state as well as in the soft state (where it can be replaced by a corona), when the jet is quenched.

The non-thermal OIR radiation has often been interpreted as a jet emission (see the review by Russell & Fender 2009). The similarities in the IR and radio light curves in microquasars, such as GRS 1915+105 (Fender et al. 1997), indeed favour a common source of variability. However, this scenario meets substantial problems in a number of other sources. For instance, in some systems the jet broken power-law model, normalized to fit the radio fluxes, significantly underpredicts the optical luminosity even after accounting for possible irradiated disc contribution (Soleri et al. 2010; Cadolle Bel et al. 2011). Sometimes the OIR slope is different from the radio as, for example, in XTE J1118+480 the OIR spectrum with $\alpha_{\rm OIR} = -0.15$ is much softer than the radio spectrum with $\alpha_{\rm R} = 0.5$ (Hynes et al. 2000; Chaty et al. 2003), but much harder than expected from the optically thin jet emission. The hot-flow scenario can reproduce the observed flat OIR spectra, at the same time the slopes in the OIR and radio do not necessarily match, as they are produced in different regions (inflow and outflow).

A rather low OIR polarization (at most a few per cent) observed in BHBs is clearly much below the high polarization observed in many extragalactic jets. On the other hand, certain types of objects, the so-called compact steep-spectrum and gigahertz peaked-spectrum radio sources, demonstrate similarly small polarization levels (0.2 and up to 7 per cent, respectively; O'Dea 1998). However, the (rest-frame) break frequency measured in these objects is quite low; thus, in the X-ray binary jets, as expected from the scaling laws the break frequency is in the (sub-) millimetre range.

The two models make different predictions for changes of the OIR spectrum during the state transitions. In the hot-flow scenario, the spectrum gradually hardens at hard-to-soft transition on the time-scales of days to weeks, corresponding to the typical time-scales on which the cold accretion disc evolves. It softens again at the reverse transition. On the other hand, one would not expect systematic changes of the jet spectral slope, as any fluctuations would propagate through the jet on time-scales of hours, much shorter than the state transition. However, if the jet power is gradually decreasing at the transition, then the dependence of the turnover frequency on the mass accretion rate suggests that $\nu_{\rm t}$ is also decreasing (Heinz & Sunyaev 2003). Thus, the jet scenario predicts softening of the OIR non-thermal spectrum at hard-to-soft state transition and hardening at the reverse transition, opposite to the hot-flow scenario.

In reality, the OIR emission can contain contributions from a number of components: the hot flow, the jet and the cold accretion disc (likely irradiated). It is also possible that in some sources there is a dip in the microwave band, where the transition from the radio jet to the hot flow occurs. The dip can be detected in the far-IR/submillimetre wavelengths, which were not systematically

studied in the past. It is thus of high interest to observe at these wavelengths, especially with the available capabilities of the Atacama Large Millimeter/submillimeter Array.

5 SUMMARY

The observed OIR flat spectra and the MeV tails evidence the significant role of non-thermal electrons in spectral formation of accreting BHBs. On the other hand, the commonly detected X-ray spectral cutoffs at $\sim$100 keV can be produced only by thermal particles. Whether these two populations belong to one component or originate from completely different places is debated. We present a model, in which the entire IR-to-X-ray/γ-ray continuum is produced by one component, the inhomogeneous hot accretion flow, present in the vicinity of compact object. The difference from the earlier studied hot geometrically thick optically thin flows is that the steady-state electron distribution in our model is hybrid, i.e. Maxwellian with a weak high-energy tail.

The X-ray spectra in our model are dominated by the radiation of the innermost regions of the hot flow. For this reason, the model inherits the advantages of the one-zone SSC model (Malzac & Belmont 2009; Poutanen & Vurm 2009) that explains well the X-ray spectral properties of BHB in their hard state, such as

(i) stable spectra with photon index $\Gamma \sim$1.6–1.9 and the cutoff at $\sim$100 keV in the hard state,
(ii) low level of the X-ray polarization,
(iii) presence of the MeV tail in the hard state,
(iv) power-law-like X-ray spectra extending to a few MeV in the soft state,
(v) softening of the X-ray spectrum with decreasing luminosity below $\sim 10^{-2} L_{\rm Edd}$,
(vi) weakness of the cold accretion disc component in the hard state, and
(vii) correlation between the spectral index, the reflection amplitude, the width of the iron line and the frequency of the QPO.

We show that the multizone consideration allows us to understand many other observables in the context of the hot-flow model:

(i) hard X-ray lags with logarithmic energy dependence,
(ii) concave X-ray spectrum,
(iii) non-thermal OIR excesses and flat spectra,
(iv) strong correlation between OIR and X-ray emission and a complicated shape of the CCF, and
(v) a complex evolution of the OIR–UV spectrum during the state transition.

We present relevant analytical expressions to estimate the hot-flow parameters from the OIR data (see equations 3, 6 and 7). Additional X-ray and γ-ray data are required to find a complete parameter set. However, the hot-flow extent can be found from the OIR data alone under certain assumptions (equations 13 and 14).

We compare the developed model to the popular jet scenario and show that in a number of cases the data favour the hot-flow interpretation. We encourage future observations in the far-IR and submillimetre wavelengths to provide the missing link between radio and IR, which would allow us to determine the contribution of the two components to the OIR emission.

ACKNOWLEDGEMENTS

The work was supported by the Finnish Graduate School in Astronomy and Space Physics (AV), the Academy of Finland grant 127512 (JP) and ERC Advanced Research Grant 227634 (IV). We thank Andrzej Zdziarski for fruitful discussions and useful comments, Marion Cadolle Bel and Dave Russell for conversations, which helped us to make the paper more understandable. We also thank anonymous referee for many useful suggestions, which helped us to better justify our model and to improve the paper.

REFERENCES

Akizuki C., Fukue J., 2006, PASJ, 58, 469
Arévalo P., Uttley P., 2006, MNRAS, 367, 801
Blandford R. D., Königl A., 1979, ApJ, 232, 34
Buxton M. M., Bailyn C. D., Capelo H. L., Chatterjee R., Dinçer T., Kalemci E., Tomsick J. A., 2012, AJ, 143, 130
Cadolle Bel M. et al., 2007, ApJ, 659, 549
Cadolle Bel M. et al., 2011, A&A, 534, A119
Casella P. et al., 2010, MNRAS, 404, L21
Chandrasekhar S., 1960, Radiative Transfer. Dover Press, New York
Chaty S., Haswell C. A., Malzac J., Hynes R. I., Shrader C. R., Cui W., 2003, MNRAS, 346, 689
Chaty S., Dubus G., Raichoor A., 2011, A&A, 529, A3
Chiang C. Y., Done C., Still M., Godet O., 2010, MNRAS, 403, 1102
Condon J. J., Dressel L. L., 1973, Astrophys. Lett., 15, 203
Constantin A., Green P., Aldcroft T., Kim D.-W., Haggard D., Barkhouse W., Anderson S. F., 2009, ApJ, 705, 1336
Corbel S., Fender R. P., Tzioumis A. K., Nowak M., McIntyre V., Durouchoux P., Sood R., 2000, A&A, 359, 251
Coriat M., Corbel S., Buxton M. M., Bailyn C. D., Tomsick J. A., Körding E., Kalemci E., 2009, MNRAS, 400, 123
Cunningham C., 1976, ApJ, 208, 534
de Bruyn A. G., 1976, A&A, 52, 439
Dermer C. D., Schlickeiser R., 1993, ApJ, 416, 458
Di Matteo T., Celotti A., Fabian A. C., 1999, MNRAS, 304, 809
Dinçer T., Kalemci E., Buxton M. M., Bailyn C. D., Tomsick J. A., Corbel S., 2012, ApJ, 753, 55
Done C., Gierliński M., Kubota A., 2007, A&AR, 15, 1
Droulans R., Belmont R., Malzac J., Jourdain E., 2010, ApJ, 717, 1022
Durant M., Gandhi P., Shahbaz T., Fabian A. P., Miller J., Dhillon V. S., Marsh T. R., 2008, ApJ, 682, L45
Durant M., Gandhi P., Shahbaz T., Peralta H. H., Dhillon V. S., 2009, MNRAS, 392, 309
Durant M. et al., 2011, MNRAS, 410, 2329
Esin A. A., McClintock J. E., Narayan R., 1997, ApJ, 489, 865
Esin A. A., Narayan R., Cui W., Grove J. E., Zhang S.-N., 1998, ApJ, 505, 854
Esin A. A., McClintock J. E., Drake J. J., Garcia M. R., Haswell C. A., Hynes R. I., Muno M. P., 2001, ApJ, 555, 483
Fabian A. C., Guilbert P. W., Motch C., Ricketts M., Ilovaisky S. A., Chevalier C., 1982, A&A, 111, L9
Fender R., 2006, in Lewin W., van der Klis M., eds, Cambridge Astrophysics Series, No. 39, Compact Stellar X-ray Sources. Cambridge Univ. Press, Cambridge, p. 381
Fender R. P., Pooley G. G., Brocksopp C., Newell S. J., 1997, MNRAS, 290, L65
Fender R. P., Garrington S. T., McKay D. J., Muxlow T. W. B., Pooley G. G., Spencer R. E., Stirling A. M., Waltman E. B., 1999, MNRAS, 304, 865
Fender R. P., Belloni T. M., Gallo E., 2004, MNRAS, 355, 1105
Frank J., King A., Raine D. J., 2002, Accretion Power in Astrophysics. Cambridge Univ. Press, Cambridge
Frontera F. et al., 2001a, ApJ, 546, 1027
Frontera F. et al., 2001b, ApJ, 561, 1006
Gallo E., Migliari S., Markoff S., Tomsick J. A., Bailyn C. D., Berta S., Fender R., Miller-Jones J. C. A., 2007, ApJ, 670, 600
Gandhi P. et al., 2008, MNRAS, 390, L29
Gandhi P. et al., 2010, MNRAS, 407, 2166
Gandhi P. et al., 2011, ApJ, 740, L13

Gelino D. M., Gelino C. R., Harrison T. E., 2010, ApJ, 718, 1
Ghisellini G., Maraschi L., Treves A., 1985, A&A, 146, 204
Ghisellini G., Haardt F., Svensson R., 1998, MNRAS, 297, 348
Gierliński M., Done C., 2003, MNRAS, 342, 1083
Gierlinski M., Zdziarski A. A., Done C., Johnson W. N., Ebisawa K., Ueda Y., Haardt F., Phlips B. F., 1997, MNRAS, 288, 958
Gierliński M., Zdziarski A. A., Poutanen J., Coppi P. S., Ebisawa K., Johnson W. N., 1999, MNRAS, 309, 496
Gierliński M., Done C., Page K., 2009, MNRAS, 392, 1106
Gilfanov M., 2010, in Belloni T., ed., The Jet Paradigm Vol. 794, Lecture Notes in Physics. Springer-Verlag, Berlin, p. 17
Gilfanov M., Churazov E., Revnivtsev M., 1999, A&A, 352, 182
Gilfanov M., Churazov E., Revnivtsev M., 2000, MNRAS, 316, 923
Ginzburg V. L., Syrovatskii S. I., 1969, ARA&A, 7, 375
Grove J. E., Johnson W. N., Kroeger R. A., McNaron-Brown K., Skibo J. G., Phlips B. F., 1998, ApJ, 500, 899
Hannikainen D. C., Hunstead R. W., Campbell-Wilson D., Wu K., McKay D. J., Smits D. P., Sault R. J., 2000, ApJ, 540, 521
Heinz S., Sunyaev R. A., 2003, MNRAS, 343, L59
Hynes R. I., Mauche C. W., Haswell C. A., Shrader C. R., Cui W., Chaty S., 2000, ApJ, 539, L37
Hynes R. I., Haswell C. A., Chaty S., Shrader C. R., Cui W., 2002, MNRAS, 331, 169
Hynes R. I. et al., 2003, MNRAS, 345, 292
Hynes R. I. et al., 2006, ApJ, 651, 401
Hynes R. I., Bradley C. K., Rupen M., Gallo E., Fender R. P., Casares J., Zurita C., 2009a, MNRAS, 399, 2239
Hynes R. I., Brien K. O., Mullally F., Ashcraft T., 2009b, MNRAS, 399, 281
Ibragimov A., Poutanen J., Gilfanov M., Zdziarski A. A., Shrader C. R., 2005, MNRAS, 362, 1435
Ikejiri Y. et al., 2011, PASJ, 63, 639
Impey C. D., Lawrence C. R., Tapia S., 1991, ApJ, 375, 46
Ingram A., Done C., 2011, MNRAS, 415, 2323
Jourdain E., Roques J. P., Chauvin M., Clark D. J., 2012a, ApJ, 761, 27
Jourdain E., Roques J. P., Malzac J., 2012b, ApJ, 744, 64
Kanbach G., Straubmeier C., Spruit H. C., Belloni T., 2001, Nat, 414, 180
Kato S., Fukue J., Mineshige S., 2008, Black-Hole Accretion Disks – Towards a New Paradigm. Kyoto Univ. Press, Kyoto
Königl A., 1981, ApJ, 243, 700
Kotov O., Churazov E., Gilfanov M., 2001, MNRAS, 327, 799
Kylafis N. D., Papadakis I. E., Reig P., Giannios D., Pooley G. G., 2008, A&A, 489, 481
Laurent P., Rodriguez J., Wilms J., Cadolle Bel M., Pottschmidt K., Grinberg V., 2011, Sci., 332, 438
Lightman A. P., Shapiro S. L., 1976, ApJ, 203, 701
Ling J. C. et al., 1997, ApJ, 484, 375
Lister M. L., 2001, ApJ, 562, 208
Loskutov V. M., Sobolev V. V., 1981, Astrofizika, 17, 535
Loskutov V. M., Sobolev V. V., 1982, Astrofizika, 18, 81
Lyubarskii Y. E., 1997, MNRAS, 292, 679
Maccarone T. J., 2005, MNRAS, 360, L68
Maccarone T. J., Coppi P. S., Poutanen J., 2000, ApJ, 537, L107
Malzac J., Belmont R., 2009, MNRAS, 392, 570
Malzac J., Belmont R., Fabian A. C., 2009, MNRAS, 400, 1512
Markoff S., Falcke H., Fender R., 2001, A&A, 372, L25
Marscher A. P., 1977, ApJ, 216, 244
Marscher A. P., Jorstad S. G., Mattox J. R., Wehrle A. E., 2002, ApJ, 577, 85
McClintock J. E. et al., 2001, ApJ, 555, 477
McConnell M. et al., 1994, ApJ, 424, 933
McConnell M. L. et al., 2002, ApJ, 572, 984
Meier D. L., 2005, Ap&SS, 300, 55
Merloni A., Di Matteo T., Fabian A. C., 2000, MNRAS, 318, L15
Mirabel I. F., Rodríguez L. F., 1994, Nat, 371, 46
Miyamoto S., Kitamoto S., 1989, Nat, 342, 773
Muno M. P., Mauerhan J., 2006, ApJ, 648, L135
Narayan R., Yi I., 1994, ApJ, 428, L13
Nayakshin S., Melia F., 1998, ApJS, 114, 269
Niedźwiecki A., Xie F.-G., Zdziarski A. A., 2012, MNRAS, 420, 1195
Nolan P. L. et al., 1981, ApJ, 246, 494
Nowak M. A., Vaughan B. A., Wilms J., Dove J. B., Begelman M. C., 1999a, ApJ, 510, 874
Nowak M. A., Wilms J., Dove J. B., 1999b, ApJ, 517, 355
O'Dea C. P., 1998, PASP, 110, 493
Pacholczyk A. G., Swihart T. L., 1967, ApJ, 150, 647
Pe'er A., Casella P., 2009, ApJ, 699, 1919
Pe'er A., Markoff S., 2012, ApJ, 753, 177
Poutanen J., 1994, ApJS, 92, 607
Poutanen J., 1998, in Abramowicz M. A., Björnsson G., Pringle J. E., eds, Theory of Black Hole Accretion Disks. Cambridge Univ. Press, Cambridge, p. 100
Poutanen J., 2001, Adv. Space Res., 28, 267
Poutanen J., 2002, MNRAS, 332, 257
Poutanen J., Coppi P. S., 1998, Phys. Scr. T, 77, 57
Poutanen J., Fabian A. C., 1999, MNRAS, 306, L31
Poutanen J., Vurm I., 2009, ApJ, 690, L97
Poutanen J., Zdziarski A. A., 2003, in Durouchoux P., Fuchs Y., Rodriguez J., eds, New Views on Microquasars. Center for Space Physics, Kolkata, p. 95
Poutanen J., Krolik J. H., Ryde F., 1997, MNRAS, 292, L21
Priedhorsky W., Garmire G. P., Rothschild R., Boldt E., Serlemitsos P., Holt S., 1979, ApJ, 233, 350
Quataert E., Narayan R., 1999, ApJ, 520, 298
Rahoui F. et al., 2012, MNRAS, 422, 2202
Revnivtsev M., Gilfanov M., Churazov E., 1999, A&A, 347, L23
Revnivtsev M., Gilfanov M., Churazov E., 2001, A&A, 380, 520
Russell D. M., Fender R. P., 2008, MNRAS, 387, 713
Russell D. M., Fender R. P., 2009, in Wachter A. D., Propst R. J., eds, Black Holes and Galaxy Formation. Nova Science Publishers, New York, p. 295
Russell D. M., Maitra D., Dunn R. J. H., Fender R. P., 2011, MNRAS, 416, 2311
Rybicki G. B., Lightman A. P., 1979, Radiative Processes in Astrophysics. Wiley-Interscience, New York
Schultz J., Hakala P., Huovelin J., 2004, Balt. Astron., 13, 581
Shadmehri M., Khajenabi F., 2005, MNRAS, 361, 719
Shahbaz T., Fender R. P., Watson C. A., O'Brien K., 2008, ApJ, 672, 510
Shakura N. I., Sunyaev R. A., 1973, A&A, 24, 337
Shidatsu M. et al., 2011, PASJ, 63, 803
Sikora M., Begelman M. C., Rees M. J., 1994, ApJ, 421, 153
Sobolev V. V., 1963, A Treatise on Radiative Transfer. Van Nostrand, Princeton
Sobolewska M. A., Papadakis I. E., Done C., Malzac J., 2011, MNRAS, 417, 280
Soleri P. et al., 2010, MNRAS, 406, 1471
Stern B. E., Poutanen J., 2006, MNRAS, 372, 1217
Uttley P., Wilkinson T., Cassatella P., Wilms J., Pottschmidt K., Hanke M., Böck M., 2011, MNRAS, 414, L60
Veledina A., Poutanen J., Vurm I., 2011a, ApJ, 737, L17
Veledina A., Vurm I., Poutanen J., 2011b, MNRAS, 414, 3330
Vurm I., Poutanen J., 2009, ApJ, 698, 293
Wardziński G., Zdziarski A. A., 2000, MNRAS, 314, 183
Wardziński G., Zdziarski A. A., 2001, MNRAS, 325, 963
Weisskopf M. C., Silver E. H., Kestenbaum H. L., Long K. S., Novick R., Wolff R. S., 1977, ApJ, 215, L65
Wills B. J., Wills D., Evans N. J. II, Natta A., Thompson K. L., Breger M., Sitko M. L., 1992, ApJ, 400, 96
Yan Z., Yu W., 2012, MNRAS, 427, L11
Zdziarski A. A., Gierliński M., 2004, Prog. Theor. Phys. Suppl., 155, 99
Zdziarski A. A., Poutanen J., Mikolajewska J., Gierlinski M., Ebisawa K., Johnson W. N., 1998, MNRAS, 301, 435
Zdziarski A. A., Lubinski P., Smith D. A., 1999, MNRAS, 303, L11
Zdziarski A. A., Grove J. E., Poutanen J., Rao A. R., Vadawale S. V., 2001, ApJ, 554, L45
Zdziarski A. A., Poutanen J., Paciesas W. S., Wen L., 2002, ApJ, 578, 357

Zdziarski A. A., Lubiński P., Gilfanov M., Revnivtsev M., 2003, MNRAS, 342, 355
Zdziarski A. A., Gierliński M., Mikołajewska J., Wardziński G., Smith D. M., Harmon B. A., Kitamoto S., 2004, MNRAS, 351, 791
Zdziarski A. A., Lubiński P., Sikora M., 2012, MNRAS, 423, 663

APPENDIX A: TYPICAL TIME-SCALES

A1 Radiative versus Coulomb time-scales

The synchrotron cooling time can be calculated as (e.g. Rybicki & Lightman 1979)

$$t_{\rm cool,s} = \frac{\gamma - 1}{|\dot{\gamma}_{\rm s}|} = \frac{1}{\gamma + 1}\left(\frac{4}{3}\frac{\sigma_{\rm T} U_{\rm B}}{m_{\rm e} c}\right)^{-1}, \quad \text{(A1)}$$

where $\dot{\gamma}_{\rm s}$ is synchrotron cooling rate. The cooling time for Compton scattering is similar. After a little algebra one can obtain

$$t_{\rm cool,s} \approx \frac{7.5\times10^{-4}}{\gamma+1}\frac{R}{c\eta_{\rm B}}\left(\frac{L}{L_{\rm Edd}}\right)^{-1}\left(\frac{R}{10R_{\rm S}}\right), \quad \text{(A2)}$$

where $\eta_{\rm B} = 3U_{\rm B}/(4\pi U_{\rm rad})$ denotes the ratio of the magnetic and radiation field energy densities. The typical time-scale of electron–electron Coulomb energy exchange at the equilibrium can be estimated as (e.g. Nayakshin & Melia 1998)

$$t_{\rm cool,Coul} = \frac{\gamma - 1}{|\dot{\gamma}_{\rm Coul}|} \approx \frac{2R}{3c}\frac{\overline{\gamma}_{\rm eq}}{\tau \ln\Lambda}\frac{z^3}{\gamma(\gamma+1)}, \quad \text{(A3)}$$

where z is the particle momentum in units of $m_{\rm e}c$, $\overline{\gamma}_{\rm eq}$ is the average Lorentz factor of the electrons in equilibrium and $\ln\Lambda$ is the Coulomb logarithm. At higher Lorentz factors the cooling is determined by radiative processes, while for lower γ the non-radiative Coulomb collisions are dominant. The relative role of radiative and Coulomb cooling changes with radius:

$$\frac{t_{\rm cool,Coul}}{t_{\rm cool,s}} \approx 56\frac{z^3\eta_{\rm B}}{\gamma\tau}\left(\frac{L}{L_{\rm Edd}}\right)\left(\frac{R}{10R_{\rm S}}\right)^{-1}, \quad \text{(A4)}$$

where we used $\overline{\gamma}_{\rm eq} = 1$ and $\ln\Lambda = 17$. Therefore, the Coulomb exchange rates start dominating the radiative cooling with an increasing size.

A2 Coulomb versus accretion time-scales

We assume that the photon spectra and electron distributions in each zone are in equilibrium; thus, the typical time-scales of equilibration should be much less than the dynamical time-scale at a given distance. To estimate the latter, we consider the properties of an advective hot flow, derived by Narayan & Yi (1994). Taking their radial velocity approximation, viscosity parameter 0.1 and assuming the adiabatic index 3/2 (Quataert & Narayan 1999), we obtain the advection/accretion time

$$t_{\rm adv} \approx 20\sqrt{\frac{R^3}{GM}}. \quad \text{(A5)}$$

We can compare the Coulomb (the radiative cooling is faster than Coulomb for $R \leq 100R_{\rm S}$) and advection time-scales (again, assuming $\overline{\gamma}_{\rm eq} = 1$)

$$\frac{t_{\rm cool,Coul}}{t_{\rm adv}} \approx 5\times10^{-4}\frac{\gamma}{\tau}\left(\frac{R}{10R_{\rm S}}\right)^{-1/2}. \quad \text{(A6)}$$

Hence, for typical parameters $\gamma \sim$1–100 and $\tau \sim$0.1–1, the cooling time-scale is shorter than the advection time.

APPENDIX B: MODIFICATIONS OF THE ORIGINAL MODEL

B1 Non-thermal fraction

One of the main assumptions in our work is that all the energy dissipated in the flow is transferred to the electrons by acceleration, i.e. 100 per cent of the power is injected in the form of power-law electrons. In reality, many other dissipation mechanisms may play a significant role in particle heating, such as electron–proton Coulomb collisions (the main energy transfer mechanism in the advective flow models), resonant interactions with plasma waves and other collective plasma effects. These acceleration processes do not lead to power-law electron distributions; instead, the Maxwellian distribution is heated as a whole, achieving higher temperature. Thus, it is important to check how robust the model is to changes in the fraction of non-thermal particles.

We note that effects of decreasing non-thermal injection fraction were considered in Malzac & Belmont (2009, fig. 9), who showed that as long as this fraction is more than ∼30 per cent, the results are very similar. However, they fixed the minimum and the maximum Lorentz factors of the injection; thus, decreasing the non-thermal fraction would result in decreasing of normalization of the injected power-law electrons. Here we investigate the effects of decreasing non-thermal energy fraction keeping the normalization of the injected power law constant by increasing $\gamma_{\rm min}$. As previously mentioned, the maximum Lorentz factor of accelerated electrons $\gamma_{\rm max} = 10^3$ is assumed. The energy fraction given to power-law electrons is calculated as

$$f_{\rm nth} = \frac{\overline{(\gamma-1)}}{\overline{[(\gamma-1)]}_{\rm nth}} = (\Gamma_{\rm inj}-1)(\Gamma_{\rm inj}-2)\int_{\gamma_{\rm min}}^{\gamma_{\rm max}}(\gamma-1)\gamma^{-\Gamma_{\rm inj}}{\rm d}\gamma, \quad \text{(B1)}$$

where the nominator corresponds to the energy given to accelerate the electrons between Lorentz factors $\gamma_{\rm min}$ and $\gamma_{\rm max}$, and denominator corresponds to the energy given in the purely non-thermal injection. For $\Gamma_{\rm inj} = 3.0$ and $\gamma_{\rm min} = 10$, the non-thermal fraction is $f_{\rm nth} = 0.19$, and for $\gamma_{\rm min} = 15$, $f_{\rm nth} = 0.13$. The rest of dissipated energy is given to electrons via stochastic heating as described in section 4.1 of Vurm & Poutanen (2009). We also consider a purely thermal model, where 100 per cent of energy gained by electrons is due to stochastic heating. For an illustration, we simulated an innermost zone ($i = 1$) of the hot flow with parameters described in Table 1. The results are shown in Fig. B1. We find that the resulting spectra are very similar for non-thermal fractions $f_{\rm nth} > 0.1$. For even smaller $f_{\rm nth}$, the spectra are harder, but slightly adjusting other parameters (magnetic field, Thomson optical depth) we can obtain spectra, which are very close to the original purely non-thermal models. At the same time, a purely thermal model has a much harder X-ray spectrum (with spectral index $\alpha = -0.43$ against $\alpha = -0.80$ for the non-thermal case) and higher equilibrium temperature ($kT_{\rm e} = 213$ keV against $kT_{\rm e} = 94$ keV for the non-thermal case), inconsistent with the existing X-ray data.

In order to describe the data with purely thermal model, a much higher magnetic field is required. Analysis of Wardziński & Zdziarski (2000) showed that purely thermal SSC cannot be the dominant radiative mechanism in majority of the X-ray binaries. However, it is interesting to test how the OIR spectrum would change in this case. Following equation 18 of Wardziński & Zdziarski (2000), the turnover frequency scales as $\nu_{\rm t} \propto B^{0.91}\tau^{0.05}T_{\rm e}^{0.95}$. As in the case of power-law electrons, it strongly depends on the magnetic field; however, the strongest

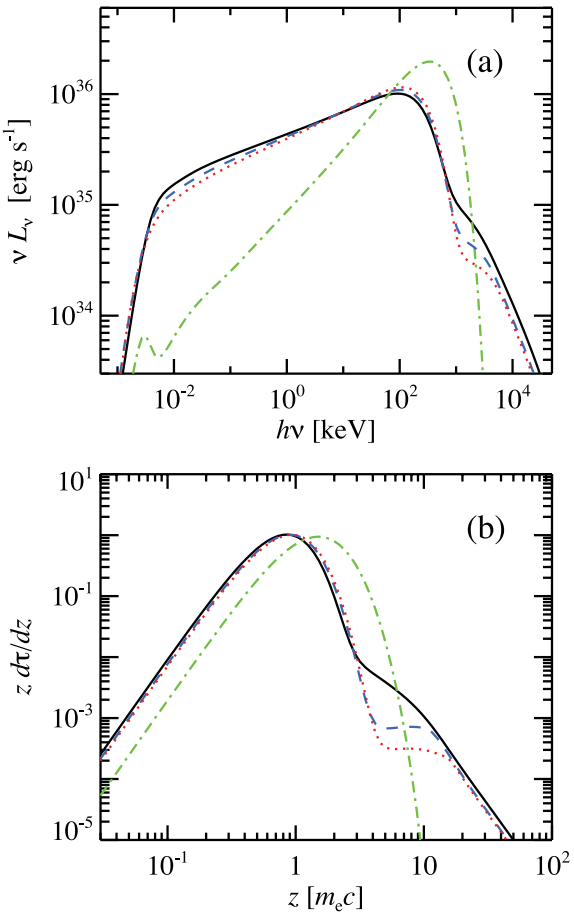

Figure B1. Effects of decreasing fraction of energy given to acceleration. Panel (a) shows resulting spectra and panel (b) gives the electron distributions. The solid black line corresponds to $f_{\rm nth} = 1.0$ (same as the purple long-dashed line in Fig. 4), $f_{\rm nth} = 0.19$ (blue dashed), $f_{\rm nth} = 0.13$ (red dotted) and $f_{\rm nth} = 0$ (thermal particles, green dot–dashed). For power-law electrons the injection index $\Gamma_{\rm inj} = 3.0$ was assumed.

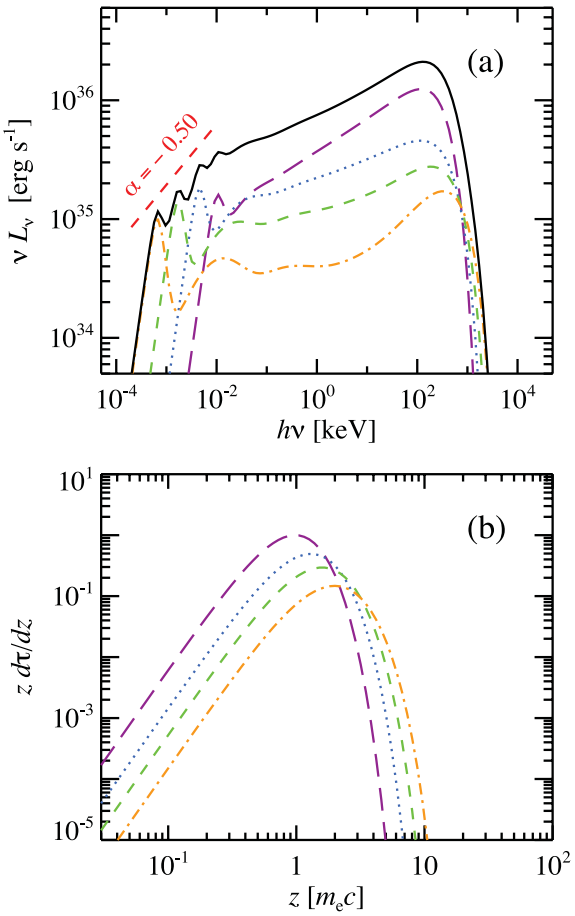

Figure B2. Same as in Figs 3 and 4, but for purely thermal electron distributions and 10 times larger magnetic field in every zone. The sharp peaks seen in the OIR are due to small number of zones considered and are not physical. The OIR spectrum is likely to be smeared and represents a power law at these wavelengths. The red dashed line is an analytical approximation for that.

dependence here is on the electron temperature. Assuming its scaling with radius $T_{\rm e} \propto R^{\kappa}$, we get

$$\nu_{\rm t} \propto R^{0.95\kappa - 0.91\beta - 0.05\theta}, \tag{B2}$$

which then implies that the OIR slope is

$$\alpha_{\rm OIR,th} = \frac{4 + 4.75\kappa - 3.55\beta - 0.25\theta}{1.9\kappa - 1.82\beta - 0.1\theta}. \tag{B3}$$

As an illustration, we performed simulations for a purely thermal model for the whole inhomogeneous hot flow with the parameters from Table 1, except that the magnetic field in every zone was taken an order of magnitude larger, $B_{i,\rm th} = 10 B_i$. This assumption is needed to match the typical X-ray spectra in the hard state ($\alpha \sim -0.7$). However, such high B is above the upper limit determined by the equipartition with protons at a virial temperature. The equilibrium electron temperature determined by the heating=cooling condition is about 20 per cent larger than in the non-thermal case (with lower B). The spectra and the electron distributions are shown in Fig. B2. We find that the scaling of the electron temperature with radius can be approximated with $\kappa \sim 0.3$. Substituting $\beta = 1.25$ and $\theta = 0.5$ gives the resulting OIR slope $\alpha_{\rm OIR,\,th} \approx -0.5$, in good agreement with the computed slope. Of course, no MeV emission is expected from purely thermal flows.

B2 Geometrical and radiative transfer effects

In this section, we investigate how the assumed geometry of the flow and the interaction between the zones affect the results. Let us first check how the thickness of the hot flow affects the spectra. In order to approximate the hot flow with a number of tori, the condition of $\Delta R_i \approx 2H_i$ should be satisfied. Taking $H/R = 0.25$ and using equation (8) we find $R_{i+1} \approx 5R_i/3$, with the innermost radius $R_1 = 3R_{\rm S}$. To cover the same distances from the BH, we now consider nine zones and scale parameters from Table 1 so that they correspond to the distance to the centre of each zone. We compare the results of calculations for $H/R = 0.25$ to those for $H/R = 0.5$ in Fig. B3. Due to the increase of local electron number density (H/R is reduced, while optical depth was kept constant), the X-ray spectrum has become harder compared to the case $H/R = 0.5$, while the OIR slopes are almost identical. The latter is not surprising, as the OIR spectral shape is determined by scaling of the hot-flow parameters, rather than by their exact values in each zone.

In our calculations we neglected the interaction between the zones and the spectrum of every zone was computed in the local approximation. However, photons from each zone can travel to the neighbouring zones. The largest effect is expected for the outer zones, because they occupy a large solid angle as viewed from the

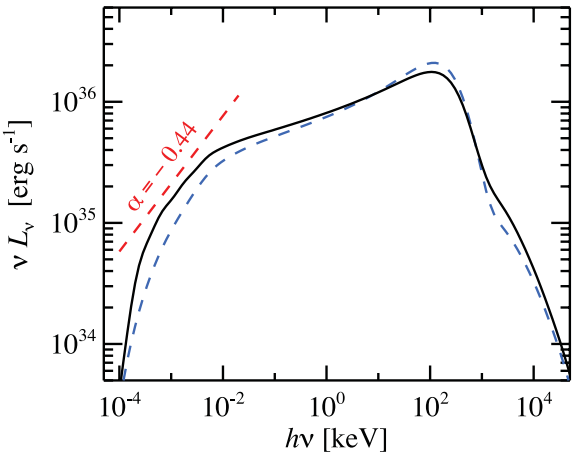

Figure B3. Spectra of a hot flow with different height-to-radius ratios. Total spectrum for $H/R = 0.25$ is shown with a blue dashed line and for $H/R = 0.5$ (same as in Fig. 4) is shown with a black solid line. The analytical approximation is shown with a red dashed line.

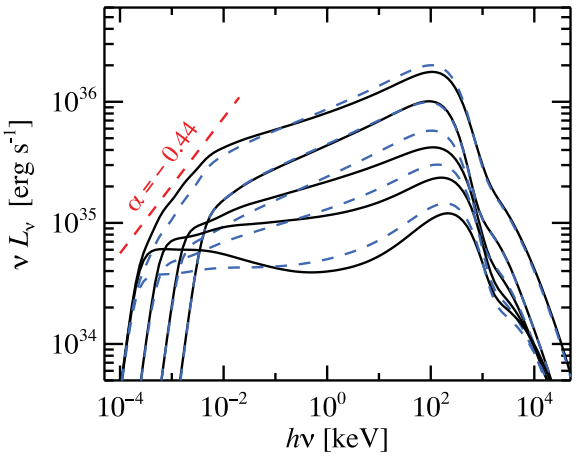

Figure B4. Spectra of the hot flow calculated accounting for the radiative transfer effects between the zones (blue dashed lines) and using the local approximation (solid black lines). The upper lines represent the total spectra. Parameters of the zones are the same as in Fig. 4 and $\Gamma_{\rm inj} = 3.0$ is assumed. The analytical approximation for the OIR spectrum (red dashed line) is sufficiently accurate for both cases.

inner zones and their luminosity is smaller than that of the inner zones. The radiative transfer effects can be approximately accounted for by first computing spectra of each zone in the local approximation and then by adding some fraction of the radiation escaping from each zones as an additional photon source for other zones. Luminosity coming from the ith zone to an adjacent $k = i \pm 1$th zone is parametrized by $\Omega_{ik}/(4\pi)L_i$, where Ω_{ik} is the solid angle occupied by kth zone as seen from ith zone. The formalism is similar to that used to simulate the outer cold disc photon injection to the hot flow. Luminosity coming from the ith zone to a non-adjacent zone j can be expressed as $\Omega_{ij}/(4\pi)L_i e^{-\tau_{ij}}$, where τ_{ij} is the photon optical depth of the medium between zones i and j (energy dependent, cumulative from different processes).

The resulting spectra accounting for the radiative transfer effects are compared to those computed in the local approximation in Fig. B4. The changes in the OIR slope are hardly visible. The X-ray spectra of the outer zones became now harder and the variation of the 2–10 keV spectral index is smaller $\Delta\alpha_{\rm X} \approx 0.03$ (versus 0.08). This effect is caused by additional photons coming from the harder spectra inner zones and scattered in the outer zones in the direction to the observer. Thus, the spectra computed in the local approximation are rather accurate and agree well with more detailed calculations.

This paper has been typeset from a TEX/LATEX file prepared by the author.

The Astrophysical Journal Letters, 737:L17 (5pp), 2011 August 10 doi:10.1088/2041-8205/737/1/L17

A SYNCHROTRON SELF-COMPTON–DISK REPROCESSING MODEL FOR OPTICAL/X-RAY CORRELATION IN BLACK HOLE X-RAY BINARIES

Alexandra Veledina[1], Juri Poutanen[1], and Indrek Vurm[2]
[1] Astronomy Division, Department of Physics, University of Oulu, P.O. Box 3000, 90014 Oulu, Finland;
alexandra.veledina@oulu.fi, juri.poutanen@oulu.fi
[2] Racah Institute of Physics, Hebrew University of Jerusalem, 91904 Jerusalem, Israel
Received 2011 May 13; accepted 2011 June 9; published 2011 July 22

ABSTRACT

The physical picture of the emission mechanisms operating in the X-ray binaries was put under question by the simultaneous optical/X-ray observations with high time resolution. The light curves of the two energy bands appeared to be connected and the cross-correlation functions observed in three black hole binaries exhibited a complicated shape. They show a dip of the optical emission a few seconds before the X-ray peak and the optical flare just after the X-ray peak. This behavior could not be explained in terms of standard optical emission candidates (e.g., emission from the cold accretion disk or a jet). We propose a novel model, which explains the broadband optical to the X-ray spectra and the variability properties. We suggest that the optical emission consists of two components: synchrotron radiation from the non-thermal electrons in the hot accretion flow and the emission produced by reprocessing of the X-rays in the outer part of the accretion disk. The first component is anti-correlated with the X-rays, while the second one is correlated, but delayed and smeared relative to the X-rays. The interplay of the components explains the complex shape of the cross-correlation function, the features in the optical power spectral density as well as the time lags.

Key words: accretion, accretion disks – black hole physics – methods: numerical – X-rays: binaries

Online-only material: color figures

1. INTRODUCTION

The physical processes giving rise to the broadband radio to X-ray spectra of accreting black holes are still under debate. There is a general consensus that the radio emission is associated with the jet and the X-rays are produced in the vicinity of the compact object. However, the origin of the IR/optical/UV emission from the black holes in low-mass X-ray binaries (LMXBs) is less certain. The contribution from the companion star in such systems is usually too faint, and the optical spectra are most likely connected to the accretion process onto the compact object and the X-ray radiation. To understand the origin of the optical emission, timing analyses of simultaneous optical and X-ray observations were performed. Such observations were for the first time carried out by Motch et al. (1983) for the black hole binary (BHB) GX 339–4. Although the duration of the observations was too short for any confident conclusion, the computed optical/X-ray cross-correlation function (CCF) revealed a complicated structure with a dip in the optical light curve, preceding the X-ray peak (the so-called precognition dip), together with an optical peak lagging the X-rays. Recently, CCFs were obtained from the much longer duration simultaneous observations in three LMXBs: XTE J1118+480 (Kanbach et al. 2001; Hynes et al. 2003), Swift J1753.5–0127 (Durant et al. 2008, 2011; Hynes et al. 2009), and GX 339–4 (Gandhi et al. 2008), all manifesting a similar structure. The observed behavior cannot be explained by a simple model with the optical radiation being produced by the reprocessed X-ray emission (Hynes et al. 2003). This hypothesis also contradicts the fact that the observed autocorrelation function (ACF) of the optical radiation is narrower than that of the X-rays (Kanbach et al. 2001; Hynes et al. 2003; Durant et al. 2009; Gandhi et al. 2010). On the other hand, study of the dependence of the CCF on the timescale of fluctuations in the light curve revealed that its overall shape remains similar, but rescaled (Malzac et al. 2003; Gandhi et al. 2010), suggesting that the emission in the two energy bands is intrinsically connected.

A number of possible mechanisms, producing such structure of the CCF, were proposed (see the discussion in Durant et al. 2011 and references therein). So far, the detailed calculations were made only in the model of Malzac et al. (2004), where both X-ray and optical emission are powered by the same magnetic energy reservoir. The model qualitatively describes the CCF and ACF of XTE J1118+480, however, with the new data on Swift J1753.5–0127, the applicability of the model was put under question. It is also doubtful that such an energetic magnetized zone is consistent with the accretion theories.

In this Letter, we suggest that the optical emission is a composition of two components. The first one is coming from the synchrotron-emitting particles in the inner hot flow and is anti-correlated with the X-ray emission, which is produced by Comptonization of the synchrotron radiation. The second one is originating from reprocessing of the X-rays by the outer parts of the cold accretion disk (Dubus et al. 1999; Gierliński et al. 2009; Chiang et al. 2010). This component is (positively) correlated and delayed relative to the X-rays. The presence of two components explains both the precognition dip and the delayed peak of the CCF. The model is capable of explaining the entire optical to the X-ray spectrum of BHBs as well as their timing properties.

2. SPECTRAL MODEL

The X-ray spectra of BHBs in their hard state are well described by Comptonization on thermal electrons (e.g., Poutanen 1998; Zdziarski & Gierliński 2004), however power-law tails detected in a number of sources (Zdziarski et al. 2001; McConnell et al. 2002) suggest the presence of non-thermal particle population in addition to the mostly thermal distribution (Poutanen & Coppi 1998). These electrons contribute both to the high-energy part of the spectrum via Compton scattering and to the

low-energy part by synchrotron radiation. Even a tiny fraction of non-thermal electrons dramatically increases the synchrotron luminosity (Wardziński & Zdziarski 2001) and thus makes it a plausible source of seed photons for Comptonization. The X-ray spectra of the hard-state BHBs (and supermassive black holes) can be modeled in terms of synchrotron self-Compton (SSC) mechanism in hybrid (thermal plus non-thermal) plasmas (Vurm & Poutanen 2008; Poutanen & Vurm 2009; Malzac & Belmont 2009; Veledina et al. 2011). The high-energy part of the spectrum is dominated by the Comptonized photons, and the low-energy part is determined by the synchrotron emission, which can extend down to the IR/optical energy bands depending on the size of the emission region.

For simplicity, we consider a spherical emission region homogeneously filled with photons and electrons. The region corresponds to a hot flow in the vicinity of the black hole (see reviews in Narayan et al. 1998; Yuan et al. 2007), with the size limited by the inner radius of the (truncated) accretion disk. We consider the energy input in the form of injected electrons with a power-law spectrum $dN_e/(dt\, d\gamma) \propto \gamma^{-\Gamma_{\rm inj}}$ extending between the Lorentz factors $\gamma_{\rm min}$ and $\gamma_{\rm max}$. The injection might result from magnetic reconnection or shock acceleration. The main mechanisms responsible for particle cooling and thermalization and formation of the spectra are cyclo-synchrotron emission and absorption, Compton scattering, and electron–electron Coulomb collisions. To find self-consistent photon spectra and electron distributions, we solve a set of kinetic equations for photons, electrons, and positrons using the numerical code developed by Vurm & Poutanen (2009).

A good description of the broadband spectra of hard-state BHBs can be achieved with the following parameters (see Poutanen & Vurm 2009): the Thomson optical depth $\tau = 1.0$, the magnetic field $B = 3 \times 10^5$ G, and the total luminosity of the region $L = 10^{37}$ erg s^{-1}. The parameters of the injection function are $\Gamma_{\rm inj} = 3$, $\gamma_{\rm min} = 1.0$, and $\gamma_{\rm max} = 10^3$. The size of the emission region R is assumed to be 30 Schwarzschild radii, which corresponds to 9×10^7 cm for a $10\,M_\odot$ black hole. For this set of parameters, the synchrotron self-absorption frequency falls in the optical energy band (1–10 eV). The resulting spectrum and the electron distribution are shown in Figure 1 (solid line).

The broadband spectra are expected to vary due to the changes of the mass accretion rate $\dot{m}$. We assume that the luminosity varies as $L \propto \dot{m}$, the optical depth as $\tau \propto \dot{m}$, and the size of the hot flow (inner cold disk radius) as $R \propto \dot{m}^{-4/3}$ (Różańska & Czerny 2000). We assume that the magnetic field and the injection index $\Gamma_{\rm inj}$ are constant. With an increase of the accretion rate, the X-ray luminosity increases, whereas the optical radiation drops due to the increased synchrotron self-absorption and vice versa (dashed and dotted lines in Figure 1). The resulting X-ray spectral behavior with hardening during the X-ray flares and softening during the X-ray dips is consistent with the observations (Gandhi et al. 2010). The decrease of the synchrotron radiation with an increase of the mass accretion rate was also found to take place in the advective disk models (Yuan et al. 2005). Thus, the optical synchrotron luminosity is expected to anti-correlate with the X-rays.

3. TIMING MODEL

3.1. Formalism

The X-ray and the optical light curves can be represented as a sum of a constant (mean) and variable components: $x(t) = \bar{x}[1 + \delta x(t)]$ and $o(t) = \bar{o}[1 + \delta o(t)]$, where δx and δo are the relative deviations from the mean. Two components contribute to the variations of the optical radiation: the synchrotron emission from the hot flow δs and the radiation coming from reprocessing of the X-rays in the accretion disk δd

$$\delta o(t) = \delta s(t)\frac{\bar{s}}{\bar{o}} + \delta d(t)\frac{\bar{d}}{\bar{o}}. \quad (1)$$

The anti-correlation between synchrotron and the X-rays (see Section 2) can be represented as

$$\delta s(t) = -\frac{\mathrm{rms_s}}{\mathrm{rms_x}}\delta x(t), \quad (2)$$

where rms denotes the fractional root mean square amplitude of variability of the corresponding components.[3] The reprocessed radiation from the disk is a convolution of the X-ray light curve with the disk response function $r(t)$:

$$\delta d(t) = \int_{-\infty}^{t} r(t - t')\delta x(t')dt'. \quad (3)$$

Assuming that the entire disk luminosity in the optical band is due to irradiation and the response is a δ-function, the fractional rms of the disk would be equal to that of the X-rays. The total

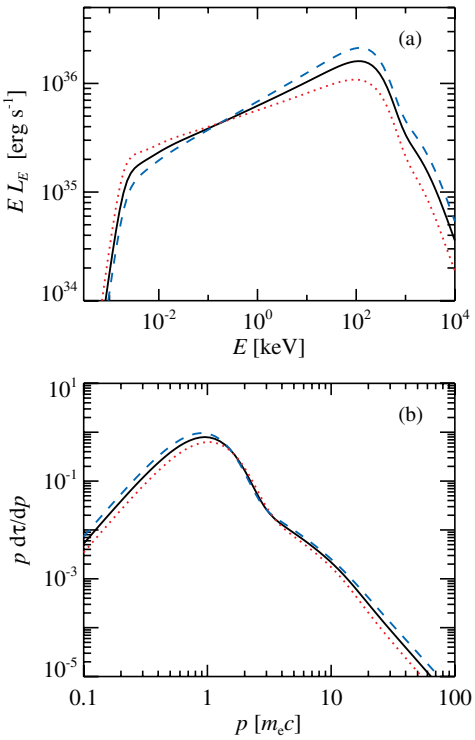

Figure 1. Simulated (a) photon spectra and (b) electron distributions for the SSC model for hybrid plasmas. Solid lines correspond to the fiducial parameter set (see the text), an increase of the accretion rate by 20% hardens the spectrum (blue dashed line) and a decrease of the accretion rate by 20% softens the spectrum (red dotted line). These spectra are associated with the inner hot flow and an additional contribution of the irradiated accretion disk is not shown.

(A color version of this figure is available in the online journal.)

[3] We assume here that the decrease of the synchrotron luminosity is simultaneous with the increase of the X-rays, neglecting possible delays (see the discussion in Section 4).

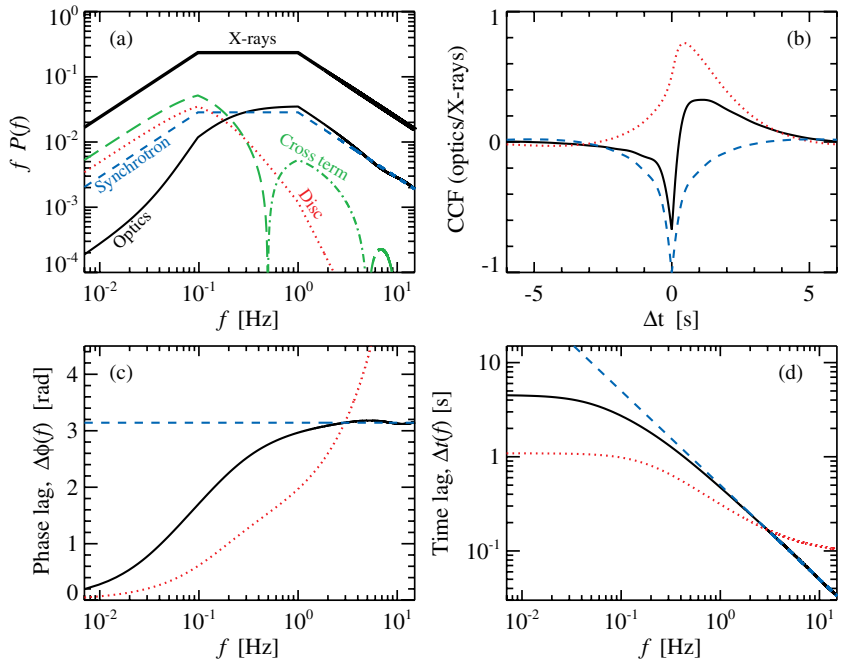

Figure 2. Results of simulations for the model with the exponential disk response function with $\tau_1 = 0.1$ and $\tau_2 = 1.0$, and $r_{\rm ds} = 1.3$. (a) The PSDs of the X-ray (double-broken PSD, thick solid line) and optical light curves (thin solid line). Three terms contributing to the optical PSD (see Equation (8)) are also shown: synchrotron (dashed line), disk (dotted line), and the cross term (positive contribution is shown by the dot-dashed line and the negative contribution by the long-dashed line). (b) The CCFs, (c) the phase lags, and (d) the time lags corresponding to the synchrotron/X-rays ($r_{\rm ds} = 0$, dashed line), reprocessed disk component/X-rays ($r_{\rm ds} \to \infty$, dotted line), and the combined optical/X-rays (solid line).

(A color version of this figure is available in the online journal.)

optical light curve can be represented as

$$\delta o(t) = \frac{{\rm rms_s}}{{\rm rms_x}} \frac{\bar{s}}{\bar{o}} \left[-\delta x(t) + r_{\rm ds} \int_{-\infty}^{t} \delta x(t') r(t-t') dt' \right], \quad (4)$$

where we introduced the ratio of the absolute contributions of the disk and the synchrotron to the variable optical component (with the assumption of a δ-function response):

$$r_{\rm ds} = \frac{{\rm rms_x}}{{\rm rms_s}} \frac{\bar{d}}{\bar{s}}. \quad (5)$$

As follows from Equation (4), the optical/X-ray CCF contains two terms: one arising from synchrotron (it is just an ACF of the X-rays with a negative sign) and another from the disk.

The Fourier transforms[4] for the optical light curves are the sum of the synchrotron $S(f) \propto -X(f)$ and the disk $D(f) = X(f)R(f)$ transforms, and according to Equation (4) can be represented as

$$O(f) = S(f) + D(f) \propto X(f)\left[-1 + r_{\rm ds} R(f)\right]. \quad (6)$$

The optical/X-ray cross-spectrum is proportional to the X-ray power spectral density (PSD, $P_{\rm X}$)

$$C(f) = X^*(f) O(f) \propto P_{\rm X}(f)\left[-1 + r_{\rm ds} R(f)\right]. \quad (7)$$

Its phase is the phase lag $\Delta\phi(f)$ and the time lag is $\Delta t(f) = \Delta\phi(f)/2\pi f$. The optical PSD consists of three terms: the synchrotron term, the disk term, and a cross term

$$P_{\rm O}(f) \propto P_{\rm X}(f)\left\{1 + r_{\rm ds}^2 |R(f)|^2 - 2 r_{\rm ds} {\rm Re}\left[R(f)\right]\right\}. \quad (8)$$

The model is fully determined by the rms in the X-ray and optical bands (${\rm rms_x}$ and ${\rm rms_o}$), the ratio $r_{\rm ds}$, the disk response function $r(t)$, and the shape of the X-ray PSD.[5]

3.2. Examples

For an illustration, we choose the double-broken power-law X-ray PSD, $P_{\rm X}(f) \propto f^0$, f^{-1}, and f^{-2} with the breaks at 0.1 and 1.0 Hz. This shape is typical for BHBs in their hard state (Gilfanov et al. 1999; Revnivtsev et al. 2001; Axelsson et al. 2005; Gandhi et al. 2008). We take ${\rm rms_x} = 1.0$ and ${\rm rms_o} = 0.3$ and consider a simple exponential response function

$$r(t) = \begin{cases} \exp\left[-(t-\tau_1)/\tau_2\right]/\tau_2, & t \geqslant \tau_1, \\ 0, & t < \tau_1, \end{cases} \quad (9)$$

where τ_1 corresponds to the delay time of the disk response and τ_2 is the response width. The corresponding Fourier image is $R(f) = \exp({\rm i}x_1)/(1 - {\rm i}x_2)$, where $x_k = 2\pi f \tau_k$. We take $\tau_1 = 0.1$ s and $\tau_2 = 1$ s. The results of simulations are shown in Figure 2.

Contributions of different terms and the total PSDs are shown in Figure 2(a). The synchrotron term (the first term in Equation (8)) has the same shape as the X-ray PSD, the disk (the second term in Equation (8)) acts as a low-pass filter, and the cross term (the last term in Equation (8)) changes sign, giving positive contribution to the high-frequency part and negative contribution to the low-frequency part. The combined contribution of the two (synchrotron and disk) components to the optical light curve strongly suppresses the low-frequency power (as they vary in anti-phase) and increases the high-frequency

[4] The Fourier transforms corresponding to $\delta x(t)$, $\delta o(t)$, $\delta s(t)$, $\delta d(t)$, and $r(t)$ are denoted as $X(f)$, $O(f)$, $S(f)$, $D(f)$, and $R(f)$, respectively, with f being the Fourier frequency.

[5] We choose such a PSD normalization so that the integral over positive frequencies gives the square of relative rms of the light curve (Miyamoto & Kitamoto 1989) $\int P_{\rm X}(f) df = {\rm rms_x^2}$.

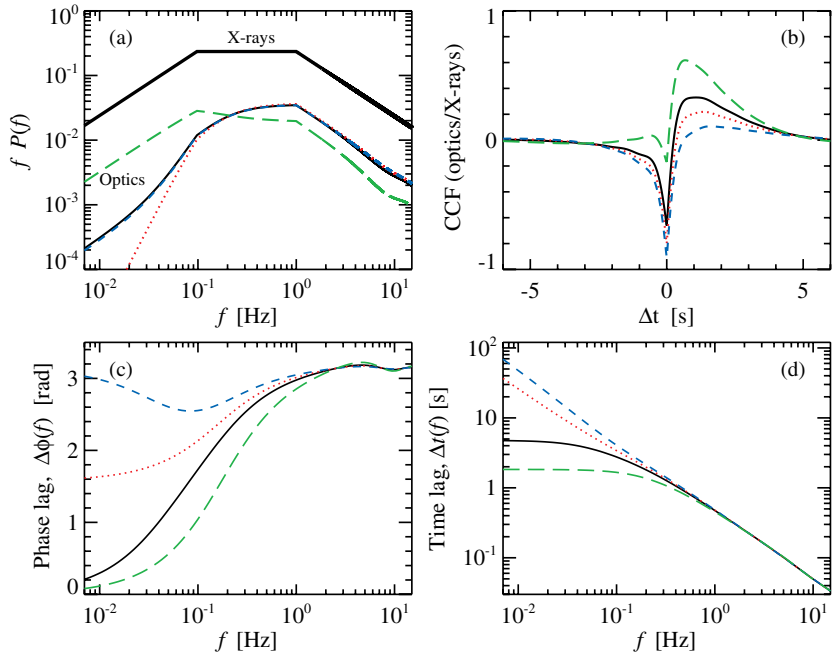

Figure 3. (a) X-ray and optical PSDs, (b) optical/X-ray CCFs, (c) optical/X-ray phase lags, and (d) time lags for various $r_{\rm ds}$. The results for $r_{\rm ds} = 0.7$, 1.0, 1.3, and 2.5 are shown by dashed, dotted, solid, and long-dashed lines, respectively. The X-ray PSD is shown with the thick solid line. Other parameters are as in Figure 2.
(A color version of this figure is available in the online journal.)

power making a bump at frequencies ∼0.1–1 Hz in the optical power spectrum (similar to that found in GX 339–4 by Gandhi et al. 2010). The excess of power at higher frequencies makes the optical ACF narrower than that of the X-rays.

The simulated CCFs for separate components and their joint contribution are shown in Figure 2(b). The width of the precognition dip depends on the shape of the X-ray PSD. The amplitudes of both negative and positive peaks are reduced, when there are two components in the optical band, as they enter Equation (4) with different signs and thus partially cancel each other. The fast rise of the CCF at zero lag is related to the interplay of the two optical components. The shape of the CCF resembles those found in Swift J1753.5–0127 (Durant et al. 2008, 2011).

The corresponding optical/X-ray phase and time lags are shown in Figures 2(c) and (d). For the assumed disk response function, the phase lag can be described by the analytical expression (Equation (29) in Poutanen 2002):

$$\tan\Delta\phi(f) = \frac{r_{\rm ds}(\sin x_1 + x_2\cos x_1)}{-1 - x_2^2 + r_{\rm ds}(\cos x_1 - x_2\sin x_1)}. \qquad (10)$$

If synchrotron dominates the optical emission (i.e., $r_{\rm ds} < 1$), then $\Delta\phi(f) \approx \pi$ and $\Delta t(f) \propto f^{-1}$ (dashed lines). Such a dependence was observed in XTE J1118+480 (Malzac et al. 2003). In a general case, the synchrotron dominates at high frequencies, while at low frequencies we get

$$\Delta\phi(f) \approx \begin{cases} \dfrac{r_{\rm ds}}{r_{\rm ds}-1}(x_1+x_2), & \text{if } r_{\rm ds} > 1, \\ \pi - \dfrac{r_{\rm ds}}{1-r_{\rm ds}}(x_1+x_2), & \text{if } r_{\rm ds} < 1. \end{cases} \qquad (11)$$

In the first case ($r_{\rm ds} > 1$), this translates into constant time lags $\Delta t \approx (\tau_1+\tau_2)r_{\rm ds}/(r_{\rm ds}-1)$.

If the X-ray PSD is fixed, three parameters control the shape of the CCF and the optical PSD: τ_1, τ_2, and $r_{\rm ds}$. The first two parameters do not affect the CCF dramatically, therefore we further study the role of $r_{\rm ds}$. An increase of $r_{\rm ds}$ obviously results in suppression of the precognition dip in the CCF (Figure 3(b)), in the disk-dominating regime $r_{\rm ds} \gg 1$ giving the CCF of simple reprocessing. At the same time, the role of this parameter in the PSD is not so straightforward, as can be seen in Figure 3(a). The low-frequency tail is maximally suppressed at $r_{\rm ds} = 1.0$ at which the disk and synchrotron nearly cancel each other. The high-frequency part is dominated by the synchrotron PSD and is almost independent of $r_{\rm ds}$. We note that for $r_{\rm ds} = 1 \pm \alpha$ (with $|\alpha| < 1$) the PSD shapes are nearly the same, while the corresponding CCFs are different (compare the dashed and the solid lines in Figures 3(a) and (b)). The phase- or time-lag spectra (Figures 3(c) and (d)) also strongly depend on $r_{\rm ds}$. The larger the value of $r_{\rm ds}$, the closer the phase spectrum is to that of simple reprocessing.

4. SUMMARY AND DISCUSSION

In this Letter, we present a spectral model capable of explaining optical/X-ray timing features observed in LMXBs. We argue that the optical emission is partially produced in the hot accretion flow (at distance $R \gtrsim 30\,R_{\rm S}$) by synchrotron radiation, which also provides seed photons for Comptonization. Additional contribution to the optical band comes from reprocessing of the X-ray emission in the cold accretion disk. We show that the presence of the two components can explain the observed shape of the CCF with the pronounced optical precognition dip. The model also reproduces another interesting feature observed in the LMXBs, namely, the optical ACF being narrower than the X-ray one. The explanation of the feature comes from the optical PSD, where the low-frequency part is suppressed and a bump appears at frequencies ∼0.1–1 Hz, both due to the presence of the cross term. The power at high frequencies originates from the interplay of the two optical components, which also results in the fast rise of the CCF at zero lag. The Fourier frequency-dependent time lags resemble the observed ones.

We note that the proposed model is simplified, as it does not account for the fact that the optical synchrotron radiation comes from the outer parts of the hot flow, while the X-rays are likely to originate from the very vicinity of the compact object. This consideration leads to two complications: first, the synchrotron should lead the X-rays by the viscous timescale of about $\Delta t \sim 0.1$ s; second, it should have less power at high frequencies compared to the X-rays. The latter is rather important as it leads to suppression of the high-frequency optical PSD, thus broadening the precognition dip. The correct shape of the X-ray PSD is essential for comparison to the observed CCF, as it influences the shape of the precognition dip dramatically, at the same time affecting the width of the optical peak at positive lags. Generally, the broader is the X-ray ACF, the broader are the two features in the CCF (as indeed is observed; Durant et al. 2008, 2011). The detailed comparison with the data will be a subject of our further investigations.

This work was supported by the Finnish Graduate School in Astronomy and Space Physics (A.V.), the Academy of Finland grant 127512 (J.P.), and the Wihuri Foundation and ERC Advanced Research Grant 227634 (I.V.). The authors thank Mike Revnivtsev and Piergiorgio Casella for useful discussions.

REFERENCES

Axelsson, M., Borgonovo, L., & Larsson, S. 2005, A&A, 438, 999
Chiang, C. Y., Done, C., Still, M., & Godet, O. 2010, MNRAS, 403, 1102
Dubus, G., Lasota, J.-P., Hameury, J.-M., & Charles, P. 1999, MNRAS, 303, 139
Durant, M., Gandhi, P., Shahbaz, T., Fabian, A. P., Miller, J., Dhillon, V. S., & Marsh, T. R. 2008, ApJ, 682, L45
Durant, M., Gandhi, P., Shahbaz, T., Peralta, H. H., & Dhillon, V. S. 2009, MNRAS, 392, 309
Durant, M., et al. 2011, MNRAS, 410, 2329
Gandhi, P., et al. 2008, MNRAS, 390, L29
Gandhi, P., et al. 2010, MNRAS, 407, 2166
Gierliński, M., Done, C., & Page, K. 2009, MNRAS, 392, 1106
Gilfanov, M., Churazov, E., & Revnivtsev, M. 1999, A&A, 352, 182
Hynes, R. I., Brien, K. O., Mullally, F., & Ashcraft, T. 2009, MNRAS, 399, 281
Hynes, R. I., et al. 2003, MNRAS, 345, 292
Kanbach, G., Straubmeier, C., Spruit, H. C., & Belloni, T. 2001, Nature, 414, 180
Malzac, J., Belloni, T., Spruit, H. C., & Kanbach, G. 2003, A&A, 407, 335
Malzac, J., & Belmont, R. 2009, MNRAS, 392, 570
Malzac, J., Merloni, A., & Fabian, A. C. 2004, MNRAS, 351, 253
McConnell, M. L., et al. 2002, ApJ, 572, 984
Miyamoto, S., & Kitamoto, S. 1989, Nature, 342, 773
Motch, C., Ricketts, M. J., Page, C. G., Ilovaisky, S. A., & Chevalier, C. 1983, A&A, 119, 171
Narayan, R., Mahadevan, R., & Quataert, E. 1998, in Theory of Black Hole Accretion Disks, ed. M. A. Abramowicz, G. Bjornsson, & J. E. Pringle (Cambridge: Cambridge Univ. Press), 148
Poutanen, J. 1998, in Theory of Black Hole Accretion Disks, ed. M. A. Abramowicz, G. Björnsson, & J. E. Pringle (Cambridge: Cambridge Univ. Press), 100
Poutanen, J. 2002, MNRAS, 332, 257
Poutanen, J., & Coppi, P. S. 1998, Phys. Scr. T, 77, 57
Poutanen, J., & Vurm, I. 2009, ApJ, 690, L97
Revnivtsev, M., Gilfanov, M., & Churazov, E. 2001, A&A, 380, 520
Różańska, A., & Czerny, B. 2000, A&A, 360, 1170
Veledina, A., Vurm, I., & Poutanen, J. 2011, MNRAS, in press (arXiv:1012.0439)
Vurm, I., & Poutanen, J. 2008, Int. J. Mod. Phys., 17, 1629
Vurm, I., & Poutanen, J. 2009, ApJ, 698, 293
Wardziński, G., & Zdziarski, A. A. 2001, MNRAS, 325, 963
Yuan, F., Cui, W., & Narayan, R. 2005, ApJ, 620, 905
Yuan, F., Zdziarski, A. A., Xue, Y., & Wu, X.-B. 2007, ApJ, 659, 541
Zdziarski, A. A., & Gierliński, M. 2004, Prog. Theor. Phys. Suppl., 155, 99
Zdziarski, A. A., Grove, J. E., Poutanen, J., Rao, A. R., & Vadawale, S. V. 2001, ApJ, 554, L45

The Astrophysical Journal, 778:165 (8pp), 2013 December 1 doi:10.1088/0004-637X/778/2/165

A UNIFIED LENSE–THIRRING PRECESSION MODEL FOR OPTICAL AND X-RAY QUASI-PERIODIC OSCILLATIONS IN BLACK HOLE BINARIES

Alexandra Veledina[1], Juri Poutanen[1], and Adam Ingram[2]
[1] Astronomy Division, Department of Physics, P.O. Box 3000, FI-90014, University of Oulu, Finland; alexandra.veledina@oulu.fi, juri.poutanen@oulu.fi
[2] Astronomical Institute "Anton Pannekoek," University of Amsterdam, Postbus 94249, 1098 GE Amsterdam, The Netherlands
Received 2013 June 10; accepted 2013 October 9; published 2013 November 13

ABSTRACT

Recent observations of accreting black holes reveal the presence of quasi-periodic oscillations (QPO) in the optical power density spectra. The corresponding oscillation periods match those found in X-rays, implying a common origin. Among the numerous suggested X-ray QPO mechanisms, some may also work in the optical. However, their relevance to the broadband—optical through X-ray—spectral properties have not been investigated. For the first time, we discuss the QPO mechanism in the context of the self-consistent spectral model. We propose that the QPOs are produced by Lense–Thirring precession of the hot accretion flow, whose outer parts radiate in optical wavelengths. At the same time, its innermost parts are emitting X-rays, which explains the observed connection of QPO periods. We predict that the X-ray and optical QPOs should be either in phase or shifted by half a period, depending on the observer position. We investigate the QPO harmonic content and find that the variability amplitudes at the fundamental frequency are larger in the optical, while the X-rays are expected to have strong harmonics. We then discuss the QPO spectral dependence and compare the expectations to the existing data.

Key words: accretion, accretion disks – black hole physics – radiation mechanisms: non-thermal – X-rays: binaries

Online-only material: color figures

1. INTRODUCTION

Accreting black holes (BH) remain among the most fascinating objects studied since the very beginning of the X-ray era. Their observed X-ray radiation is variable on a wide range of timescales, displaying dramatic changes in spectral shape between the power-law-dominated hard state and the quasi-thermal soft state over timescales of weeks (Zdziarski & Gierliński 2004). Strong variability is also seen on far shorter (down to ∼10 ms) timescales. Among the most prominent features commonly observed in the power spectral density (PSD) of BH binaries are low-frequency quasi-periodic oscillations (QPOs; Remillard & McClintock 2006; Done et al. 2007), with a characteristic frequency that evolves from ∼0.1–10 Hz at spectral transitions from the hard to the soft state. A growing number of low-mass X-ray binaries have also been found to exhibit similar QPOs in the optical and UV PSDs (Motch et al. 1983, 1985; Imamura et al. 1990; Steiman-Cameron et al. 1997; Hynes et al. 2003; Durant et al. 2009; Gandhi et al. 2010). The optical, UV, and X-ray QPOs in XTE J1118+480 have been observed to share a common (within uncertainties) characteristic frequency whilst evolving over nearly 2 months of observations (Hynes et al. 2003). In the X-rays, the QPO frequency is correlated with the low-frequency break of the broadband noise (Wijnands & van der Klis 1999; Belloni et al. 2002). Hints of such a correlation in the optical can also be found in the existing data (Gandhi et al. 2010; Hynes et al. 2003), however, the significance is too low to make any conclusive statements. It is therefore suggestive that X-ray and optical QPOs are formed by a common mechanism which is somehow related to the production of aperiodic variability (broadband noise). However, there is no consensus in the literature as to the origin of X-ray QPOs and so far no optical QPO mechanism has been suggested.

Proposed X-ray QPO mechanisms are generally based either on the misalignment of the BH and binary system spins (e.g., Stella & Vietri 1998) or on oscillation modes of the accretion flow itself (e.g., Wagoner et al. 2001). Many of them, however, discuss QPO production separately and do not consider its relation to the aperiodic X-ray variability. Probably the most promising QPO model to date was proposed in Ingram et al. (2009), where the oscillations arise from the precession of orbits around the BH due to misalignment of the BH and orbital spins known as Lense–Thirring precession. Similar models proposed earlier considered the precession of a test mass (Schnittman et al. 2006), leading to a strong dependence of the predicted QPO frequency on BH spin, inconsistent with the observations. The model of Ingram et al. (2009) considers the precession of the entire hot flow, which leads to a much weaker spin dependence. We note that the precession of the entire flow as a solid body can only be possible in the case of a hot geometrically thick accretion flow (Fragile et al. 2007), while a cold thin disk would produce a steady warp in the plane perpendicular to the BH spin (Bardeen & Petterson 1975; Kumar & Pringle 1985). Recently, it was shown that the physical parameters of the hot flow picked to match the observed QPO frequency are also consistent with those required to produce the characteristic frequencies of the broad band noise (Ingram & Done 2011), thus a global connection between the QPO and aperiodic variability was established.

This variability model ultimately requires a geometry where the cold (Shakura & Sunyaev 1973) accretion disk is truncated at a particular radius and the BH vicinity is occupied by a type of hot accretion flow (the truncated disk model; Esin et al. 1997; Poutanen et al. 1997). The power law component of the X-ray spectrum can be understood in this geometry as Compton upscattering of cold seed photons by hot electrons in the flow. The seed photons are often assumed to be provided by the disk, however, in the hard state when the truncation radius is large (∼30 R_S where $R_S = 2GM/c^2$ is the Schwarzschild radius), the luminosity of disk photons incident on the flow is

insufficient to reproduce the observed spectra and an additional source of seed photons is required. This can be provided by synchrotron radiation in the flow. Compton up-scattering of the resulting internally produced seed photons (the synchrotron self-Compton mechanism) can successfully reproduce the observed hard state spectra (Malzac & Belmont 2009; Poutanen & Vurm 2009). Let us note that an array of accretion geometries can explain the observed spectra but the Lense–Thirring QPO model is compatible only with the truncated disk model considered here.

Lately, it was shown that the hot flow synchrotron emission can contribute to optical and even IR (OIR) wavelengths (Veledina et al. 2013), thus these wavelengths are tightly connected to the X-ray component. Hence, the spectral model also predicts the connection between the OIR and the X-ray aperiodic variability. However, simultaneous analysis of light curves in these wavelengths (Motch et al. 1983; Kanbach et al. 2001; Hynes et al. 2003; Durant et al. 2008; Gandhi et al. 2010) has revealed a complicated connection between them, which can be understood if one considers several components contributing to the optical (Veledina et al. 2011), namely the hot accretion flow and the reprocessed radiation. Additionally, the jet optically thin synchrotron emission can also be significant (e.g., Casella et al. 2010). These three components presumably can be responsible for the OIR QPOs.

In Section 2 we develop a quantitative model for the low-frequency OIR and X-ray QPOs, which are produced by Lense–Thirring precession of a hot accretion flow. We make predictions for the OIR QPO profiles and compare them to those expected in the X-rays. We then calculate the phase lags and harmonic content expected from this model. In Section 3, we discuss the limitations of the model and possible improvements and compare the model predictions with the data. We summarize our findings in Section 4.

2. HOT FLOW QPO MODEL

2.1. Assumptions

In this section, we outline our assumptions. We consider a hot accretion flow extending from an inner radius to the truncation radius of the cold outer disk and a spin axis misaligned with that of the BH by an angle β. In the Kerr metric, test particle orbits out of the plane of BH rotation undergo Lense–Thirring precession due to the dragging of inertial frames, with a frequency $\nu_{\rm LT}(R) \propto \sim R^{-3}$. In the case of a hot accretion flow, this differential precession creates a warp which propagates through the flow on a time scale shorter than the precession period. This can cause the entire flow to precess as a solid body at a frequency given by a surface-density-weighted average of $\nu_{\rm LT}(R)$ (Fragile et al. 2007). If the flow is assumed to extend from the disk truncation radius to the innermost stable circular orbit, the dependence of the precession frequency on BH spin is too strong and the maximum precession frequency is too high to be consistent with observations. In order to put the Lense–Thirring frequencies into the observed QPO range, from ∼0.03 Hz (Vikhlinin et al. 1994) up to ∼13 Hz (Remillard et al. 1999), one needs to account for the torque created by frame dragging, which truncates the inner flow at a fairly large (inner) radius ($\gtrsim 3\,R_{\rm S}$, see Equation (22) of Lubow et al. 2002, where $x = 1$ should be taken) and effectively cancels out much of the spin dependence of precession (Ingram et al. 2009). This effect has since been seen in simulations (Fragile 2009). We reproduce the dependence of the QPO frequency on the outer radius of the hot flow in Figure 1. Since we aim to model the hard state, we assume a fairly large truncation radius of $R_{\rm out} = 30\,R_{\rm S}$, leading to a predicted precession frequency consistent with the observed QPO frequency in this state ($\lesssim$0.3 Hz). When $R_{\rm out}$ decreases (corresponding to transition to the hard-intermediate state), $\nu_{\rm QPO}$ grows up to 5–20 Hz.

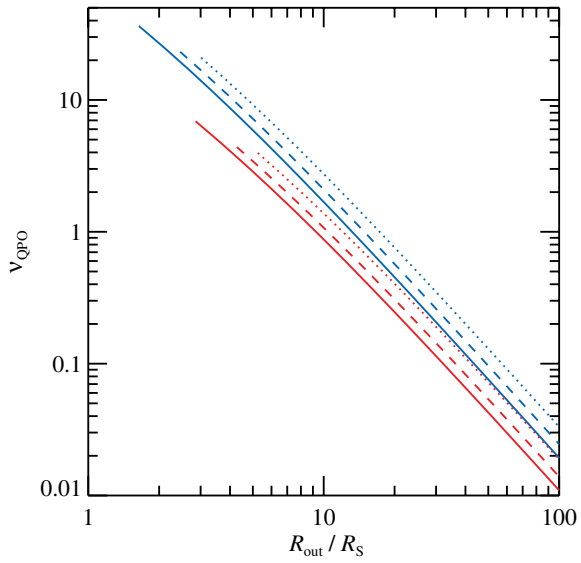

Figure 1. Possible QPO frequencies as a function of the hot flow outer radius ($R_{\rm out}$), calculated for a $10M_\odot$ BH according to Equation (43) of Fragile et al. (2007), with an inner radius equal to $R_{\rm in} = 1.5\,(H/R)^{-4/5}a^{2/5}\,R_{\rm S}$ (Lubow et al. 2002), for spins of $a = 0.2$ (solid), 0.3 (dashed), and 0.5 (dotted). Red lines correspond to $H/R = 0.2$ and blue lines correspond to $H/R = 0.4$.

(A color version of this figure is available in the online journal.)

Although the condition on the flow height-to-radius ratio, H/R, for the fast propagation of warps which allows solid body precession is $H/R > \alpha \sim 0.1$, where α is the dimensionless viscosity parameter (Papaloizou & Pringle 1983; Fragile et al. 2007), a H/R significantly less than unity is likely (Kato et al. 2008). Thus, we approximate the flow as a flat disk. This approximation is satisfactory for systems with a low enough inclination for the flow never to be seen edge-on at any point in the precession cycle. We illustrate in our plots the regions of parameter space where this condition is not met. In order to calculate the emitted flux, we must make an assumption about the radial dependence of energy dissipation per unit area in the flow. We assume the standard profile for a thin disk (Shakura & Sunyaev 1973)

$$q(R) \propto R^{-3}\sqrt{1-\frac{R_{\rm in}}{R}}, \qquad (1)$$

where $R_{\rm in}$ is the hot flow inner radius, which we assume to be equal 3 $R_{\rm S}$ (for parameters in Figure 1 it takes the values ∼2–5 $R_{\rm S}$). The profile is not strictly appropriate for a hot flow in general relativity (Novikov & Thorne 1973; Kato et al. 2008), but is fine for illustration in the absence of a standard equivalent for hot flows. The details of the energy dissipation profile do not play an important role. For calculations of the angular dependence of the emergent radiation we take into account relativistic effects using the Schwarzschild metric (see Section 2.3). Since we are considering Lense–Thirring precession, this is obviously only an approximation to the more appropriate Kerr metric. However, the Schwarzschild metric provides a very good approximation at distances more than 3 $R_{\rm S}$ from the BH.

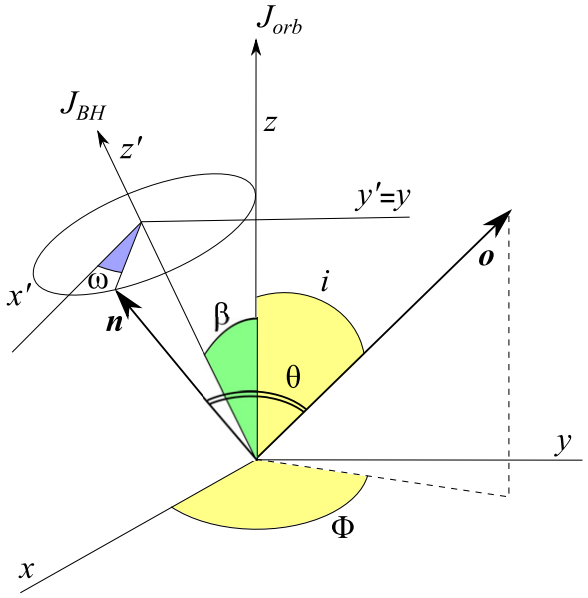

Figure 2. Schematic representation of the hot flow producing X-ray and optical QPOs. Coordinate systems connected with the orbital plane xyz and with the BH spin $x'y'z'$ are shown. Plane xy coincides with the orbital plane and y is parallel to y'. Axis z' is aligned with the BH spin, which is inclined by the angle β to the orbital spin. Position of the observer $\hat{\boldsymbol{o}}$ is described by the azimuthal angle Φ and binary inclination i. The current position of the hot flow normal $\hat{\boldsymbol{n}}$ is characterized by the precession angle (phase) ω. Relative to the direction to the observer, it makes an angle θ, which depends on ω.

(A color version of this figure is available in the online journal.)

We take into account only direct images, because the higher-order images are much weaker. The reason for this is that the hot flow we consider has an optical depth of the order of unity, thus most of the photons initially emitted away from the observer would be blocked by the flow itself (or by the outer cold disk). The only possibility for those photons to reach the observer is to go through the rather small gap between the inner edge of the hot flow ($\sim 3\,R_S$) and the BH. In addition, photons coming in the higher-order images are generally emitted at grazing angles to the flow surface and therefore their strength is diminished by the corresponding cosine factor. In order to estimate the accuracy of the described approach, we compared fluxes obtained using our light-tracing procedure with those obtained using the GEOKERR code in Kerr geometry (Dexter & Agol 2009; A. Ingram et al., in preparation) including all higher-order images, but accounting for obscuration by the hot flow and the outer cold disk. For the parameters considered in this work, we find our results to be accurate within a few per cent for any spin value up to $a = 0.998$, and for more realistic spins of $a = 0.3, 0.5$ the difference is below 1%.

2.2. Geometry

Figure 2 shows the geometry we consider for the precessing hot accretion flow. We define the coordinate system xyz tied to the binary orbital plane and the system $x'y'z'$, associated with the BH spin. The z-axis is perpendicular to the binary orbital plane, z' is aligned with the BH spin and β is the angle between them. The x-axis is defined by the intersection of the orbital plane and the plane formed by the z and z' axes (i.e., the projection of the z'-axis onto the y-axis is always zero). Finally, the x'-axis also belongs to the plane formed by vectors z and z', and forms angle β with the x-axis (i.e., $y' = y$). The position of the observer is described by the vector $\hat{\boldsymbol{o}}$ which, in xyz coordinates, is given by

$$\hat{\boldsymbol{o}} = (\sin i \cos\Phi, \sin i \sin\Phi, \cos i), \tag{2}$$

where i is the binary inclination and Φ is the azimuth of the observer measured from the x-axis. The instantaneous normal to the hot flow is denoted by $\hat{\boldsymbol{n}}$. It precesses around the BH spin axis (z') with the precession angle ω measured from the x'-axis. Thus $\hat{\boldsymbol{n}}$ aligns with the z-axis when $\omega = \pi$ and has a maximal misalignment of 2β when $\omega = 0$. It is given, in $x'y'z'$ coordinates, by $\hat{\boldsymbol{n}} = (\sin\beta\cos\omega, \sin\beta\sin\omega, \cos\beta)$. Note, we use a hat to denote unit vectors throughout.

We are interested in the orientation of the hot flow surface relative to the observer, namely the scalar product $\hat{\boldsymbol{o}}\cdot\hat{\boldsymbol{n}} = \cos\theta$. In order to calculate it, we write $\hat{\boldsymbol{n}}$ in xyz coordinates by rotating the $x'y'z'$ coordinate system counter-clockwise by angle β around the y'-axis to get

$$\hat{\boldsymbol{n}} = (\sin\beta\cos\beta(1+\cos\omega), \sin\beta\sin\omega, \cos^2\beta - \sin^2\beta\cos\omega). \tag{3}$$

Thus, the equation for $\cos\theta$ is

$$\begin{aligned}\cos\theta = {} & \sin\beta\cos\beta\sin i\cos\Phi\,(1+\cos\omega) \\ & + \sin\beta\sin\omega\sin i\sin\Phi + \cos i\,(\cos^2\beta - \sin^2\beta\cos\omega).\end{aligned} \tag{4}$$

2.3. Formalism

We consider a simplified problem with a precessing flat disk (slab). The specific flux observed far from the BH from a ring of thickness dR at radius R in the direction that makes an angle θ to the surface normal can be expressed as

$$dF_E(R,\theta) = \frac{R\,dR}{D^2} q_E(R) f(R,\theta). \tag{5}$$

Here, D is the distance to the observer, $q_E(R)$ is the surface flux per energy interval at a given radius and the factor $f(R,\theta)$ accounts for the angular dependence of the observed flux. The latter factor depends on the spectral slope of the radiation.

The flux observed from the whole hot flow is then

$$F_E(\theta) = \frac{\int q_E(R)\,R\,dR}{D^2}\,\overline{f}(\theta), \tag{6}$$

where we introduced the radially averaged angular factor:

$$\overline{f}(\theta) = \frac{\int q_E(R)\,R\,dR\,f(R,\theta)}{\int q_E(R)\,R\,dR}. \tag{7}$$

In general, the specific intensity emerging from a surface element depends on the zenith angle ζ' (primed are quantities in the comoving frame). We consider here two cases for the emission pattern from the flow surface:

1. X-ray emission from accreting BHs is produced by Comptonization in an optically translucent flow with Thomson optical depth $\tau \sim 1$. In this case, the angular dependence of the specific intensity can approximately be described by (Poutanen & Gierliński 2003)

$$I'(\zeta') \propto 1 + b\cos\zeta', \tag{8}$$

where $b \approx -0.7$ (for exact solutions see Sunyaev & Titarchuk 1985; Viironen & Poutanen 2004).

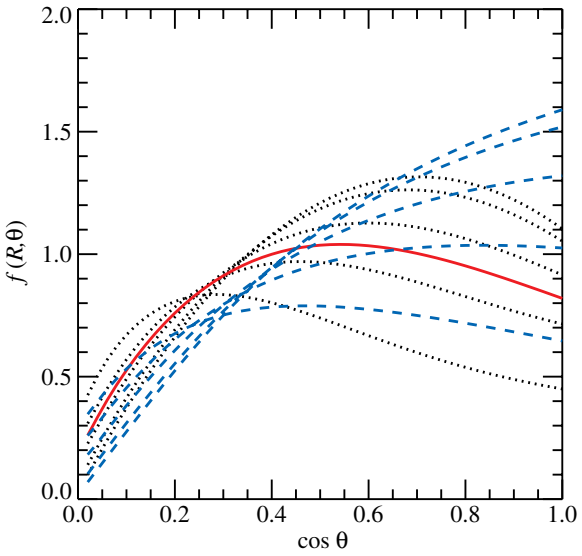

Figure 3. Angular dependence of the observed flux $f(R,\theta)$ as a function of the angle between the observer direction and the normal to the flow. The black dotted lines represent result for the X-ray emission pattern (Equation (8)) corresponding to Comptonization in an optically translucent flow. The blue dashed lines correspond to the partially self-absorbed synchrotron emission expected in the optical (given by the pattern from Equation (9)). Curves from the top to the bottom correspond to $R/R_S = 100$, 30, 10, 5 and 3. The solid red line corresponds to the flux $\overline{f}(\theta)$ from the accretion flow between 3 and 30 R_S emitting the X-rays with the standard emissivity profile (1).

(A color version of this figure is available in the online journal.)

2. Optical synchrotron radiation is produced in the outer parts of the flow, in a partially self-absorbed regime. The dominant contribution to the observed flux comes from those parts, which have an optical depth for synchrotron self-absorption $\tau_{SA} \sim 1$. Assuming a tangled magnetic field and homogeneous source function throughout the vertical extent of the flow, the intensity of radiation can be expressed as

$$I'(\zeta') \propto 1 - \exp(-\tau_{SA}/\cos\zeta'). \quad (9)$$

We assume that the emergent spectrum from all surface elements is a power law with photon index $\Gamma = 1.7$ for the X-rays and $\Gamma = 1$ for the optical emission. This allows us to approximate the energy dissipation profile as $q_E(R) \propto q(R)$. To compute the factor $f(R,\theta)$ we take into account gravitational redshift, Doppler effect, relativistic aberration, time dilation and light bending in the Schwarzschild metric following techniques presented by Poutanen & Gierliński (2003) and Poutanen & Beloborodov (2006). Figure 3 shows the resulting angular flux dependence with X-rays and optical represented by black dotted and blue dashed lines, respectively. We plot the function $f(R,\theta)$ for narrow rings at $R/R_S = 100$, 30, 10, 5 and 3 from top to bottom. We also show (by red solid line) the angular distribution of the flux from the accretion flow spread from 3 to 30 R_S, $\overline{f}(\theta)$, emitting the X-rays according to the standard profile given by Equation (1). At large radii $R \gtrsim 30\,R_S$, the relativistic effects are negligible resulting in the angular dependence $f(R,\theta) \propto I'(\theta)\cos\theta$.

2.4. Results

As a first step, we take the X-ray and optical emission to originate from narrow rings with $R = 5\,R_S$ and $R = 30\,R_S$, respectively, and compute corresponding QPO waveforms. We set $\beta = 10^\circ$ and $i = 60^\circ$, 80°. The profiles $f(R,\theta)$ (with θ given by Equation (4)) are shown in Figure 4 for four different observer azimuths: $\Phi = 0^\circ$, 60°, 120° and 180°. Again, the black dotted lines are X-rays and the blue dashed line represents the optical. Clearly the phase difference between optical and X-ray profiles depends on the observer's azimuth and inclination: for $i = 60^\circ$ and large Φ the two light curves are in phase, while for low Φ they are 180° out of phase. This is because the range of $\cos\theta$ covered as the precession angle ω unwinds from 0 to 2π depends on the chosen set of parameters (β, i, Φ). The range of $\cos\theta$ for every case is shown in Figure 4 with a green dash–dotted line. For small $\cos\theta$ (panels (c) and (d)), both optical and X-ray observed fluxes are increasing functions of $\cos\theta$ (see Figure 3), while for large $\cos\theta$ (panels (a) and (b)) optical flux is a growing and X-ray flux is a decreasing function of $\cos\theta$. The later is reflected in the anti-correlation of the two light curves.

For inclinations $i \gtrsim 80^\circ$, eclipses are possible when the observer is situated opposite the BH spin projection on the orbital plane, i.e., at $\Phi > 90^\circ$. In such a situation, the harmonic content is dramatically increased and the X-ray and optical light curves are always in phase, as here $\cos\theta < 0.5$ (thus both fluxes have monotonic dependence on $\cos\theta$, see Figure 3). However, we need to keep in mind that at such large inclinations the central source might be blocked completely by the outer rim of the cold disk.

We note that the amplitude of the optical QPO for every Φ is higher than in the X-rays. Again, the behavior can be understood from Figure 3: the dependence of the optical flux (blue dashed line at 30 R_S) on $\cos\theta$ is much stronger than that in the X-rays (black dotted line at 5 R_S). This occurs both due to the different emission pattern and because the relativistic effects are stronger at smaller R (due to stronger gravitational curvature and faster Keplerian motion).

For the cases (b)–(d), the X-ray flux maximum is reached not when $\cos\theta$ is maximal, i.e., when the flow is mostly face-on, but when it is inclined at a larger angle (see Figure 3). This leads to the double-peak structures in the X-ray profiles, unlike in the optical (optical flux reaches maximum only at maximal $\cos\theta$, i.e., when the flow is mostly face-on). This gives the X-ray QPO profiles a stronger harmonic content than the optical.

The X-ray light curves expected from the whole hot flow occupying the region 3–30 R_S can be computed from the factor $\overline{f}(\theta)$ (with θ given by Equation (4)). They are shown by red solid lines in Figure 4. We see that their behavior is very similar to that corresponding to a narrow ring at 5 R_S. This is due to the similarities in the angular dependence of the fluxes (see Figure 3, solid line and dotted line corresponding to 5 R_S). The emission pattern from a ring at $\sim$7 R_S would be nearly identical to that of the whole extended flow, and so assuming all of the flux to come from close to this radius provides a good approximation.

We analyze the harmonic content of our light curves by directly computing Fourier coefficients. We show the fractional root mean square (rms) variability amplitudes of the first harmonic (referred to below as the fundamental) and the second harmonic (hereafter referred to as the harmonic) as the contour plots at the plane observer azimuth Φ – observer inclination i (Figure 5). The azimuthal angle spans the interval from 0 to 180°, because the results depend on $\cos\Phi$ only. The X-rays are assumed to be coming from the whole flow extending from 3 to 30 R_S with a standard emissivity profile given by Equation (1). The X-ray rms is shown by red lines. The optical again is assumed coming from 30 R_S and its rms is shown by blue lines.

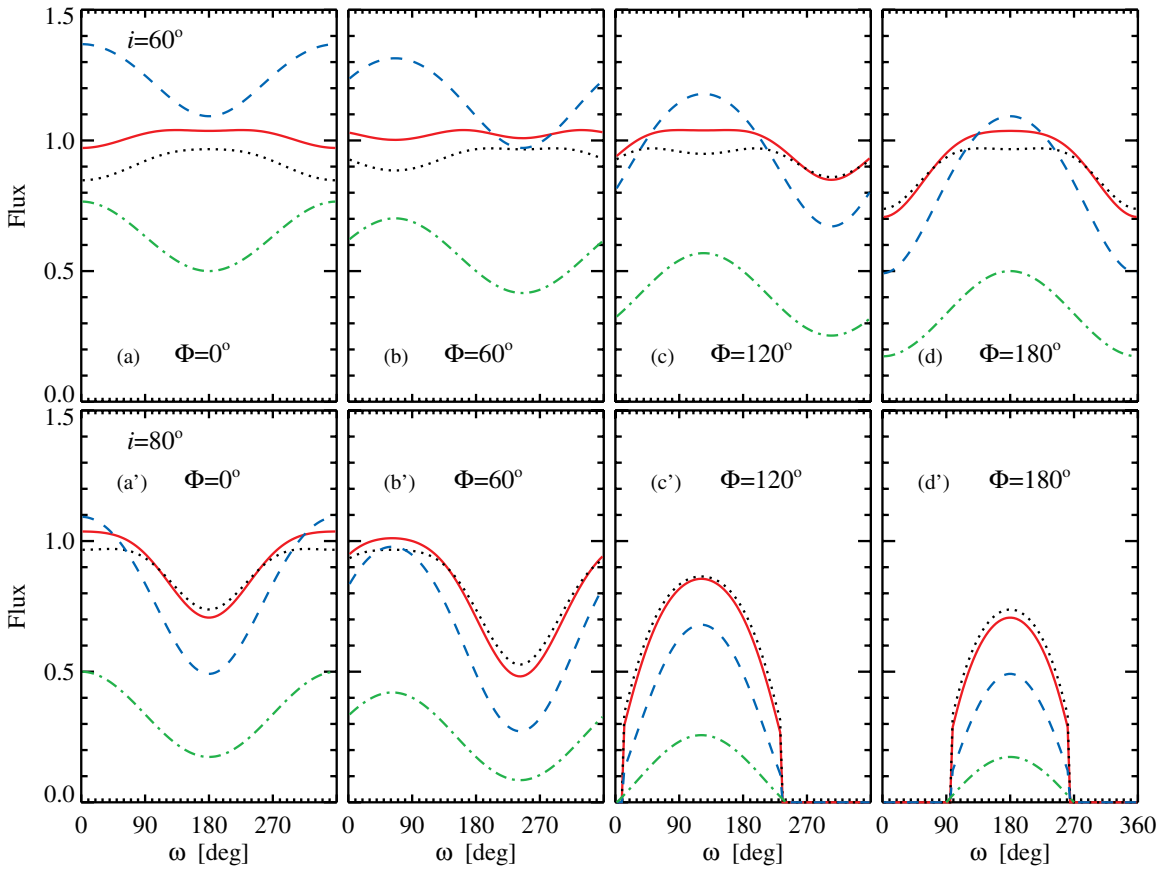

Figure 4. Possible QPO waveforms for the four cases of the observer's azimuthal angle. The parameters are: $\beta = 10°$, $i = 60°$ (upper panels) and $i = 80°$ (lower panels). X-ray profiles are calculated for a ring at $R = 5\,R_S$ (black dotted lines) and for the full hot flow extending from 3 to 30 R_S (red solid lines). The optical profiles are for $R = 30\,R_S$ (blue dashed lines). Green dash–dotted lines represent variations of $\cos\theta$ for each case.

(A color version of this figure is available in the online journal.)

Behavior of the X-ray and optical fundamental is shown in Figures 5(a) and (b), respectively. The optical rms increases monotonically with both i and Φ. The X-ray rms drops to zero at inclinations between 45° and 65°, depending on Φ, where the light curve shows a double bump structure (thus, the harmonic here is non-zero). At higher inclinations rms increases again. At high inclinations and large Φ in the shaded region, self-eclipses of the disk become possible, causing dramatic increase of rms. The dash–dotted black line separates the regions, where the phase difference between the optical/X-ray fundamental QPOs shifts from 0 to π. Also the amplitude of the X-ray fundamental turns zero along this line.

Figures 5(c) and (d) present the contour plot of the harmonic rms for X-rays and optical, respectively. Here the rms is monotonically growing with both i and Φ up to rather large $i \gtrsim 70°$ (i.e., $\sim 90° - 2\beta$). At large inclinations eclipses become possible (see right panels of Figure 4). In that case, both rms show very erratic behavior and depend strongly on i, first rapidly rising and then dropping to nearly zero (at somewhat different places of the plane shown by black dashed lines), but here the higher harmonics are strong. This is easily seen in Figures 5(e)–(g) which show the rms behavior as a function of i for fixed Φ.

We see that, for the chosen parameters, the optical fundamental is stronger than the X-ray fundamental for all observer azimuths whereas the X-ray harmonic is nearly always stronger than the optical harmonic. Without eclipses, the optical harmonic is typically ten times weaker than the fundamental, while the X-ray harmonic can be even stronger than the corresponding fundamental. For better visualization we also plot a cross-section of these contour plots in Figures 5(h) and (i) for two representative inclinations $i = 60°$ and 80°, respectively. The first is the mean possible inclination of an arbitrary observer, while the second is chosen to show the role of eclipses. Here we additionally show the case of the X-rays from a narrow ring at 5 R_S by black lines. In panel (h), we clearly see a drop of the fundamental X-ray rms at $\Phi = 50$–100° and in panel (i) a rapid growth of rms when eclipses become possible at $\Phi \sim 80°$.

3. DISCUSSION

3.1. Comparison with Observations

Our results show that the X-ray light curves have strong harmonics, while optical harmonics are weaker for most of sets (i, Φ). Indeed, harmonics are often found in the X-ray PSDs (e.g., Rodriguez et al. 2004), but no optical harmonics have been reported so far. This can also be seen in the (quasi-) simultaneous data of Motch et al. (1983, Figure 2), where both optical and X-ray PSDs show a QPO at ∼0.05 Hz, two harmonics ∼0.1 Hz and ∼0.15 Hz are seen in the X-ray, but not in the optical PSD. Our simulations suggest that the rms amplitudes of the fundamental harmonic in the optical are expected to be larger. Unfortunately, the data with both X-ray and optical QPOs detected are not strictly simultaneous, thus the PSDs are plotted in arbitrary units (Motch et al. 1983; Hynes et al. 2003). In the available simultaneous data of Swift J1753.5–0127, the optical

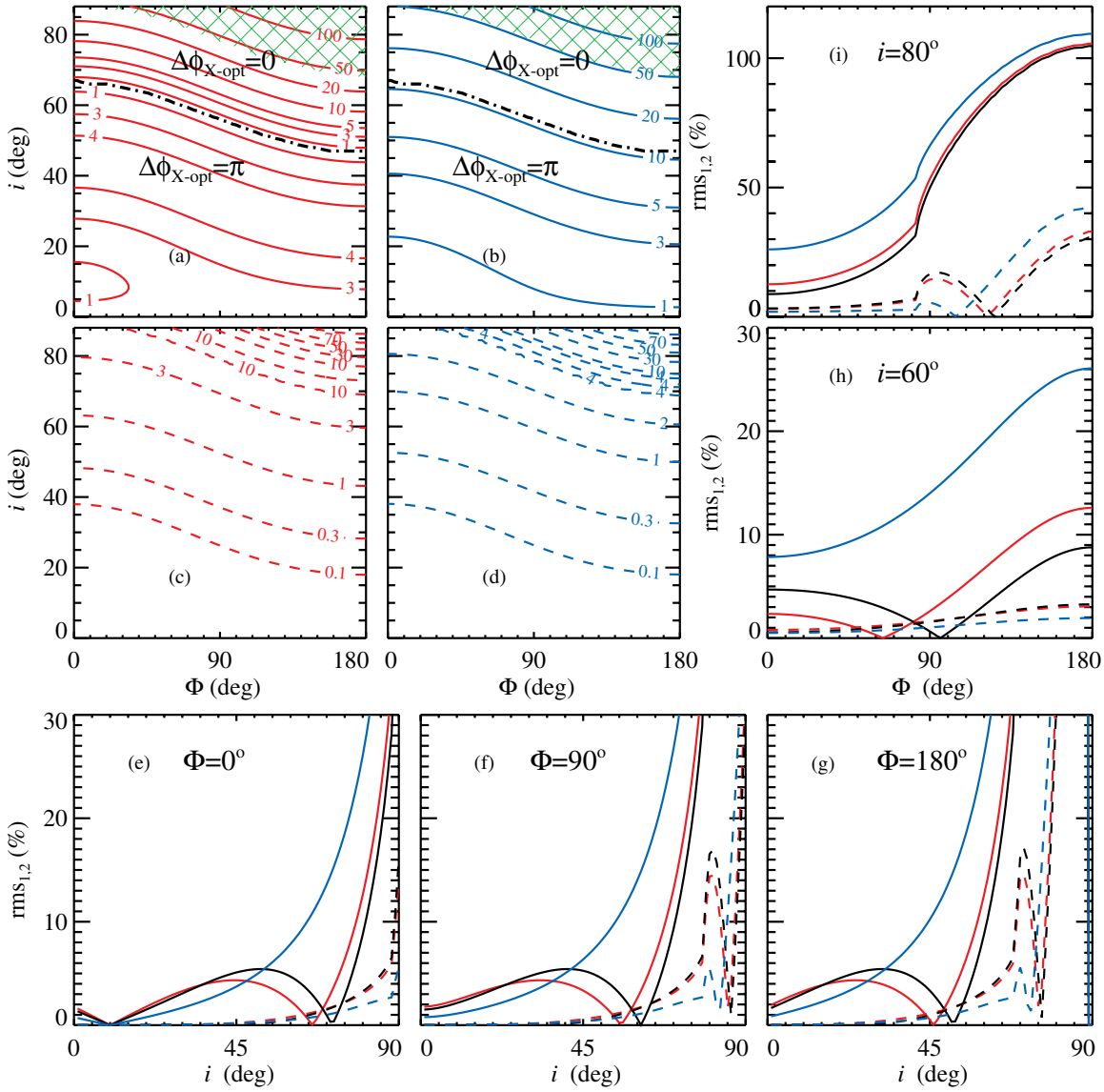

Figure 5. Fractional rms amplitudes (in percent) as functions of i and Φ. The upper left four panels present the contour plots for X-ray (a and c) and optical (b and d) fractional rms amplitudes on the plane i–Φ. The upper panels (a and b) are for the fundamental, while the two lower panels (c and d) show the harmonic. Eclipses are possible in the shaded regions marked on the top panels. The dash–dotted black line separates the regions, where the phase difference between the optical/X-ray fundamental QPOs shifts from 0 to π. The amplitude of the X-ray fundamental turns zero along this line. Three bottom panels present the cross-section of these plots at the azimuthal angles $\Phi = 0^\circ$ (e), 90° (f), and 180° (g). The panels on the right show the cross-section at two inclinations $i = 60^\circ$ (h) and 80° (i). The X-rays (red curves) are assumed to originate from a hot disk extending from 3 to 30 R_S emitting according to the standard emissivity profile given by Equation (1), while the optical (blue curves) corresponds to a narrow ring at $R = 30\ R_S$. The solid curves present the rms for the fundamental and the dashed curves give the harmonic. The rms for the X-rays from a narrow ring at $R = 5\ R_S$ are shown in the panels (e)–(i) by black curves, which show similar behavior to the full hot flow case.

(A color version of this figure is available in the online journal.)

QPO is present with rms = 4%–11%, while the upper limit on the X-ray QPO rms at the same frequency is 3% (Durant et al. 2009). In GX 339–4 situation is similar, the optical QPO is present at rms = 3%, while the upper limit on the X-ray QPO rms at the same frequency is 7.5% (Gandhi et al. 2010). This is consistent with our model which predicts that the X-ray QPO is there, just at a low rms. On the other hand, we, of course, cannot rule out there being no QPO at all. In order to check the presence of the X-ray QPO in the data (which is related to the optical QPO), one may search for modulations at the corresponding frequency in the cross-correlation function. These oscillations are indeed present in the 2007 data on Swift J1753.5–0127 (see Durant et al. 2008; A. Veledina et al. in preparation) and hints of them can also be seen in the GX 339–4 data (Gandhi et al. 2010, Figure 21).

In Figure 1 we reproduced the range of possible QPO frequencies (the same for optical and X-rays) as a function of the hot flow outer radius. Since the dependence on parameters is not too strong, it is feasible to determine $R_{\rm out}$ for a given $\nu_{\rm QPO}$. In realistic situation, $R_{\rm out}$ fluctuates together with the mass accretion rate, leading to a change of the QPO frequency and broadening of the QPO features in the PSD. We note that the given frequencies were computed under the assumption of the rotation of the hot flow as a solid body, which breaks down for a large hot flow, limiting the outer radii, where the QPOs can be observed.

The lowest QPO frequencies ∼0.05 Hz (optical) and ∼0.03 Hz (X-rays) were observed in the hard state. According to Figure 1, we find the hot flow outer radius can be $\sim 100\,R_{\rm S}$, and even larger for $H/R > 0.4$ or spin $a > 0.5$. In this case, the optical and IR wavelengths are dominated by the radiation of the translucent parts of the hot flow (see e.g., Veledina et al. 2013, Figure 3: optical wavelengths are dominated by the radiation coming from $\sim 30\,R_{\rm S}$).

During the state transition, with the rise of the mass accretion rate, the outer shells of the hot flow are gradually replaced by the cold accretion disk (Esin et al. 1997, 1998; Poutanen et al. 1997). As the outer radius of the hot flow decreases, an increase of the QPO frequency occurs. This is seen in the data as correlated changes in the spectral slope and QPO frequency (see, e.g., Gilfanov 2010), and expected in the precession model of Fragile et al. (2007) and Ingram et al. (2009). Simultaneously, a sharp drop of the IR radiation is expected, with fluxes at longer wavelengths dropping just before those at shorter wavelengths. While the cold accretion disk is sufficiently far away, the X-ray spectrum does not change significantly, as the amount of cold disk photons are not enough to make it softer. The noticeable X-ray spectral transition starts when the cold disk is rather close to the BH, at radii about $10\,R_{\rm S}$ (Figure 5 of Veledina et al. 2013). For such a small hot flow, IR wavelengths belong to the optically thick (self-absorbed) part of the spectrum, which is very hard, with spectral index up to $\alpha = 5/2$ ($F_\nu \propto \nu^\alpha$). Thus, in the hard-intermediate state we expect to see the QPO feature with frequencies $\gtrsim$1 Hz in the near-IR, but not in the mid-IR or longer wavelengths, which would likely be very faint, probably, too faint to be detectable. The optical/X-ray phase lags in both translucent and opaque cases are expected to be the same (see below), either 0 or π depending on the observer azimuthal angle and inclination. Maximum optical/near-IR QPO frequency in our model is the same as in the X-rays ∼10 Hz (for a $10\,M_\odot$ BH).

We discussed in detail the OIR QPOs produced only by the hot accretion flow, however, these presumably may originate from other components, such as reprocessed X-ray radiation (for low QPO frequencies) and the jet (if it is entirely driven by the accretion flow). It is likely that the component giving major contribution to the observed flux also produces the QPOs, because of their rather large rms. Simultaneous data of SWIFT J1753.5–0127 at late stages of the outburst (Durant et al. 2009, Figure 6; see also Chiang et al. 2010, Figure 5) suggest that the optical lies on the continuation of the X-ray power law, as expected in the hot flow scenario (Veledina et al. 2013). Some irradiation may also play a role (as supported by the cross-correlation studies of Hynes et al. 2009 during the outburst peak), but the jet is very faint in this object. Thus the optical QPOs are likely produced by the hot flow. This is therefore suggestive that the hot flow scenario also works in other objects displaying QPOs, such as XTE J1118+480 and GX 339–4.

3.2. Unaccounted Effects

Because we aimed to have as few parameters as possible, the model we consider is rather simplified. In a more realistic problem, a number of additional effects could also be accounted for, namely, the wavelength dependence of the optical profiles, occultations of the hot flow by the cold accretion disk, effects of the hot flow geometry, e.g., its finite and radius-dependent thickness, presence of the large-scale magnetic field, and presence of other spectral components in the optical, such as the reprocessed emission and the jet. Let us now consider possible consequences of these effects.

1. The optical QPO profiles were calculated assuming these wavelengths belong to the partially self-absorbed regime. However, if the flow is small (e.g., $R \lesssim 10\,R_{\rm S}$), the optical (and even more certainly the IR) is likely to be in the self-absorbed part of the spectrum ($\tau_{\rm SA} \gg 1$). In this case, the intensity of escaping radiation is isotropic and the flux depends only on the surface area of the flow projected to the line of sight modified by relativistic effects. The QPO waveforms in this case are not much different from the previously considered case of emission at the self-absorption frequency, but the rms of the fundamental is somewhat larger and the harmonic is weaker.
2. For calculations of the X-ray QPO profiles, we adopted a simple prescription for the angular dependence of the specific intensity from the hot flow given by Equation (8). Obviously, it is only an approximation to the real angular dependence that should be computed using the full Compton scattering kernel (see, e.g., Poutanen & Svensson 1996). The intensity $I(\zeta')$ in reality should depend on the photon energy as well as on τ and temperature, with both being functions of the accretion rate and the distance from the BH. We do not expect that the general topology of the solution will change, but the details (e.g., the position of the line separating the phase lag $\Delta\phi_{\rm X-opt} = 0$ and π in Figure 5) might differ. The result will also depend on the X-ray energy band.
3. Hard state BHBs are known to have radio jets (Fender 2006). Theoretical models for the jet launching require the presence of the large scale magnetic field. In that case, the synchrotron emissivity within the hot flow is no longer isotropic, but depends on the pitch angle α to the magnetic field as $\sin^2\alpha$. This would lead to a different angular dependence of the escaping intensity. For a poloidal field, radiation would be more beamed along the hot flow surface leading to a luminosity angular dependence similar to that in the X-rays. In this case, the optical waveforms are expected to have more harmonic content.
4. Possible occultations of the hot flow by coverage of the inner parts of the cold accretion disk or by its flared outer parts may occur. These would lead to the asymmetry of the optical (and X-ray) QPO profiles and absence of the secondary peak in the X-ray profiles. As with the considered occultations at high inclinations, this would lead to an increase of the fundamental rms and harmonic content. Additionally, the optical and X-ray profiles will no longer be in phase (or in anti-phase).
5. We considered a simple case with a flat precessing disk, but in reality, the hot flow has finite thickness. This does not have much effect on the profiles for low inclinations. Self-eclipses of the hot flow will appear at somewhat lower inclinations, but, on the other hand, emission from the outer side of the hot flow will be visible and the eclipses will not be so deep. Thus, the increase in rms will not be as significant and the harmonic content will be somewhat lower.
6. When estimating the rms we assumed that the optical emission is produced entirely by the hot flow. In reality, additionally there is reprocessed emission from the outer disk that might be dominant at longer wavelengths as well as possibly optically thin, soft emission from the radio jet that might contribute to the emission at shorter wavelengths.

These components not only contribute to the flux diluting the rms from the hot flow, but also in principle can be variable at the QPO frequency. As reprocessing occurs in the outer part of the accretion disk, it acts as a low-pass filter (e.g., Veledina et al. 2011), reducing signal at high frequencies. Thus the reprocessing is not expected to vary at relatively high QPO frequencies. Whether the jet can produce QPOs at the same frequency as the inner hot flow precesses is not clear. The Lense–Thirring effect generally cannot cause the jet precession unless the jet is driven entirely by the accretion flow (Nixon & King 2013). Hence, the presence of several components in the spectrum typically will reduce the rms amplitude of the optical QPO by a factor $1 + r$, where $r = (F_{E,\rm jet} + F_{E,\rm repr})/F_{E,\rm hf}$ is the ratio of the observed fluxes at a given energy produced by the jet and reprocessing to that of the hot flow.

4. SUMMARY

A number of BH binaries have recently been found to show QPO features in their optical PSDs. Recently, it has been shown that similar QPOs in X-rays are well explained by Lense–Thirring precession of the hot accretion flow. Here we propose that OIR QPOs originate from the same process, namely that the outer parts of the precessing hot flow are radiating in the optical (by non-thermal synchrotron), producing QPOs at frequencies matching those in the X-rays.

We calculate the possible OIR profiles and make predictions for the phase difference with the X-rays. The phase shift can be either 0 (at high inclinations) or π (at low inclinations), with the boundary between these cases depending on the azimuthal angle of the observer. We also investigate the harmonic content and show dependence of the rms on parameters for two first harmonics. Here we show that the X-ray QPOs should have a smaller rms than the OIR QPOs at the fundamental frequency. On the other hand, the X-ray QPOs should have a much stronger harmonic.

We discuss possible QPO frequencies and their connection to the broadband spectral properties. At the hard-to-soft state transition we expect the OIR QPO frequency to increase, always being the same as in the X-rays, up to $\sim$10 Hz in the hard-intermediate state. The broadband spectrum is expected to change in such a way that the emission at longer wavelengths drops before the subsequent drop at shorter wavelengths (infrared, optical). After that the X-ray transition occurs. In the hard state, the QPO feature is sometimes absent (not significant) in the X-ray PSD, but detected in the optical. Their common origin can be established through the cross-correlation analysis, where the oscillations at corresponding frequency can be present. Using future X-ray missions with high time-resolution capability, such as *LOFT*, together with the corresponding high time-resolution instruments in the optical, we will be able to confirm or discard this.

This work was supported by the Finnish Graduate School in Astronomy and Space Physics (A.V.).

REFERENCES

Bardeen, J. M., & Petterson, J. A. 1975, ApJL, 195, L65
Belloni, T., Psaltis, D., & van der Klis, M. 2002, ApJ, 572, 392
Casella, P., Maccarone, T. J., O'Brien, K., et al. 2010, MNRAS, 404, L21
Chiang, C. Y., Done, C., Still, M., & Godet, O. 2010, MNRAS, 403, 1102
Dexter, J., & Agol, E. 2009, ApJ, 696, 1616
Done, C., Gierliński, M., & Kubota, A. 2007, A&ARv, 15, 1
Durant, M., Gandhi, P., Shahbaz, T., Peralta, H. H., & Dhillon, V. S. 2009, MNRAS, 392, 309
Durant, M., Gandhi, P., Shahbaz, T., et al. 2008, ApJL, 682, L45
Esin, A. A., McClintock, J. E., & Narayan, R. 1997, ApJ, 489, 865
Esin, A. A., Narayan, R., Cui, W., Grove, J. E., & Zhang, S.-N. 1998, ApJ, 505, 854
Fender, R. 2006, in Compact Stellar X-Ray Sources, ed. W. H. G. Lewin & M. van der Klis (Cambridge Astrophysics Series, No. 39; Cambridge: Cambridge Univ. Press), 381
Fragile, P. C. 2009, ApJL, 706, L246
Fragile, P. C., Blaes, O. M., Anninos, P., & Salmonson, J. D. 2007, ApJ, 668, 417
Gandhi, P., Dhillon, V. S., Durant, M., et al. 2010, MNRAS, 407, 2166
Gilfanov, M. 2010, in The Jet Paradigm, ed. T. Belloni (Lecture Notes in Physics, Vol. 794; Berlin: Springer), 17
Hynes, R. I., Haswell, C. A., Cui, W., et al. 2003, MNRAS, 345, 292
Hynes, R. I., O'Brien, K., Mullally, F., & Ashcraft, T. 2009, MNRAS, 399, 281
Imamura, J. N., Kristian, J., Middleditch, J., & Steiman-Cameron, T. Y. 1990, ApJ, 365, 312
Ingram, A., & Done, C. 2011, MNRAS, 415, 2323
Ingram, A., Done, C., & Fragile, P. C. 2009, MNRAS, 397, L101
Kanbach, G., Straubmeier, C., Spruit, H. C., & Belloni, T. 2001, Natur, 414, 180
Kato, S., Fukue, J., & Mineshige, S. 2008, Black-Hole Accretion Disks—Towards a New Paradigm (Kyoto: Kyoto Univ. Press)
Kumar, S., & Pringle, J. E. 1985, MNRAS, 213, 435
Lubow, S. H., Ogilvie, G. I., & Pringle, J. E. 2002, MNRAS, 337, 706
Malzac, J., & Belmont, R. 2009, MNRAS, 392, 570
Motch, C., Ilovaisky, S. A., Chevalier, C., & Angebault, P. 1985, SSRv, 40, 219
Motch, C., Ricketts, M. J., Page, C. G., Ilovaisky, S. A., & Chevalier, C. 1983, A&A, 119, 171
Nixon, C., & King, A. 2013, ApJL, 765, L7
Novikov, D. I., & Thorne, K. S. 1973, in Black Holes (Les Astres Occlus), ed. C. Dewitt & B. S. Dewitt (New York: Gordon & Breach), 343
Papaloizou, J. C. B., & Pringle, J. E. 1983, MNRAS, 202, 1181
Poutanen, J., & Beloborodov, A. M. 2006, MNRAS, 373, 836
Poutanen, J., & Gierliński, M. 2003, MNRAS, 343, 1301
Poutanen, J., Krolik, J. H., & Ryde, F. 1997, MNRAS, 292, L21
Poutanen, J., & Svensson, R. 1996, ApJ, 470, 249
Poutanen, J., & Vurm, I. 2009, ApJL, 690, L97
Remillard, R. A., & McClintock, J. E. 2006, ARA&A, 44, 49
Remillard, R. A., McClintock, J. E., Sobczak, G. J., et al. 1999, ApJL, 517, L127
Rodriguez, J., Corbel, S., Kalemci, E., Tomsick, J. A., & Tagger, M. 2004, ApJ, 612, 1018
Schnittman, J. D., Homan, J., & Miller, J. M. 2006, ApJ, 642, 420
Shakura, N. I., & Sunyaev, R. A. 1973, A&A, 24, 337
Steiman-Cameron, T. Y., Scargle, J. D., Imamura, J. N., & Middleditch, J. 1997, ApJ, 487, 396
Stella, L., & Vietri, M. 1998, ApJL, 492, L59
Sunyaev, R. A., & Titarchuk, L. G. 1985, A&A, 143, 374
Veledina, A., Poutanen, J., & Vurm, I. 2011, ApJL, 737, L17
Veledina, A., Poutanen, J., & Vurm, I. 2013, MNRAS, 430, 3196
Viironen, K., & Poutanen, J. 2004, A&A, 426, 985
Vikhlinin, A., Churazov, E., Gilfanov, M., et al. 1994, ApJ, 424, 395
Wagoner, R. V., Silbergleit, A. S., & Ortega-Rodríguez, M. 2001, ApJL, 559, L25
Wijnands, R., & van der Klis, M. 1999, ApJ, 514, 939
Zdziarski, A. A., & Gierliński, M. 2004, PThPS, 155, 99

Mon. Not. R. Astron. Soc. **000**, 1–7 (2014) Printed 20 August 2014 (MN LATEX style file v2.2)

Reprocessing model for the optical quasi-periodic oscillations in black hole binaries

Alexandra Veledina[1,2⋆] and Juri Poutanen[2]
[1] *Astronomy Division, Department of Physics, PO Box 3000, FI-90014 University of Oulu, Finland*
[2] *Tuorla Observatory, Department of Physics and Astronomy, University of Turku, Väisäläntie 20, FI-21500 Piikkiö, Finland*

20 August 2014

ABSTRACT
A number of black hole X-ray transients show quasi-periodic oscillations (QPOs) in the optical (infrared) and X-ray bands at the same frequency, which challenge models for production of radiation at these wavelengths. We propose a model where the optical radiation is modulated by the oscillating X-ray flux resulting in varying irradiation of the outer parts of the accretion disc. The proposed QPO mechanism inevitably takes place in the systems with sufficiently small ratio of the outer disc radius to the QPO period. We show that, unlike in the case of the aperiodic variability, it is not possible to obtain the optical QPO profiles from those observed in the X-rays through the transfer function, because of different X-ray signals seen by the disc and by the observer. We demonstrate that with the increasing QPO frequency, occurring at the rising phase of the X-ray outburst, the rms should be constant for sufficiently low frequencies, then to increase reaching the peak and finally to drop substantially when the QPO period becomes comparable to the light-crossing time to the outer disc. We predict that the QPO rms in this model should increase towards shorter wavelengths and this fact can be used to distinguish it from other QPO mechanisms.

Key words: accretion, accretion discs – black hole physics – X-rays: binaries

1 INTRODUCTION

The significant influence of the X-ray source on the structure and spectral properties of the standard accretion disc was noticed already in the pioneering study by Shakura & Sunyaev (1973) of the optically thick geometrically thin α-discs. The temperature distribution in such irradiated discs around black holes (BHs) was calculated in a number of works (see e.g. Cunningham 1976; Frank et al. 2002). Though the precise dependence of the effective temperature on radius differ in these models, the general expectation is that X-ray irradiation dominates over internal viscous dissipation in the outer part of the accretion disc, which consequently dominates the emission in the optical/infrared (OIR) wavelengths.

The prediction was then confirmed by the OIR luminosity and the specific shape of the OIR spectra in a number of BH binaries (van Paradijs & McClintock 1994; Gierliński et al. 2009; Zurita Heras et al. 2011; Curran et al. 2012). The signature of reprocessed X-ray emission are also seen in optical/X-ray cross-correlation function (CCF, Hynes et al. 1998, 2009), displaying a single, a few second broad peak at positive optical lags, as well as in the transfer function determined directly from the light curves (O'Brien et al. 2002). Additional support comes from the detection of optical flares following X-ray bursts (e.g. Grindlay et al. 1978; McClintock et al. 1979; Hynes et al. 2006a). On the other hand, sometimes the complex shape of the CCFs displaying the so-called precognition dip cannot be explained solely by the irradiation of the disc (Motch et al. 1983; Kanbach et al. 2001; Durant et al. 2008; Hynes et al. 2009; Gandhi et al. 2010), an additional contribution of another source, likely of synchrotron origin, is required (Malzac et al. 2004; Veledina et al. 2011).

Simultaneous presence of at least two optical components is also required by the shape of the power spectral density (or, equivalently, the auto-correlation function): while the optical photons are thought to originate from a somewhat larger region compared to the X-rays, the power spectrum does not have the characteristic suppression of the high-frequency noise, instead, an additional Lorentzian peaking at higher frequencies (with respect to the X-rays) is required (Kanbach et al. 2001; Gandhi et al. 2010). That Lorentzian might be a manifestation of the interplay of different optical components one related to the synchrotron radiation from the hybrid hot flow and another to the irradiated disc (Veledina et al. 2011).

⋆ E-mail: alexandra.veledina@gmail.com

Apart from the broadband noise, the quasi-periodic oscillations (QPOs) were detected in the optical (Motch et al. 1983; Durant et al. 2009; Gandhi et al. 2010) and UV (Hynes et al. 2003) wavelengths at frequencies 0.05–0.13 Hz. The X-ray power-density spectra demonstrate similar features known as the type-C low-frequency QPOs (see Casella et al. 2005, for classification). The two months of observations revealed that the optical, UV and the X-ray QPOs in BH binary XTE J1118+480 share a common (within uncertainties) characteristic frequency whilst evolving with time (Hynes et al. 2003). This suggests that the QPOs in these three energy bands are parts of the same process. One or several components responsible for the optical emission – the hot accretion flow (Veledina et al. 2013b), the jet (e.g. Hynes et al. 2006b) and the irradiated disc (Gierliński et al. 2009) – are all natural candidates for the QPO origin. Because the principal oscillation mechanisms and the geometrical properties are substantially different, these three models should be distinguishable by the observational characteristics. The hot flow QPO model was considered in Veledina et al. (2013a). In this work we develop a quantitative model for the low-frequency QPOs arising from reprocessing.

One of most promising mechanisms to produce X-ray QPOs is based on the misalignment of the accretion flow and the BH spin. The QPOs there arise due to the Lense-Thirring (solid-body) precession of the whole inner hot flow (Fragile et al. 2007; Ingram et al. 2009; Ingram & Done 2011). Recalling that the cold accretion discs are likely to be flared (e.g. Shakura & Sunyaev 1973; Frank et al. 2002), any temporal variations of the X-ray flux should be reflected in the reprocessed radiation. In this paper we introduce a model of optical QPO produced by reprocessing of the X-ray modulated flux. We present detailed calculations of the QPO profiles and amplitudes. Even without any calculations we can predict that the optical QPO have to be visible if the light-crossing time to the outer disc is shorter than the QPO period. We discuss then how the optical QPOs arising from the reprocessing can be distinguished from those produced by other QPO mechanisms (i.e., produced by the hot accretion flow or by the jet).

2 GEOMETRY AND FORMALISM

2.1 X-ray QPOs

We consider a simple scenario of a flat precessing disc radiating in the X-ray band. We associate this geometry with the hot accretion flow around a Kerr BH, which undergoes solid-body Lense-Thirring precession because of the misalignment of the BH and orbital spins (Fragile et al. 2007; Ingram et al. 2009; Ingram & Done 2011). The general geometry is shown in Fig. 1 (left). We define the coordinate system xyz associated with the binary orbital plane and the system $x'y'z'$, tied to the BH spin. The z-axis is aligned with the orbital spin and z' is aligned with the BH spin. The angle between them is denoted by β. We further choose axis $y = y'$. The precession occurs around the BH spin axis with the precession angle ω measured from x'-axis, so that the instantaneous hot flow normal $\hat{\boldsymbol{n}}$[1] is aligned with the orbital spin axis at $\omega = \pi$ and has a maximal misalignment of 2β when $\omega = 0$. The observer position is described by $\hat{\boldsymbol{o}} = (\sin i \cos\Phi, \sin i \sin\Phi, \cos i)$ in xyz coordinates, where i is the binary inclination and Φ is the azimuth of the observer measured from the x-axis. The hot flow normal is given by $\hat{\boldsymbol{n}} = (\sin\beta\cos\omega, \sin\beta\sin\omega, \cos\beta)$ in $x'y'z'$ coordinates. It translates to

$$\hat{\boldsymbol{n}} = \big(\sin\beta\cos\beta(1+\cos\omega), \sin\beta\sin\omega, 1-\sin^2\beta(1+\cos\omega)\big) \quad (1)$$

in xyz coordinates.

The X-ray QPOs arise from the different orientation of the hot flow relative to the observer, described by the scalar product $\hat{\boldsymbol{o}}\cdot\hat{\boldsymbol{n}} = \cos\theta$. It is easy to show that

$$\begin{aligned}\cos\theta &= \sin\beta\cos\beta\sin i\cos\Phi\ (1+\cos\omega) + \\ &+ \sin\beta\sin\omega\sin i\sin\Phi + \cos i\ [1-(1+\cos\omega)\sin^2\beta].\end{aligned} \quad (2)$$

The flux observed from one ring of the flat disc with radius r, thickness dr and a surface normal which makes an angle θ to the line of sight far from the BH can be expressed as

$$dF_E(r,\theta) = \frac{r\ dr}{D^2} q_E(r) f_E(r,\theta). \quad (3)$$

Here, D is the distance to the observer, $q_E(r)$ is the surface flux per energy interval at a given radius and the factor $f_E(r,\theta)$ accounts for the angular dependence of the observed flux and is calculated from the specific intensity emerging from a surface element. In general, the specific intensity depends on the zenith angle. X-ray emission from accreting BHs is produced by Comptonization in an optically translucent flow with Thomson optical depth $\tau \sim 1$. In this case, the local angular dependence of the radiation intensity can approximately be described by (Poutanen & Gierliński 2003)

$$I'_E(\zeta') \propto 1 + b\cos\zeta', \quad (4)$$

here the primes denote quantities in the frame comoving with the considered element, ζ' is the zenith angle and the parameter $b \approx -0.7$ (for exact solutions see Sunyaev & Titarchuk 1985; Viironen & Poutanen 2004). We assume that the emergent spectrum from all surface elements is a power law with photon index $\Gamma = 1.7$. To calculate the observed flux, we take into account gravitational redshift, Doppler shift, time dilation and light bending in the Schwarzschild metric[2] following techniques presented in Poutanen & Gierliński (2003) and Poutanen & Beloborodov (2006). In the absence of the standard energy dissipation profile relevant to the hot flow in general relativity, we take the standard profile of a thin disc (Shakura & Sunyaev 1973)

$$q_E(r) \propto \sqrt{1-\frac{3R_\mathrm{S}}{r}}\, r^{-3}, \quad (5)$$

which is suitable for illustration. Here $R_\mathrm{S} = 2GM/c^2$ is the Schwarzschild radius of the BH. We define the weighted angular emissivity function as

$$\overline{f}_E(\theta) = \frac{\int f_E(r,\theta)\ q_E(r)\ r\ dr}{\int q_E(r)\ r\ dr}, \quad (6)$$

where the integration is performed over the hot flow surface with the radius varying between 3 and $100R_\mathrm{S}$. The observed flux is

[1] We use a hat to denote unit vectors throughout.

[2] This gives very similar results to using the more appropriate Kerr metric for the $r > 3R_\mathrm{S}$ case we consider here.

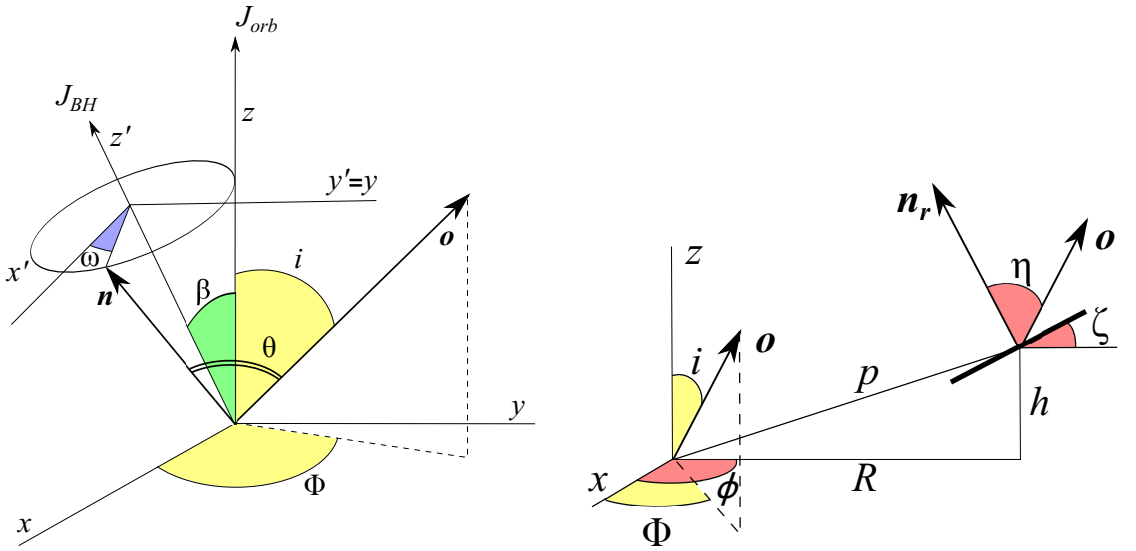

Figure 1. Schematic representation of the hot flow producing X-ray and optical QPOs. Left: Coordinate systems connected with the orbital plane xyz and with the BH spin $x'y'z'$ are shown. Plane xy coincides with the orbital plane and y is parallel to y'. Axis z' is aligned with the BH spin, which is inclined by the angle β to the orbital spin. Position of the observer $\boldsymbol{o}$ is described by the azimuthal angle Φ and binary inclination i. The position of the normal to the hot flow $\boldsymbol{n}$ is characterized by the precession angle/phase ω. It makes an angle θ with the direction to the observer, which depends on ω. Right: Schematic representation of the reprocessing geometry. The surface element is at radius r and height h from the central X-ray source, its normal makes angle ζ with the orbital spin and angle η with the line-of-sight.

$$F_E = \frac{4\pi \int q_E(r)\ r\ dr}{4\pi\ D^2}\ \overline{f}_E(\theta). \quad (7)$$

The angular dependence of the X-ray flux is shown in Fig. 3 of Veledina et al. (2013a), where further details on the precessing hot flow model can be found.

2.2 Reprocessing model

In the reprocessing model, the optical emission is directly related to the central source X-ray flux that shines upon the outer part of the disc. Here we follow formalism developed by Poutanen (2002) for X-ray reflection from a flared disc. We assume that the reprocessing into optical wavelengths occurs in a ring extending from radius $R_{\rm in}$ to $R_{\rm out}$, which is large compared to the extent of the X-ray source, which therefore can be considered as an anisotropic point source. We assume the power-law dependence of height on radius $h = H(r/R_{\rm out})^{\rho}$. The parameters describing the disc shape are the ratio $H/R_{\rm out}$ and the power-law index ρ. The ring surface makes an angle ζ with the orbital plane that is a function of r:

$$\tan\zeta = \rho\frac{h}{r} = \rho\frac{H}{R_{\rm out}}\left(\frac{r}{R_{\rm out}}\right)^{\rho-1} \quad (8)$$

(see Fig. 1, right). The standard accretion disc has $\rho = 9/8$ (Shakura & Sunyaev 1973), while the irradiated disc may have $\rho = 9/7$ (Frank et al. 2002), thus we only consider cases with $\rho > 1$. In the frame related to the orbital plane, the observer's coordinates are

$$\hat{\boldsymbol{o}} = (\sin i\cos\Phi, \sin i\sin\Phi, \cos i), \quad (9)$$

the radius-vector $\boldsymbol{p}$ pointing towards a surface element has coordinates

$$\boldsymbol{p} = (r\cos\phi, r\sin\phi, h), \quad (10)$$

and the normal to the element is

$$\hat{\boldsymbol{n}}_{\rm r} = (-\sin\zeta\cos\phi, -\sin\zeta\sin\phi, \cos\zeta). \quad (11)$$

The optical light-curve from such a ring can generally be written as

$$L_{\rm repr}(t) \propto \int_{-\infty}^{t} dt' \int_{R_{\rm in}}^{R_{\rm out}} \frac{r\,dr\cos\xi}{4\pi p^2\cos\zeta} \int_0^{2\pi} d\phi L_{\rm X}^{\alpha}(t', \boldsymbol{p})\delta(t-t'-\Delta t(\phi))\cos\eta. \quad (12)$$

Here $L_{\rm X}(t', \boldsymbol{p})$ is the X-ray luminosity in the direction of the disc element, i.e. at angle $\theta_{\rm e} = \arccos(\hat{\boldsymbol{n}}\cdot\hat{\boldsymbol{p}})$ relative to the hot flow normal, emitted from the central source at time t'. The index α may depend on the wavelength where reprocessing signal is measured. For example, assuming that disc radiation is a blackbody of some temperature T and remembering that $T \propto L_{\rm X}^{1/4}$, it is obvious that in the Rayleigh-Jean part of the spectrum $\alpha \approx 1/4$, while closer to the peak of the reprocessed emission, in the UV range, α is close to unity or may even exceed 1 in the Wien tail of the spectrum. In reality, of course, for a given wavelength α varies, because of the varying temperature of the irradiated disc. Here, we ignore this effect and concentrate on the geometrical factors which are dominant.

The δ-function accounts for the geometrical time-delays:

$$\begin{aligned}\Delta t(\phi) &= \frac{1}{c}(p - \boldsymbol{p}\cdot\hat{\boldsymbol{o}}) \quad (13)\\ &= \frac{1}{c}\left[\sqrt{r^2+h^2} - h\cos i - r\sin i\cos(\Phi-\phi)\right].\end{aligned}$$

We neglect the reprocessing time, which is orders of magnitude smaller than any other timescales considered here. The area of the surface element is $r\ dr\ d\phi/\cos\zeta$ and the projection of this element on the line connecting it to the X-ray source is proportional to

$$\cos\xi = -\hat{\boldsymbol{n}}_{\rm r}\cdot\hat{\boldsymbol{p}} = \frac{(\rho-1)h/r}{\sqrt{1+(h/r)^2}}\cos\zeta. \quad (14)$$

Let us assume for simplicity that the angular distribution of reprocessed radiation follows Lambert law, implying that the luminosity of the disc element per unit solid angle depends linearly on its projection on the observer's sky, which is proportional to

$$\cos\eta = \hat{\boldsymbol{n}}_{\rm r}\cdot\hat{\boldsymbol{o}} = \cos i\cos\zeta - \sin i\sin\zeta\cos(\Phi-\phi). \quad (15)$$

Using the δ-function to take the integral over t' and rewriting the light curve in terms of the QPO phases of the signal corresponding to the arrival and emission times $\omega = 2\pi\nu_{\rm QPO}t$ and $\omega' = 2\pi\nu_{\rm QPO}t'$, we get:

$$L_{\rm repr}(\omega) \propto \int\limits_{R_{\rm in}}^{R_{\rm out}} \frac{dr}{2\pi r}\frac{(\rho-1)h/r}{(1+(h/r)^2)^{3/2}}\int\limits_0^{2\pi} d\phi\ \cos\eta\,\overline{f}_{\rm X}^{\alpha}(\cos\theta_{\rm e}), \quad (16)$$

where the X-ray flux $\overline{f}_{\rm X}$ in the direction of the elements depends on the angle between the hot flow normal $\hat{\boldsymbol{n}}$ and vector $\boldsymbol{p}$ (see equations (1) and (10)):

$$\cos\theta_{\rm e} = \hat{\boldsymbol{n}}\cdot\hat{\boldsymbol{p}} = \frac{1}{\sqrt{1+(h/r)^2}}\left\{\left[1-(1+\cos\omega')\sin^2\beta\right]\frac{h}{r} + \cos\phi\sin\beta\cos\beta(1+\cos\omega') + \sin\phi\sin\beta\sin\omega'\right\}, \quad (17)$$

where

$$\omega' = \omega - \frac{2\pi\nu_{\rm QPO}}{c}\left[\sqrt{r^2+h^2} - h\cos i - r\sin i\cos(\Phi-\phi)\right]. \quad (18)$$

For the disc surface element at radius r and azimuth ϕ to contribute to the observed flux, three conditions have to be satisfied:

(i) the irradiation condition (the X-ray source is seen from the ring surface element), i.e. $\cos\theta_{\rm e} > 0$;

(ii) the visibility condition (the observer sees the ring surface), i.e. $\cos\eta > 0$ or, equivalently, $\cos(\Phi-\phi) < \cot i\cot\zeta$;

(iii) the reprocessed photons are not blocked by the disc on their way to the observer, i.e.

$$\tan i < \frac{\sqrt{R_{\rm out}^2 - r^2\sin^2(\Phi-\phi)} - r\cos(\Phi-\phi)}{H-h}. \quad (19)$$

The model parameters can be divided into two groups: the disc parameters ρ, $H/R_{\rm out}$, $R_{\rm in}/R_{\rm out}$, $\nu_{\rm QPO}R_{\rm out}/c$, and α and the orientation parameters i, Φ and β. The parameters α and β only affect the signal rms, rather than the profile shape. The first three parameters also make rather minor changes to the QPO signal as we discuss below. Thus the model in reality has only three main parameters: $\nu_{\rm QPO}R_{\rm out}/c$, which controls the smearing of the X-ray QPO signal in the disc, and the orientation parameters i and Φ.

3 RESULTS

3.1 QPO profiles

In contrast to the model with QPOs from the hot flow (Veledina et al. 2013a), here optical profiles depend on the QPO frequency. If the QPO period is much shorter than the corresponding light travel time to the outer disc ($\nu_{\rm QPO}R_{\rm out}/c \gg 1$), the variability amplitude of the optical QPO should go to zero. For very long QPO periods, $\nu_{\rm QPO}R_{\rm out}/c \ll 1$, the delays due to light travel time can be neglected and the QPO profiles just reflect variations of the illumination of the disc by the X-ray source and of the viewing angle of the disc surface. For the parameters $R_{\rm out} \sim 10^{10}-10^{12}$ cm (typical for low-mass X-ray binaries) and the QPO range between $10^{-3} \lesssim \nu_{\rm QPO} \lesssim 10$, the possible range of parameter $\nu_{\rm QPO}R_{\rm out}/c$ is between 3×10^{-4} and 300. It is therefore clear that the limiting cases discussed above can, in principle, be realised.

The integrals in equation (16) should generally be computed numerically, however, it is interesting to consider a case when they can be taken analytically. This can also be used as a benchmark for the precise numerical calculations. Let us first consider the situation where the reprocessing occurs in a thin ring ($R_{\rm in} \cong R_{\rm out}$), which is located sufficiently close to the X-ray source ($\nu_{\rm QPO}R_{\rm out}/c \ll 1$), i.e. the response is immediate and we can put $\omega = \omega'$. In addition, the ring is located high enough above the orbital plane and the angle β is small enough so that the X-ray source is always seen from the entire ring (this translates to the condition $\cos\theta_{\rm e} > 0$ at any phase). We assume that the emission pattern of the central source follows the Lambert law, which leads to the emissivity function $\overline{f}_{\rm X} \propto \cos\theta_{\rm e}$ (we also put $\alpha = 1$). Finally, we consider the observer above the orbital plane, i.e. $i = 0$. Under this conditions, the integral in equation (16) is reduced to the simple sinusoidal pattern $L_{\rm repr}(\omega) \propto 1 - C\cos\omega$, where $C > 0$ depends on the chosen parameters. This analytical solution, though, is unlikely to be realized in a realistic situation.

We investigate the effect of changing parameters on the QPO profiles by the direct calculations of reprocessing light-curves. Optical and X-ray QPO profiles are calculated by assuming a radial emissivity $q_E(r)$ for each band. We fix $\beta = 10^\circ$ and an observer inclination $i = 60^\circ$ and consider changing ρ, $H/R_{\rm out}$, $R_{\rm in}/R_{\rm out}$ and $\nu_{\rm QPO}R_{\rm out}/c$. We find that the parameter ρ does not alter the profile shapes and only affects the amplitudes of oscillations (with higher rms obtained for the cases when the observer sees relatively larger disc area), while the decrease of $R_{\rm in}/R_{\rm out}$ results in somewhat faster response and more smearing of the signal, i.e. lower rms. The increase of parameter $H/R_{\rm out}$ generally introduces a larger phase shift of the optical light-curve, in addition, the larger is this parameter, the lower is the optical variability rms. This results from the decrease of the X-ray rms towards lower inclinations (or, essentially, towards lower angles $\theta_{\rm e}$). The major affect on the QPO profiles comes from changing parameter $\nu_{\rm QPO}R_{\rm out}/c$. We consider three cases: $\nu_{\rm QPO}R_{\rm out}/c = 10^{-2}$, 0.5 and 2. The resulting profiles are shown in Fig. 2.

It is evident that the optical QPOs arising from reprocessing have larger amplitudes than those seen in the X-rays by the distant observer (with their ratio reaching a factor of 10 at low azimuth $\Phi < 60^\circ$). We have studied the QPO profiles at the i–Φ plane and found that this is true for majority of the simulations (except for the area with $i \gtrsim 70^\circ$ and $\Phi \gtrsim 120^\circ$, which, however, cannot be described properly with the presented model, because the effects of non-zero thickness of the hot flow become important). The main reason for that is the strong increase of the rms in X-rays with increasing viewing angle (i.e., inclination in the case of observer and the corresponding angle $\pi/2-\xi$ for the disc). Small opening angles (realistic values are between 6° and

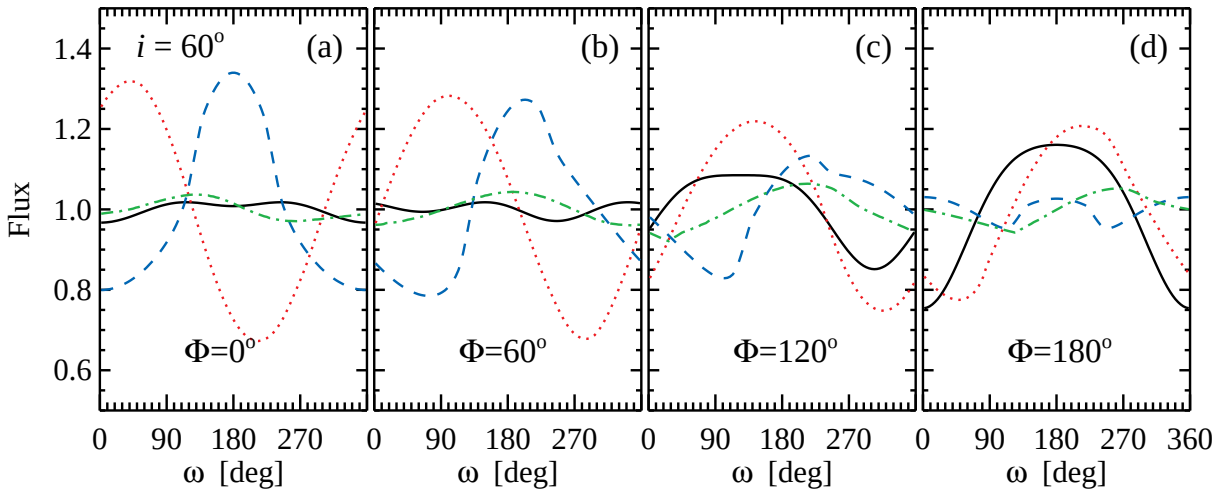

Figure 2. Possible QPO profiles for the three cases of the parameter $\nu_{\rm QPO}R_{\rm out}/c$: 10^{-2} (blue dashed), 0.5 (red dotted) and 2 (green dot-dashed). The system inclination is fixed $i = 60^\circ$ and four different observer's azimuthal angles Φ are considered (panels a-d). X-ray profiles are calculated for the full hot flow extending from 3 to $100R_{\rm S}$ (black solid lines) assuming black hole spin inclination of $\beta = 10^\circ$. Other parameters of the reprocessing model are $R_{\rm in}/R_{\rm out} = 0.5$, $H/R_{\rm out} = 0.2$, $\rho = 1.5$ and $\alpha = 1$.

22°, see de Jong et al. 1996 and references therein) thus result in substantially higher variation amplitudes of the X-rays seen by the disc relative to those seen by the observer. In addition, the X-ray variability seen by the disc is different from that seen by the observer for the same reason. This means that it is not feasible to find any kind of the QPO response function, which could give the optical QPO profiles from the observed X-ray QPOs.

Another interesting observation is that at $\nu_{\rm QPO} \ll c/R_{\rm out}$ the optical QPO profile strongly depends on Φ, being nearly sinusoidal at small Φ, with the growing harmonic content at larger Φ, where the amplitude of the fundamental drops significantly. At higher $\nu_{\rm QPO} \sim c/R_{\rm out}$, the profiles are more sinusoidal with a low harmonic content.

We finally note that the overall optical rms can be reduced by the presence of other, non-oscillating or oscillating out-of-phase, components. For instance, additional constant flux may arise because of the viscous heating in the disc. Also, the X-ray source likely has a non-zero thickness, thus the entire disc has an additional constant irradiated component. And finally, reflection of the X-rays from the optically thin corona or wind would produce a nearly constant illumination over the disc surface leading to the reduction of the QPO amplitude.

3.2 QPO amplitude dependence on Fourier frequency

Often the optical QPO profile cannot be measured and the only available information is its rms. The ratio of the light-crossing time to the outer disc to the QPO period, $\nu_{\rm QPO}R_{\rm out}/c$, is the major factor affecting the rms, see Fig. 3. The constant level at low frequencies reflects the fact that the light-travel time to the outer disc is much below the QPO period, so that the response can be considered as immediate. The QPO profile is then completely determined by the varying illumination of the outer disc due to precession of the anisotropic and non-axisymmetric X-ray source. We see that the constant level is very different for different observer's azimuth Φ, being close to 20 per cent at $\Phi \sim 0^\circ$ and dropping to nearly zero at $\Phi \sim 180^\circ$ (we note that the harmonic here is stronger).

At high $\nu_{\rm QPO}$, the rms drops dramatically due to smearing. Rather unexpectedly we find that the rms has a strong peak at $\nu_{\rm QPO}R_{\rm out}/c \sim 1/2$. The peak does not appear only for inclination $i = 0$. For $\Phi \lesssim 60^\circ$, the rms reaches 17–25 per cent, depending on the inclination. At larger $\Phi \gtrsim 120^\circ$, the rms is about 15 per cent which is substantially larger than that at low $\nu_{\rm QPO}$. This resonance-like feature results from the fact that the reprocessing signals from the closest and furthest (to the observer) parts of the disc are coming in phase.

We conclude here that the optical QPOs arising from reprocessing of the X-ray radiation from an anisotropic precessing source can be identified in the data using its frequency dependence. The rms is predicted to be constant at low frequencies, to have a peak at $\nu_{\rm QPO}R_{\rm out}/c \sim 1/2$ and disappear at $\nu_{\rm QPO,max}R_{\rm out}/c \sim 1$. The critical QPO frequency depends on the disc size, which is itself a function of binary separation, $R_{\rm out} \approx 0.6a$ (for small mass ratios; see Warner 1995). Using the 3rd Kepler's law, we can relate it to the orbital period (in hours):

$$\nu_{\rm QPO,max} \approx \frac{2}{3} P_{\rm h}^{-2/3} (M/10{\rm M}_\odot)^{-1/3} \ {\rm Hz}. \qquad (20)$$

3.3 QPO amplitude dependence on the wavelength

An alternative way to identify the reprocessing QPO in the data is from its wavelength dependence. Different wavelengths correspond to different parts of the irradiated disc (blackbody) spectrum, resulting in variation of parameter α (introduced in equation 12). Combining relations $T \propto L_{\rm X}^{1/4}$ and $B_\nu(T) \propto L_{\rm X}^{\alpha(\nu)}$, we get

$$\alpha(\nu) = \frac{1}{4}\frac{\partial \ln B_\nu(T)}{\partial \ln T} = \frac{h\nu}{4kT}\left(1 - e^{-h\nu/kT}\right)^{-1}. \qquad (21)$$

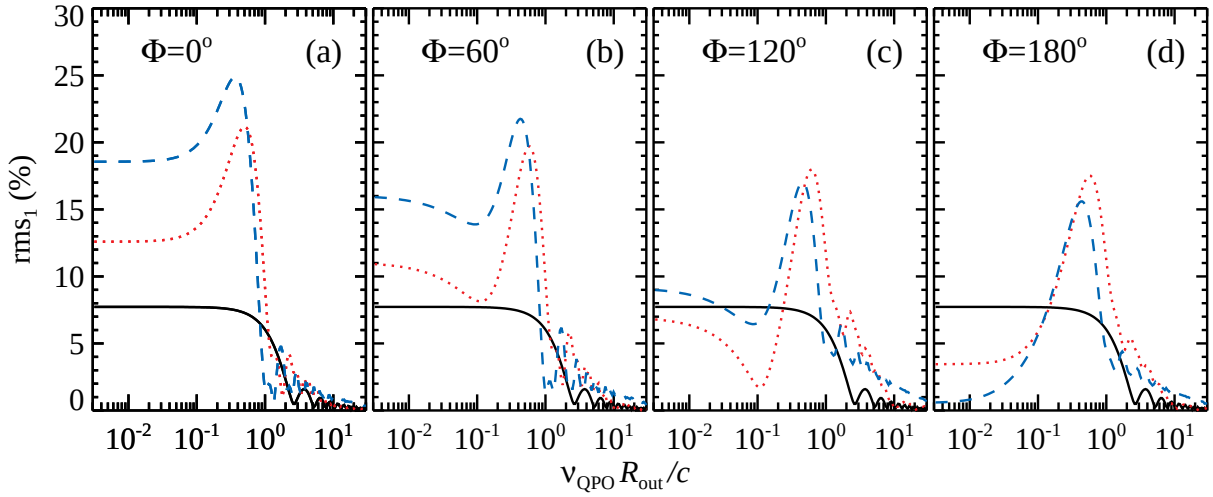

Figure 3. The dependence of the rms at the fundamental frequency on $\nu_{\rm QPO}R_{\rm out}/c$ for different observer's azimuth $\Phi = 0, 60, 120$ and $180°$ (panels a-d, respectively) and three different inclinations, $i = 0, 40°$ and $60°$ shown by solid black, dotted red and dashed blue curves.

In this paper, we considered cases with the linear response, $\alpha = 1$, which takes place close to the wavelengths of the blackbody peak. For the irradiated disc temperature of about 10 000 K, this corresponds to U-filter. The rms is higher at shorter wavelengths, where α exceeds 1 and it is smaller at longer wavelengths, where it tends to the Rayleigh-Jeans value $\alpha = 1/4$. Thus at long wavelengths the optical (or rather IR) QPO should have four times smaller rms than those computed here. On the other hand, in the Wien part of the spectrum α can exceed unity and the QPO amplitude grows.

In addition to the wavelength dependence of the reprocessing QPO itself, it is likely that additional spectral component influence that. The irradiated disc spectrum may be contaminated by the emission from the hot flow, jet, or circumstellar dust, which likely reduce the overall rms, with a somewhat larger suppression at longer wavelengths because their spectra are significantly redder than the spectrum of the disc. This fact further strengthens the dependence of rms on the wavelength, which should grow towards shorter wavelengths.

3.4 Comparison with the data

The low-frequency QPO range observed in the X-rays is $\sim 10^{-2} - 10$ Hz. In the optical, the highest frequency which could be explained by the irradiated disc model is $\sim$1 Hz (corresponding to the size of a system with a few hour orbital period). Short-period systems are then promising candidates to look for the irradiation QPOs. For relatively small discs, present in systems with periods of a few hours, the temperature at the outer edge of the disc is substantially higher, roughly $T_{\rm out} \propto F_{\rm X}^{1/4} \propto R_{\rm out}^{-1/2} \propto P_{\rm orb}^{-1/3}$, where $P_{\rm orb}$ is the orbital period (we assumed that the X-ray luminosity is the same). Thus, irradiation gives significant contribution to the UV flux, but not to the IR, where the disc is likely very dim compared to other components. The discs in the long-period systems are large enough and cool enough to give significant contribution to the IR, however the QPOs in such systems are expected to be seen only at relatively low frequencies.

In GX 339–4, the optical QPO frequency was seen to vary between 0.05 and 0.13 Hz (Motch et al. 1983; Imamura et al. 1990; Steiman-Cameron et al. 1997; Gandhi et al. 2010). The QPO features were observed in three filters simultaneously (Gandhi et al. 2010). They have systematically larger rms in the redder filters for all three nights of observations (see their table 4), though only the difference in rms observed during the third night are statistically significant. The system period is rather long, about 42 h (Casares & Jonker 2014), so that the maximum reprocessing QPO (see equation 20) is expected to be at $\nu_{\rm QPO,max} \approx 0.055$ Hz, where we assumed $M = 10{\rm M}_\odot$. Thus the observed QPOs are likely produced either by the hot flow or in the jet.

SWIFT J1753.5–0127 is one of the shortest-period systems with $P_{\rm orb} \approx 3$ h (Zurita et al. 2008; Neustroev et al. 2014). The optical QPOs in this object were observed during the simultaneous X-ray exposure (Hynes et al. 2009; Durant et al. 2009). The computed optical/X-ray CCFs do not resemble those of the irradiated disc, on the contrary, a prominent optical precognition dip is detected. The dip may be a signature of the hot flow synchrotron emission (Veledina et al. 2011), and its amplitude relative to the positive peak (attributed to irradiation) implies that the hot flow is a dominant source of optical photons, and hence the QPOs.

Interestingly, rms of the UV QPOs in XTE J1118+480 was found to somewhat increase with the increasing frequency (Hynes et al. 2003), though the significance of this result is yet unclear. The system is otherwise a good candidate to expect the irradiated QPOs: it has a rather short-period of about 4 h (Casares & Jonker 2014) and it was also found to demonstrate the precognition dip structure in the CCFs (Kanbach et al. 2001), however the dip amplitude is significantly smaller than that of the peak. Moreover, the dip in the UV/X-ray CCF is even less prominent (Hynes et al. 2003), thus we anticipate that the proposed mechanism could be important in this system.

4 SUMMARY

We developed a model for the optical QPOs arising from the irradiation of the accretion disc by varying X-ray flux. Assuming that the inner part of the accretion disc is occupied by a precessing hot accretion flow (radiating in the X-rays) with the prescribed emission pattern, we calculate the optical profiles. The oscillations at the precession period appear due to the changing of the illumination conditions. We note that the distant observer sees the X-ray source at an angle different from that seen from the outer disc. This means that simple use of the disc transfer function relating the observed X-ray and optical light-curves is insufficient to reproduce optical profiles – the additional knowledge of the X-ray emission pattern is required.

We find that the QPO rms is nearly constant for sufficiently low frequencies, $\nu_{\rm QPO}R_{\rm out}/c \lesssim 0.1$, it then increases to achieve the maximum at $\nu_{\rm QPO}R_{\rm out}/c \sim 1/2$ and drops dramatically at higher frequencies. This is an identifying feature of the proposed mechanism, by which it can be distinguished from the optical QPOs arising from the hot flow. Another way to recognise it is the dependence of the rms on the wavelength, where the increase of the variability amplitude towards shorter wavelengths is expected.

The described QPO mechanism inevitably should play a role in all systems with the sufficiently small ratio of the outer disc size to the QPO period. However, the observed oscillation amplitudes are expected to be lower than predicted here because of the substantial non-variable background. As other components, which do potentially contribute to the optical emission (e.g. the hot flow and the jet), can also generate QPOs, finding the signatures of reprocessed emission in the oscillating signal becomes a challenging task. The most promising low-mass X-ray binary systems, which are expected to have optical QPO due to reprocessing, are those showing a prominent positive peak in the optical/X-ray CCF, corresponding to the irradiation delays of the aperiodic X-ray variability. It is also preferable to search for these types of QPOs in the UV, where the disc radiation dominates and the QPO rms reaches the maximum, while other components are relatively dim.

ACKNOWLEDGEMENTS

The work was supported by the Finnish Doctoral Programme in Astronomy and Space Physics (AV) and by the Academy of Finland grant 268740 (JP).

REFERENCES

Casares J., Jonker P. G., 2014, Sp. Sci. Rev., in press
Casella P., Belloni T., Stella L., 2005, ApJ, 629, 403
Cunningham C., 1976, ApJ, 208, 534
Curran P. A., Chaty S., Zurita Heras J. A., 2012, A&A, 547, A41
de Jong J. A., van Paradijs J., Augusteijn T., 1996, A&A, 314, 484
Durant M., Gandhi P., Shahbaz T., Fabian A. P., Miller J., Dhillon V. S., Marsh T. R., 2008, ApJ, 682, L45
Durant M., Gandhi P., Shahbaz T., Peralta H. H., Dhillon V. S., 2009, MNRAS, 392, 309
Fragile P. C., Blaes O. M., Anninos P., Salmonson J. D., 2007, ApJ, 668, 417
Frank J., King A., Raine D. J., 2002, Accretion Power in Astrophysics. Cambridge University Press, Cambridge
Gandhi P. et al., 2010, MNRAS, 407, 2166
Gierliński M., Done C., Page K., 2009, MNRAS, 392, 1106
Grindlay J. E., McClintock J. E., Canizares C. R., Cominsky L., Li F. K., Lewin W. H. G., van Paradijs J., 1978, Nature, 274, 567
Hynes R. I. et al., 2003, MNRAS, 345, 292
Hynes R. I., Horne K., O'Brien K., Haswell C. A., Robinson E. L., King A. R., Charles P. A., Pearson K. J., 2006a, ApJ, 648, 1156
Hynes R. I., O'Brien K., Horne K., Chen W., Haswell C. A., 1998, MNRAS, 299, L37
Hynes R. I., O'Brien K., Mullally F., Ashcraft T., 2009, MNRAS, 399, 281
Hynes R. I. et al., 2006b, ApJ, 651, 401
Imamura J. N., Kristian J., Middleditch J., Steiman-Cameron T. Y., 1990, ApJ, 365, 312
Ingram A., Done C., 2011, MNRAS, 415, 2323
Ingram A., Done C., Fragile P. C., 2009, MNRAS, 397, L101
Kanbach G., Straubmeier C., Spruit H. C., Belloni T., 2001, Nature, 414, 180
Malzac J., Merloni A., Fabian A. C., 2004, MNRAS, 351, 253
McClintock J. E., Canizares C. R., Cominsky L., Li F. K., Lewin W. H. G., van Paradijs J., Grindlay J. E., 1979, Nature, 279, 47
Motch C., Ricketts M. J., Page C. G., Ilovaisky S. A., Chevalier C., 1983, A&A, 119, 171
Neustroev V., Veledina A., Poutanen J., Zharikov S. V., Tsygankov S. S., Sjoberg G., Kajava J. J. E., 2014, MNRAS, submitted
O'Brien K., Horne K., Hynes R. I., Chen W., Haswell C. A., Still M. D., 2002, MNRAS, 334, 426
Poutanen J., 2002, MNRAS, 332, 257
Poutanen J., Beloborodov A. M., 2006, MNRAS, 373, 836
Poutanen J., Gierliński M., 2003, MNRAS, 343, 1301
Shakura N. I., Sunyaev R. A., 1973, A&A, 24, 337
Steiman-Cameron T. Y., Scargle J. D., Imamura J. N., Middleditch J., 1997, ApJ, 487, 396
Sunyaev R. A., Titarchuk L. G., 1985, A&A, 143, 374
van Paradijs J., McClintock J. E., 1994, A&A, 290, 133
Veledina A., Poutanen J., Ingram A., 2013a, ApJ, 778, 165
Veledina A., Poutanen J., Vurm I., 2011, ApJ, 737, L17
Veledina A., Poutanen J., Vurm I., 2013b, MNRAS, 430, 3196
Viironen K., Poutanen J., 2004, A&A, 426, 985
Warner B., 1995, Cataclysmic variable stars, Vol. 28. Cambridge University Press, Cambridge
Zurita C., Durant M., Torres M. A. P., Shahbaz T., Casares J., Steeghs D., 2008, ApJ, 681, 1458
Zurita Heras J. A., Chaty S., Cadolle Bel M., Prat L., 2011, MNRAS, 413, 235

Mon. Not. R. Astron. Soc. **000**, 1–13 (2014) Printed 5 September 2014 (MN LATEX style file v2.2)

Colours of black holes: infrared flares from the hot accretion disc in XTE J1550–564

Juri Poutanen[1,2⋆] Alexandra Veledina[2,1] and Mikhail G. Revnivtsev[3]
[1] *Tuorla Observatory, University of Turku, Väisäläntie 20, FI-21500 Piikkiö, Finland*
[2] *Astronomy Division, Department of Physics, PO Box 3000, FI-90014 University of Oulu, Finland*
[3] *Space Research Institute, Russian Academy of Sciences, Profsoyuznaya 84/32, 117997 Moscow, Russia*

Submitted to MNRAS on 2014 June 29

ABSTRACT
Outbursts of the black hole (BH) X-ray binaries are dramatic events occurring in our Galaxy approximately once a year. They are detected by the X-ray telescopes and often monitored at longer wavelengths. We analyse the X-ray and optical/infrared (OIR) light-curves of the BH binary XTE J1550–564 during the 2000 outburst. By using the observed extreme colours as well as the characteristic decay timescales of the OIR and X-ray light-curves, we put strong constraints on the extinction towards the source. We accurately separate the contributions to the OIR flux of the irradiated accretion disc and a non-thermal component. We show that the OIR non-thermal component appears during the X-ray state transitions both during the rising and the decaying part of the outburst at nearly the same X-ray hardness but at luminosities differing by a factor of 3. The line marking the quenching/recovery of the non-thermal component at the X-ray hardness - flux diagram seems to coincide with the "jet line" that marks the presence of the compact radio jet. The inferred spectral shape and the evolution of the non-thermal component during the outburst, however, are not consistent with the jet origin, but are naturally explained in terms of the hybrid hot flow scenario, where non-thermal electrons emit synchrotron radiation in the OIR band. This implies a close, possibly causal connection between the presence of the hot flow and the compact jet. We find that the non-thermal component is hardening during the hard state at the decaying stage of the outburst, which indicates that the acceleration efficiency is a steep function of radius at low accretion rate.

Key words: accretion, accretion discs – black hole physics – radiation mechanisms: non-thermal – X-rays: binaries

1 INTRODUCTION

The optical/infrared (OIR) spectra of black hole (BH) low-mass X-ray binaries often show an excess above the standard (Shakura & Sunyaev 1973) accretion disc emission (e.g., Hynes et al. 2000, 2002; Gelino, Gelino, & Harrison 2010). In some cases the spectrum can be described by a power-law of index close to zero (i.e. $F_\nu \propto \nu^0$). There are three possible candidates that may account for this emission: the irradiated disc (Cunningham 1976; Gierliński et al. 2009), hot accretion flow (Veledina et al. 2013b) and the jet (Hynes et al. 2002; Gallo et al. 2007). Sometimes the OIR fluxes are higher than expected from any candidate alone (Chaty et al. 2003; Gandhi et al. 2010), and the complex optical/X-ray cross-correlation functions (Kanbach et al. 2001; Durant et al. 2008) support this anticipation, suggesting contribution of two components simultaneously (Veledina et al. 2011a). The source of OIR emission cannot be determined by only using photometric data and some additional information about the OIR-X-ray connection, short time-scale variability properties and the long-term spectral variations is required (see review in Poutanen & Veledina 2014). The latter is particularly important when trying to separate emission of different components.

The entire transition of the BH transient XTE J1550–564 from the hard to the soft state and back during its 2000 outburst was monitored by Yale 1 m telescope at CTIO in the V, I and H filters (Jain et al. 2001a). The light-curve structure cannot be simply explained by the fast rise-exponential decay pattern, expected in the case of standard or irradiated disc. An additional component, manifesting itself through strong flares, is required. Recently Russell et al.

⋆ E-mail: juri.poutanen@utu.fi

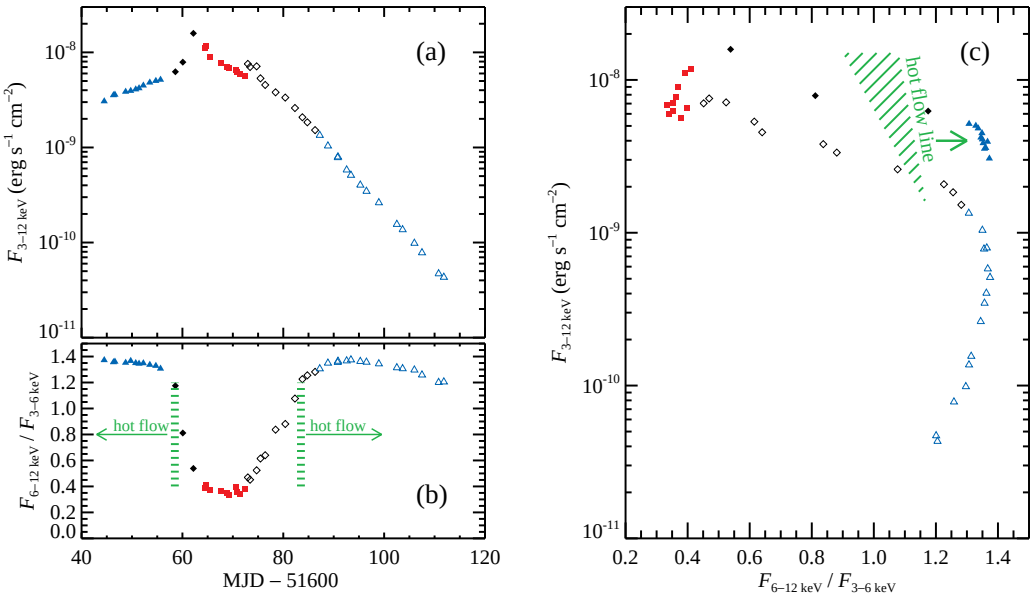

Figure 1. (a) Light curve of XTE J1550–564 (flux in the 3–12 keV band) and (b) the evolution of the hardness ratio (i.e. ratio of fluxes in the energy bands 6–12 and 3–6 keV) during the 2000 outburst. (c) The hardness-flux diagram. Different symbols and colours highlight outburst stages defined from the hardness ratio (see text). The times and the positions of quenching/recovery of the non-thermal OIR component ("hot flow line") are marked by green ribbons.

(2010, 2011) suggested that this component originates in a radio-emitting jet, however, multiple errors in these works make this interpretation doubtful. Here we re-analyse the available OIR and X-ray data. From the characteristic decay time-scales in the X-rays and in different OIR filters we infer the typical accretion disc temperature during the soft state. This immediately translates to the constraints on the extinction towards the source, poorly known before. Using the OIR light curves we accurately extract the non-disc non-thermal component and show evolution of its spectral shape during the flare. We find that the additional component may originate in the hot accretion flow, if a small fraction of energy is injected in the form of non-thermal electrons that emit synchrotron radiation.

2 LIGHT CURVES AND EXTINCTION

2.1 Data

The X-ray data on the 2000 outburst of XTE J1550–564 covering 2.5–25 keV range from the Proportional Counter Array (PCA) spectrometer (Jahoda et al. 2006) on board the *Rossi X-ray Timing Explorer (RXTE)* were analysed with the HEASOFT package (version 6.15) and response matrices were generated using PCARSP (11.7.1). The instrumental background of the PCA detectors was estimated with `CM_bright_VLE` model. At the position of the source XTE J1550–564 there is additional sky background from the so-called Galactic Ridge (see Revnivtsev et al. 2006, and references therein) which provides the flux at the level of $F_{3-20\,\mathrm{keV}} \sim 1.2\times10^{-11}$ erg s^{-1} cm^{-2} within field of view of PCA (~ 1 deg^2). In order to account for this additional background we have used *RXTE*/PCA observations of XTE J1550–564 in 2001 April when the source was already in quiescence. All the spectral data were fitted using

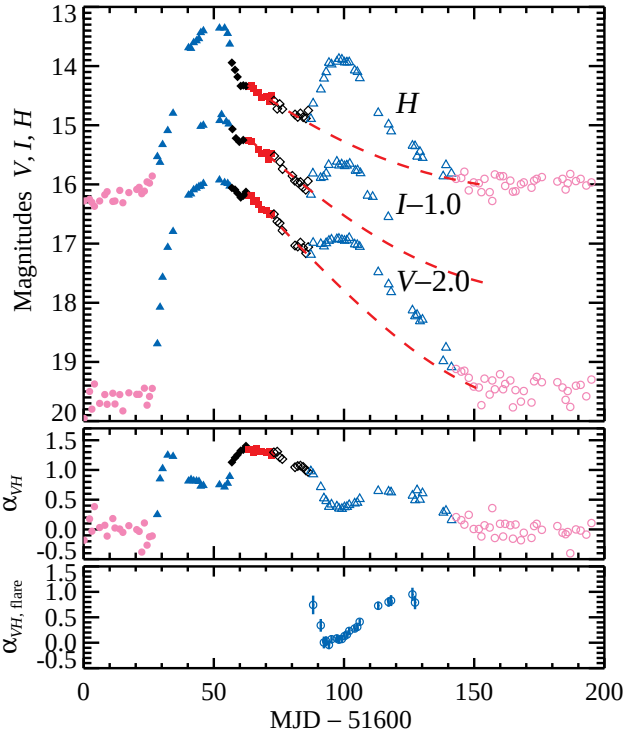

Figure 2. Light curve of XTE J1550–564 in three filters V, I and H during the 2000 outburst. The V- and I-magnitudes are shifted upwards by 2.0 and 1.0, respectively. Pink symbols correspond to the quiescent state, other symbols are the same as in Fig. 1. The red dashed lines show the evolution of the irradiated disc during the second flare (see Sect. 3.4). The middle panel show the power-law spectral index of the intrinsic spectrum α_{VH} corrected for extinction (with $A_V = 5.0$) determined from the V–H colour using equation (9). The lower panel shows the evolution of the spectral index of the flare component.

Table 1. Parameters of the system adopted from Orosz et al. (2011).

Orbital period	$P_{\rm orb}$	37 h
Distance	D	4.38 kpc
Black hole mass	M_1	$9.1 M_\odot$
Companion mass	M_2	$0.3 M_\odot$
Inclination	i	75°
Separation	a	$11.85 R_\odot$
Radius of the companion	R_2	$1.75 R_\odot$
Roche lobe size	$R_{L,1}$	$7.7 R_\odot$
Effective temperature of the companion	$T_{\rm eff}$	4475 K

XSPEC 12.8.1g package (Arnaud 1996), assuming 1 per cent systematic uncertainty. To estimate fluxes from the source, we have fitted the spectral data with a standard for BHs DISKBB+POWERLAW model and corrected the model fluxes in the specific energy bands by the ratio of the data to the model. For a more detailed spectral modelling we also fitted the data with a hybrid Comptonization model COMPPS (Poutanen & Svensson 1996) and a cutoff power-law model with Compton reflection PEXRAV (Magdziarz & Zdziarski 1995). Interstellar absorption was taken into account using WABS model with the neutral hydrogen column density of $N_{\rm H} = 0.80 \times 10^{22}$ cm^{-2} (Miller et al. 2003).

The X-ray light curve is shown in Fig. 1 together with the evolution of the hardness ratio as well as with the hardness-flux diagram. It is coloured according to the hardness ratio. The hard state is shown by blue triangles, while the transitions from the hard to the soft state and back are shown by black diamonds. The filled and open symbols correspond to the rising and decaying phases of the outburst, respectively. The soft state with the nearly constant hardness ratio is shown by red squares.

The OIR data from the 2000 outburst in V, I and H-filters have been presented by Jain et al. (2001a). To convert magnitudes to fluxes we use the zero points of 3636, 2416, and 1021 Jy and the effective wavelengths of 545, 798, and 1630 nm for filters V, I and H, respectively (Bessell et al. 1998). We show the daily-averaged OIR light curves in Fig. 2. The colour code is the same as in Fig. 1, with additional magenta points corresponding to the quiescent state of the source. The fast rise exponential decay morphology is accompanied here with flares, which are most prominent in the H-filter.

2.2 Soft state and implications for the disc temperature

During the soft (and the following intermediate) state the OIR emission is likely originating in the irradiated accretion disc alone. This is supported by a simple exponential shape of the light curves in both the OIR and X-ray bands. This knowledge can be used to estimate the accretion disc temperature. The first constraint relates the peak X-ray luminosity to the reprocessed optical flux. The effective temperature at the outer radius of the irradiated disc dominating the OIR emission is $T_{\rm eff,irr} = [\eta(1-A)L_{\rm X}/(4\pi R_{\rm irr}^2 \sigma_{\rm SB})]^{1/4}$, where A is the disc albedo and the factor $\eta \approx \frac{H}{R}\left(\frac{d\ln H}{d\ln R} - 1\right)$ gives the cosine between the normal to the outer disc and the direction to the central X-ray source (Frank et al. 2002). The disc size $R_{\rm irr}$ is a fraction of the Roche lobe (Eggleton 1983, see parameters in Table 1),

$$R_{L,1} = a\frac{0.49q^{2/3}}{0.6q^{2/3} + \ln(1+q^{1/3})}. \quad (1)$$

For measured $a = 11.85 R_\odot$ and $q = 1/30$, we get $R_{L,1} = 7.7 R_\odot$. The maximum disc size limited by tidal forces is (Warner 1995) $R_{\rm irr} \lesssim 0.6a/(1+q) \approx 4.8 \times 10^{11}$ cm.

To estimate η, we take the disc half-opening angle of 12° (de Jong et al. 1996), i.e. $H/R \sim 0.2$. The logarithmic derivative $d\ln H/d\ln R - 1$ takes values 1/8 for the standard and 2/7 for the irradiated discs (Frank et al. 2002), which we adopt in the following and get $\eta \approx 0.06$. A typical albedo A of mostly neutral material is below 0.5 even for a very hard power-law spectrum extending to 100 keV (Basko et al. 1974; Magdziarz & Zdziarski 1995) and is expected to be below 0.1 for the blackbody-like X-ray spectra with $kT_{\rm bb} \sim 1.5$ keV in the soft state. The bolometric luminosity at the peak of the 2000 outburst was $\approx 10^{38}$ erg s^{-1} (see Sect. 3.5). Because only photons with energy above 2 keV thermalize efficiently (Suleimanov et al. 1999), we use $L_{>2{\rm keV}} \approx 5 \times 10^{37}$ erg s^{-1} and finally get $T_{\rm eff,irr} \gtrsim 11\,000$ K. The temperature can be lower if the X-rays are so strongly anisotropic that the flux directed towards the outer disc is significantly lower than that at the observed inclination of $i = 75°$. However, if the outer disc is inclined at a similar angle of $\sim 80°$ (de Jong et al. 1996), practically no difference is expected.

Further constraints are coming from the comparison of the decay rates in the X-ray and optical bands (Endal et al. 1976; van Paradijs & McClintock 1995). The general idea is to compare the derivative of the observed flux over temperature to that of the known function – a simple blackbody or the irradiated disc model spectrum. Because the decay rate is an injective (i.e. one-to-one) function of temperature, we immediately obtain the absolute value of $T_{\rm eff}$.

If we ignore energy dissipation intrinsic to the disc (which is possible for high X-ray luminosities), the effective temperature of the irradiated disc varies with the X-ray luminosity as $T_{\rm eff} \propto L_{\rm X}^{1/4}$. Some deviations from this law are possible if the emission pattern is changing. Because the X-ray light curve shows some flares at the transition from the soft to the intermediate state, we have selected the soft-state segment of the data (red squares in Fig. 1) and fitted the X-ray flux there with an exponential profile. We obtain the e-folding time of $\tau_{\rm X} = 10.0 \pm 0.1$ days. This translates to the time of temperature decay $\tau_{\rm T} = 4\tau_{\rm X} = 40$ d, i.e.:

$$\partial \ln T_{\rm eff}/\partial t = -1/40 \text{ d}^{-1}. \quad (2)$$

We then fit the soft- and intermediate state OIR light-curves together with the values in the quiescence at MJD 51645–51650 with a constant plus an exponentially decaying component. For I-filter, we adopt the constant $I = 19$ in quiescence taken from the earlier observations (Jain et al. 2001b). The e-folding time-scale is then related to the derivative of the logarithm of the flux of the varying (disc) component:

$$\partial \ln F_\lambda/\partial t = -1/\tau_\lambda \text{ d}^{-1}. \quad (3)$$

We find $\tau_\lambda = 22.6 \pm 0.8$, 26.0 ± 1.0, and 31.3 ± 2.0 days for the V, I and H bands, respectively. The decay of the blackbody flux due to the decreasing temperature can be computed as

$$\frac{\partial \ln B_\lambda}{\partial \ln T_{\rm eff}} = \frac{y}{1-\exp(-y)}, \quad (4)$$

where $y = hc/\lambda kT_{\rm eff} = 1.44/(\lambda_\mu T_4)$, λ_μ is the wavelength in microns and $T_4 = 10^{-4}T_{\rm eff}$. The value for the logarithmic derivative is then obtained by dividing equation (3) by equation (2). Solving the resulting equation for $T_{\rm eff}$ we get the average effective soft- and intermediate-state temperatures of 20 800, 19 540, and 17 500 K, with the errors on individual measurements much smaller than the spread between the values.

We checked the possibility of neglecting the constant flux in the OIR light-curves, which resulted in the decay times for the V, I and H bands $\tau_\lambda = 23.8 \pm 0.7$, 29.2 ± 1.1, and 39.2 ± 2.0 days, respectively. These values translate to the temperatures 23 200 and 27 400 K for V and I-filters and for the H-filter temperature exceeds 200 000K. If instead only the soft state light curve is fitted with the exponential, we get $\tau_\lambda = 29.5 \pm 2.7$, 32.7 ± 3.6, and 41.9 ± 5.4 days, which correspond to $T_{\rm eff}$ in excess of 40 000 K for V and I-filters and again no solution is possible for the H-filter.

We also checked, whether the irradiated disc model gives any improvement compared to the simple blackbody. In this case equation (4) can be rewritten as

$$\frac{\partial \ln F_{{\rm irr},\lambda}}{\partial \ln T_{\rm out}} = y_{\rm o} \frac{\displaystyle\int_{r_{\rm io}}^{1} \frac{\exp(y_{\rm o}x^\beta)}{[\exp(y_{\rm o}x^\beta)-1]^2} x dx}{\displaystyle\int_{r_{\rm io}}^{1} \frac{x\ dx}{\exp(y_{\rm o}x^\beta)-1}}, \qquad (5)$$

where β is the power-law index of the radial temperature dependence $T(R) \propto R^{-\beta}$, $r_{\rm io} = R_{\rm in}/R_{\rm out}$ is the ratio of the inner to outer disc radius and $y_{\rm o} = hc/\lambda kT_{\rm out}$. In Rayleigh-Jeans regime $y_{\rm o} \ll 1$, the logarithmic derivative takes the minimum value of $(1-\beta/2)/(1-\beta)$. We see that for realistic $\beta = 3/7$–$1/2$ (Cunningham 1976; Frank et al. 2002), the model minimum derivatives are larger than the observed values, thus no solution is possible. Hence, the simple irradiated disc does not give a good description to the shape of the light curve.

We conclude here that from the simple estimate of the maximum disc size and peak X-ray luminosity, the outer disc temperature has to be above 11 000 K in the soft and intermediate states, while from the light curve behaviour we get $T_{\rm eff} \gtrsim 18\,000$ K. Thus we conservatively assume that $T_{\rm eff} \gtrsim 15\,000$ K during the peak of the 2000 outburst.

2.3 Extinction towards XTE J1550–564 and spectral index – colour relation

Optical extinction towards XTE J1550–564 can be estimated from the hydrogen column density. The FTOOLS routine NH (Dickey & Lockman 1990) gives $N_{\rm H} = 0.9 \times 10^{22}$ cm^{-2}. Tomsick et al. (2001) has obtained $N_{\rm H} = (0.85^{+0.22}_{-0.24}) \times 10^{22}$ cm^{-2} using *Chandra* observations in the end of the 2000 outburst. Similar result, $N_{\rm H} = (0.88^{+0.12}_{-0.09}) \times 10^{22}$ cm^{-2}, was obtained by Corbel et al. (2006) again from the *Chandra* observations in a quiescent state. The most accurate measurement of $N_{\rm H} = (0.80 \pm 0.04) \times 10^{22}$ cm^{-2}, which we use for X-ray data analysis, is from the *Chandra* observations during the peak of the 2000 outburst (Miller et al. 2003). Thus, all measurements are consistent with $N_{\rm H}$ lying in the interval $(0.75-1)\times10^{22}$ cm^{-2}. However, these results are inconsistent with the earlier estimate of the extinction $A_V = 2.2 \pm 0.3$ based on interstellar optical absorption lines (Sánchez-Fernández et al. 1999). The later measurements and modelling of Orosz et al. (2011) imply $A_V \approx 4.75$. The Predehl & Schmitt (1995) relation, $A_V = 5.59\ N_{\rm H}/10^{22}$, gives $A_V = 4.2 - 5.6$.

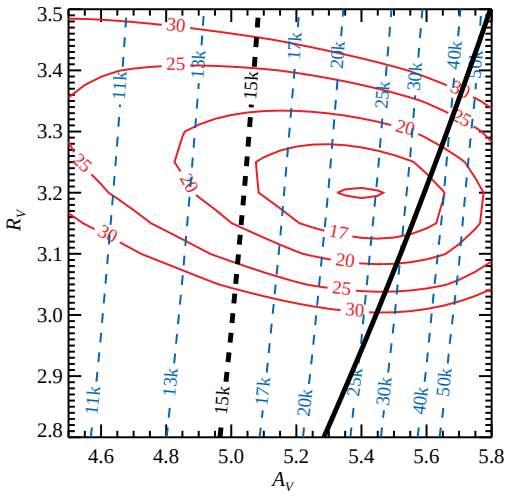

Figure 3. Contours of χ^2 (red solid curves) for the blackbody fit to the OIR data in the soft and intermediate state (MJD 51663–51676) at the plane A_V–R_V. The dashed contour lines show the average temperature in these states varying from about 10 000 K for $A_V = 4.5$ to 30 000 K for $A_V = 5.5$. The thick dashed black line marks the position of the average $T_{\rm eff} = 15\,000$ K, thus the region to the left of this line is forbidden. The region to the right of the thick solid black line corresponds to $\alpha_{VI} > 2$, i.e. harder than the Rayleigh-Jean and therefore is forbidden.

Another way of estimating A_V is to use constraints on the disc temperature from Sect. 2.2. We have converted the OIR magnitudes to fluxes and fitted the three-point spectra obtained in the soft and intermediate states with the blackbody disc of the constant radius $R_{\rm irr}$ and varying temperature:

$$F_\nu(T_{\rm eff}) = \cos i\ B_\nu(T_{\rm eff})\ \pi R_{\rm irr}^2/D^2. \qquad (6)$$

The extinction A_V was allowed to vary. We also checked how the shape of the extinction curve affects the results by varying R_V. We used the extinction law of Cardelli et al. (1989) corrected by O'Donnell (1994). All together we fitted 13 one-day-averaged spectra (39 points) using 14 fitting parameters ($R_{\rm irr}$ and 13 temperatures) with 25 d.o.f. The contours of χ^2 on the plane R_V–A_V are shown in Fig. 3. We see that the best-fit is achieved for $R_V = 3.2$ and $A_V = 5.4$. The effective disc radius is $R_{\rm irr} = 2.85 \times 10^{11}$ cm, which is 40 per cent smaller than the maximal possible disc size limited by tidal forces. We should remember, however, that the actual emission area is likely a ring, not a circular disc, therefore the actual disc size is larger. We also plot at the same plane the average temperature from the best-fitting models. The lower limit on the typical temperature $T_{\rm eff} > 15\,000$ K obtained in Sect. 2.2 can be now transformed to a lower limit of $A_V > 5.0$. These results are almost in dependent of R_V.

Two more constraints can be obtained from the extreme colours shown by XTE J1550–564. For that it is useful to get the relations between colours and the corresponding intrinsic (without absorption) spectral indices α of the power-law

spectrum $F_\nu \propto \nu^\alpha$. The apparent magnitude in any filter is defined as

$$m_\nu = -2.5 \log F_\nu / F_{\nu,0} + A_\nu, \quad (7)$$

where A_ν is the extinction, F_ν is the intrinsic flux without absorption and $F_{\nu,0}$ is the zero point. The slope between bands i and j can be computed as

$$\alpha_{ij} \equiv \frac{\log\left(\frac{F_i}{F_j}\right)}{\log\left(\frac{\nu_{\rm eff},i}{\nu_{\rm eff},j}\right)} = \frac{m_i - m_j - A_i + A_j - 2.5\log\left(\frac{F_{i,0}}{F_{j,0}}\right)}{2.5\log\left(\frac{\lambda_{\rm eff},i}{\lambda_{\rm eff},j}\right)}, \quad (8)$$

where $\lambda_{\rm eff}$ are the effective wavelengths of the corresponding filters. The slopes between the considered bands V, I and H are then:[1]

$$\alpha_{VH} = 1.16 + 0.69\,A_V - 0.84\,(V-H), \quad (9)$$

$$\alpha_{IH} = 1.21 + 0.55\,A_V - 1.29\,(I-H), \quad (10)$$

$$\alpha_{VI} = 1.07 + 0.94\,A_V - 2.42\,(V-I). \quad (11)$$

where we used the ratios $A_I/A_V = 0.61$ and $A_H/A_V = 0.185$ obtained for $R_V = 3.2$.

The bluest spectra observed from XTE J1550–564 during a brighter outburst in 1998 (Jain et al. 1999), which had $V - I = 1.8$ (for $V = 16.8$ and $I = 15.0$). have to be softer than the Rayleigh-Jean tail of the blackbody, i.e. $\alpha_{VI} < 2$. Using equation (11), we now immediately get a firm upper limit on $A_V \lesssim 5.6 + 0.75\,(R_V - 3.2)$ shown by a thick black solid line in Fig. 3.

On the other hand, the reddest spectra in the beginning and the end of the 2000 outburst still consistent with the blackbody have $V - H \approx 5.3$. According to the disc instability models (Dubus et al. 2001; Lasota 2001; Frank et al. 2002), for the outburst to start, the outer disc temperature has to be above the hydrogen ionisation temperature of about 6000 K. The blackbody of this temperature has $\alpha_{VH} \approx 0.1$. Thus, we get the lower limit from equation (9): $A_V \gtrsim 4.9$, which is nearly identical to the constraint we get from the soft state spectra in Sect. 2.2.

We conclude that a realistic range of the extinction is $A_V = 5.0 - 5.6$. In the further discussion we adopt $A_V = 5.0$ (and $R_V = 3.2$), with extinction in other filters is then $A_I = 3.05$ and $A_H = 0.92$. Note that if we assume larger A_V, the typical spectral indices would then be larger than given by equations (9)–(11). This does not change qualitatively the behaviour of the source and does not affect any of the conclusions.

[1] These transformation laws correct the erroneous expressions presented in Russell et al. (2011), which have wrong scalings and give index α of about 1.0 too small. They have used the wavelength and the zero point of the J-filter instead of those for the H-filter in the equation similar to our equation (9), while in the equation corresponding to our equation (10), they have taken the values for the Johnson I-filter instead of the Kron-Cousins I-filter (Dipankar Maitra and David Russell, priv. comm.).

3 SPECTRAL PROPERTIES

3.1 V vs $V - H$ diagram

Fig. 4(a) represents the V versus $V - H$ colour-magnitude diagram (CMD). The symbols correspond to the outburst stages identified from the X-ray hardness ratio (Fig. 1). The path the source makes on the diagram is illustrated in the upper right corner with arrows. The black line corresponds to theoretical colour–magnitude relation for a blackbody of different temperatures with the disc radius determined from the best-fit to the soft and intermediate state spectra (assuming $A_V = 5$). The upper x-axis at the CMD shows the slope α of the intrinsic spectrum between the corresponding bands converted from the colour using equation (9).

At the beginning of the outburst their evolution can be well described by a blackbody of increasing temperature, until the colour $V - H \sim 4.0$ is achieved. After that, the source becomes significantly redder than a blackbody of the corresponding V magnitude. This behaviour can be interpreted as an appearance of an additional, non-thermal component. At the X-ray hard-to-soft transition, the source returns to the blackbody track at almost constant V magnitude (horizontal track in the CMD), indicating the quenching of the additional component around MJD 51659. In the soft and in the beginning of the following intermediate state, the OIR colours are well described by a blackbody of decreasing temperature. During the reverse transition, we observe reappearance of the red component around MJD 51683, again as a horizontal track in the CMD. Then the source slowly decays towards the quiescence along the blackbody track of the same normalization as during the soft state, which is, however, slightly larger than that at the rising phase of the outburst. The peculiar fast changes in the H-band at almost constant V band put constraints on the possible origin of non-thermal emission.

We also have checked, whether additional contribution from the secondary star affects the overall shape of the magnitude–colour relation. We used the atmosphere templates of Castelli & Kurucz (2004) for a K3 star with $\log g = 3.5$, $T_{\rm eff} = 4500$ K and radius of $1.75 R_\odot$ (Orosz et al. 2011). The secondary has a minor effect on the CMD, except for quiescence, where the model becomes slightly redder than the data. If, however, we assume a larger extinction, e.g. $A_V = 5.2$, the blackbody temperature corresponding to the soft state increases to 20 000–25 000 K and the total theoretical CMD then well describes the data even in the quiescent state. Because we are not interested in this state (and for the sake of simplicity of the model), we further do not account for the secondary contribution.

3.2 I vs $I - H$ diagram

We also plot the I versus $I - H$ CMD in Fig. 4(b). The behaviour of the source in this diagram is very similar to that in the V vs $V - H$ CMD. The blackbody track (black solid line) for the same parameters as in Fig. 4(a) provides a good fit to the data from MJD 51660 at the end of the hard-to-soft transition, in the soft state and in the beginning of the soft-to-hard transition until about MJD 51683. In the middle of the soft-to-hard transition, the source becomes redder indicating the presence of the additional component. The X-ray

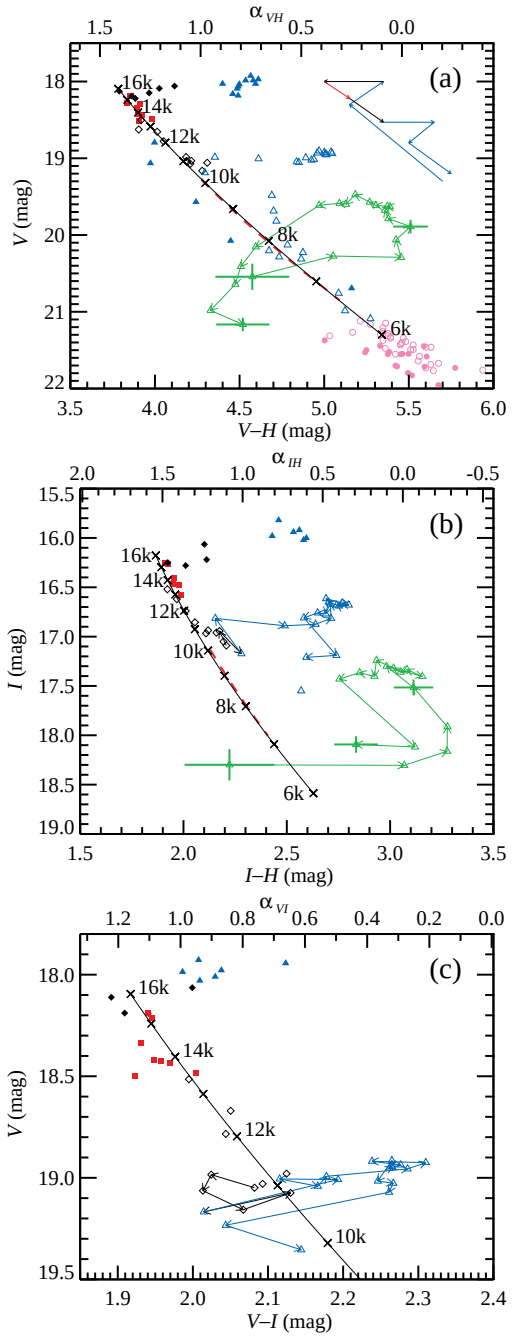

Figure 4. The observed (a) V vs $V-H$, (b) I vs $I-H$ and (c) V vs $V-I$ CMDs. The coloured track in the upper right corner of panel (a) illustrates the path XTE J1550–564 follows at the diagram. The black solid lines represent the theoretical curves for the blackbody disc of radius $R_{\rm irr} = 2.85\times10^{11}$ cm inclined at $i = 75°$ at distance of 4.38 kpc (Orosz et al. 2011) of different temperatures (in units of thousands of Kelvin, marked next to the line). The model magnitudes were reddened following the extinction law of Cardelli et al. (1989) and O'Donnell (1994) with $A_V = 5$ and $R_V = 3.2$. The upper x-axes show the intrinsic spectral indices in the corresponding wavelength bands given by equations (9)–(11). The red dashed line represents the disc component extrapolated to the time of the flare in the hard state (see Fig. 2). The blue and black arrows connect points in the end of intermediate and beginning of the hard states. The green track shows the path made by the flare component during the hard state starting from MJD 51688 (see Sect. 3.4).

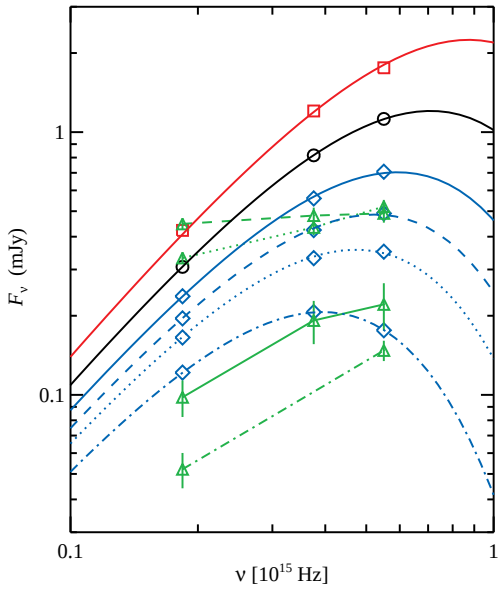

Figure 5. Examples of spectra (corrected for extinction) and the best-fitting blackbody model of constant emission area. Data taken in the soft state on MJD 51665 and in the intermediate state on MJD 51676 are shown by red squares and black circles, respectively. In the hard state, the disc fluxes on MJD 51688, 51697, 51706 and 51726 obtained by interpolation are shown by blue diamonds and the flare component by green triangles. The best-fitting blackbody models are shown by solid, dashed, dotted, dot-dashed blue lines, respectively. The errors are not shown for most data points, because they are smaller than the size of the symbols.

hardness during the moments of appearance/disappearance of this component was nearly the same (see Fig. 1c), corresponding to the X-ray spectrum with photon index $\Gamma \approx 1.9$ and reflection amplitude $\Omega/(2\pi) \approx 1$.

An interesting additional detail is a hook-like evolution (marked by blue arrows) at the end of the hard state, before the flare in the H filter. This feature arises because several data points at the beginning of the hard state are redder at lower I-flux compared to the data points a few days later, which makes the spectrum bluer (larger α_{IH}) at a higher $I-$flux. This behaviour cannot be an artefact of interpolation between non-simultaneous points in the H-filter and can be interpreted as the flare starting first in the I-band, then proceeding to the H-band. This is consistent with the shape of the flare spectra (see Sect. 3.4 and Fig. 5).

The spectral index α_{IH} (upper x-axis) at the peak of the flare (when the spectrum is softest in the hard state) is identical to α_{VH}, implying a single power-law component going through all three filters. We note that taking larger values of extinction results in a larger α (harder spectra), but the effect is larger for α_{VH} than for α_{IH}, thus the spectrum would no longer be described by a single power-law.

3.3 V vs $V-I$ diagram

The general evolution of the source at the V vs $V-I$ CMD shown in Fig. 4(c) is very similar to those for other filters as described above. However, at this diagram the appearance

of the additional non-thermal component is easier to see. Around MJD 51683, in the middle of the intermediate state, the spectrum becomes bluer, which is reflected in motion of the source at $V = 19$ to the left from the blackbody model line by $\Delta(V - I) \approx 0.1$ (shown by black arrows). This implies that the additional component has a spectrum harder than the blackbody spectrum at this moment of $\alpha_{VI} \approx 0.7$. The spectrum becomes redder that the corresponding blackbody at MJD 51688. Only at this moment, the flare starts to become easily visible in the light curves.

3.4 Flares and the non-thermal component

The underlying behaviour of light-curves in V, I, and H filters is naturally explained with the evolving temperature of the accretion disc, which responds to changes in the X-ray luminosity (i.e., due to changes of the reprocessing flux). The CMDs as well as the spectra at the soft and the following intermediate states suggest that the OIR emission comes from the irradiated accretion disc that is modelled here as a blackbody (see Fig. 5 and Sections 3.1 and 3.2). The flares that occur in the intermediate/hard states can be interpreted as the appearance of an additional, non-thermal component. The first flare starts at the rising phase of the outburst and it is therefore impossible to separate it from the underlying disc emission. On the other hand, the second flare occurs at the exponentially decaying stage and it is possible to subtract the disc emission in order to isolate the flaring component.

To obtain the disc emission at the time of the second flare, we use the same model as in Sect. 2.2, i.e. we fit the light-curves in every filter with the constant plus exponential that represents the irradiated disc. The fit is applied to the times MJD 51663–51683 for all filters and MJD 51750–51755 for V and H-filters. The first interval correspond to the soft and intermediate states where there no signatures of the additional component, while the second interval correspond to the quiescent state. Unfortunately, no I-filter data exist after MJD 51717 and similarly to Sect. 2.2 we fix the constant corresponding to $I = 19$. The best-fitting models are shown in Fig. 2 by dashed red curves. After the fitting, we check that the magnitudes and colours of the extrapolated disc component are consistent with the blackbody of the same size as before the flare (compare red dashed lines in Fig. 4 to the black solid lines representing the blackbody model). We see that the typical accuracy of the magnitudes of the interpolated blackbody component is better than 0.03.

By subtracting the blackbody flux at every moment, we extract the flaring non-thermal component. The evolution of colours and spectral indices of the flare is shown in Fig. 4 by green triangles connected by arrows. The typical errors are shown by crosses for a few points. From Fig. 4(a) we see that the flare starts with the hard index $\alpha_{VH} = 0.75 \pm 0.20$, then softens down to $\alpha_{VH} \approx 0$ and then hardens again to $\alpha_{VH} = 0.7 - 0.8$. The time evolution of α_{VH} of the total spectrum and of the flaring component is shown in the middle and lower panels of Fig. 2.

The flare path in I and H filters is seen in Fig. 4(b). The evolution is similar to the $V - H$ colours, but the spectrum is even harder at the start of the flare with $\alpha_{IH} = 1.1 \pm 0.3$, implying that the spectrum hardens towards longer wavelengths (see green solid line in Fig. 5). At the peak of the flare $\alpha_{IH} \approx +0.2$ nearly identical to α_{VH} implying that the spectrum in three filters is close to a power-law of the same index. At the end of the flare the spectrum in I and H band is less reliable, because of the growing error in the disc flux in I-filter.

The flare becomes visible in the light curves only in the beginning of the hard state at MJD 51688, but substantial deviations from the blackbody spectrum occur already at MJD 51683 as can be seen from the $V - I$ colour evolution shown in Fig. 4(c). In the end of intermediate state, during MJD 51683–51687 the total spectrum is bluer than the black body with $\alpha_{VI} \approx 0.7$ and reaches $\alpha_{VI} \approx 1$. This implies than the slope of the flare spectrum between I and V filters is substantially larger than unity, because the flare contribution to the total flux at this moment is still rather low.

Fig. 5 demonstrates the evolution of the disc and the flare spectra during the outburst. We see that the flare spectrum is a broken power-law just at the start of the flare, but is consistent later with a simple power-law. Assuming a larger extinction, e.g. $A_V = 5.2$, results in α larger by about 0.2, but the qualitative behaviour remains the same. We note here that our conclusions on the evolution of the flare spectrum are based on the assumption that the blackbody normalization did not change during the decaying phase of the outburst. This is supported by the absence of significant variations in the normalization from the soft state to the end of the hard state as well as the quiescence.

3.5 OIR – X-ray relation

Once we have separated the non-thermal component in the OIR band, it is worth looking at a larger picture by understanding the relation between the OIR flare spectrum and the X-rays. Fig. 6 shows the broad-band OIR/X-ray spectra of XTE J1550–564 taken at different states. Similar X-ray data from the 2000 outburst of XTE J1550–564 were presented before by Yuan et al. (2007) and Xue et al. (2008).

The soft state X-ray spectrum (taken on MJD 51665) is dominated by a strong thermal component from the optically thick accretion disc. There is a high-energy tail above 20 keV. These non-thermal tails are well explained by non-thermal Comptonization in the hot corona above the disc (Poutanen & Coppi 1998; Gierliński et al. 1999; Zdziarski & Gierliński 2004). The thermally-looking component itself cannot be explained by a simple standard disc model, but requires a contribution from thermal Comptonization. The whole X-ray spectrum thus can be fitted with a hybrid Comptonization model such as EQPAIR (Coppi 1999) or COMPPS (Poutanen & Svensson 1996) models in XSPEC. Here we used the latter. We do not discuss here the best-fitting parameters of the model, just because the aim of the fitting is only to show the shape of the spectrum, which is rather independent of the model choice. The extrapolation of the standard cold accretion disc DISKBB spectrum to lower energies reveals that it cannot contribute more than a few percent to the observed OIR flux, which is dominated by the reprocessed radiation from the outer disc with the total (unabsorbed) luminosity of $L_{\rm repr} \approx 7.3 \times 10^{35}$ erg s^{-1}. This has to be compared to the total (unabsorbed) X-ray luminosity in the 0.01–1000 keV band of $L_{\rm X} \approx 1.2 \times 10^{38}$ erg s^{-1}. Assuming the same angular dependence of radiation for both

components, the ratio of luminosities gives the total reprocessing efficiency of $\epsilon_{\rm repr} \approx 6\times10^{-3}$. The intermediate state spectrum (on MJD 51676) is nearly identical to the soft state spectrum, with a slightly lower temperatures and the X-ray and outer disc luminosities of $L_{\rm X} \approx 7.1\times10^{37}$ erg s^{-1} and $L_{\rm repr} \approx 3.2\times10^{35}$ erg s^{-1}, respectively, giving nearly the same reprocessing efficiency of $\epsilon_{\rm repr} \approx 4.5\times10^{-3}$.

In the hard state, we used the cutoff power-law model with Compton reflection (PEXRAV model in XSPEC; Magdziarz & Zdziarski 1995) for modelling and estimating the luminosities, because there are no any signatures of the thermal emission from the standard accretion disc in the X-ray band. We assumed a cutoff at 200 keV which is typical for a BH X-ray binary. During the three considered days (MJD 51688, 51697 and 51706), the spectral shape varied very little, with the power-law photon index being nearly identical at $\Gamma \approx 1.65$ (i.e. $\alpha \approx -0.65$) and the reflection amplitude $\Omega/(2\pi)$ decreasing from about unity to 0.3. The X-ray luminosity took the values of $L_{\rm X} \approx (16, 5.6, 1.5)\times10^{36}$ erg s^{-1}. The X-ray spectrum taken on MJD 51697 extrapolated to the OIR band (see blue lines in Fig. 6, where we plotted only the flare spectrum in the OIR) matches rather well with the OIR power-law. At the beginning of the hard state, at MJD 51688 (solid blue line), the extrapolation of the X-ray power-law is an order-of-magnitude above the OIR flux. On the other hand, later in the hard state, on MJD 51706, the X-rays underpredict the OIR emission.

In addition to the flare component, the emission from the irradiated disc (not shown in Fig. 6) was also steadily declining with $L_{\rm repr} \approx (16, 9.5, 6.3)\times10^{34}$ erg s^{-1} at the same three dates. This gives the reprocessing efficiency of $\epsilon_{\rm repr} \approx (1, 1.7, 4.2)\times10^{-2}$. Thus we see a clear trend of increasing $\epsilon_{\rm repr}$ with decreasing X-ray luminosity. This trend has also been reported for other BH transients (e.g. Gierliński et al. 2009). There could be at least two reason for such a change. Firstly, the geometry of the accretion disc and therefore the emission pattern changes during the soft-to-hard transition. In the soft state, the emission from optically thick standard disc is beamed perpendicular to its plane, hence the outer disc sees less radiation than the observer at 75° inclination. In the hard state, however, the emission from optically thin hot disc is much more isotropic (see e.g. Veledina et al. 2013a). Secondly, the reprocessing efficiency is higher for harder spectra, because the soft X-rays are absorbed in the very surface layers producing mostly UV lines and recombination continua (Suleimanov et al. 1999; see also discussion in Gierliński et al. 2009). We can account for the second effect by dividing $L_{\rm repr}$ by the luminosity above 2 keV, getting the reprocessing efficiency of $\epsilon_{\rm repr} \approx 1.2\times10^{-2}$ and 0.8×10^{-2} in the soft and intermediate states, respectively, and $\epsilon_{\rm repr} \approx (1.2, 2.1, 5.2)\times10^{-2}$ in the hard state. This reprocessing efficiency is still rather modest because for the disc half-opening angle of 12° (de Jong et al. 1996) we expect $\epsilon_{\rm repr} \lesssim 0.15$ assuming albedo of 0.3. The observed reprocessing efficiency can actually be even lower, because at low fluxes a significant fraction of the OIR radiation can be produced by the (ignored here) secondary star and/or the bulge located at the impact point of the accretion stream.

4 ORIGIN OF NON-THERMAL COMPONENT

4.1 Jet?

The non-thermal OIR component seen in XTE J1550–564 was attributed to the jet synchrotron emission in a number of works (Corbel et al. 2001; Russell et al. 2010, 2011). The aforementioned works used the optical data, originally published in Jain et al. (2001a), the same as used in this work. Corbel et al. (2001) obtained optical $V-I$ spectral index $\alpha = -2.6$ (assuming $A_V = 2.2$) on 2000 June 1 (MJD 51697), in contrast to the obtained by us the flare spectral index $\alpha \approx 0$ (for $A_V = 5.0$). The source of discrepancy is the extinction value, poorly known at that time.

The studies by Russell et al. (2010, 2011) present the separation of the non-thermal emission using the light-curve fitting method. They claimed that the spectral indices of the non-thermal component are in the range $-1.5 \lesssim \alpha \lesssim -0.5$, again suggesting the non-thermal optically thin jet emission. However, these works suffer from the major errors in formulae for transformation of the colours to indices (see Sect. 2.3). Furthermore, their fits to the disc light curve in V and I-filters are significantly above the data points just before the flare (see fig. 2 in Russell et al. 2010) leading to overestimation of the disc contribution and to over-subtraction of the flux in those filters resulting in a much too soft flare spectrum. These flawed fits have greatly affected the first few points of the flare, where the non-thermal V flux was small, hence only spectral hardening during the flare was detected, while we obtain that the flare starts with hard spectrum with $\alpha \approx +0.75$, which softens to $\alpha \approx 0$ and then hardens again (see Fig. 4). Such behaviour is clearly inconsistent with the optically thin jet spectrum. The jet radio emission was indeed optically thin in the soft state, with $\alpha_{\rm radio} = -0.46 \pm 0.03$ (Fig. 7), but it does not contribute at all to the OIR spectrum, which was consistent with the blackbody.

On the other hand, the radio emission in the hard state close to the peak of the second flare, on MJD 51697.14 was optically thick with $\alpha_{\rm radio} = 0.36\pm0.09$ (Corbel et al. 2001). However, the OIR flare spectrum has a different slope and does not lie on the continuation of the radio spectrum (see green points in Fig. 7). Connecting those requires a break in the spectrum in the far-IR, which is inconsistent with the simplest jet models where main parameters follow the power-law radial dependences with constant indices (Blandford & Königl 1979; Königl 1981). The strongest arguments against the jet contribution to the OIR, however, come from the rather hard OIR spectra of the flare. Firstly, the hook-like behaviour on the $I-H$ CMD at the beginning of the flare (Fig. 4b), a broken power-law flare spectrum which hardens towards red on MJD 51688 (greed solid line in Fig. 5) as well as the hard flare spectrum with $\alpha > 1$ in the end of the intermediate state (see Sect. 3.3 and Fig. 4c) are not consistent with the jet spectrum extending from radio to the OIR band. Secondly, later in the hard state, the flare spectrum has $\alpha \sim 1$. If it were optically thick jet emission, the radio flux would be about 5 orders of magnitude below what was observed just a few days before. We find this highly improbable. Furthermore, it is difficult to understand how a substantial decrease in the accretion rate could lead to formation of the outflow which is optically thick up to the OIR

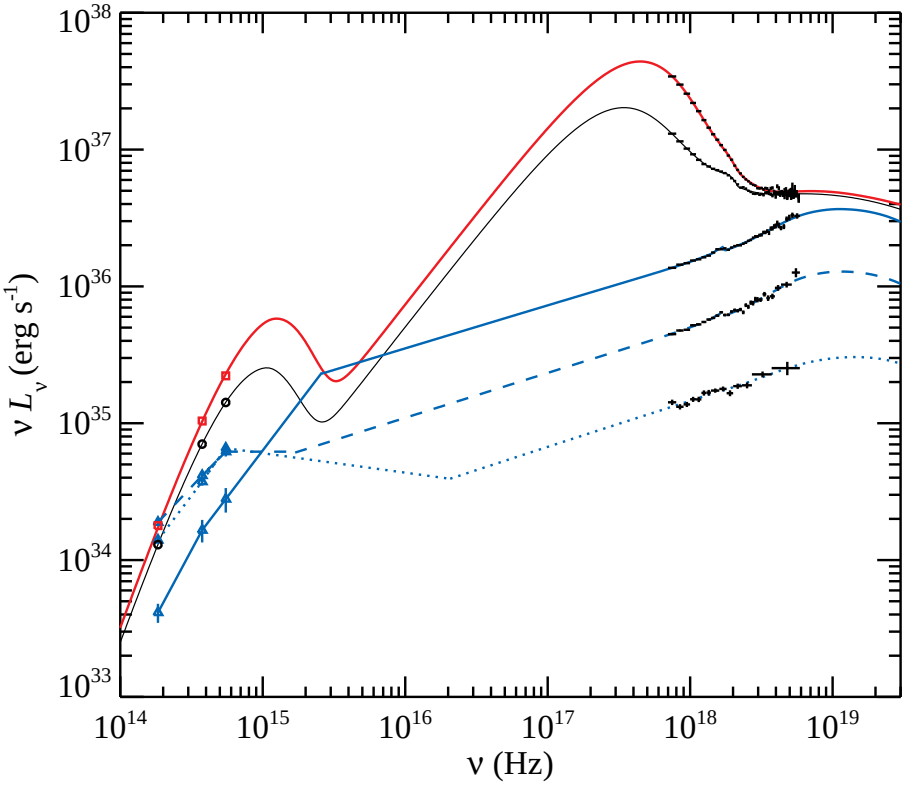

Figure 6. Broadband OIR to the X-ray spectral energy distribution of XTE J1550–564. The black crosses are the *RXTE*/PCA data. Spectra are plotted for the same dates as in Fig. 5, excluding the last one, which has very unreliable X-ray spectrum because of the strong background due to the Galactic ridge emission. The soft state at MJD 51665 data and the model are shown by red squares and the curve, the intermediate state at MJD 51676 (black symbols), and the hard state data at MJD 51688, 51697, and 51706 by blue triangles and by solid, dashed, and dotted curves, respectively. The blackbody component from the irradiated disc is shown in the OIR for the soft and intermediate states, while for the hard state only the flare component (same as in Fig. 5) is shown. The hard state OIR model spectra are somewhat arbitrarily connected to the power-law extrapolated from the X-ray data.

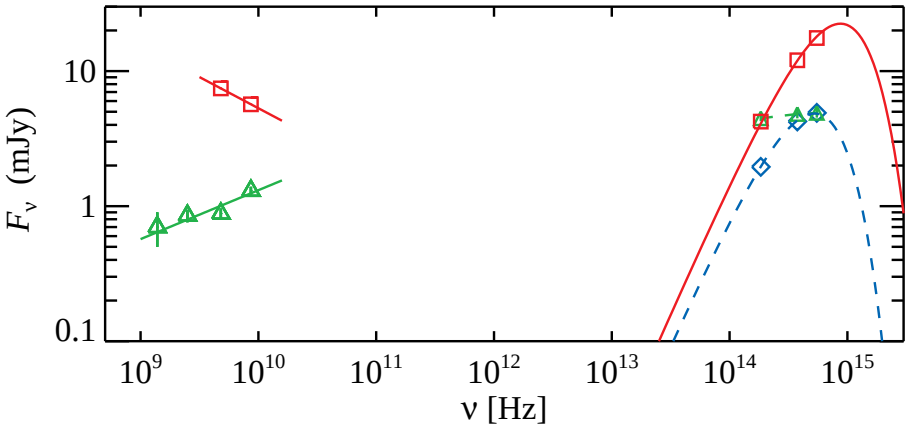

Figure 7. Broadband radio to optical spectral energy distribution of XTE J1550–564 at MJD 51665 (red squares) and 51697 (green triangles and blue diamonds). The radio data is taken from Corbel et al. (2001) and the OIR data from Jain et al. (2001a). We plot the blackbody with temperature and normalization as inferred from the light-curves and the CMD. The additional emission is due to the non-thermal component (shown with green symbols). In the soft state, the radio jet does not contribute at all to the OIR band, and in the hard state the flare OIR spectrum has a different slope $\alpha \approx 0$ that does not lie on the continuation of the radio power-law with $\alpha_{\rm radio} \approx 0.36$.

band. The weakness of the jet in the OIR band also implies that the jet cannot possibly contribute to the X-rays.

OIR flares were observed in a number of BH X-ray binaries. It was noticed that the beginning of the flare nearly coincides with the radio brightening (Kalemci et al. 2013). We find that the position of XTE J1550–564 at the X-ray hardness-flux diagram at the times of quenching/recovery of the OIR non-thermal component (see Fig. 1c) closely resembles the "jet line" (Belloni et al. 2011). This coincidence can be interpreted in two alternative ways: (i) both OIR and radio emission originate from one component (jet), or (ii) both are causally connected, but originate in different places. As we showed above, the first interpretation is at odds with the spectral evolution of the OIR flare. In the second interpretation, the OIR flare may originate in the geometrically thick hot flow (see below), while the radio is produced in the jet. The coincidence can be interpreted as a simultaneous appearance of the hot flow and the jet. This is indeed expected as in modern MHD simulations the jet seems to form only if there is collimation by a geometrically thick accretion flow. In the soft state, when the cold, geometrically thin disc extends all the way to the innermost stable orbit, the jet is weak.

4.2 Hot accretion flow

It was usually assumed that the electrons in the hot flow follow thermal distribution and in that case synchrotron emission in luminous BH X-ray binaries cannot possibly be of importance (Wardziński & Zdziarski 2000), because of strong self-absorption. However, even if the flow contains a small, energetically unimportant tail of non-thermal electrons, situation changes dramatically, as the synchrotron luminosity increases by orders of magnitude (Wardziński & Zdziarski 2001; Veledina et al. 2013b). This results in two effects: firstly, the seed photons for Comptonization in the hot flow now can be dominated by the non-thermal synchrotron instead of the cold truncated accretion disc (Malzac & Belmont 2009; Poutanen & Vurm 2009) and, secondly, the synchrotron radiation can dominate the OIR emission from the BH (Veledina et al. 2013b; Poutanen & Veledina 2014). The range of wavelengths where the hot flow emits is determined by its size: the larger is the truncation radius of the cold accretion disc, the lower is the frequency where synchrotron radiation is still not absorbed. The self-absorption (turn-over) frequency is (Veledina et al. 2013b)

$$\nu_{\rm t} \approx 3\times10^{15}(B/10^6\ {\rm G})^{\frac{p+2}{p+4}}\,[\tau(p-1)]^{\frac{2}{p+4}}\ {\rm Hz}, \qquad (12)$$

where B is the magnetic field strength, τ is the Thomson optical depth of non-thermal electrons and p is the slope the electron distribution.

For the radial dependences $B\propto R^{-\beta}$ and $\tau\propto R^{-\theta}$ the self-absorption frequency scales as $\nu_{\rm t}\propto R^{-[\beta(p+2)+2\theta]/(p+4)}$ and the total OIR spectrum from a hot flow is composed of contributions of synchrotron peaks (in partially opaque regime) coming from different radii. The hot flow spectrum constitutes a power-law with the spectral index (Veledina et al. 2013b)

$$\alpha_{\rm OIR} = \frac{5\theta+\beta(2p+3)-2p-8}{\beta(p+2)+2\theta}. \qquad (13)$$

At frequencies above $\nu_{\rm t}$ for the smallest, most compact zone of the accretion disc, the synchrotron spectrum is optically thin with $\alpha=-(p-1)/2$. If the optical depth of thermal electrons is high enough, thermal Comptonization can dominate completely over the optically thin synchrotron, the latter therefore might be invisible in the total spectrum. At frequencies below the self-absorption frequency for the largest, most transparent zone, the spectrum is optically thick with $\alpha=5/2$.

Below we follow the hybrid hot flow scenario as described in details in Veledina et al. (2013b). We discuss now how it can explain the broad-band spectrum and the features seen in the CMD. We also discuss what are the implications for the physical parameters in the vicinity of the BH.

4.2.1 Broad-band spectrum

The broad-band OIR-to-X-ray spectra in the soft and intermediate states are fully consistent with the standard accretion disc with the addition of the emission from non-thermal/hybrid electrons in the hard X-rays and the irradiated disc in the OIR band (see Fig. 6). The X-ray non-thermal emission can presumably be associated with the corona above the accretion disc, as in these states the hot inner flow either is non-existent or very small. Because of high luminosity of the standard disc, electron cooling is dominated by Compton scattering, hence the synchrotron component from the corona is negligible. Indeed, there are no any signatures of this emission in the OIR band.

In the hard state, the whole OIR to X-ray spectrum can be explained by a synchrotron self-Compton model where the synchrotron emission from non-thermal electrons is Comptonized by the thermal population of electrons (Poutanen & Vurm 2009; Veledina et al. 2013b). At the beginning of the hard state (MJD 51688), the accretion rate $\dot{M}$ is high, the synchrotron self-absorption frequency of the innermost zone is at $\approx 3\times10^{15}$Hz (corresponding to $B\sim10^6$ G and $\tau\sim1$, see equation (12)), while $\nu_{\rm t}\sim3\times10^{14}$ Hz for the outermost zone of the hot flow resulting in a break to harder spectrum below that frequency. This explains a fact that the extrapolation of the X-ray power-law overpredicts the OIR flux (solid blue lines in Fig. 6). Later in the hard state, during the peak of the OIR flare (on MJD 51697), $\dot{M}$ and therefore B and τ have dropped, the hot flow has grown in size and $\nu_{\rm t}$ for both inner- and outermost zones have decreased. This results in a flat power-law spectrum in the OIR band (see dashed blue lines in Fig. 6 and the SH transition in Fig. 8 for a schematic presentation of the spectral evolution). Because at lower $\dot{M}$ the total optical depth has likely decreased, the synchrotron peak became more pronounced. Later in the hard state (on MJD 51706; dotted blue lines in Fig. 6), when the optical depth in the hot flow drops further, the OIR/X-ray spectrum cannot be represented by a broken power-law any longer. Instead, it seems that there are two bumps in the OIR and the X-rays (similar to the spectra of blazars). Such double-peaked spectra are generally expected in the hot flow scenario at luminosities below a few per cent of the Eddington, at low optical depths (see fig. 6 in Narayan et al. 1998 and fig. 5 in Veledina et al. 2011b).

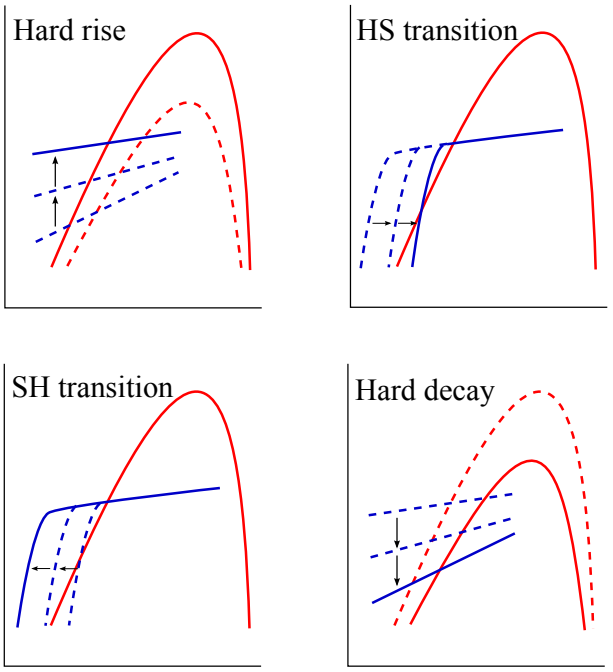

Figure 8. The schematic evolution of the OIR spectra of the irradiated disc and the flare components from the hot flow during the outburst. At the rising phase of the outburst, in the hard state, the disc temperature is steadily growing together with the luminosity of the non-thermal component. At the hard-to-soft transition, the X-ray luminosity is nearly constant resulting in a nearly constant disc emission; the hot flow size shrinks affecting the synchrotron self-absorption frequency, which is increasing. At the soft state (not shown here), the non-thermal synchrotron component may not exist at all, because the hot flow has disappeared. At the soft-to-hard transition, the hot flow appears and its size steadily grows resulting in a rapid evolution of the self-absorption frequency. In the following hard state, the X-ray as well as the disc luminosity drop; the non-thermal component decays even faster and becomes harder.

4.2.2 Horizontal tracks in CMD

The OIR spectrum of the hot flow constitutes a power-law, which extends down to the self-absorption frequency $\nu_{\rm t}$ of the outermost parts. During the rising phase of the outburst, the cold accretion disc shrinks, gradually replacing the hot flow at smaller and smaller radii. Thus $\nu_{\rm t}$ shifts to higher frequencies (see Fig. 8). Once the $\nu_{\rm t}$ crosses the H-filter, the emission at these wavelengths becomes self-absorbed and further, even rather small increase of the transition frequency results in rapid decrease of the H-flux. At the same time, the V filter experiences minor changes, until the $\nu_{\rm t}$ reaches it. At the decay phase of the outburst, the cold disc recedes, thus the transition frequency moves towards longer wavelengths, and the rapid flux increase in H filter occurs. This behaviour naturally explains the horizontal tracks we see in the CMDs (Fig. 4).

The V–I CMD (Fig. 4c) also shows a nearly horizontal movement but to the left of the blackbody track in the end of the soft-to-hard transition corresponding to the hardening of the spectrum. This is a natural consequence of the appearance of a hard hot flow component which compensates the decreasing disc flux in the V-filter but does not contribute much to the I-filter.

It is interesting to note that the horizontal tracks appear at different luminosities. These levels correspond to a factor of 1.35 difference in the outer accretion disc temperature, while the X-ray hard-to-soft and soft-to-hard transitions occur at luminosities that differ by a factor of 3. This is consistent with a simple relation $T_{\rm eff} \propto L_{\rm X}^{1/4}$. Thus, the horizontal tracks in the OIR CMDs and the X-ray hysteresis loop are both manifestation of the same phenomenon. We finally note that the hot flow emission in the OIR band disappears/appears in the intermediate states at the rising and decaying stages of the outburst around MJD 51659 and 51683, respectively (see Fig. 4b,c), at a similar X-ray hardness (see Fig. 1c). This strongly argues in favour of a similar truncation radius of the cold disc at these moments in spite of a factor of three difference in X-ray luminosity.

4.2.3 $I-H$ hook

At the hard-to-soft transition, when the cold disc truncation radius decreases, hot flow model predicts a quenching of the emission at longer wavelengths before that at shorter wavelengths. For instance, quenching the emission in the H filter results in a rapid colour change at an almost constant I-magnitude, as indeed seen in the I versus $I-H$ CMD (Fig. 4b). Then, quenching of the emission in I filter is expected, however, it is more difficult to see in this diagram, because both the magnitude and the colour change, at the same time the thermal emission is increased, partially compensating for the drop in I filter. The behaviour is tentatively seen in Fig. 4(b), where the return to the blackbody track goes along the horizontal line (at constant I), then the I flux also decreases. However, due to large error bars and small number of data points, the evolution is also consistent with a decrease of the emission in both filters, I and H.

The situation is different at the reverse, soft-to-hard transition. With receding cold disc, the hot flow emission is recovered at shorter wavelengths before longer wavelengths. We thus expect the evolution to proceed as follows: first, the spectrum follows a cooling blackbody, then the I flux increases, thus both colour and magnitude change in the opposite direction (towards upper left in Fig. 4b), then the H flux increases and the horizontal track appears. Such a behaviour is indeed seen as a hook at the $I-H$ CMD. The rise of the emission in the I filter before the H filter cannot be accounted for by the jet model. It is thus a good proxy for discriminating between the jet and the hot flow scenario.

4.2.4 Hot flow size and radial structure

When the OIR flare becomes visible in the very beginning of the hard state at the decaying stage of the outburst, the non-thermal component has spectral index $\alpha_{IH} \approx 1$, which is smaller than the value 2.5 corresponding to the self-absorbed spectrum. This indicates that $\nu_{\rm t}$ lies between the I and H filters. Approximating the hot flow spectrum at these wavelengths with a broken power-law (see Fig. 5), we obtain $\nu_{\rm t} \approx 3 \times 10^{14}$ Hz, from which we can infer the hot flow size at this moment of time. Using equation (13) of Veledina et al. (2013b), which was derived under an assumption of power-law radial dependences of the magnetic field strength and the electron density, we get

$$R = 3 \times 10^{22}/\nu_{\rm t} \approx 10^8 \text{ cm} \approx 35 R_{\rm S}, \quad (14)$$

where $R_{\rm S} = 2GM/c^2 = 2.7 \times 10^6$ cm is the Schwarzschild radius of the $9.1 M_\odot$ BH. This value should be considered as a rough estimate, to be improved by detailed spectral modelling.

We find that the non-thermal spectrum does not stay power-law of one particular spectral index, but is hardening towards the end of the flare. According to equation (13), α depends on indices θ, β and p. Let us assume that changes in α are predominantly caused by changes in the radial distribution of the optical depth, while β is fixed at a value of 5/4 for advective flows (Shadmehri & Khajenabi 2005). For softest $\alpha = 0.0$ and hardest $\alpha = 1.0$, we obtain a change of θ from ~ 0.55 to 3.0 if we fix $p = 3$ (the precise value has minor effect on the results). The value of θ for the soft spectrum is similar to that found in ADAF flows (Kato et al. 2008), however, the value obtained from the hard spectrum is quite an extreme, as it requires a highly inhomogeneous configuration. We should remember, however, that here θ describes the distribution of non-thermal electrons, not their bulk. Thus, high values of θ might imply that electron acceleration is not efficient at large radii. If instead we choose to fix $\theta = 0.5$, we get $\beta = 1.3$ for the soft spectrum (which is close to the standard value in ADAFs), while for the hard spectrum we get $\beta = 3.1$, again suggesting an extreme stratification of the magnetic field strength. In reality, the structure of both the magnetic field and the optical depth is likely to change when the accretion rate decreases, with the general trend, apparent from the above exercise, such that the flow becomes more stratified with strong gradients.

5 SUMMARY

We have carefully analysed the OIR and X-ray light curves of XTE J1550–564. From the e-folding times in different wavebands, we obtained the outer accretion disc temperature in excess of 15 000 K during the soft/intermediate states. Using this temperature together with the extreme OIR colours observed from XTE J1550–564, we put strong constraints on the extinction towards the source, $5.0 \lesssim A_V \lesssim 5.6$. This allowed us to relate the observed OIR colours to the slopes of the intrinsic spectrum.

During the soft state, the OIR spectrum is well described by the blackbody (associated with the irradiated disc) of exponentially decaying temperature and a constant normalization, while during the X-ray state transitions and the hard states, strong non-thermal flares are observed. By interpolating the decaying flux of thermal emission to the hard state, we have accurately separated the contribution of the flare from the disc. Importantly, the spectrum of the subtracted thermal component was shown to be consistent with the blackbody of the same normalization as before the flare. We further demonstrated how the spectrum of the non-thermal component evolves. On the decaying phase of the outburst, the flare starts with an apparent break in the power-law spectrum that is harder in the near-IR with $\alpha \approx 1$. The spectrum then becomes a power-law and softens to $\alpha \approx 0$ at the peak of the flare. It hardens again as the source fades. In the hybrid hot flow scenario, this hardening possibly indicates that the electron acceleration is not efficient at large radii at low accretion rates.

The evolution of the spectral shape is consistent with the hot accretion flow scenario, where the size of the flow varies with the accretion rate. In the hard state, the flow is large and the OIR spectrum constitutes a power-law. During the hard-to-soft transition, the flow collapses and the low-energy spectral cutoff (corresponding to the synchrotron self-absorption frequency) moves from the infrared to the UV. In the soft state, the hot flow may not exist at all and its non-thermal emission is quenched. At the reverse transition, the cold disc retreats and the hot flow grows in size leading to an increase of the contribution of the non-thermal component from the hot flow to the OIR spectrum and strong reddening of the source. This transition occurs at a lower accretion rate which manifests itself as the hysteresis loop in the X-ray hardness-flux diagram and as different levels of the horizontal tracks in the OIR CMDs. We find that quenching and recovery of the hot flow OIR emission occurs at about the same X-ray hardness during the intermediate state. The position of the source at the at the X-ray hardness - flux diagram when this happens (the hot flow line) seems to coincide with the jet line that marks the presence of the compact radio jet. This implies a close connection between the presence of the hot flow and the compact jet. We roughly estimate the hot flow size, at the moment when OIR flare starts to be visible in the light curves, to be 10^8cm $\approx 35 R_{\rm S}$.

ACKNOWLEDGEMENTS

The work was supported by the Finnish Doctoral Programme in Astronomy and Space Physics (AV), the Academy of Finland grant 268740 (JP) and the Russian Science Foundation grant RNF 14-12-01287 (MGR). We thank David Russell for useful discussions and the OIR data on XTE J1550–564, Charles Bailyn for information about the filters used at the Yale telescope, and Vitaly Neustroev for information on photometric standards. This research has made use of data provided by the High Energy Astrophysics Science Archive Research Center (HEASARC), which is a service of the Astrophysics Science Division at NASA/GSFC and the High Energy Astrophysics Division of the Smithsonian Astrophysical Observatory.

REFERENCES

Arnaud K. A., 1996, in Jacoby G. H., Barnes J., eds, ASP Conf. Ser. Vol. 101, Astronomical Data Analysis Software and Systems V. Astron. Soc. Pac., San Francisco, p. 17
Basko M. M., Sunyaev R. A., Titarchuk L. G., 1974, A&A, 31, 249
Belloni T. M., Motta S. E., Muñoz-Darias T., 2011, Bull. Astron. Soc. India, 39, 409
Bessell M. S., Castelli F., Plez B., 1998, A&A, 333, 231
Blandford R. D., Königl A., 1979, ApJ, 232, 34
Cardelli J. A., Clayton G. C., Mathis J. S., 1989, ApJ, 345, 245
Castelli F., Kurucz R. L., 2004, astro-ph/0405087
Chaty S., Haswell C. A., Malzac J., Hynes R. I., Shrader C. R., Cui W., 2003, MNRAS, 346, 689

Coppi P. S., 1999, in Poutanen J., Svensson R., eds, ASP Conf. Ser. Vol. 161, High Energy Processes in Accreting Black Holes. Astron. Soc. Pac., San Francisco, p. 375
Corbel S. et al., 2001, ApJ, 554, 43
Corbel S., Tomsick J. A., Kaaret P., 2006, ApJ, 636, 971
Cunningham C., 1976, ApJ, 208, 534
de Jong J. A., van Paradijs J., Augusteijn T., 1996, A&A, 314, 484
Dickey J. M., Lockman F. J., 1990, ARA&A, 28, 215
Dubus G., Hameury J.-M., Lasota J.-P., 2001, A&A, 373, 251
Durant M., Gandhi P., Shahbaz T., Fabian A. P., Miller J., Dhillon V. S., Marsh T. R., 2008, ApJ, 682, L45
Eggleton P. P., 1983, ApJ, 268, 368
Endal A. S., Devinney E. J., Sofia S., 1976, Ap. Letters, 17, 131
Frank J., King A., Raine D. J., 2002, Accretion Power in Astrophysics. Cambridge Univ. Press, Cambridge
Gallo E., Migliari S., Markoff S., Tomsick J. A., Bailyn C. D., Berta S., Fender R., Miller-Jones J. C. A., 2007, ApJ, 670, 600
Gandhi P. et al., 2010, MNRAS, 407, 2166
Gelino D. M., Gelino C. R., Harrison T. E., 2010, ApJ, 718, 1
Gierliński M., Done C., Page K., 2009, MNRAS, 392, 1106
Gierliński M., Zdziarski A. A., Poutanen J., Coppi P. S., Ebisawa K., Johnson W. N., 1999, MNRAS, 309, 496
Hynes R. I., Haswell C. A., Chaty S., Shrader C. R., Cui W., 2002, MNRAS, 331, 169
Hynes R. I., Mauche C. W., Haswell C. A., Shrader C. R., Cui W., Chaty S., 2000, ApJ, 539, L37
Jahoda K., Markwardt C. B., Radeva Y., Rots A. H., Stark M. J., Swank J. H., Strohmayer T. E., Zhang W., 2006, ApJS, 163, 401
Jain R. K., Bailyn C. D., Orosz J. A., McClintock J. E., Remillard R. A., 2001a, ApJ, 554, L181
Jain R. K., Bailyn C. D., Orosz J. A., McClintock J. E., Sobczak G. J., Remillard R. A., 2001b, ApJ, 546, 1086
Jain R. K., Bailyn C. D., Orosz J. A., Remillard R. A., McClintock J. E., 1999, ApJ, 517, L131
Kalemci E., Dinçer T., Tomsick J. A., Buxton M. M., Bailyn C. D., Chun Y. Y., 2013, ApJ, 779, 95
Kanbach G., Straubmeier C., Spruit H. C., Belloni T., 2001, Nature, 414, 180
Kato S., Fukue J., Mineshige S., 2008, Black-Hole Accretion Disks — Towards a New Paradigm. Kyoto University Press, Kyoto
Königl A., 1981, ApJ, 243, 700
Lasota J.-P., 2001, New Astron. Rev., 45, 449
Magdziarz P., Zdziarski A. A., 1995, MNRAS, 273, 837
Malzac J., Belmont R., 2009, MNRAS, 392, 570
Miller J. M. et al., 2003, MNRAS, 338, 7
Narayan R., Mahadevan R., Quataert E., 1998, in Abramowicz M. A., Bjornsson G., Pringle J. E., eds, Theory of Black Hole Accretion Disks. Cambridge University Press, Cambridge, p. 148
O'Donnell J. E., 1994, ApJ, 422, 158
Orosz J. A., Steiner J. F., McClintock J. E., Torres M. A. P., Remillard R. A., Bailyn C. D., Miller J. M., 2011, ApJ, 730, 75
Poutanen J., Coppi P. S., 1998, Phys. Scr., T77, 57
Poutanen J., Svensson R., 1996, ApJ, 470, 249
Poutanen J., Veledina A., 2014, SSRv, in press (arxiv:1312.2761)
Poutanen J., Vurm I., 2009, ApJ, 690, L97
Predehl P., Schmitt J. H. M. M., 1995, A&A, 293, 889
Revnivtsev M., Sazonov S., Gilfanov M., Churazov E., Sunyaev R., 2006, A&A, 452, 169
Russell D. M., Maitra D., Dunn R. J. H., Fender R. P., 2011, MNRAS, 416, 2311
Russell D. M., Maitra D., Dunn R. J. H., Markoff S., 2010, MNRAS, 405, 1759
Sánchez-Fernández C. et al., 1999, A&A, 348, L9
Shadmehri M., Khajenabi F., 2005, MNRAS, 361, 719
Shakura N. I., Sunyaev R. A., 1973, A&A, 24, 337
Suleimanov V., Meyer F., Meyer-Hofmeister E., 1999, A&A, 350, 63
Tomsick J. A., Corbel S., Kaaret P., 2001, ApJ, 563, 229
van Paradijs J., McClintock J. E., 1995, in Lewin W. H. G., van Paradijs J., van den Heuvel E. P. J., eds, Cambridge Astroph. Ser. No. 26. X-ray binaries. Cambridge Univ. Press, Cambridge, p. 58
Veledina A., Poutanen J., Ingram A., 2013a, ApJ, 778, 165
Veledina A., Poutanen J., Vurm I., 2011a, ApJ, 737, L17
Veledina A., Poutanen J., Vurm I., 2013b, MNRAS, 430, 3196
Veledina A., Vurm I., Poutanen J., 2011b, MNRAS, 414, 3330
Wardziński G., Zdziarski A. A., 2000, MNRAS, 314, 183
Wardziński G., Zdziarski A. A., 2001, MNRAS, 325, 963
Warner B., 1995, Cataclysmic variable stars, Cambridge Astroph. Ser. No. 28. Cambridge Univ. Press, Cambridge
Xue Y., Wu X.-B., Cui W., 2008, MNRAS, 384, 440
Yuan F., Zdziarski A. A., Xue Y., Wu X.-B., 2007, ApJ, 659, 541
Zdziarski A. A., Gierliński M., 2004, Prog. Theor. Phys. Suppl., 155, 99

Monthly Notices
of the
ROYAL ASTRONOMICAL SOCIETY

Mon. Not. R. Astron. Soc. **414,** 3330–3343 (2011) doi:10.1111/j.1365-2966.2011.18635.x

A self-consistent hybrid Comptonization model for broad-band spectra of accreting supermassive black holes

Alexandra Veledina,[1⋆] Indrek Vurm[1,2,3] and Juri Poutanen[1]

[1]*Astronomy Division, Department of Physics, PO Box 3000, FIN-90014 University of Oulu, Finland*
[2]*Racah Institute of Physics, Hebrew University of Jerusalem, 91904 Jerusalem, Israel*
[3]*Tartu Observatory, 61602 Tõravere, Tartumaa, Estonia*

Accepted 2011 March 2. Received 2011 March 2; in original form 2010 November 23

ABSTRACT

The nature of the broad-band spectra of supermassive accreting black holes in active galactic nuclei (AGNs) is still unknown. The hard X-ray spectra of Seyferts as well as of Galactic stellar-mass black holes (GBHs) are well represented by thermal Comptonization, but the origin of the seed photons is less certain. The MeV tails observed in GBHs provide evidence in favour of non-thermal electron tails and it is possible that such electrons are also present in the X-ray-emitting regions of AGNs.

Using simulations with the kinetic code that self-consistently models electron and photon distributions, we find that the power-law-like X-ray spectra in AGNs can be explained in terms of the synchrotron self-Compton radiation of hybrid thermal/non-thermal electrons, similarly to the hard/low state of GBHs. Under a very broad range of parameters, the model predicts a rather narrow distribution of photon spectral slopes consistent with that observed from low-ionization nuclear emission-line regions and Seyferts at luminosities less than 3 per cent of the Eddington luminosity. The entire infrared to X-ray spectrum of these objects can be described in terms of our model, suggesting a tight correlation between the two energy bands. We show that the recently found correlation between the slope and the Eddington ratio at higher luminosities can be described by the increasing fraction of disc photons in the emitting region, which may be associated with the decreasing inner radius of the optically thick accretion disc. The increasing flux of soft photons is also responsible for the transformation of the electron distribution from nearly thermal to almost completely non-thermal. The softer X-ray spectra observed in narrow-line Seyfert galaxies may correspond to non-thermal Comptonization of the disc photons, predicting that no cut-off should be observed up to MeV energies in these sources, similarly to the soft-state GBHs.

Key words: accretion, accretion discs – radiation mechanisms: non-thermal – galaxies: Seyfert – X-rays: galaxies.

1 INTRODUCTION

Accreting radio-quiet supermassive black holes (SMBHs) residing in the centres of quasars, Seyfert galaxies, narrow-line Seyfert 1 galaxies (NLSy1s) and some fraction of low-ionization nuclear emission-line regions (LINERs) in many respects are analogous to the Galactic stellar-mass black holes (GBHs) in X-ray binaries. In the X-ray/soft γ-ray band, the spectra of Seyferts can be represented by a sum of a power-law-like continuum which cuts off at a few hundred keV and a reflection component with the iron fluorescent Kα line believed to be produced by reprocessing the intrinsic power law by cold opaque matter, probably the accretion disc (Nandra & Pounds 1994). The 2–10 keV intrinsic spectral energy slope (defined as $F_E \propto E^{-\alpha}$) of the power law $\alpha \sim 0.9$–1.0, which is ubiquitously found in Seyferts, is somewhat larger than what is measured in GBHs in their hard state $\alpha \sim 0.6$–0.8 (e.g. Zdziarski, Lubinski & Smith 1999). NLSy1s having softer X-ray spectra than Seyferts probably represent a state with higher accretion rate (in Eddington units) similar to the soft/very high state of GBHs (Pounds, Done & Osborne 1995).

The seemingly similar X-ray slopes of Seyferts triggered the efforts to find a physical model which would explain such spectral stability. The non-thermal models became popular (see Svensson 1994, for a review). These invoke the injection of high-energy leptons into the system with subsequent Compton cooling by accretion disc photons and photon–photon pair productions initiating pair cascades. Saturated cascades produce intrinsic spectra with $\alpha \approx 0.9$

⋆E-mail: alexandra.veledina@oulu.fi

(Zdziarski & Lightman 1985; Svensson 1987), which become consistent with the X-ray spectra of Seyferts after accounting for the hardening due to Compton reflection (George & Fabian 1991). The pair-cascade models, on the other hand, predict a strong tail above 300 keV and an annihilation line which have never been observed. The *CGRO*/OSSE observations of the brightest Seyfert 1 galaxy NGC 4151 constrain the fraction of the energy going to non-thermal injection to be less than 50 per cent, while the rest of the power going to thermal heating (Zdziarski, Lightman & Maciolek-Niedzwiecki 1993; Zdziarski, Johnson & Magdziarz 1996). The existing upper limits on the average flux of Seyferts above 100 keV are compatible with the presence of weak non-thermal tails (e.g. Gondek et al. 1996; Johnson et al. 1997). The more recent *INTEGRAL* observations (Lubiński et al. 2010) have not improved those constraints.

The non-detectable high-energy tail in Seyfert galaxies can also be interpreted in terms of pure thermal models, where the power is equally shared among all the thermal particles. The spectra indeed can be well described by Comptonization on *thermal* 50–150 keV electrons (see e.g. Zdziarski et al. 1997; Poutanen 1998; Zdziarski 1999). The stability of the spectral slopes can be interpreted as the evidence of the radiative feedback between the hot X-ray-emitting plasma and the cool accretion disc, which is assumed to be a sole source of the seed photons for Comptonization. The slab–corona model, where the hot plasma sandwiches the accretion disc (see e.g. Haardt & Maraschi 1991, 1993), predicts too soft spectra due to large flux of the reprocessed ultraviolet (UV) photons (Stern et al. 1995). Malzac, Dumont & Mouchet (2005) showed that the hard spectrum can be achieved if one assumes a large ionization parameter of the disc, but in this case the model fails on the predicted reflection properties. Localized active regions atop a cool disc (Haardt, Maraschi & Ghisellini 1994; Stern et al. 1995; Poutanen & Svensson 1996; Svensson 1996) are more photon-starved and can produce much harder spectra in agreement with observations. However, in this case, it is difficult to understand why there is a preferential slope, as it is a strong function of the separation of the active region from the disc.

The detection of the MeV tails in the spectra of the GBH Cyg X-1 in both hard and soft states (McConnell et al. 2002) implies the presence of a significant non-thermal component in the electron distribution. The power-law-looking spectra extending to the MeV energies in other soft-state GBHs (Grove et al. 1998; Zdziarski et al. 2001) are consistent with being produced by non-thermal Comptonization (Poutanen & Coppi 1998; Poutanen 1998). By analogy, the electrons in Seyferts also might have a non-thermal population. More probably, in both types of sources, the electron distribution is hybrid in both hard and soft states (Poutanen & Coppi 1998; Poutanen 1998; Coppi 1999), with the non-thermal fraction increasing for softer spectra. However, non-thermal particles could be spatially separated from the thermal ones.

The presence of the non-thermal particles, even if they are not energetically dominant, has a strong impact on the emitted spectrum, because the synchrotron emission can increase by orders of magnitude even if only 1 per cent of the electron energy is in the power-law tail (Wardziński & Zdziarski 2001). As most of the synchrotron emission is self-absorbed, this process plays an important role in shaping the electron distribution by thermalizing particles via the emission and absorption of synchrotron photons, the so-called synchrotron boiler (Ghisellini, Guilbert & Svensson 1988; Ghisellini, Haardt & Svensson 1998).

It was recently shown that under the conditions of GBHs, Coulomb collisions and the synchrotron boiler efficiently thermalize electrons producing a thermal population at low energies even if the electrons were originally non-thermal (Vurm & Poutanen 2008; Malzac & Belmont 2009; Poutanen & Vurm 2009). The hard spectrum of GBHs can be fully accounted for by the synchrotron self-Compton (SSC) mechanism in the resulting hybrid electrons. In this picture, the disc photons are not required to interact with the hot X-ray-emitting plasma at all. This mechanism also gives a rather stable X-ray slope for a large range of parameters, relieving the need for the feedback between the disc and the active region.

As many of the radiative processes depend only on the compactness of the source, but not on its luminosity or size separately, one may think that the spectra of Seyferts can also be described in terms of hybrid Comptonization models. However, not all processes can be scaled away. The aim of this paper is to study in details the spectral formation in relativistic hybrid plasmas in the vicinity of a SMBH. One of our goals is to learn how the results scale with the mass of the compact object. We also test the role of bremsstrahlung in SSC models and, finally, we compare the model with the data on Seyferts and NLSy1s.

2 MODEL DESCRIPTION

2.1 Geometry

It is commonly accepted that the main process responsible for X-ray spectra of radio-quiet active galactic nuclei (AGNs) is (nearly) the thermal Comptonization of soft seed photons by energetic electrons. The nature of the seed photons is less understood. The two main candidates are the standard cool accretion disc (Shakura & Sunyaev 1973) and the synchrotron emission from the hot electron populations. We model both types of seed photon sources.

The geometry of the X-ray-emitting region also remains unclear. It can be the inner hot part of the accretion flow which can be radiatively inefficient as well as efficient (see reviews in Narayan, Mahadevan & Quataert 1998; Yuan 2007). The disc–corona models are also popular (Galeev, Rosner & Vaiana 1979; Haardt & Maraschi 1991, 1993; Haardt et al. 1994; Stern et al. 1995; Poutanen & Svensson 1996; Poutanen 1998). The slab (plane-parallel) corona (Haardt & Maraschi 1991, 1993) is unlikely to be realized, as it produces Comptonization spectra which are too soft compared to the observed $\alpha \sim 1$ (Stern et al. 1995). The corona can also be patchy and consist of isolated active regions atop a cool accretion disc (Galeev et al. 1979; Haardt et al. 1994; Stern et al. 1995). This kind of geometry can produce spectra of almost arbitrary hardness if only soft photons reprocessed in the disc are considered. The corona does not need to be static, but can have a substantial bulk velocity away from the disc or towards it (Beloborodov 1999b). In this work, we consider a spherically symmetric region, which can be either the inner hot part of the accretion flow or a blob of the gas above the accretion disc. No anisotropy in geometry or seed photons is taken into account.

2.2 Main parameters

In most of the simulations, we assumed that the active region has a size of $R = 10R_{\rm S}$, where $R_{\rm S} = 2GM_{\rm BH}/c^2$ is the Schwarzschild radius of the black hole of mass $M_{\rm BH}$, as one can expect most of the energy to be liberated within a region of a corresponding size. It is convenient to introduce a compactness parameter, which is independent of the black hole mass:

$$l_{\rm inj} = \frac{L_{\rm inj}}{R}\frac{\sigma_{\rm T}}{m_{\rm e}c^3} \simeq 10^3 \frac{L_{\rm inj}}{L_{\rm Edd}}\frac{10R_{\rm S}}{R}, \quad (1)$$

where $L_{\rm Edd} = 4\pi\mu_{\rm e} G M_{\rm BH} m_{\rm p} c/\sigma_{\rm T} = 1.3 \times 10^{38} M_{\rm BH}/{\rm M}_\odot \ {\rm erg\ s^{-1}}$, $\sigma_{\rm T}$ is the Thomson cross-section, $\mu_{\rm e} = 2/(1+X)$ and X is the hydrogen fraction.

The importance of synchrotron processes is determined by the magnetization parameter $\eta_B = U_B R^2 c/L_{\rm inj}$, where $U_B = B^2/(8\pi)$ is the magnetic energy density and $L_{\rm inj} \approx \frac{4\pi}{3} R^2 c U_{\rm rad}$ ($U_{\rm rad}$ is the radiation energy density). The equipartition of magnetic and radiation energy densities occurs at $\eta_B \approx 0.25$. The magnetic field can be expressed in terms of adopted parameters as

$$B = \left(\frac{8\pi m_{\rm e} c^2}{\sigma_{\rm T}} \frac{\eta_B l_{\rm inj}}{R}\right)^{1/2} \approx 10^3 \left(\frac{\eta_B l_{\rm inj}}{M_7 R/10 R_{\rm S}}\right)^{1/2} {\rm G}, \quad (2)$$

where $M_7 = M_{\rm BH}/10^7\,{\rm M}_\odot$.

We assume that the released energy is given to the electrons. The transfer of energy is modelled as a power-law injection: $dN_{\rm e}/(dt\ d\gamma) \propto \gamma^{-\Gamma_{\rm inj}}$ extending from the low-energy Lorentz factor $\gamma_{\rm le} = 1.0$ to high-energy cut-off at $\gamma_{\rm he} = 10^3$. The Thomson optical depth of the electrons is chosen at the beginning and fixed during each simulation, that is, the number of particles is conserved. The injected electrons increase the optical depth; therefore, to keep it constant throughout the simulations, the same amount of electrons is removed from the system. This action simulates the effect of re-acceleration. The total luminosity of the system L is equal to the net power $L_{\rm inj} = \frac{4\pi}{3} R^3 \dot{N}_{\rm e} (\overline{\gamma}_{\rm inj} - \overline{\gamma}_{\rm eq}) m_{\rm e} c^2$, where $\overline{\gamma}_{\rm inj}$ and $\overline{\gamma}_{\rm eq}$ are the mean Lorentz factors of the injected and the equilibrium distributions, respectively.

We also consider an additional source of soft photons from the accretion disc in the form of the blackbody radiation injected homogeneously to the system. The parameters that describe them are the temperature $T_{\rm d}$ and the ratio of the disc luminosity to the injected power $f = L_{\rm disc}/L_{\rm inj}$.

Thus, the main parameters of the model are the mass of the compact object, $M_{\rm BH}$, size of the active region, $R/R_{\rm S}$, magnetization parameter, η_B, Eddington ratio, $L/L_{\rm Edd}$, ratio f of the disc seed photon luminosity to the injected luminosity, injection slope, $\Gamma_{\rm inj}$, and the Thomson optical depth $\tau = R\sigma_{\rm T} n_{\rm e}$.

2.3 Characteristic time-scales

There are three time-scales important in our simulations: light-crossing time $t_{\rm lc}$, cooling time $t_{\rm cool}$ and re-acceleration time $t_{\rm ra}$.

The re-acceleration time is calculated for a given optical depth and required injection energy as

$$t_{\rm ra} = \frac{4\pi}{3} \frac{R}{c} \frac{\tau \overline{\gamma}_{\rm inj}}{l_{\rm inj}}, \quad (3)$$

corresponding to the average time of the removal of the electrons from the system (as modelled in the code). For large optical depth, the re-acceleration time is larger than the light-crossing time and thus it can be associated with the escape time. In the case of low optical depth, $t_{\rm ra} < t_{\rm lc}$, and it cannot be thought of as the escape time itself, but interpreted as the time between re-accelerations.

The synchrotron cooling time can be calculated as

$$t_{\rm cool,s} \equiv \frac{\gamma - 1}{|\dot{\gamma}_{\rm s}|} = \frac{1}{\gamma + 1} \left(\frac{4}{3} \frac{\sigma_{\rm T} U_B}{m_{\rm e} c}\right)^{-1} = \frac{1}{\gamma + 1} \frac{3}{4} \frac{R/c}{\eta_B l_{\rm inj}}, \quad (4)$$

where $\dot{\gamma}_{\rm s}$ is the synchrotron cooling rate. Similarly, one can determine the cooling time by Compton scattering (e.g. Rybicki & Lightman 1979):

$$t_{\rm cool,cs} \equiv \frac{\gamma - 1}{|\dot{\gamma}_{\rm cs}|} = \frac{1}{\gamma + 1} \left(\frac{4}{3} \frac{\sigma_{\rm T} U_{\rm rad}}{m_{\rm e} c}\right)^{-1} = \frac{1}{\gamma + 1} \frac{\pi R/c}{l_{\rm inj}}. \quad (5)$$

The ratio of the two time-scales is roughly

$$\frac{t_{\rm cool,s}}{t_{\rm cool,cs}} = \frac{U_{\rm rad}}{U_B} = \frac{3}{4\pi\eta_B}. \quad (6)$$

For most of the simulations, the synchrotron cooling time is comparable to (or more than) the Compton cooling time.

The e–e Coulomb losses at the equilibrium can be estimated as (e.g. Nayakshin & Melia 1998):

$$t_{\rm cool,Coul} \equiv \frac{\gamma - 1}{|\dot{\gamma}_{\rm Coul}|} \approx \frac{2R}{3c} \frac{\overline{\gamma}_{\rm eq}}{\tau \ln\Lambda} \frac{p^3}{\gamma(\gamma+1)}, \quad (7)$$

where $\ln\Lambda$ is the Coulomb logarithm (we take $\ln\Lambda = 16$). The bremsstrahlung cooling time is larger (approximately by the inverse of the fine structure constant $1/\alpha_{\rm fs} \approx 137$). At higher energies, the cooling is determined by radiative processes, while for lower energies non-radiative Coulomb collisions are dominant. The relevant scaling is

$$\frac{t_{\rm cool,Coul}}{t_{\rm cool,cs}} \approx \frac{2\overline{\gamma}_{\rm eq}}{3\pi \ln\Lambda} \frac{p^3}{\gamma} \frac{l_{\rm inj}}{\tau}. \quad (8)$$

The ratio of the synchrotron cooling and re-acceleration times can be approximated as ($\overline{\gamma}_{\rm inj} \approx 2$ in our simulations):

$$\frac{t_{\rm cool,s}}{t_{\rm ra}} \approx \frac{0.1}{\tau\eta_B} \frac{1}{\gamma + 1} \quad (9)$$

and the ratio of the Coulomb cooling to re-acceleration time can be written as

$$\frac{t_{\rm cool,Coul}}{t_{\rm ra}} \approx 5.6 \frac{\overline{\gamma}_{\rm eq} p^3}{\tau^2 \gamma(\gamma+1)} \left(\frac{L}{L_{\rm Edd}}\right) \left(\frac{R}{10 R_{\rm S}}\right)^{-1}. \quad (10)$$

As long as the optical depth is not too low, the average cooling time is less than the re-acceleration time. This condition is satisfied for the majority of simulations presented in this paper.

2.4 Radiative processes and numerical simulations

The gravitational energy released as matter goes down the potential well of the black hole heats the protons and can be transferred to electrons via various mechanisms, for instance, Coulomb collisions with protons, magnetic reconnection, collective plasma effects or shock acceleration. The accelerated electrons subsequently cool, producing a radiation field in the region. The presence of the latter strongly affects the electron distribution. Due to acceleration processes operating in the system, the electron distribution might not be Maxwellian. Even a small non-thermal tail (with the energy content of only 1 per cent) can significantly increase the net (after accounting for self-absorption) synchrotron emission up to $\sim 10^5$ times (Wardziński & Zdziarski 2001) and therefore affect the spectrum of the Comptonized component.

For a given particle distribution (Maxwellian, power law or hybrid), one can easily calculate the emission spectrum, but the former in turn depends on the radiation field. Thus, to find an equilibrium spectrum, which is self-consistent with the electron distribution, one has to solve coupled time-dependent kinetic equations for all the particle species present in the system.

The formal equilibrium solution of the kinetic equation for electrons, when cooling dominates over the escape, can be written as (Blumenthal & Gould 1970):

$$\frac{dN_{\rm eq}}{d\gamma} \propto \frac{1}{\dot{\gamma}} \int_{\gamma}^{\gamma_{\rm he}} \gamma'^{-\Gamma_{\rm inj}} d\gamma', \quad (11)$$

where $dN_{\rm eq}/d\gamma$ represents the equilibrium particle distribution and $\dot{\gamma}$ is the sum of all possible cooling rates. In the radiative (Compton

and synchrotron) cooling dominated regime, $\dot{\gamma} \propto \gamma^2$, while if the electrons exchange energies predominantly by Coulomb collisions, then $\dot{\gamma} \propto \gamma^0$. Substituting the cooling rates into equation (11) and integrating (hereinafter we consider $\Gamma_{\rm inj} \geq 2$), one gets the equilibrium electron distribution in the form $\mathrm{d}N_{\rm eq}/\mathrm{d}\gamma \propto \gamma^{-s}$ with

$$s = \begin{cases} \Gamma_{\rm inj} + 1, \ \dot{\gamma} \propto \gamma^2 \ \text{(Compton, synchrotron)} \\ \Gamma_{\rm inj} - 1, \ \dot{\gamma} \propto \gamma^0 \qquad \text{(Coulomb)}. \end{cases} \tag{12}$$

In a general case, it is necessary to account for particle heating and thermalization; therefore, it is impossible to find an analytical solution; the problem has to be solved numerically.

We consider electrons, positrons and photons. The neutrality of the plasma is provided by protons, which are assumed to be at rest and participate only in electron–proton bremsstrahlung. The following elementary processes are taken into account. The particles interact with each other via Coulomb (Møller/Bhabha) collisions. The cooling/heating of the electrons (and positrons) occurs by emitting and absorbing synchrotron radiation, bremsstrahlung emission (electron–proton, electron–electron, positron–positron, electron–positron) and Compton scattering. The seed soft photons for Compton scattering can be provided by the synchrotron as well as by the accretion disc. Photon–photon pair production and pair annihilation are also taken into account; however, these processes play a minor role for considered parameters.

We assume particle and photon distributions to be homogeneous and isotropic. The calculations are done in a one-zone geometry with a tangled magnetic field. The photon escape from the region is modelled by the escape probability formalism. The escaping photon distribution can be described by the differential luminosity $L_E = \mathrm{d}L/\mathrm{d}E$ or differential compactness $l_E = (l_{\rm inj}/L)\, L_E$.

To obtain the equilibrium spectrum, a system of time-dependent kinetic equations for the distribution functions of photons, electrons and positrons are solved using the code described in details by Vurm & Poutanen (2009), extended to include bremsstrahlung processes. This code is similar to the previous codes of that sort by Coppi (1992, 1999), but includes the synchrotron boiler (Ghisellini et al. 1988, 1998) and treats Coulomb thermalization more accurately due to a grid in electron momenta extended to low values. A code very similar to ours was recently developed by Belmont, Malzac & Marcowith (2008).

3 RESULTS

In this section, we present a detailed investigation of the features of equilibrium photon and electron distributions arising from variations in different parameters. We consider pure SSC models in Section 3.1. In Section 3.2, we investigate the role of bremsstrahlung in SSC models. Spectral formation with the contribution of the accretion disc photons is described in Section 3.3. Specific parameters of each simulation can be found in Table 1.

3.1 SSC models

Let us first consider pure SSC models putting $f = 0$, that is, with no contribution from the accretion disc. We study how variations in the parameters influence the spectral energy distribution (particularly, the slope α in the range 2–10 keV) and the electron distribution. For the fiducial parameters, we take $M_{\rm BH} = 10^7\,\mathrm{M}_\odot$, $\Gamma_{\rm inj} = 3.0$, $\tau = 1.0$, $\eta_B = 0.1$ and $L/L_{\rm Edd} = 10^{-2}$ (see Fig. 1, solid line). The equilibrium electron distribution consists of a Maxwellian part with $kT_{\rm e} = 93$ keV and a power-law tail with the slope determined by the radiative cooling $s = \Gamma_{\rm inj} + 1 = 4$. The synchrotron emission coming from thermal electrons is completely self-absorbed and the low-energy part of the spectrum arises from the synchrotron produced by a non-thermal electron population only (with Lorentz factors $\gamma \gtrsim 30$). On the other hand, the high-energy Comptonization component, cutting off at $\sim$100 keV, is mostly produced by the Maxwellian part of the electron distribution. Above the cut-off energy, there is a high-energy tail resulting from the Comptonization on the non-thermal electrons.

3.1.1 Dependence on the magnetic field

Let us consider the influence of the strength of magnetic field on spectral formation. The energy density of typical magnetic fields in the vicinity of black holes is assumed to be of the order of the equipartition with the radiation field or gas energy density (Galeev et al. 1979). In Fig. 1, the equilibrium spectra and electron distributions are shown for $\eta_B = 0.1$, 1.0 and 10. When the role of the magnetic field increases, it causes the increasing emission in the low-energy part of the spectrum, where the main contribution comes from the synchrotron mechanism. Subsequently, the electron cooling occurs faster (for the comparison with the re-acceleration time, see equation 9). This implies the decreasing role of inverse-Compton scattering on non-thermal electrons and thus leads to a weaker high-energy tail in the photon distribution. The resulting Comptonized spectrum becomes softer. As electrons lose more energy in synchrotron emission and cool more efficiently, the non-thermal tail drops and the thermal part of the distribution extends to higher energies. At the same time, the peak of the thermal distribution is determined by Coulomb processes; thus, the equilibrium temperature is independent of the magnetization. Although the electron temperatures are almost identical in these simulations, the slopes are different. This is due to the fact that the slope is determined by both thermal and non-thermal electron populations, with a harder spectral index in the case of a more powerful electron tail.

One can note in Fig. 1(b) that the normalization of the electron tail at $\gamma < 10$ does not scale inversely proportional to magnetization. The competing processes determining the normalization (and shape) of the high-energy tail are Compton and synchrotron cooling. Their relative role in tail formation is determined by the magnetization parameter (see equation 6). With the increasing role of the magnetic field, the cooling becomes dominated by synchrotron processes, and from this moment the normalization scales inversely with η_B. Also at high Lorenz factors, Compton scattering plays a less important role, because cooling occurs partially in Klein–Nishina regime.

3.1.2 Dependence on the mass

Variations in the mass correspond to variations of two parameters simultaneously: the Schwarzschild radius and the Eddington luminosity. If we fix the Eddington ratio and the size (in Schwarzschild radii), then the compactness parameter becomes independent of the mass. The spectral energy distribution l_E is not expected to change much. However, the temperature of the accretion disc photons as well as the magnetic field strength (and characteristic synchrotron frequencies) do depend on the mass.

If the seed photons for Comptonization come from an accretion disc, the size and disc temperature scale as $R \propto M_{\rm BH}$ and $T_{\rm d} \propto M_{\rm BH}^{-1/4}$, respectively (see e.g. Frank, King & Raine 2002). For the black holes with higher masses and the same compactness, the Comptonized spectrum becomes broader and the X-ray spectra of

Table 1. Model parameters and results.

Run	Figure	$M_{\rm BH}/{\rm M}_\odot$	$L/L_{\rm Edd}$	$R/R_{\rm S}$	$\Gamma_{\rm inj}$	τ	η_B	f	$\alpha_{[2-10]}$	$kT_{\rm e}$ (keV)
1[a]	1	10^7	10^{-2}	10	3.0	1.0	0.1	0	0.800	93
2	1	10^7	10^{-2}	10	3.0	1.0	1.0	0	0.888	95
3	1	10^7	10^{-2}	10	3.0	1.0	10	0	0.965	96
4	2	10	10^{-2}	10	3.0	1.0	0.1	0	0.779	99
5	2	10^3	10^{-2}	10	3.0	1.0	0.1	0	0.789	96
6	2	10^5	10^{-2}	10	3.0	1.0	0.1	0	0.795	94
1[a]	2	10^7	10^{-2}	10	3.0	1.0	0.1	0	0.800	93
7	2	10^9	10^{-2}	10	3.0	1.0	0.1	0	0.804	93
8	3	10	10^{-2}	10	3.0	1.0	1.0	0	0.908	94
9	3	10^3	10^{-2}	10	3.0	1.0	1.0	0	0.905	93
10	3	10^5	10^{-2}	10	3.0	1.0	1.0	0	0.896	94
11	3	10^7	10^{-2}	10	3.0	1.0	1.0	0	0.882	95
12	3	10^9	10^{-2}	10	3.0	1.0	1.0	0	0.880	96
13	4	10	10^{-3}	10	3.0	0.3	0.1	0	0.899	122
14	4	10^3	10^{-3}	10	3.0	0.3	0.1	0	0.896	122
15	4	10^5	10^{-3}	10	3.0	0.3	0.1	0	0.895	121
16	4	10^7	10^{-3}	10	3.0	0.3	0.1	0	0.890	121
17	4	10^9	10^{-3}	10	3.0	0.3	0.1	0	0.886	120
18	5	10^7	10^{-2}	10	3.0	0.1	0.1	0	0.935	50–100[b]
19	5	10^7	10^{-2}	10	3.0	0.3	0.1	0	0.889	50–100[b]
1[a]	5	10^7	10^{-2}	10	3.0	1.0	0.1	0	0.800	93
20	5	10^7	10^{-2}	10	3.0	3.0	0.1	0	0.746	33
21	5	10^7	10^{-2}	10	3.0	10	0.1	0	0.603	7
2	8	10^7	10^{-2}	10	3.0	1.0	1.0	0	0.888	95
22	8	10^7	10^{-3}	10	3.0	1.0	1.0	0	0.889	102
23	8	10^7	10^{-4}	10	3.0	1.0	1.0	0	0.890	108
24	9	10^7	10^{-2}	10	2.0	1.0	0.1	0	0.915	39
1[a]	9	10^7	10^{-2}	10	3.0	1.0	0.1	0	0.800	93
25	9	10^7	10^{-2}	10	3.5	1.0	0.1	0	0.749	105
26	10	10^7	10^{-2}	300	3.0	1.0	1.0	0	0.886	107
27[c]	10	10^7	10^{-2}	300	3.0	1.0	1.0	0	0.853	105
1[a]	11	10^7	10^{-2}	10	3.0	1.0	0.1	0	0.800	93
28	11	10^7	0.03	10	3.0	1.0	0.1	0.1	0.898	63
29	11	10^7	0.1	10	3.0	1.0	0.1	0.3	1.030	36
30	11	10^7	0.3	10	3.0	1.0	0.1	1.0	1.191	16
31	11	10^7	1	10	3.0	1.0	0.1	3.0	1.335	4
32	13	10^8	1.0	10	3.5	1.0	0.25	10	1.640	3

[a]The fiducial parameter set. [b]The value of the temperature is not well defined as the electron distribution is poorly fitted by the Maxwellian. [c]The spectrum was calculated including bremsstrahlung.

Seyferts are expected to be softer than those of GBHs at the same ratio f (Zdziarski et al. 2003) for $\alpha < 1$.

The situation is more complicated for the SSC mechanism. The low-energy part of the spectrum is determined by synchrotron radiation which is strongly self-absorbed up to some critical frequency, the so-called turnover frequency $\nu_{\rm t}$. For the hybrid electron distribution, containing Maxwellian and power-law parts, there are two corresponding turnover frequencies: thermal $\nu_{\rm t}^{\rm th} \propto B^{0.91}$ (e.g. Mahadevan 1997; Wardziński & Zdziarski 2000) and power law (e.g. Rybicki & Lightman 1979; Wardziński & Zdziarski 2001):

$$\nu_{\rm t}^{\rm pl} \propto B^{\frac{s+2}{s+4}} \propto R^{-\frac{s+2}{2s+8}} \propto M_{\rm BH}^{-\frac{s+2}{2s+8}}, \tag{13}$$

where we used equation (2), obtaining the last scaling. Here $s = \Gamma_{\rm inj} + 1$, if the cooling of particles emitting around the turnover frequency is dominated by the synchrotron radiation or Compton scattering and $s = \Gamma_{\rm inj} - 1$, if Coulomb collisions dominate (see equation 12). In our simulations, the synchrotron radiation coming from the Maxwellian part of the electron distribution is completely self-absorbed and only non-thermal electrons are responsible for the synchrotron radiation coming from the region. Using equation (2), we then deduce (for $\Gamma_{\rm inj} = 3.0$):

$$\nu_{\rm t} \propto \left(\frac{\eta_B l}{R}\right)^{0.33/0.38}. \tag{14}$$

The lower and upper limits of the power-law index correspond to Coulomb and radiative regimes, respectively. Moreover, for the pure SSC simulations, the synchrotron-emitting particles are in the radiative cooling regime (i.e. the cooling by Coulomb is negligible). The turnover frequency is generally smaller for more massive objects (see Figs 2–4) and lower magnetizations. The latter effect can be seen in Fig. 1; however, the dependence on η_B is weak since the effects of the increasing magnetic field and decreasing normalization of the tail of the electron distribution due to stronger cooling nearly cancel each other out. We find that for different values of the

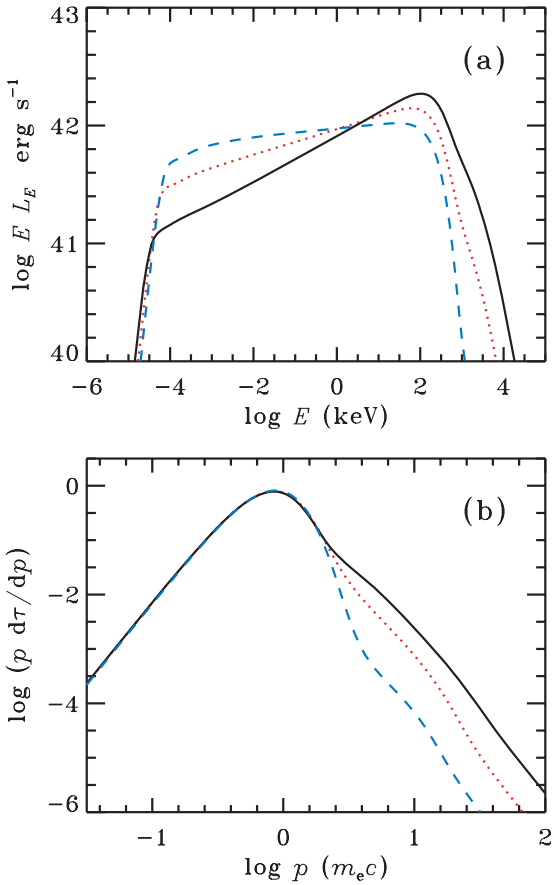

Figure 1. Equilibrium spectra (upper panel) and electron distributions (lower panel) for SSC models with the varying magnetization parameter: $\eta_B = 0.1$ (black solid line), 1.0 (red dotted line), 10 (blue dashed line). Other parameters are fiducial. Runs 1–3 from Table 1. [Correction added after online publication 2011 May 20: figure replaced, with corrected normalization.]

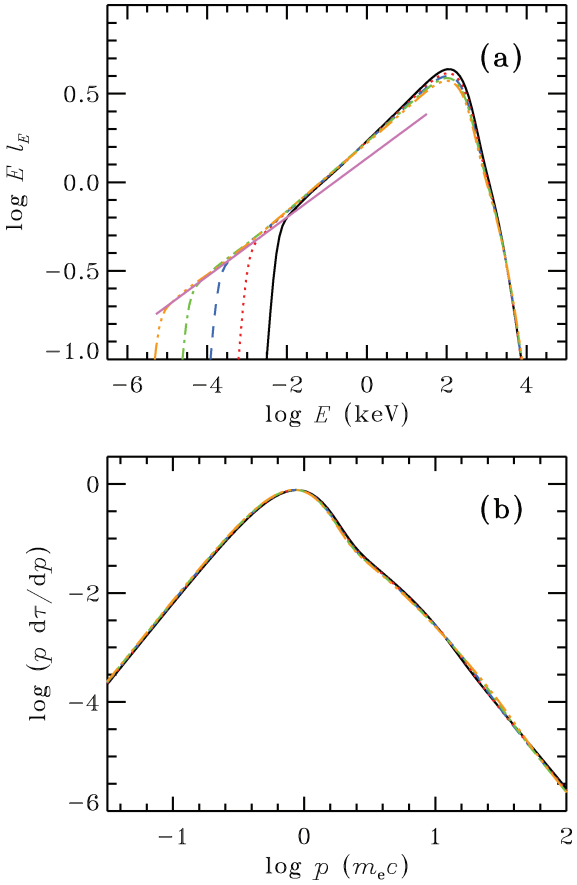

Figure 2. Equilibrium spectra (differential compactness, upper panel) and electron distributions (lower panel) for SSC models with varying masses of the black hole: $M = 10$ (black solid line), 10^3 (red dotted line), 10^5 (blue dashed line), $10^7\,\mathrm{M}_\odot$ (green dot–dashed line) and $10^9\,\mathrm{M}_\odot$ (yellow three-dot–dashed line). Other parameters are fiducial. The broadest spectrum corresponds to the highest mass. The magenta line corresponds to the power law of the energy index $\alpha = 5/6$. Runs 1 and 4–7 from Table 1.

magnetization parameter, the slope of the thermal Comptonization component can become harder or softer with increasing mass (Figs 2 and 3), depending on its initial value and the slope of the non-thermal electron distribution. The electron distribution is independent of the mass due to the fact that cooling and heating (re-acceleration) times scale with the mass similarly; thus, their ratio is independent of the mass (see equations 9 and 10).

The synchrotron luminosity at ν_t can be estimated by remembering that the intensity at the turnover frequency is just a source function of the power-law electrons and that the relativistic electron of the Lorentz factor γ emits most of the synchrotron power at frequency $\nu \simeq 2\gamma^2\nu_B$ (where $\nu_B = eB/2\pi m_\mathrm{e}c$ is the cyclotron frequency). Then, the compactness of the synchrotron photon spectrum at ν_t scales as (Rybicki & Lightman 1979):

$$E\,l_{E,\mathrm{synch}} \propto \frac{R\nu_\mathrm{t}^{7/2}}{\sqrt{\nu_B}} \propto B^{\frac{s-3}{s+4}} \propto R^{-\frac{s-3}{2s+8}} \propto M_\mathrm{BH}^{-\frac{s-3}{2s+8}}. \quad (15)$$

Eliminating the mass using equation (13), we get the dependence of differential compactness (at a turnover frequency) on the photon energy:

$$E\,l_{E,\mathrm{synch}} \propto E^{\frac{s-3}{s+2}}. \quad (16)$$

This corresponds to a power law of the energy index $\alpha = 5/(s+2)$. In Figs 2 and 3, the magenta line corresponds to $s = \Gamma_\mathrm{inj} + 1 = 4$, giving $E\,l_{E,\mathrm{synch}} \propto E^{1/6}$ (i.e. $\alpha = 5/6$). For an initial spectral index α, increasing the mass of the compact object leads to softer SSC spectra if $s < 5/\alpha - 2$. For the canonical value $\alpha \approx 0.7$ in the hard-state spectra of GBHs, we get $s < 5$ (or equivalently $\Gamma_\mathrm{inj} < 4$). For a steep spectral slope to start with at $10\,\mathrm{M}_\odot$ (for instance, the slope as in Fig. 3), we get a more stringent constraint than $s < 5/0.908 - 2 \approx 3.5$ and $\Gamma_\mathrm{inj} < 2.5$. Thus, a hard electron injection function is required to get the systematically softer spectra in Seyferts in terms of the SSC mechanism, keeping all the parameters (except M_BH) constant.

We emphasize here that whether the spectrum hardens or softens with the increasing mass depends both on the initial (for $M_\mathrm{BH} = 10\,\mathrm{M}_\odot$) slope and the scaling of the seed photon compactness. The power-law slope of the Comptonization component will tend asymptotically to the value $\alpha = 5/(s+2)$ (thus, hardening or steepening) with the increasing mass of the object, independently of other parameters, leading to a stability of the spectrum. In models with the seed photons coming from the accretion disc (with $f =$ constant), this asymptotic slope is $\alpha = 1$.

In Fig. 4, we plot spectra and electron distributions obtained for the same parameters as in Fig. 2, but for lower τ and L/L_Edd. The tail in the electron distribution becomes relatively stronger, resulting in more luminous synchrotron emission. This softens the Comptonized part of the spectrum (compared to the cases in Fig. 2). The slopes of electron distributions between momenta $p = 1$ and

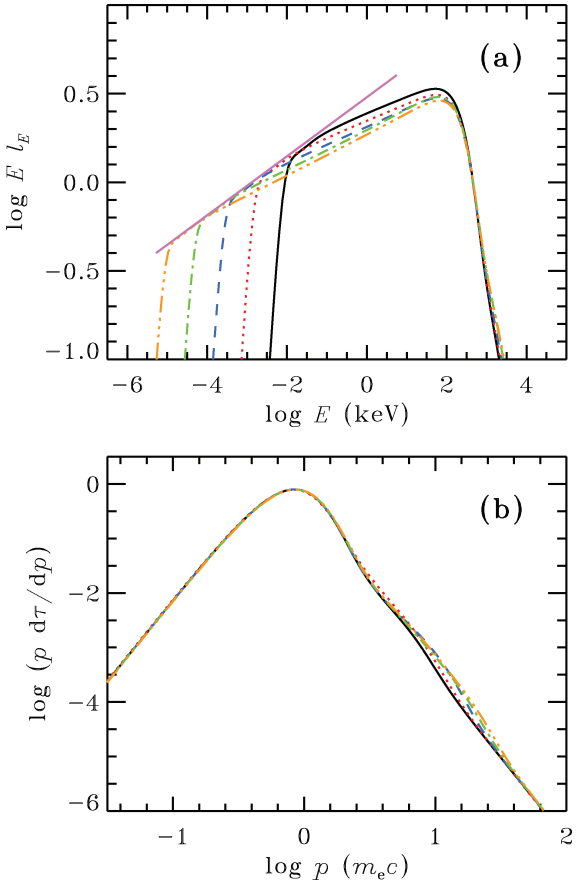

Figure 3. Same as in Fig. 2(a), but for $\eta_B = 1.0$. Runs 8–12 from Table 1.

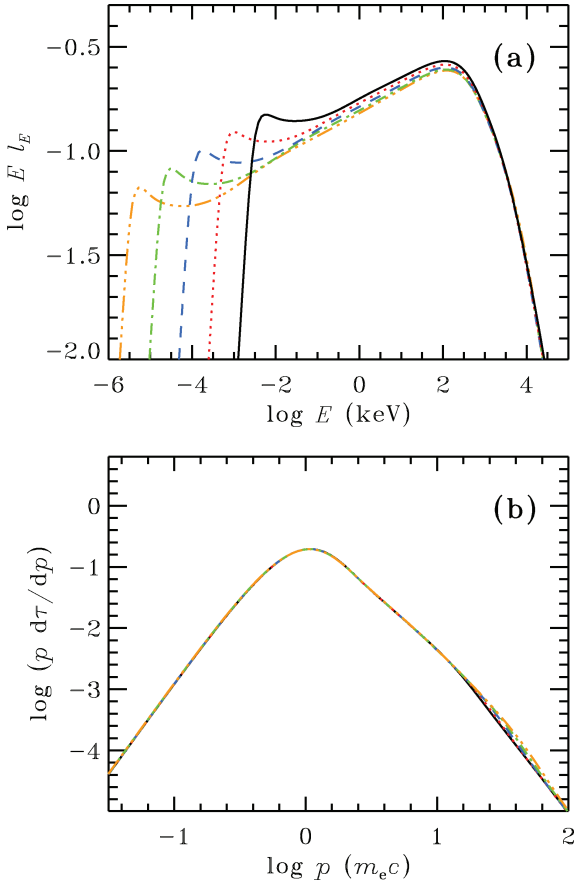

Figure 4. Same as in Fig. 2, but for $L/L_{\rm Edd} = 10^{-3}$ and $\tau = 0.3$. Runs 13–17 from Table 1.

10 resemble the injection function, implying inefficient cooling at these energies. Below the peak, the Coulomb collisions dominate the re-acceleration, leading to the formation of the Maxwellian distribution, and for $p > 10$, radiative cooling softens the electron distribution.

3.1.3 *Dependence on the optical depth*

Now let us consider the role of the optical depth. Again, we take the fiducial parameters and let τ vary. As the optical depth grows, the electrons have more time to cool before being re-accelerated, leading to a drop in the electron temperature (Fig. 5b). Lower temperature and higher optical depth lead to efficient thermalization by Coulomb collisions, driving a larger fraction of particles to a Maxwellian distribution. As the electron temperature decreases, the peak of the thermally Comptonized spectrum also moves to lower energies (see Fig. 5a). At the same time, the number of particles in the non-thermal tail of the electron distribution decreases, leading to weaker partially self-absorbed synchrotron emission. The source therefore becomes photon-starved and the spectrum hardens.

At low optical depths, the particles do not have time to cool between re-accelerations and the electron distribution resembles the injection function with a hard tail. The synchrotron emission is therefore strong and dominates the emission in the 0.1–10 eV range for $\tau = 0.1$.

The effect of the hardening of the spectrum with increasing optical depth was found for both GBHs and SMBHs, irrespective of the values of the other parameters (see Fig. 6), suggesting that it has the strongest influence on the slope.

3.1.4 *Dependence on the Eddington ratio*

The change in the Eddington ratio is closely connected to the change in the accretion rate, which, in turn, affects the optical depth. The latter is rather obvious: if the accretion time is constant, the higher is the matter supply, the higher is the density and therefore the optical depth. We assume that $\tau \propto \dot{M}$. For different types of accretion modes (corresponding to efficient and inefficient flows), the observed X-ray luminosity depends on the accretion rate in a different manner. To investigate the spectral formation at various accretion rates, we consider a simple power-law scaling

$$\tau = \tau_0 \left(\frac{L}{L_{\rm Edd}} \right)^{\theta}, \qquad (17)$$

where $\tau_0 = 1.0$, and $\theta = 0.5$, which corresponds to radiatively inefficient accretion ($\tau \propto \dot{M}$ and $L \propto \dot{M}^2$), $\theta = 1.0$ corresponding to radiatively efficient accretion and $\theta = 0$, that is, constant optical depth (ad hoc).

The results of simulations are shown in Figs 7 and 8. The spectral index is almost independent of the Eddington ratio, if the optical depth remains constant and bremsstrahlung is not accounted for. The turnover frequency is smaller for lower Eddington ratios: the fraction of the magnetic energy (η_B) remains constant; therefore, the magnetic field itself decreases as $B \propto (L/L_{\rm Edd})^{1/2}$, leading to the reduction in $\nu_{\rm t}$. The spectral slopes in the 2–10 keV range are determined by Comptonization on thermal electrons. Our simulations show that for the case of constant optical depth, the Maxwellian part

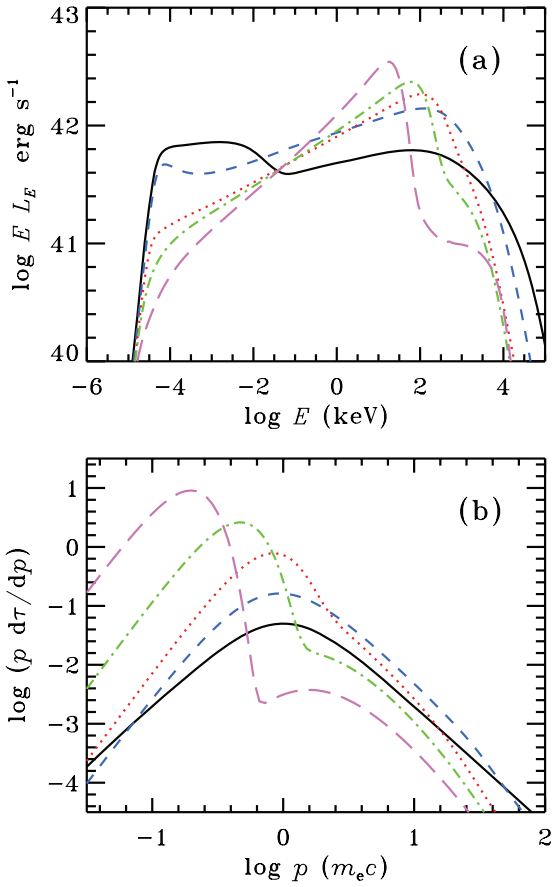

Figure 5. Equilibrium spectra (upper panel) and electron distributions (lower panel) for SSC models with varying optical depths $\tau = 0.1$, 0.3, 1, 3 and 10. The hardest spectrum and the coldest electron distribution correspond to the highest τ. Other parameters are fiducial. Runs 1 and 18–21 from Table 1. [Correction added after online publication 2011 May 20: figure replaced, with corrected normalization.]

of the distribution remains almost unchanged. The Comptonized slope can be approximated as (Beloborodov 1999a):

$$\alpha \simeq \frac{9}{4} y^{-2/9} - 1, \tag{18}$$

where $y = 4(\Theta_e + 4\Theta_e^2)\tau(\tau + 1)$ is the Compton parameter and $\Theta_e = kT_e/mc^2$ is the dimensionless temperature of electron distribution. Hence, for constant optical depth, equal temperatures of the Maxwellian distribution give the same slope of the Comptonization spectrum (see Fig. 8). When the optical depth changes together with the Eddington ratio, the electron temperature is no longer conserved and the spectral slope changes too. At sufficiently low luminosities and relatively high optical depths, the X-ray spectrum is no longer dominated by Comptonization, but instead determined by bremsstrahlung.

Because the injection and cooling rates scale the same way with the Eddington ratio, the electron distribution at energies producing synchrotron emission above the turnover frequency

$$\gamma \gtrsim \gamma_t \simeq \sqrt{\frac{\nu_t}{2\nu_B}} \approx 4.2 \times 10^{-4} \sqrt{\frac{\nu_t}{B}} \approx 30 \tag{19}$$

has a power-law shape with $s = \Gamma_{inj} + 1$ and does not change in the cases plotted in Fig. 8. Using equations (13) and (15), one gets the dependence of El_E/l (the spectral distribution scaled to the total

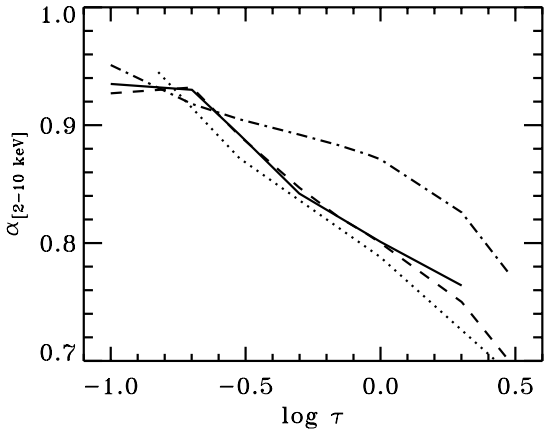

Figure 6. Dependence of the spectral slope on the optical depth for various sets of parameters ($M_{BH}/M_\odot$, L/L_{Edd}, Γ_{inj}) = (10^7, 10^{-2}, 3.0) (solid line), (10^7, 10^{-3}, 3.0) (dashed line) and (10^7, 10^{-2}, 2.0) (dot–dashed line). The corresponding dependence for GBHs with parameters (10, 10^{-2}, 3.0) is shown with the dotted line. Other parameters are fiducial.

compactness) on the turnover frequency for the constant R:

$$\frac{El_E}{l} \propto \frac{R\nu_t^{7/2}}{l\sqrt{\nu_B}} \propto E^{\frac{s-3}{s+2}}, \tag{20}$$

giving $\alpha = 5/(s + 2) = 5/6$, which happens to be very close to the X-ray spectral index 0.89. Thus, the spectral slope in this case is conserved.

The three electron distributions differ much in the range of Lorentz factors between $\gamma \sim 3$ and 20. The effect is due to the increasing role of Coulomb cooling for lower Eddington ratios (compared to radiative cooling, see equation 8). For the adopted parameters and $\gamma \approx 10$, the ratio of radiative (Compton) to Coulomb time-scales is

$$\frac{t_{cool,Coul}}{t_{cool,cs}} \approx 2.8\, l_{inj}. \tag{21}$$

Thus, for $L/L_{Edd} = 10^{-2}$ ($l_{inj} \approx 10$), the Compton cooling dominates, but for $L/L_{Edd} = 10^{-4}$ (with $l_{inj} \approx 0.1$), the slope of the electron tail at γ between 3 and 20 is predominantly determined by Coulomb collisions and $s \approx \Gamma_{inj} - 1 = 2$ (see equation 12). Coulomb collisions also cause the heating of thermal electrons to slightly higher temperatures.

3.1.5 Dependence on the injection slope

The exact mechanism responsible for the particle acceleration in the inner parts of accretion flow is poorly understood. It can be related to weak shocks within the accretion flow or reconnection of the magnetic field. The slope of the injected electrons is strongly model-dependent. On the observational side, the slope in GBHs can be estimated from the MeV tails (McConnell et al. 2002), but for AGNs the observations are not yet very constraining (Gondek et al. 1996; Johnson et al. 1997).

To investigate the dependence of the results on the injection slope, we consider three cases with $\Gamma_{inj} = 2.0$, 3.0 and 3.5. The variable injection slope influences the spectrum mainly through its strong effect on the strength of the partially self-absorbed synchrotron radiation produced by non-thermal electrons. Generally, the synchrotron spectrum from the hybrid electron distribution can be divided into four parts (Wardziński & Zdziarski 2001): at low energies, emission and absorption are dominated by thermal electrons (Rayleigh–Jeans spectrum), at slightly higher energies, the

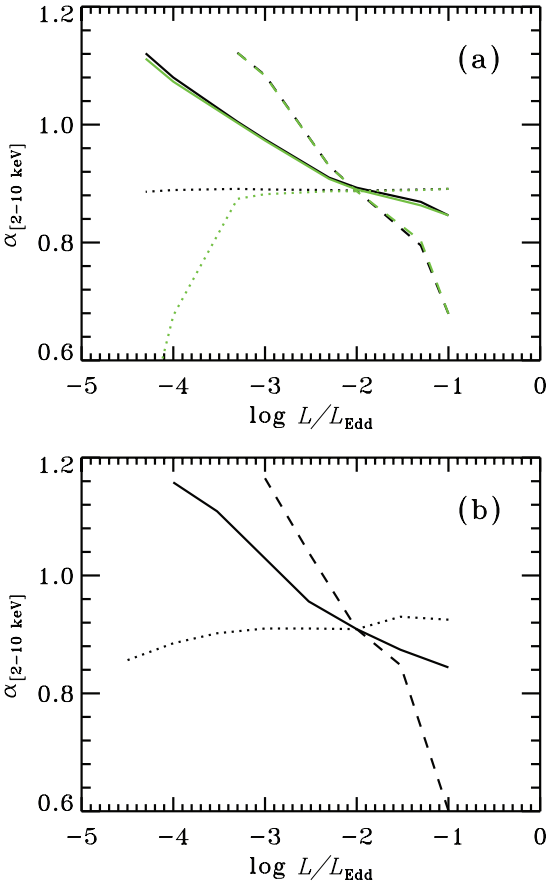

Figure 7. Dependence of the spectral slope on the Eddington ratio for pure SSC models. (a) SMBH ($M_{\mathrm{BH}} = 10^7 \mathrm{M}_\odot$, $\eta_B = 1.0$) and (b) GBH ($M_{\mathrm{BH}} = 10\mathrm{M}_\odot$, $\eta_B = 1.0$). Different dependencies of the optical depth on the luminosity are shown: $\tau \propto L^{1/2}$ (solid line), $\tau \propto L$ (dashed line), $\tau =$ constant (dotted line). The curves intersect at $L = 10^{-2} L_{\mathrm{Edd}}$, where $\tau = 1.0$. The light (green) curves correspond to all radiation processes taken into account, while for the black curves the bremsstrahlung is neglected.

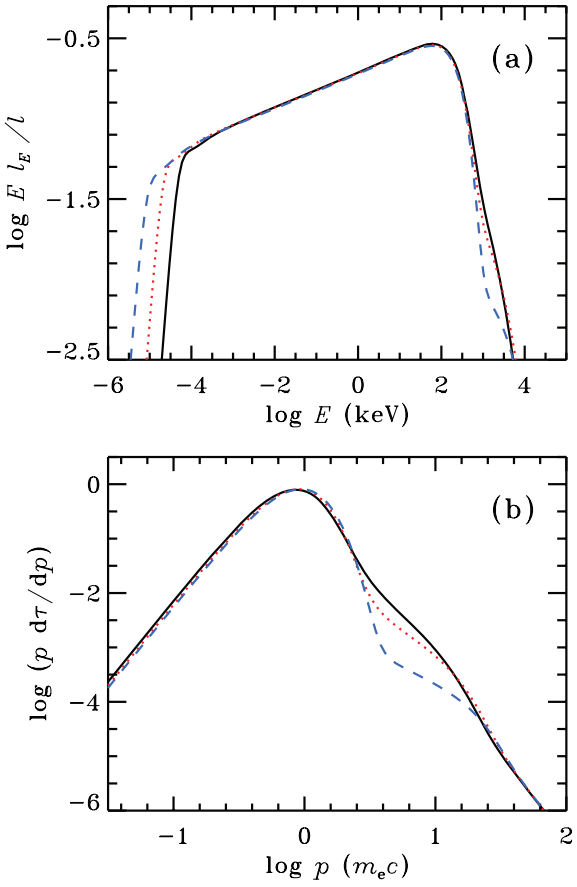

Figure 8. Equilibrium spectra (normalized to the total compactness, upper panel) and electron distributions (lower panel) for pure SSC models with varying Eddington ratios: $L/L_{\mathrm{Edd}} = 10^{-2}$ (black solid line), 10^{-3} (red dotted line) and 10^{-4} (blue dashed line). The optical depth is constant in these simulations, $\eta_B = 1.0$ and other parameters are fiducial. Runs 2, 22 and 23 from Table 1.

emission from non-thermal electrons becomes dominant, but the absorption is still determined by the thermal population. Then, the non-thermal absorption becomes more important and the spectrum is proportional to the source function of non-thermal electrons. Finally, at high energies, the non-thermal emission becomes optically thin with the spectral index $\alpha = (s-1)/2$.

The cases $\Gamma_{\mathrm{inj}} = 2.0$ and 3.5 are qualitatively different, as in the former case, the number of electrons emitting above the turnover frequency is large and the synchrotron spectrum is flat (with $\alpha = 1$ corresponding to $s = 3$, see Fig. 9). This leads to a large amount of soft photons available for Comptonization, strong cooling of the electrons and a softer Comptonized spectrum. For high values of Γ_{inj}, the number of electrons emitting above the turnover frequency is reduced together with the synchrotron luminosity causing higher electron temperature and a harder Comptonized spectrum.

3.2 The role of bremsstrahlung in SSC models

We have discussed the spectral formation under the joint action of synchrotron and Compton processes. Let us now consider how the free–free emission affects the resulting spectra. Major contribution comes from electron–electron and electron–proton collisions (the amount of positrons is negligibly small in our simulations; thus, the number of protons is approximately equal to the number of electrons). The bremsstrahlung emission coefficients depend on the square of the number density of electrons, while the Compton emissivity depends on the product of the number density of particles and photons. Generally, one would expect the former processes to play a dominant role in the medium with high particle and low photon number densities. The relevant scalings are $n_{\mathrm{e}} \propto \tau/R$ and $n_{\mathrm{ph}} \propto L t_{\mathrm{esc}}/R^3 \propto L/R^2$. Then, the bremsstrahlung emission coefficient scales as $j_{\mathrm{br}} \propto \tau^2/R^2$ and Compton scattering emission as $j_{\mathrm{cs}} \propto L\tau/R^3$. The relative importance of bremsstrahlung emission is thus characterized by the ratio

$$j_{\mathrm{br}}/j_{\mathrm{cs}} \propto \tau R/L \propto \tau/l. \qquad (22)$$

The effect of bremsstrahlung on the spectral slope for different dependencies of τ on L/L_{Edd} can be seen in Fig. 7. From equation (22), we see that for a given Eddington ratio (and size), its importance primarily depends on the optical thickness of the source. In the cases considered in Fig. 7, the free–free radiation only affects the slope in the case where τ is kept constant (i.e. large). Thus, bremsstrahlung processes can be energetically important for the system of larger size (and small compactness). This can correspond to some type of radiatively inefficient accretion (Narayan et al. 1998). An example of the resulting spectrum is shown in Fig. 10. If the optical depth decreases together with the Eddington ratio, bremsstrahlung emission remains negligible.

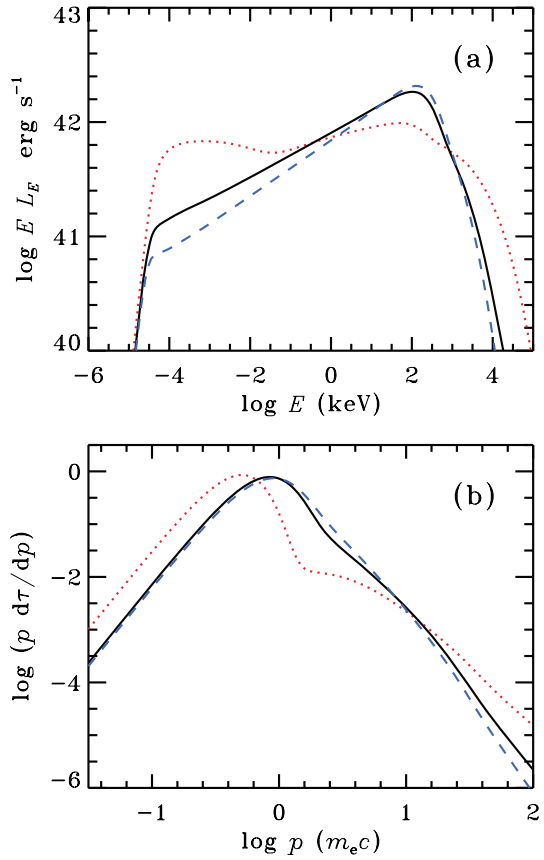

Figure 9. Equilibrium spectra (upper panel) and electron distributions (lower panel) for pure SSC models with varying injection slopes: $\Gamma_{\rm inj} = 2.0$ (red dotted line), 3.0 (black solid line) and 3.5 (blue dashed line). Other parameters are fiducial. Runs 1, 24 and 25 from Table 1. [Correction added after online publication 2011 May 20: figure replaced, with corrected normalization.]

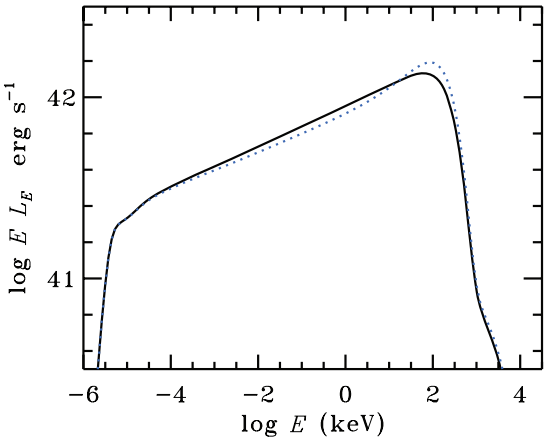

Figure 10. Spectra of a SMBH, where the size of the active region is assumed to be $R = 300R_{\rm S}$. Runs 26 and 27 from Table 1. Spectra are calculated without accounting for bremsstrahlung processes (black solid line) and including those (blue dotted line). [Correction added after online publication 2011 May 20: figure replaced, with corrected normalization.]

However, even if bremsstrahlung is energetically not significant, it still can produce a hardening of the otherwise power-law-like spectrum above a few keV, making the overall spectrum concave. Such a spectral complexity might have been a reason for the existence of soft excess in the GBH Cyg X-1 (Ibragimov et al. 2005). In Seyferts, the data are not of the same quality to detect such a hardening.

3.3 Influence of the accretion disc and slope–luminosity correlation

So far we have considered pure SSC models, where the only source of soft seed photons is synchrotron radiation. This regime can be realized at sufficiently low accretion rates, when the disc is far away from the region in which the majority of energy is liberated. For black holes in X-ray binaries, there is strong evidence that the disc inner radius changes with the accretion rate. The spectral slope correlates with the amplitude of reflection, the width of the iron line and the characteristic frequencies of variability (Gilfanov, Churazov & Revnivtsev 1999; Zdziarski et al. 1999; Revnivtsev et al. 2001; Ibragimov et al. 2005). Similar correlations are found in Seyfert galaxies in individual sources (Magdziarz et al. 1998; Nandra et al. 2000) as well as in the set of AGNs (Zdziarski et al. 1999; Lubiński & Zdziarski 2001; Matt 2001; Papadakis et al. 2002; Zdziarski et al. 2003).

The spectral transitions in GBHs are characterized by the dramatic change in the spectral shape with corresponding changes in the electron distribution. In the hard state, the electrons are mostly thermal probably only with a weak tail which is responsible for the production of MeV photons (McConnell et al. 2002). In the soft state, the electrons have mostly non-thermal, power-law-like distribution producing long tail extending up to 10 MeV (Poutanen & Coppi 1998; Poutanen 1998). The strong variation in the electron distribution can be caused mostly by the increasing Compton cooling when the disc moves in as the accretion rate increases (Vurm & Poutanen 2008; Malzac & Belmont 2009; Poutanen & Vurm 2009). Here we repeat simulations presented in aforementioned papers, but for the parameters typical for SMBHs.

Once the disc moves sufficiently close to the X-ray-emitting region, the seed photons from the disc start dominating over the internally produced synchrotron photons. We simulate this process by injecting additional blackbody photons to the simulation volume. We parametrize the importance of these photons by the relative fraction to the luminosity dissipated in the active region $f \equiv L_{\rm disc}/L_{\rm inj}$. These seed photons are injected homogeneously into the region. We expect that f is a strong function of the cold inner disc radius, which in turn depends on the accretion rate and total luminosity. We assume a power-law dependence

$$f = f_0 \left(\frac{L}{L_{\rm Edd}} \right)^{\beta}, \tag{23}$$

where β and f_0 are the parameters to be determined from the data or theory. The results of simulations for $\beta = 1$ and $f_0 = 3$ are shown in Fig. 11. As the fraction f increases, the disc quickly replaces synchrotron radiation as a dominant source of seed photons for Compton upscattering. Strong soft radiation field implies faster cooling, leading to a decrease in the electron temperature and a more pronounced high-energy tail. This, in turn, leads to the decline of the Compton parameter associated with the thermal population and the spectrum softens (see equation 18). The role of thermal Comptonization in the formation of the high-energy spectrum becomes progressively weaker and is taken over by Compton scattering on the non-thermal population of electrons. For high f, the spectrum is dominated by the disc blackbody, whereas the soft non-thermal tail extends to several MeV without a cut-off. The shape of the spectrum above $\sim$100 keV strongly depends on the assumed maximum electron Lorentz factor $\gamma_{\rm he}$.

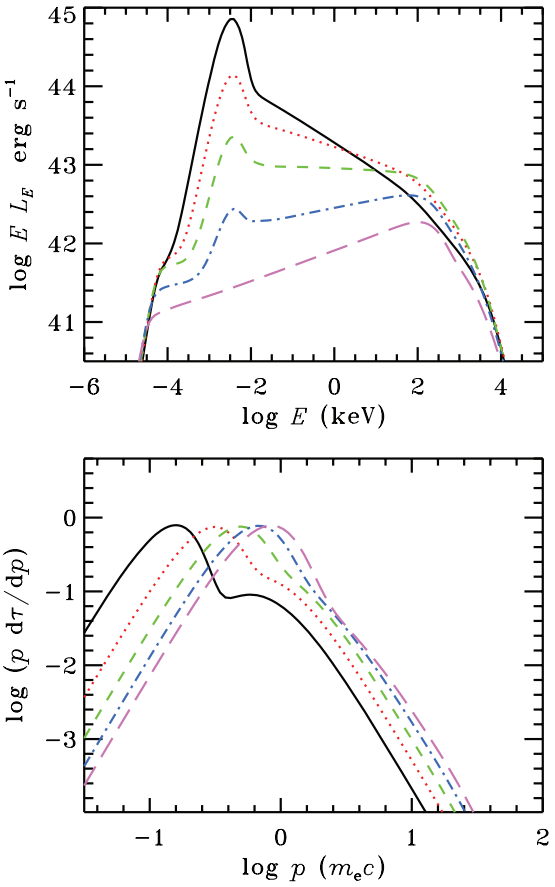

Figure 11. Equilibrium spectra and electron distributions for different Eddington ratios (from the top to bottom) $L/L_{\rm Edd} = 0.01$, 0.03, 0.1, 0.3 and 1, and varying disc contributions $f = 0$, 0.1, 0.3, 1 and 3. Runs 1 and 28–31 from Table 1. The disc temperature is assumed to be $T_{\rm d} = 10^4$ K. [Correction added after online publication 2011 May 20: figure replaced, with corrected normalization.]

4 OBSERVED SPECTRAL PROPERTIES OF SUPERMASSIVE BLACK HOLES

Among the first surveys on X-ray spectral indices of AGNs, Nandra & Pounds (1994) have noted that the majority of Seyfert 1 galaxies have the spectral energy index $\alpha = 0.95$ with small dispersion, $\sigma = 0.15$. However, the addition of NLSy1s broadened the range of spectral indices (Brandt, Mathur & Elvis 1997). After that, the energy indices $\alpha \sim 1.0$ were also found for $z \lesssim 6$ type I radio-quiet quasars (e.g. Porquet et al. 2004; Shemmer et al. 2006). Lately, it became clear that dispersion depends on the sample: the more objects are considered, the wider is the spread (see e.g. fig. 8 in Burlon et al. 2011). Also recent studies revealed a tight correlation between the spectral slope and the luminosity of the object in Eddington units (e.g., Wang, Watarai & Mineshige 2004; Shemmer et al. 2006; Vasudevan & Fabian 2007; Middleton, Done & Schurch 2008; Sobolewska & Papadakis 2009; Vasudevan & Fabian 2009; Zhou & Zhao 2010). In contrast, the low-luminosity AGNs (e.g. LINERs) tend to have rather stable spectral slopes with the average $\alpha \sim 1$.

A standard view is that at low mass accretion rates the vicinity of the black hole is occupied by a hot radiatively inefficient accretion flow (Narayan et al. 1998; Yuan, Quataert & Narayan 2003; Yuan 2010). In the case of very large accretion rates typical for NLSy1s and quasars, the standard cold accretion disc extends all the way down to the last stable orbit around the central black hole with the hard X-rays being probably produced in the accretion disc corona. In the intermediate case represented by Seyfert galaxies, the cold disc is probably truncated and the X-rays are produced in the inner hot flow. Let us now apply our model to the observed properties of AGNs at different accretion rates.

We assume the dependence $f(L)$ given by equation (23) together with $\tau(L)$ given by equation (17). The coefficients and the indices can be obtained from the direct comparison with the data. Fig. 12 (solid line) shows the dependence of the spectral slope on the Eddington ratio for a model with $\tau = (L/L_{\rm Edd})^{1/2}$ and $f = 2(L/L_{\rm Edd})$. The model describes well the observed slopes for a very broad range of luminosities, as we show below. The self-absorption frequency is sufficiently low for objects with high masses and the synchrotron emission falls in the infrared range. This model predicts an intimate relation between the infrared/optical and X-ray variability in low-luminosity objects.

4.1 LINERs and stability of the spectral slope

LINERs are defined by narrow optical emission lines of low ionization (Heckman 1980). A fraction of LINERs are believed to host an AGN, with mass accretion rates far below Eddington. The X-ray spectrum can well be fitted with a single power law of $\alpha \sim 1.0$–1.2 (González-Martín et al. 2009b), which shows very little intrinsic absorption and weak (or absent) signatures of Fe Kα emission or Compton reflection (Ho 2008, and references therein). Thus, the data suggest no accretion disc in the vicinity of the central black hole, making LINERs appropriate candidates for a pure SSC mechanism. We have taken the spectral indices from the sample of González-Martín et al. (2009b) and the corresponding Eddington ratios from Satyapal et al. (2005) (where available). Additionally, for some objects, we took the black hole mass from González-Martín et al. (2009a) and X-ray luminosity from González-Martín et al. (2009b) and calculated Eddington ratios, assuming a typical LINER X-ray-to-bolometric correction $\kappa = 1.8$. Then, the data were binned into sections of one decade in $L/L_{\rm Edd}$ and averaged. Individual data points as well as the average spectral indices (and their dispersion) are shown in Fig. 12. The average spectral index is consistent with a stable value ∼1.0 and shows no correlation with luminosity.

Our simulations show that the spectral slopes produced by a SSC mechanism are very stable. Among all the parameters, the optical depth affects the slope most dramatically. For a wide range of parameters changing by orders of magnitude ($\eta_B = 0.1$–10, $\tau =$ 0.1–3.0 and $\Gamma = 2$–4), the corresponding spectral index variations are within $\Delta\alpha \lesssim 0.4$. The typical values are ∼0.8–1.0 and do not depend very much on the mass of the central object. We also found that increasing the central mass at the same Eddington ratio leads to the asymptotic index $\alpha = 5/(s+2)$. For the steady-state index of the electron distribution $s = 3$–5, we have $\alpha \approx 0.7$–1, again consistent with the observed hard spectra. This argues in favour of the SSC mechanism as the origin of the broad-band spectra in LINERs.

4.2 Seyfert galaxies

A typical X-ray spectrum of a Seyfert galaxy can be decomposed into an underlying power law and a component arising from the reflection and reprocessing of the intrinsic emission. We are interested in the formation of the intrinsic emission. The low-luminosity end of the Seyfert distribution at $L/L_{\rm Edd} \sim 10^{-2}$ has intrinsic spectral slopes $\alpha \sim 1$ very similar to that of LINERs (see Fig. 12). Thus, these sources can also well be described by a pure SSC model.

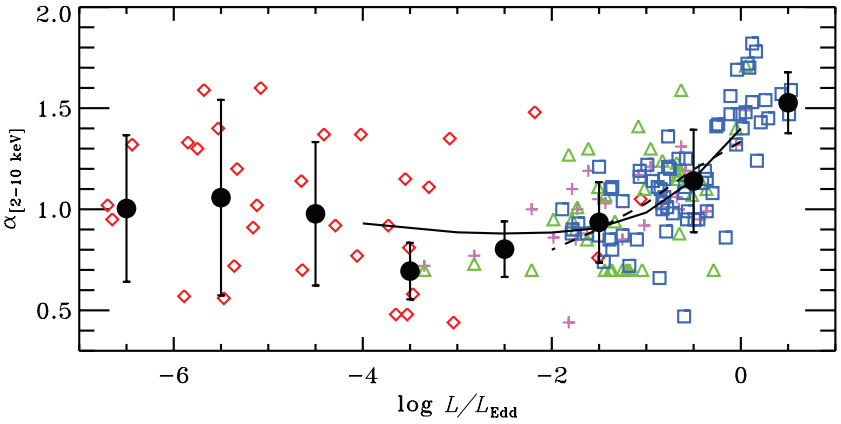

Figure 12. Dependence of the spectral slope on the Eddington ratio. The red diamonds mark LINERs (compilation from Satyapal et al. 2005; González-Martín et al. 2009b). Other symbols correspond to the data on Seyfert galaxies and quasars: magenta crosses (Zhou & Zhao 2010), blue squares (Zhou & Zhang 2010) and green triangles (Vasudevan & Fabian 2009), offset up by 0.2 to correct for reflection. The black filled circles show the averaged data (binned into intervals of one decade in L/L_{Edd}) with the corresponding dispersion. The black solid line shows the result of our simulations with parameters $f_0 = 2$ and $\beta = 1$ from equation (23) and $\tau_0 = 1.0$ and $\theta = 0.5$ from equation (17). The dashed line corresponds to $f_0 = 3$ and $\beta = 1$ and the constant optical depth $\tau = 1.0$ (corresponding spectra and electron distributions are shown in Fig. 11).

We note, however, that Seyferts demonstrate spectral variations with varying flux. The dependence between the X-ray spectral slope and the X-ray flux for individual objects can often be fitted with a power law (Chiang et al. 2000; Done, Madejski & Życki 2000; Shih, Iwasawa & Fabian 2002; Chiang & Blaes 2003; Lamer et al. 2003). Similar correlations were found for GBHs, for example, in Cyg X-1 (Zdziarski et al. 2002). If we interpret the observed correlation in terms of the varying disc contribution $f(L)$ given by equation (23) and assume that the spectral slope is determined by the accretion rate only (within small uncertainties corresponding to specific parameters of the system), the data require $\beta \gtrsim 2$. This implies a strong dependence of the inner radius of the accretion disc on the mass accretion rate.

More recently, Sobolewska & Papadakis (2009) presented the statistical analysis of the correlation for 10 AGNs. The average α–F correlation was shown to be less steep than that for each individual object. This effect might be caused by the fact that the same spectral slope in their data correspond to different Eddington ratios in different objects. Thus, a tight correlation for any individual object is somewhat smeared out when considering an ensemble of sources. The reason for this smearing might be the badly determined mass of the central object. A similar slope–luminosity (in Eddington units) correlation is also observed in a large sample of Seyferts and quasars (Vasudevan & Fabian 2009; Zhou & Zhao 2010; Zhou & Zhang 2010) as shown in Fig. 12. We can interpret this correlation in terms of the varying contribution from the disc to the total luminosity and an increasing role of the disc photons for Comptonization. The dependence of the spectral slope on the Eddington ratio is shown in Fig. 12. Two cases are considered: (1) varying optical depth $\tau = (L/L_{\mathrm{Edd}})^{1/2}$ with the disc luminosity fraction $f = 2(L/L_{\mathrm{Edd}})$; and (2) the constant optical depth $\tau = 1.0$ with $f = 3(L/L_{\mathrm{Edd}})$ (the spectra and electron distributions for this case are shown in Fig. 11). In both cases, a strong correlation α–L/L_{Edd} was found. The best-fitting relation $\alpha \propto 0.3\log(L/L_{\mathrm{Edd}})$ found by Zhou & Zhao (2010) matches well the corresponding lines from our simulations. Thus, at high luminosities, $L/L_{\mathrm{Edd}} \gtrsim 3 \times 10^{-2}$, the observed spectral softening can be explained by the motion of the inner radius of the accretion disc towards the black hole and the increasing role of the accretion disc in supplying soft seed photons for Comptonization in the X-ray-emitting region (corona or inner hot flow).

4.3 Narrow-line Seyfert 1 galaxies and quasars

NLSy1s seem to form a distinct class of Seyferts. They are identified by narrow optical permitted and forbidden lines. The UV properties are unusual for the presence of both low- and high-ionization lines. Their X-ray spectra are on average steeper than those of NLSy1s (Middleton, Done & Gierliński 2007), with commonly observed strong soft excess and frequently detected high-amplitude variability. The Eddington ratios are on average higher than in broad-line Sy1s (e.g. Komossa 2008). The power spectral density (PSD) spectrum of the NLSy1 NGC 4051 is similar to the PSD of the soft state of Cyg X-1, but shifted to lower frequencies (McHardy et al. 2004). Similar to the soft state of GBHs, one can expect that the two Seyfert classes differ by the presence of the accretion disc close to the compact object. If the disc extends very close to the SMBH, most of the energy is radiated in the UV range and completely ionizes the medium around. Hence, the lines in NLSy1s can be produced only in the region far away from the central object, where the gas velocities are relatively low (Brandt et al. 1994).

Soft excess is an ubiquitously observed feature in the 0.4–1 keV range in NLSy1s and radio-quiet quasars. It can be modelled by a cool Comptonization component (Pounds et al. 1995; Vaughan et al. 2002); however, its position in the spectrum seems to be independent of the central black hole mass, temperature of the accreting disc and luminosity of the object. Gierliński & Done (2004) proposed an alternative formation scenario where the excess arises from the smeared absorption of the highly ionized oxygen and iron present in the hot wind from the accretion disc. For the quasar PG 1211+143, they obtained the slope of the intrinsic spectrum of $\alpha \approx 1.7$ in the range 0.4–10 keV. This spectrum can be well reproduced by our model where the luminosity of the seed photons from the disc exceeds by 10 times the power injected to electrons (see Fig. 13). This results in a soft, power-law-like spectrum in the X-ray band produced by non-thermal Comptonization. In this model, no cut-off is expected up to high ($\gg$100 keV) energies.

5 CONCLUSIONS

We have studied the spectral formation in hot non-thermal plasmas under the conditions relevant to the vicinities of SMBHs in AGNs,

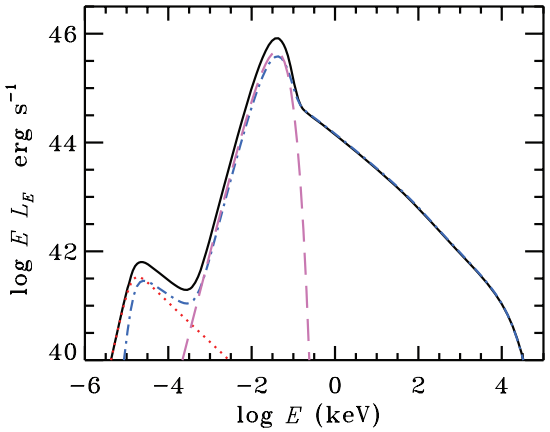

Figure 13. A hybrid Comptonization model for NLSy1s and quasars. The solid line corresponds to the total spectrum. Contribution from different processes: synchrotron (dotted line), Compton scattering (dot–dashed line, sum of thermal and non-thermal) and disc blackbody (dashed line). The parameters are $M_{\rm BH} = 10^8 {\rm M}_\odot$, $L/L_{\rm Edd} = 1.0$, $\tau = 1.0$, $\eta_B = 0.25$, $\Gamma_{\rm inj} = 3.5$ and $f = 10$. [Correction added after online publication 2011 May 20: figure replaced, with corrected normalization.]

using a self-consistent SSC model. We show that the SSC model can reproduce the exponential cut-off at energies above ∼100 keV and the power-law X-ray continuum with energy spectral indices $\alpha \sim 0.8$–1.0 observed in low-luminosity Seyferts and LINERs. The entire infrared/optical to X-ray spectrum in these objects can be produced by the SSC mechanism, suggesting a strong correlation between the two energy bands. No specific conditions are required to stabilize the slope for a wide range of parameters (magnetization, optical depth, injection slope, Eddington ratio and black hole mass).

We have demonstrated the difference in scaling of the SSC model and the two-phase disc–corona models. While in the latter case one would expect systematically softer spectra from objects with higher masses, in the case of SSC, there exists a limiting slope (when the mass of the central object tends to infinity) $\alpha = 5/(s + 2)$, which depends only on the slope of the tail of the electron distribution. Comptonization spectra can get systematically softer for objects of higher masses, if the electron injection function is sufficiently hard.

We have tested the role of bremsstrahlung emission in SSC models. We found that even though the process is not energetically significant, in certain cases, it leads to the hardening of the power law above a few keV and makes the overall X-ray spectrum concave.

We have also studied the role of additional soft blackbody photons from the accretion disc. With the increasing amount of soft photons, the equilibrium Maxwellian temperature drops and the X-ray spectrum softens. The resulting spectra look similar to the GBHs in their soft state, which in the case of SMBHs are likely to be represented by NLSy1s and quasars. We have found that it is possible to explain the spectral slope–flux correlation, widely discussed in the literature, by parametrizing the fraction of the disc photons in the medium as a power-law function of the Eddington ratio. This implies that the inner radius of the truncated accretion disc is a strong function of the accretion rate.

ACKNOWLEDGMENTS

We thank the referee, Chris Done, for suggestions, which led to the significant improvement of this paper. This work was supported by the Finnish Graduate School in Astronomy and Space Physics (AV), the Wihuri Foundation and ERC Advanced Research Grant 227634 (IV) and the Academy of Finland Grant 127512 (JP).

REFERENCES

Belmont R., Malzac J., Marcowith A., 2008, A&A, 491, 617
Beloborodov A. M., 1999a, in Poutanen J., Svensson R., eds, ASP Conf. Ser. Vol. 161, High Energy Processes in Accreting Black Holes. Astron. Soc. Pac., San Francisco, p. 295
Beloborodov A. M., 1999b, ApJ, 510, L123
Blumenthal G. R., Gould R. J., 1970, Rev. Mod. Phys., 42, 237
Brandt W. N., Fabian A. C., Nandra K., Reynolds C. S., Brinkmann W., 1994, MNRAS, 271, 958
Brandt W. N., Mathur S., Elvis M., 1997, MNRAS, 285, L25
Burlon D., Ajello M., Greiner J., Comastri A., Merloni A., Gehrels N., 2011, ApJ, 728, 58
Chiang J., Blaes O., 2003, ApJ, 586, 97
Chiang J., Reynolds C. S., Blaes O. M., Nowak M. A., Murray N., Madejski G., Marshall H. L., Magdziarz P., 2000, ApJ, 528, 292
Coppi P. S., 1992, MNRAS, 258, 657
Coppi P. S., 1999, in Poutanen J., Svensson R., eds, ASP Conf. Ser. Vol. 161, High Energy Processes in Accreting Black Holes. Astron. Soc. Pac., San Francisco, p. 375
Done C., Madejski G. M., Życki P. T., 2000, ApJ, 536, 213
Frank J., King A., Raine D. J., 2002, Accretion Power in Astrophysics. Cambridge Univ. Press, Cambridge
Galeev A. A., Rosner R., Vaiana G. S., 1979, ApJ, 229, 318
George I. M., Fabian A. C., 1991, MNRAS, 249, 352
Ghisellini G., Guilbert P. W., Svensson R., 1988, ApJ, 334, L5
Ghisellini G., Haardt F., Svensson R., 1998, MNRAS, 297, 348
Gierliński M., Done C., 2004, MNRAS, 349, L7
Gilfanov M., Churazov E., Revnivtsev M., 1999, A&A, 352, 182
Gondek D., Zdziarski A. A., Johnson W. N., George I. M., McNaron-Brown K., Magdziarz P., Smith D., Gruber D. E., 1996, MNRAS, 282, 646
González-Martín O., Masegosa J., Márquez I., Guainazzi M., 2009a, ApJ, 704, 1570
González-Martín O., Masegosa J., Márquez I., Guainazzi M., Jiménez-Bailón E., 2009b, A&A, 506, 1107
Grove J. E., Johnson W. N., Kroeger R. A., McNaron-Brown K., Skibo J. G., Phlips B. F., 1998, ApJ, 500, 899
Haardt F., Maraschi L., 1991, ApJ, 380, L51
Haardt F., Maraschi L., 1993, ApJ, 413, 507
Haardt F., Maraschi L., Ghisellini G., 1994, ApJ, 432, L95
Heckman T. M., 1980, A&A, 87, 152
Ho L. C., 2008, ARA&A, 46, 475
Ibragimov A., Poutanen J., Gilfanov M., Zdziarski A. A., Shrader C. R., 2005, MNRAS, 362, 1435
Johnson W. N., McNaron-Brown K., Kurfess J. D., Zdziarski A. A., Magdziarz P., Gehrels N., 1997, ApJ, 482, 173
Komossa S., 2008, Rev. Mex. Astron. Astrofis. Ser. Conf., 32, 86
Lamer G., McHardy I. M., Uttley P., Jahoda K., 2003, MNRAS, 338, 323
Lubiński P., Zdziarski A. A., 2001, MNRAS, 323, L37
Lubiński P., Zdziarski A. A., Walter R., Paltani S., Beckmann V., Soldi S., Ferrigno C., Courvoisier T., 2010, MNRAS, 408, 1851
McConnell M. L. et al., 2002, ApJ, 572, 984
McHardy I. M., Papadakis I. E., Uttley P., Mason K. O., Page M. J., 2004, Nucl. Phys. B, 132, 122
Magdziarz P., Blaes O. M., Zdziarski A. A., Johnson W. N., Smith D. A., 1998, MNRAS, 301, 179
Mahadevan R., 1997, ApJ, 477, 585
Malzac J., Belmont R., 2009, MNRAS, 392, 570
Malzac J., Dumont A. M., Mouchet M., 2005, A&A, 430, 761
Matt G., 2001, in White N. E., Malaguti G., Palumbo G. G. C., eds, AIP Conf. Proc. Vol. 599, X-ray Astronomy: Stellar Endpoints, AGN, and the Diffuse X-ray Background. Am. Inst. Phys., Melville, NY, p. 209
Middleton M., Done C., Gierliński M., 2007, MNRAS, 381, 1426

Middleton M., Done C., Schurch N., 2008, MNRAS, 383, 1501
Nandra K., Pounds K. A., 1994, MNRAS, 268, 405
Nandra K., Le T., George I. M., Edelson R. A., Mushotzky R. F., Peterson B. M., Turner T. J., 2000, ApJ, 544, 734
Narayan R., Mahadevan R., Quataert E., 1998, in Abramowicz M. A., Bjornsson G., Pringle J. E., eds, Theory of Black Hole Accretion Disks. Cambridge Univ. Press, Cambridge, p. 148
Nayakshin S., Melia F., 1998, ApJS, 114, 269
Papadakis I. E., Petrucci P. O., Maraschi L., McHardy I. M., Uttley P., Haardt F., 2002, ApJ, 573, 92
Porquet D., Reeves J. N., O'Brien P., Brinkmann W., 2004, A&A, 422, 85
Pounds K. A., Done C., Osborne J. P., 1995, MNRAS, 277, L5
Poutanen J., 1998, in Abramowicz M. A., Björnsson G., Pringle J. E., eds, Theory of Black Hole Accretion Disks. Cambridge Univ. Press, Cambridge, p. 100
Poutanen J., Coppi P. S., 1998, Phys. Scr. T, 77, 57
Poutanen J., Svensson R., 1996, ApJ, 470, 249
Poutanen J., Vurm I., 2009, ApJ, 690, L97
Revnivtsev M., Gilfanov M., Churazov E., 2001, A&A, 380, 520
Rybicki G. B., Lightman A. P., 1979, Radiative Processes in Astrophysics. Wiley Interscience, New York
Satyapal S., Dudik R. P., O'Halloran B., Gliozzi M., 2005, ApJ, 633, 86
Shakura N. I., Sunyaev R. A., 1973, A&A, 24, 337
Shemmer O., Brandt W. N., Netzer H., Maiolino R., Kaspi S., 2006, ApJ, 646, L29
Shih D. C., Iwasawa K., Fabian A. C., 2002, MNRAS, 333, 687
Sobolewska M. A., Papadakis I. E., 2009, MNRAS, 399, 1597
Stern B. E., Poutanen J., Svensson R., Sikora M., Begelman M. C., 1995, ApJ, 449, L13
Svensson R., 1987, MNRAS, 227, 403
Svensson R., 1994, ApJS, 92, 585
Svensson R., 1996, A&AS, 120, C475
Vasudevan R. V., Fabian A. C., 2007, MNRAS, 381, 1235
Vasudevan R. V., Fabian A. C., 2009, MNRAS, 392, 1124
Vaughan S., Boller T., Fabian A. C., Ballantyne D. R., Brandt W. N., Trümper J., 2002, MNRAS, 337, 247
Vurm I., Poutanen J., 2008, Int. J. Mod. Phys., 17, 1629
Vurm I., Poutanen J., 2009, ApJ, 698, 293
Wang J., Watarai K., Mineshige S., 2004, ApJ, 607, L107
Wardziński G., Zdziarski A. A., 2000, MNRAS, 314, 183
Wardziński G., Zdziarski A. A., 2001, MNRAS, 325, 963
Yuan F., 2007, in Ho L. C., Wang J.-W., eds, ASP Conf. Ser. Vol. 373, The Central Engine of Active Galactic Nuclei. Astron. Soc. Pac., San Francisco, p. 95
Yuan F., 2010, preprint (arXiv:1002.3012)
Yuan F., Quataert E., Narayan R., 2003, ApJ, 598, 301
Zdziarski A. A., 1999, in Poutanen J., Svensson R., eds, ASP Conf. Ser. Vol. 161, High Energy Processes in Accreting Black Holes. Astron. Soc. Pac., San Francisco, p. 16
Zdziarski A. A., Lightman A. P., 1985, ApJ, 294, L79
Zdziarski A. A., Lightman A. P., Maciolek-Niedzwiecki A., 1993, ApJ, 414, L93
Zdziarski A. A., Johnson W. N., Magdziarz P., 1996, MNRAS, 283, 193
Zdziarski A. A., Johnson W. N., Poutanen J., Magdziarz P., Gierlinski M., 1997, in Winkler C., Courvoisier T. J.-L., Durouchoux Ph., eds, ESA SP-382, The Transparent Universe. ESA, Noordwijk, p. 373
Zdziarski A. A., Lubinski P., Smith D. A., 1999, MNRAS, 303, L11
Zdziarski A. A., Grove J. E., Poutanen J., Rao A. R., Vadawale S. V., 2001, ApJ, 554, L45
Zdziarski A. A., Poutanen J., Paciesas W. S., Wen L., 2002, ApJ, 578, 357
Zdziarski A. A., Lubiński P., Gilfanov M., Revnivtsev M., 2003, MNRAS, 342, 355
Zhou X., Zhang S., 2010, ApJ, 713, L11
Zhou X., Zhao Y., 2010, ApJ, 720, L206

This paper has been typeset from a TEX/LATEX file prepared by the author.

Space Sci Rev
DOI 10.1007/s11214-013-0033-3

Modelling Spectral and Timing Properties of Accreting Black Holes: The Hybrid Hot Flow Paradigm

Juri Poutanen · Alexandra Veledina

Received: 29 October 2013 / Accepted: 10 December 2013

Abstract The general picture that emerged by the end of 1990s from a large set of optical and X-ray, spectral and timing data was that the X-rays are produced in the innermost hot part of the accretion flow, while the optical/infrared (OIR) emission is mainly produced by the irradiated outer thin accretion disc. Recent multiwavelength observations of Galactic black hole transients show that the situation is not so simple. Fast variability in the OIR band, OIR excesses above the thermal emission and a complicated interplay between the X-ray and the OIR light curves imply that the OIR emitting region is much more compact. One of the popular hypotheses is that the jet contributes to the OIR emission and even is responsible for the bulk of the X-rays. However, this scenario is largely ad hoc and is in contradiction with many previously established facts. Alternatively, the hot accretion flow, known to be consistent with the X-ray spectral and timing data, is also a viable candidate to produce the OIR radiation. The hot-flow scenario naturally explains the power-law like OIR spectra, fast OIR variability and its complex relation to the X-rays if the hot flow contains non-thermal electrons (even in energetically negligible quantities), which are required by the presence of the MeV tail in Cyg X-1. The presence of non-thermal electrons also lowers the equilibrium electron temperature in the hot flow model to $\lesssim 100$ keV, making it more consistent with observations. Here we argue that any viable model should simultaneously explain a large set of spectral and timing data and show that the hybrid (thermal/non-thermal) hot flow model satisfies most of the constraints.

Keywords Accretion, accretion discs · Black hole physics · Radiation mechanisms: non-thermal · X-rays: binaries

J. Poutanen (✉) · A. Veledina
Astronomy Division, Department of Physics, PO Box 3000, 90014 University of Oulu, Finland
e-mail: juri.poutanen@gmail.com

A. Veledina
e-mail: alexandra.veledina@oulu.fi

Published online: 01 January 2014

1 Introduction

Models for accretion onto a black hole (BH) have been discussed now for more than 40 years. During the last 10–15 years we have seen a dramatic increase in the amount of information on the BH X-ray binaries (BHBs). Spectral details (iron lines and Compton reflection), spectral transitions, and variability on various time scales has been studied in unprecedented details with the new generation X-ray telescopes such as *Rossi X-ray Timing Explorer (RXTE)* and *XMM-Newton*. Excellent recent reviews are devoted to these advances (Zdziarski and Gierliński 2004; Remillard and McClintock 2006; Done et al. 2007; Done 2013; Gilfanov 2010).

In addition to the X-ray data, we have seen an explosion of information coming from other wavelengths: radio, sub-mm, infrared, optical, UV, MeV and nowadays even from the GeV range. What is even more spectacular is that the properties of the BHs at these other wavebands are correlated with the X-ray flux and X-ray states. Among the most impressive achievements we find the discovery of correlated fast variability in the optical/infrared (OIR) band and in the X-rays (Kanbach et al. 2001; Durant et al. 2008; Gandhi et al. 2008) with some hints actually coming already 30 years ago (Motch et al. 1983). This got theoreticians to scratch their heads and invent new models that often were in disagreement with previously established theories and contradicted many other available data.

Here we discuss some of the recent discoveries. We would like to note that the time for theoretical (phenomenological) models based purely on spectral properties are long gone. In order to be considered seriously, any model has to address many observed facts together.

This review consists of two parts. In the first one, we discuss the most recent reincarnation of the hot flow model, which now also considers the role of the non-thermal particles. In the second part, we discuss recent observational advances. We review the spectral data in various energy bands concentrating on the X-rays and the OIR. Then we discuss the observed temporal properties and correlated variability in different energy bands, as well as more complicated temporal-spectral statistics such as Fourier resolved spectra. In this review we will concentrate on the hard state and interpret the observations in terms of the hot flow model.

2 Hot Flow Models

2.1 Comptonization Models for the X-Ray Emission

At high accretion rates exceeding typically 10 % of the Eddington value, BHs are in the "soft state" and have thermally looking spectra peaking in the standard 2–10 keV X-ray band, which are consistent with the thin α-disc model (Shakura and Sunyaev 1973; Novikov and Thorne 1973). These thermally-dominated spectra presumably depend only on the accretion rate, the BH mass and spin and the inclination. They potentially can be used to determine the BH spin if the distance to the source and e.g. the BH mass and inclination are known (see McClintock et al. 2013). However, often strong power-law tails are seen (see Fig. 2). This tails are interpreted as a signature of non-thermal "corona" atop of the standard Shakura-Sunyaev disc (Fig. 1b).

At the lower accretion rate, BHs are often found in the "hard state" and their spectra do not even remotely look thermal, but are close to the power-law in the X-ray band with a sharp cutoff at about 100 keV (e.g. Gierlinski et al. 1997; Zdziarski et al. 1998). These are well described by the thermal Comptonization model (see Zdziarski et al. 1997; Poutanen

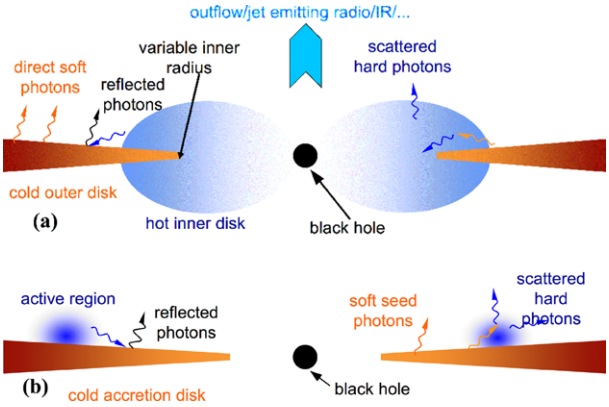

Fig. 1 (**a**) A schematic representation of the likely geometry in the hard state, consisting of a hot inner accretion flow surrounded by optically-thick cold accretion disc. The hot flow constitutes the base of the jet (with the counter-jet omitted from the figure for clarity). The disc is truncated far away from the minimum stable orbit, but it may overlap with the hot flow. The soft photons emitted by the disc (and possibly internally produced synchrotron photons) are Compton upscattered in the hot flow, and emission from the hot flow is partly Compton-reflected from the disc. (**b**) The likely geometry in the soft state consisting of flares/active regions above an optically-thick accretion disc extending close to the minimum stable orbit. The soft photons emitted by the disc are Compton upscattered in the flares by non-thermal electrons producing power-law spectra extending to γ-rays. Emission from the flares is partly Compton-reflected from the disc. From Zdziarski and Gierliński (2004)

1998, for reviews). The nature of the hard state emission and origin of the hot electrons has been already discussed in the 1970s (Shapiro et al. 1976; Ichimaru 1977) and is commonly associated with either a hot inner flow close to the BH (Esin et al. 1997, 1998; Poutanen et al. 1997; Narayan et al. 1998; Yuan and Zdziarski 2004) or a corona above the accretion disc (Galeev et al. 1979; Haardt and Maraschi 1993; Haardt et al. 1994; Stern et al. 1995b; Poutanen and Svensson 1996; Beloborodov 1999b, see Fig. 1a for a possible geometry).

Knowing the slope of the hard state spectra (with photon index $\Gamma = 1.6$–1.8) we can easily estimate the ratio of the total emitted power L to the soft seed photon luminosity $L_{\rm s}$ entering Comptonization region, i.e. the amplification factor $A = L/L_{\rm s}$. Beloborodov (1999a) found an approximate relation between Γ and A for the Comptonized spectra:

$$\Gamma = \frac{7}{3}(A-1)^{-\delta}, \tag{1}$$

where $\delta = 1/6$ for BHBs and $\delta = 1/10$ for AGNs and the typical seed photon temperatures of 0.2 keV for BHBs and 5 eV for AGNs were assumed. If indeed the disc photons are being Comptonized, we get $A \approx 10$ for BHBs in their hard state. This fact puts serious constraints on the geometry of the emission region (Poutanen 1998; Beloborodov 1999a) and immediately rules out simple slab-corona models which predict much smaller amplification $A \lesssim 2$ and softer spectra because of the efficient X-ray reprocessing in the cold disc (Stern et al. 1995b). Assuming that coronal plasma has a mildly relativistic velocity away from the cold disc (Beloborodov 1999b; Malzac et al. 2001) one can in principle reconcile that model with the observed slopes as well as with the correlated changes of the spectral hardness and the amount of Compton reflection from the disc, but still one would have troubles explaining their correlations with the iron line width and characteristic variability frequencies (see Sect. 3.1).

If the accretion flow geometry is such that the inner part is occupied by the hot flow and the outer is the standard cold disc, the seed photons for Comptonization might be internal to the hot flow or come from the outer disc. For the truncation radius of the cold disc of more than $30R_{\rm S}$ (where $R_{\rm S}=2GM/c^2$ is the Schwarzschild radius), most of the disc photons go directly to the observer and therefore the disc should be very prominent in the total spectrum. Furthermore, the luminosity in disc photons being Comptonized in the region of major gravitational energy release ($<10R_{\rm S}$) would be only about 1 % of the total luminosity resulting in an amplification factor of a hundred and a very hard Comptonization spectrum (see Eq. (1)). Neither is observed. An overlap of the inner hot flow with the cold disc (Poutanen et al. 1997; see Fig. 1a) was proposed as a solution to this, but does not really solve the problem, because most of the energy is dissipated within $10R_{\rm S}$. Thus the disc should come to radii below $10R_{\rm S}$. Another solution is that cold clouds embedded into the flow reprocess hard photons (Celotti et al. 1992; Krolik 1998; Zdziarski et al. 1998; Poutanen 1998) increasing thus the number of seed soft photons.

Alternatively, the hot flow itself can generate enough soft photons by synchrotron emission of the same hot electrons that emit the X-rays, if the electron temperature $T_{\rm e}$ is sufficiently high to overcome the self-absorption problem. The spectrum from the hot optically thin advection-dominated accretion flows (ADAF) indeed is produced mostly by synchrotron self-Compton (SSC) mechanism (Narayan and Yi 1994, 1995; Narayan et al. 1998; Yuan and Narayan 2014). Detailed radiative transfer calculations accounting for non-local Compton effect coupled with dynamics (also in the Kerr metric) predict, however, $T_{\rm e}$ exceeding the observed values of 50–100 keV by at least a factor of 2 (see Fig. 3 in Yuan et al. 2007, Fig. 1d in Xie et al. 2010 and Figs. 5 and 6 in Niedźwiecki et al. 2012). Most of the problems get solved if the electrons have a reasonably strong non-thermal tail. In this case, synchrotron emission becomes much more efficient (Wardziński and Zdziarski 2001) increasing the cooling, softening the spectrum and lowering $T_{\rm e}$ to the values which agree with observations. This is the essence of the hybrid Comptonization (or rather hybrid SSC) models developed for bright accreting BHs (Poutanen and Coppi 1998; Coppi 1999; Poutanen and Vurm 2009; Malzac and Belmont 2009; Veledina et al. 2011b, 2013a) that are described below in more details. Non-thermal electrons can also play a role in low-luminosity systems such as Sgr A* (Mahadevan 1998; Özel et al. 2000; Yuan et al. 2003). However, in these conditions the equilibrium electron temperature is very high ($\sim$ MeV) and the optical depth is very low, so that thermal synchrotron radiation is very effective. The role of the non-thermal electrons is then reduced to production of tails at higher and lower frequencies around the dominating thermal synchrotron peak.

2.2 Hybrid Comptonization Model

Arguments in favour of the presence of non-thermal particles in the accretion flow come from the significant detection of the MeV tails in the hard state spectra of Cyg X-1 (see McConnell et al. 1994, 2002; Ling et al. 1997; Jourdain et al. 2012a; Zdziarski et al. 2012, see Fig. 2) and marginally in GX 339–4 (Droulans et al. 2010). Also in the soft state, power-law tails extending to hundreds of keV and up to possibly 10 MeV are present (Grove et al. 1998; Gierliński et al. 1999; Zdziarski et al. 2001; McConnell et al. 2002, see Fig. 2) and are well described by non-thermal/hybrid Comptonization (Poutanen 1998; Poutanen and Coppi 1998; Gierliński et al. 1999; Coppi 1999). What is the nature of the non-thermal particles is an open question.

On the theoretical ground, it is expected that the electrons get some of the energy via Coulomb collisions with hot, nearly virial protons (as assumed in ADAF models) or diffu-

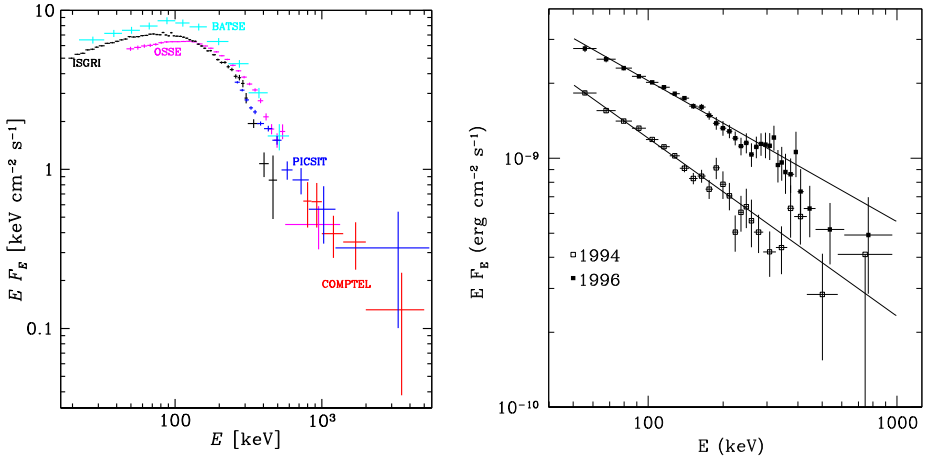

Fig. 2 Hard (*left panel*) and soft (*right*) state spectra of Cyg X-1. From Zdziarski et al. (2012) and Gierliński et al. (1999)

sive acceleration by MHD turbulence, resulting in "thermal heating", i.e. energy is transferred to the thermal population of electrons. However, some fraction of the energy can be transferred to them in the form of injection of relativistic electrons by shock acceleration (Fragile and Blaes 2008; Das et al. 2009; Henisey et al. 2012), magnetic reconnection (Ding et al. 2010; Riquelme et al. 2012; Hoshino 2013), or electron-position pair production by decay of pions born in proton-proton collisions (Mahadevan 1998). Because the microphysics of electron acceleration and heating in the hot flow is not well established from first principles, one can use a phenomenological prescription, where some fraction of the total power is given to the electrons as heating and the rest of the energy is given by non-thermal injection of power-law electrons. Such hybrid thermal/non-thermal models are reviewed by Coppi (1999). Models with the least number of free parameters are either purely thermal or purely non-thermal. Because the first option clearly contradicts the data, we consider in the following the second non-thermal option. Of course, the assumption that the electrons receive 100 % of their energy in the form of non-thermal injection is not realistic. Fortunately, the results are not very sensitive to the actual value of non-thermal injection fraction as long as it exceeds 10 % (see Appendix B1 in Veledina et al. 2013a). The reason is that even for pure non-thermal injection the steady-state electron distribution is thermal at low energies due to thermalisation via Coulomb collisions between electrons as well as via synchrotron self-absorption (Ghisellini et al. 1988, 1998; Nayakshin and Melia 1998; Vurm and Poutanen 2009). At higher energies a tail develops, whose shape is determined by the injection and the competition between various cooling/thermalisation mechanisms.

The most advanced hybrid models solve simultaneously for the momentum distribution of all considered particles, electrons and positrons (sometimes also protons), as well as the photons. This either can be done via Monte-Carlo simulations (e.g. Stern et al. 1995a), or by solving coupled kinetic equations (Coppi 1992, 1999; Belmont et al. 2008; Vurm and Poutanen 2009). The processes that need to be accounted for under the conditions of the hot flows are Compton scattering, synchrotron emission and absorption, pair production, Coulomb collisions (between leptons as well as with protons), and bremsstrahlung. The radiative transfer can be easily handled exactly with Monte-Carlo approach, while usually with the kinetic approach an escape probability formalism in a single-zone approximation is

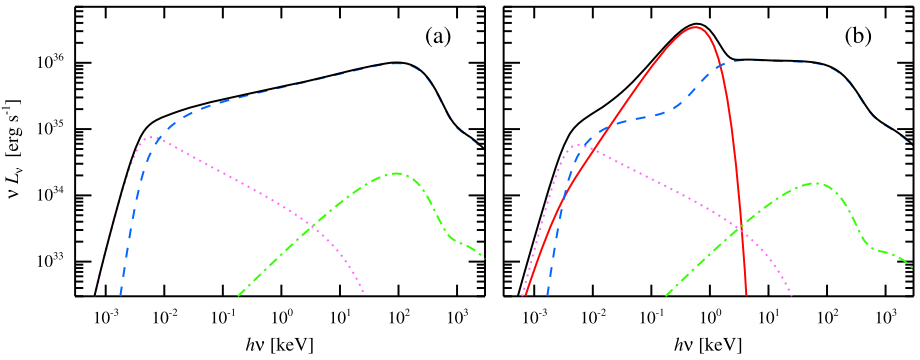

Fig. 3 Spectrum from the one-zone hot flow. (**a**) Spectral decomposition of the hybrid SSC model. The pink dotted line is the non-thermal synchrotron, the blue dashed is its Comptonization spectrum, and the *green dot-dashed curve* is the bremsstrahlung component. (**b**) Same as (**a**), but with the disc photons (*red triple-dot-dashed curve*) dominating the seed photons distribution. Now below 1 keV Comptonization spectrum is produced by SSC, while at higher energies Comptonization of the cold disc photons dominates

used. A single-zone approximation works reasonably well if most of the escaping radiation at all wavelengths is dominated by some narrow range of radii. For the X-ray production this is fine, because most of the energy is dissipated in the accretion flow spread from say $3R_{\rm S}$ to $10R_{\rm S}$. On the other hand, this approximation fails in the OIR. Here the outer zones of the hot flow can dominate the energy output in those bands as the inner zones are opaque for that radiation. Because the radiation from the inner zones can affect the energy balance and the escaping radiation from the outer zones, a multi-zone treatment with the radiative transfer is required (Veledina et al. 2013a).

The simplest model is described by the size, the magnetic field strength B, Thomson optical depth τ, the total injected power L, the spectrum of the injected electrons and the spectrum and luminosity of the external (blackbody/cold accretion disc) photons. For an extended multi-zone flow one can assume that the electron energy injection rate as well as B and τ have power-law distributions with radius, $B(R) \propto R^{-\beta}$, $\tau(R) \propto R^{-\theta}$ and thus the additional parameters, e.g., β and θ have to be introduced. Many parameters can be directly determined from observations or taken from theoretical accretion disc models. Now let us describe the main properties of such hybrid models.

2.3 Basic Properties of Hybrid Accretion Flows

If the truncation radius of the cold disc is significantly larger than the region of the major energy dissipation (i.e. $R_{\rm tr} > 30R_{\rm S}$), then the X-ray spectrum is dominated by the radiation from the innermost zone of the hot flow. Here locally generated non-thermal synchrotron photons are Comptonized by the thermal electron population (see Fig. 3a). Here we note that the internally generated synchrotron photons are much more efficient in cooling the plasma than the external disc photons. The first obvious difference comes from the geometry: all synchrotron photons are injected within the hot flow and have a chance to be Comptonized, while in the disc case only a small fraction gets to the hot flow. The second difference comes from the fact that the synchrotron photons have much smaller energies than the cold disc photons. Therefore, in order to produce the same spectral slope of the Comptonization continuum (with nearly the same total power), the synchrotron luminosity can be smaller by a factor a several than the disc luminosity intercepted by the hot flow. In other words, the

amplification factor given by Eq. (1) is now closer to 50 than 10 (because we need to use $\delta \approx 1/10$).

At a few per cent of the Eddington luminosity corresponding to the bright hard state, the low-energy electrons are thermalised by Coulomb collisions and synchrotron self-absorption to the typical electron temperatures T_e of about 100 keV (Poutanen and Vurm 2009; Malzac and Belmont 2009; Veledina et al. 2011b). The hybrid model produces surprisingly stable spectra with photon index $\Gamma \sim 1.6$–1.8 largely independent of the model parameters (Fig. 3a). The high-energy electron tail can be approximated by a power-law, which is softer than the injected distribution due to the cooling. The observed MeV tail is produced by Compton up scattering of the 100 keV photons by these non-thermal electrons. The outer zones of the hot flow have softer spectra because of the additional cooling by the cold disc photons and because of more transparent conditions for the synchrotron radiation (see Fig. 3b). The overall X-ray spectrum is thus concave.

The OIR spectrum consists of two components: the multi-colour (possibly irradiated) cold accretion disc and the synchrotron radiation from the hot flow. Similarly to the inhomogeneous synchrotron models developed for extragalactic jets (Marscher 1977; Blandford and Königl 1979), the non-thermal synchrotron spectrum of the hot flow is a power-law $F_\nu \propto \nu^\alpha$ with the index (Veledina et al. 2013a):

$$\alpha_{\rm OIR} = \frac{5\theta + \beta(2p+3) - 2p - 8}{\beta(p+2) + 2\theta}, \tag{2}$$

where p and θ are the indices of the equilibrium distribution of electrons, $n_e(R, \gamma) \propto R^{-\theta}\gamma^{-p}$, at Lorentz factor γ emitting at the self-absorption frequency. Typically, spectral indices are $\alpha_{\rm OIR} \sim 0 \pm 0.5$. The turn-over at longer wavelengths is determined by the extent of the hot flow, while the transition to the optically thin synchrotron emission is hidden by the Comptonization spectrum (Fig. 3a).

The disc spectrum can be split also into two components: the inner warmer standard disc heated by viscous forces and the outer cooler disc heated by the X-rays. In the OIR one expects the dominance of the irradiated disc, which has the radial temperature dependence $T_{\rm irr} \propto R^{-3/7}$ (Cunningham 1976). Presence of the irradiated disc can be reflected in the optical echoes (Hynes et al. 1998; O'Brien et al. 2002), the X-ray time-lags (see Poutanen 2002, and references therein) and in the optical/X-ray cross-correlation function (Hynes et al. 2009a; Veledina et al. 2011a). Its signatures are also seen in the spectrum (e.g., Hynes et al. 2002; Gierliński et al. 2009). For typical parameters of LMXBs with the disc size of 10^{11} cm and the X-ray luminosity of 10^{37} erg s^{-1} the temperature of the outer disc is about $T_{\rm irr} \sim 20\,000$ K. The relative role of the components varies with the wavelength. The disc spectrum is hard in the OIR band, while the hot flow produces an excess emission dominating below $\sim$1 eV (see Fig. 4a and Fig. 6).

At smaller accretion rates below a few percent of the Eddington value, the flow becomes more transparent to the synchrotron photons leading to their increasing role in cooling and resulting in slightly *softer* X-ray spectra (Veledina et al. 2011b). At higher accretion rates associated with the transition to the soft state (see Fig. 4), the outer zones of the hot flow gradually collapse, so that the disc truncation radius $R_{\rm tr}$ decreases (Poutanen et al. 1997; Esin et al. 1997). This leads to the rising role of the disc as a source of seed photons, which increases Compton cooling, leads to spectral softening and causes changes in the electron distribution from mostly thermal to nearly non-thermal (Poutanen and Coppi 1998; Poutanen and Vurm 2009; Malzac and Belmont 2009; Veledina et al. 2011b). This transition is accompanied by the increase in the reflection amplitude that scales with the solid angle at which the cold disc is seen from the hot flow. The OIR hot flow luminosity drops first

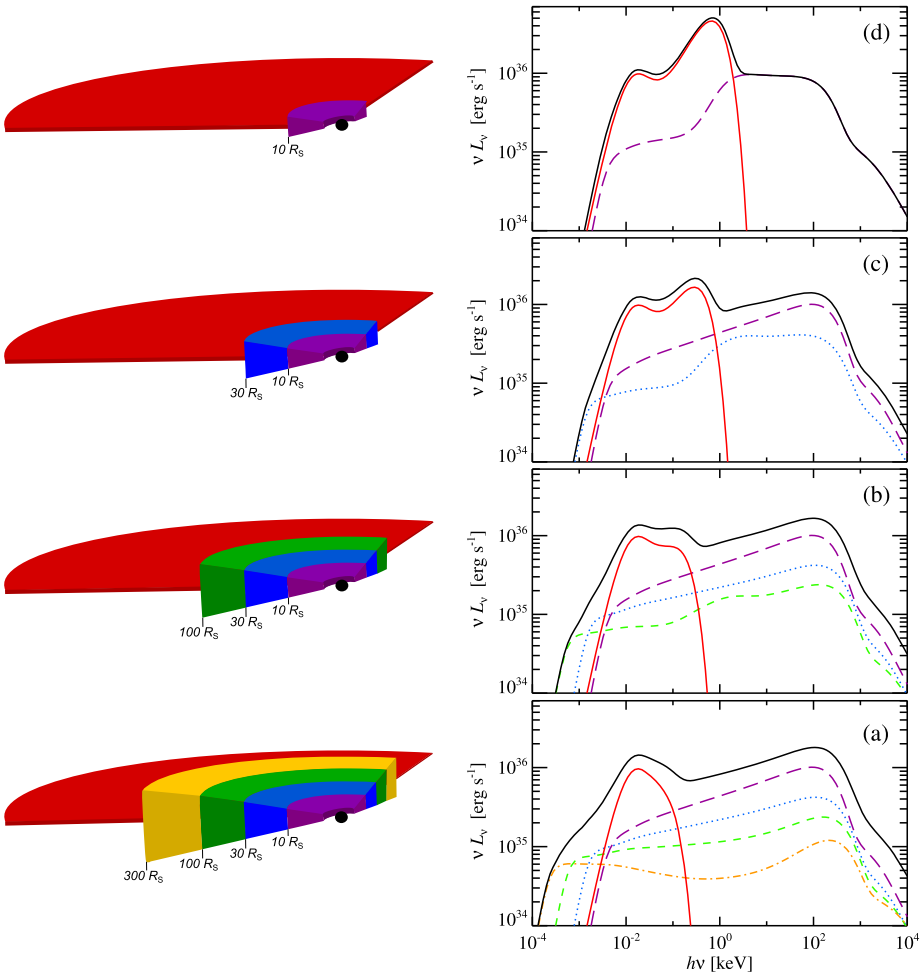

Fig. 4 *Left panels*: Schematic picture of the evolution of the hot flow size during spectral state transitions. In the low-luminosity hard state, the geometrically thick inner hot flow is large dominating the radiative energy output. With increasing accretion rate (from lower to upper panels) the outer zones of the hot flow gradually collapse swallowed by the cold thin accretion disc. For illustrative purposes, the hot flow is split into four zones with outer radii $10R_S$ (*violet*, zone 1), $30R_S$ (*blue*, zone 2), $100R_S$ (*green*, zone 3) and $300R_S$ (*yellow*, zone 4). *Red* outer component represents the truncated cold accretion disc. *Right panels*: corresponding spectral evolution at the state transition. Contribution of different zones are marked with different lines: zone 1 (*violet long-dashed*), zone 2 (*blue dotted*), zone 3 (*green short-dashed*), zone 4 (*orange dot-dashed*) and outer cold irradiated disc (*red three-dot-dashed*). At the *lower panel*, the hot flow spectrum was calculated not accounting for the seed photons from the disc. An IR excess is clearly visible above the irradiated disc spectrum. Collapse of the hot flow leads to dramatic changes in the OIR hot flow synchrotron spectrum. Changes in the X-ray spectral shape are insignificant until the truncation radius becomes as small as $10R_S$. The Comptonization spectrum from the hot-flow zone closest to the cold disc consists of two separate continua produced by Comptonization of the synchrotron and the cold disc photons, with the latter being dominant source of seed photons in this zone (see also Fig. 3b). For simplicity, in this illustration the total luminosity is kept constant. Adapted from Veledina et al. (2013a)

at longer wavelengths, where the outer zones radiate (see Fig. 4). Note that the X-ray spectrum changes much later, when the truncation radius comes closer to the zone of the main energy dissipation of about $10R_S$. At this moment, the Comptonization spectrum of the remaining hot flow consists of two segments: the hybrid SSC dominates at lower energies, while Comptonization of the disc photons takes over at energies above the cold disc peak (see Fig. 3b). Similarly curved spectra are expected for the hot flow zones closest to the cold disc (Fig. 4). The corresponding time delay between sharp luminosity changes at different wavelengths scale with the timescale of state transition and, depending on the separation of the wavelengths and accretion parameters, can be as short as hours (e.g., if one observes in different optical filters), as long as a few days (e.g., IR and UV) or weeks (e.g. IR and X-rays). The opposite evolution should be observed in the soft-to-hard spectral transition when the accretion rate drops after the outburst peak. Here first the X-ray spectral transition starts and at a timescale of a week or so the emission in the OIR peaks, when the size of the hot flow becomes large enough for the OIR synchrotron photons to escape.

At a high accretion rate, the accretion disc extends to the last stable orbit and the source switches to the soft state. In this case, no inner hot flow exists, but a non-thermal magnetically powered corona still could be present (Fig. 1b). Its presence is supported by the existence of the X-ray/γ-ray power-law tails. The non-thermal synchrotron from the corona may be present in the OIR band, but at a much lower level, because the electron cooling is dominated now by Comptonization of the disc photons. Actually, such a non-thermal corona atop the cold disc (in addition to the hot inner flow) may be present also in the hard state, but its emission scaled with the cold disc luminosity is weak.

3 Observational Properties

3.1 X-ray/γ-Ray Spectra

Let us first briefly summarise what we know about the spectral properties of BHBs. Further details can be found in reviews by Poutanen (1998), Zdziarski and Gierliński (2004), Done et al. (2007), and Done (2013). In the hard-state, the spectra constitute a power-law in the X-ray band with a rather stable spectral slope (with photon index $\Gamma \sim 1.6-1.9$ and ubiquitous sharp cut-off at around 100 keV (Gierlinski et al. 1997; Zdziarski et al. 1998; Ibragimov et al. 2005; see Fig. 10a in Zdziarski and Gierliński 2004). The shape of the spectra allows us to conclude that they are produced by (nearly) thermal Comptonization (e.g. Poutanen 1998; Zdziarski and Gierliński 2004, see Fig. 5). When the high-quality data above 100 keV were available (e.g. with OSSE/*CGRO* or IBIS/*INTEGRAL* or HXD-GSO/*Suzaku*) the electron temperature (measured with the accuracy of about 10 %)[1] was always lying in the interval 50–120 keV (e.g. Gierlinski et al. 1997; Zdziarski et al. 1998; Poutanen 1998; Aref'ev et al. 2004; Makishima et al. 2008), with temperature increasing with decreasing luminosity. The hard-state accreting BHBs also show weak but distinctive MeV tails (McConnell et al. 1994, 2002; Ling et al. 1997; Droulans et al. 2010; Jourdain et al. 2012a; Zdziarski et al. 2012, see

[1]Note that the electron temperature can be measured only if high-quality data are available above 100 keV and accurate Comptonization models such as COMPPS (Poutanen and Svensson 1996) or EQPAIR (Coppi 1999) are used for fitting. Using the exponentially cut-off power-law for the fits and identifying the e-folding energy with the electron temperature is dangerous, because that model does not correctly describe the shape of Comptonization continuum (see e.g. Fig. 5 in Zdziarski et al. 2003). This can result in over-estimation of T_e by a factor of 3–6.

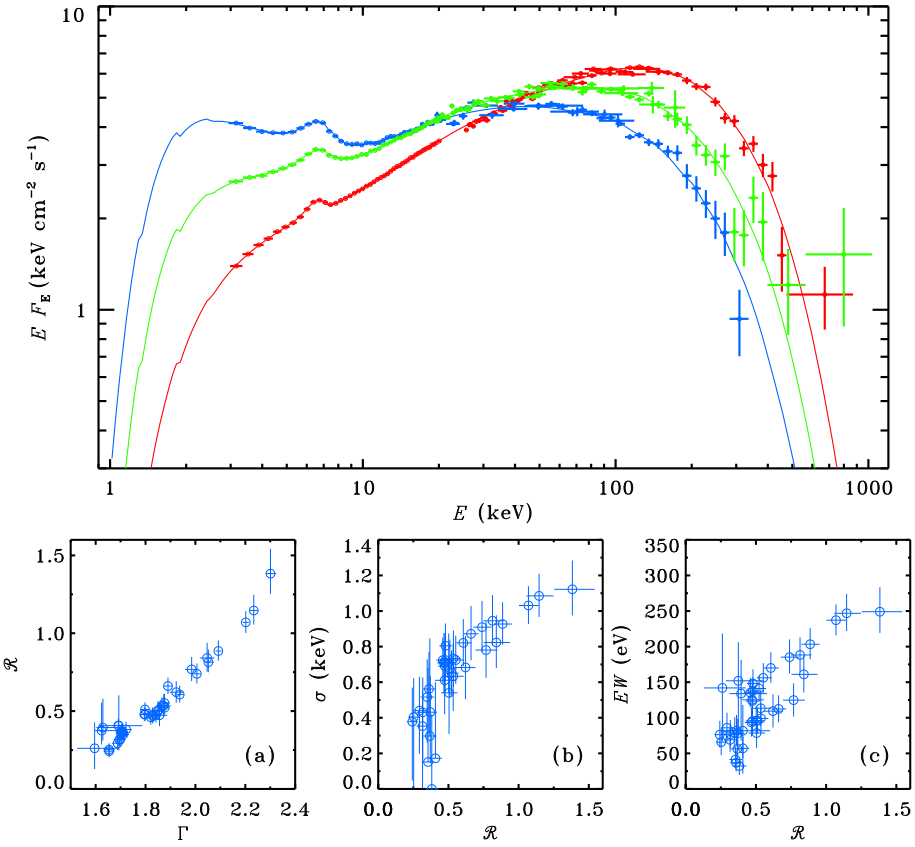

Fig. 5 Spectral variations of Cyg X-1 in its hard/intermediate state as shown in the top panel. The lower panels show correlation between the amplitude of Compton reflection $\mathcal{R}$, photon spectral index Γ, width σ and the equivalent width of the iron line. Adapted from Ibragimov et al. (2005)

Fig. 2). Such spectra are consistent with the hybrid hot-flow model. During the transition to the soft state, T_e is reduced. However, because of the growing importance of non-thermal tail, the spectral cutoff energy may actually increase (Poutanen and Vurm 2009).

The fact that the spectra are stable in the hard state with variable luminosity and never have $\Gamma < 1.6$ argues in favour of the hybrid SSC as the main emission mechanism. If the outer cold disc were the seed photons provider, one expects harder and strongly variable spectra when the truncation radius is changing in the soft-to-hard transition. Moreover, the best studied BHs, Cyg X-1 and GX 339–4, clearly have a concave spectrum that can be fitted with two Comptonization continua (Frontera et al. 2001; Ibragimov et al. 2005; Makishima et al. 2008; Shidatsu et al. 2011; Yamada et al. 2013). The inhomogeneous hot flow model naturally explains such spectra by the radial dependence of the slope of Comptonization spectrum. The spectral curvature can also appear if a non-thermal corona (similar to that producing power-law tail in the soft state) exists above the cold disc during the hard state too (Ibragimov et al. 2005).

In addition to the smooth continuum, in both states a Compton reflection feature and the fluorescent iron line at 6.4 keV originating from cool opaque matter (likely the cool accretion disc) are often detected. The strength of Compton reflection is correlated with the

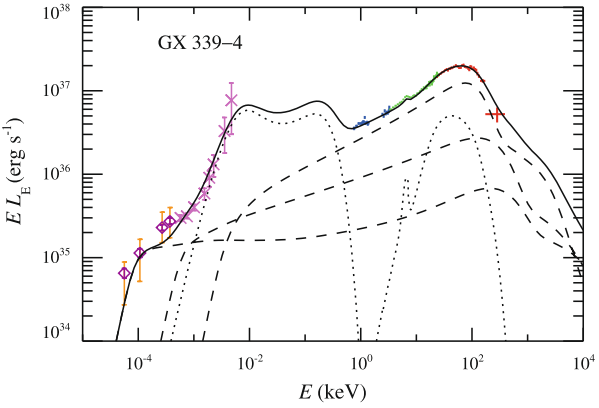

Fig. 6 Broad-band spectrum (corrected for absorption) of GX 339–4 in its hard state around March 5, 2010 from the mid-IR to the hard X-rays (Cadolle Bel et al. 2011). The *dashed lines* show contribution of different zones of the hot accretion flow (Veledina et al. 2013a), the *dotted lines* represent the spectra of the irradiated and standard discs as well as Compton reflection. From Veledina et al., in prep.

X-ray slope (Zdziarski et al. 1999, 2003), with the width of the iron line as well as with the quasi-periodic oscillation (QPO) frequency (Gilfanov et al. 1999; Revnivtsev et al. 2001; Ibragimov et al. 2005; Gilfanov 2010, see lower panels in Fig. 5). During the outbursts of BH transients, in the hard state the iron line width correlates well with the luminosity (Kolehmainen et al. 2014). These data are consistent with the hot-flow paradigm where all correlation are basically controlled by the cold disc truncation radius.

At luminosities above a few per cent of Eddington, BHBs show a strong correlation between spectral index and luminosity. At lower luminosities the trend is reversed, i.e. spectra become softer with decreasing luminosity (Wu and Gu 2008; Sobolewska et al. 2011). Similarly, an indication of the reverse trend was detected in low-luminosity AGNs (Constantin et al. 2009; Gu and Cao 2009). This was interpreted as a change of the source of seed photons for Comptonization from the disc photons dominating at higher luminosities to the synchrotron at lower luminosities. The whole spectral index—luminosity dependence is well explained by the hybrid hot flow model (see Figs. 7 and 12 in Veledina et al. 2011b). At very small luminosities, the flow becomes more transparent for the synchrotron radiation increasing the photon input and softening the Comptonization spectra.

3.2 Broad-Band Spectra and Infrared Flares

Numerous multiwavelength campaigns were conducted over the past decade. Broadband radio to X-ray spectral energy distributions (SEDs) for many BHBs were constructed (e.g. Hynes et al. 2000; McClintock et al. 2001; Chaty et al. 2003; Cadolle Bel et al. 2007, 2011; Durant et al. 2009). The OIR emission is normally dominated by the (irradiated) disc, but the IR excesses are observed in a number of sources: XTE J1859+226 (Hynes et al. 2002), GX 339–4 (Gandhi et al. 2011; Shidatsu et al. 2011; Buxton et al. 2012; Dinçer et al. 2012; Rahoui et al. 2012), A0620–00 (Gallo et al. 2007), SWIFT J1753.5–0127 (Chiang et al. 2010), V404 Cyg (Hynes et al. 2009b), XTE J1550–564 (Jain et al. 2001; Russell et al. 2011). In some cases the OIR spectrum can be described by a pure power-law $F_\nu \propto \nu^\alpha$ with index α close to zero (e.g. $\alpha_{\rm OIR} = -0.15$ in XTE J1118+480, see Esin et al. 2001; Chaty et al. 2003). Sometimes the OIR excess spectrum is rather soft with $\alpha \approx -0.7$ (see Kalemci et al. 2013, for a recent overview). The IR excesses were previously explained by the jet (Hynes et al. 2002; Gallo et al. 2007) or the dust heated by the secondary star (Muno and Mauerhan 2006). Veledina et al. (2013a) recently argued that the OIR excess emission may also be produced by synchrotron radiation from the hot flow.

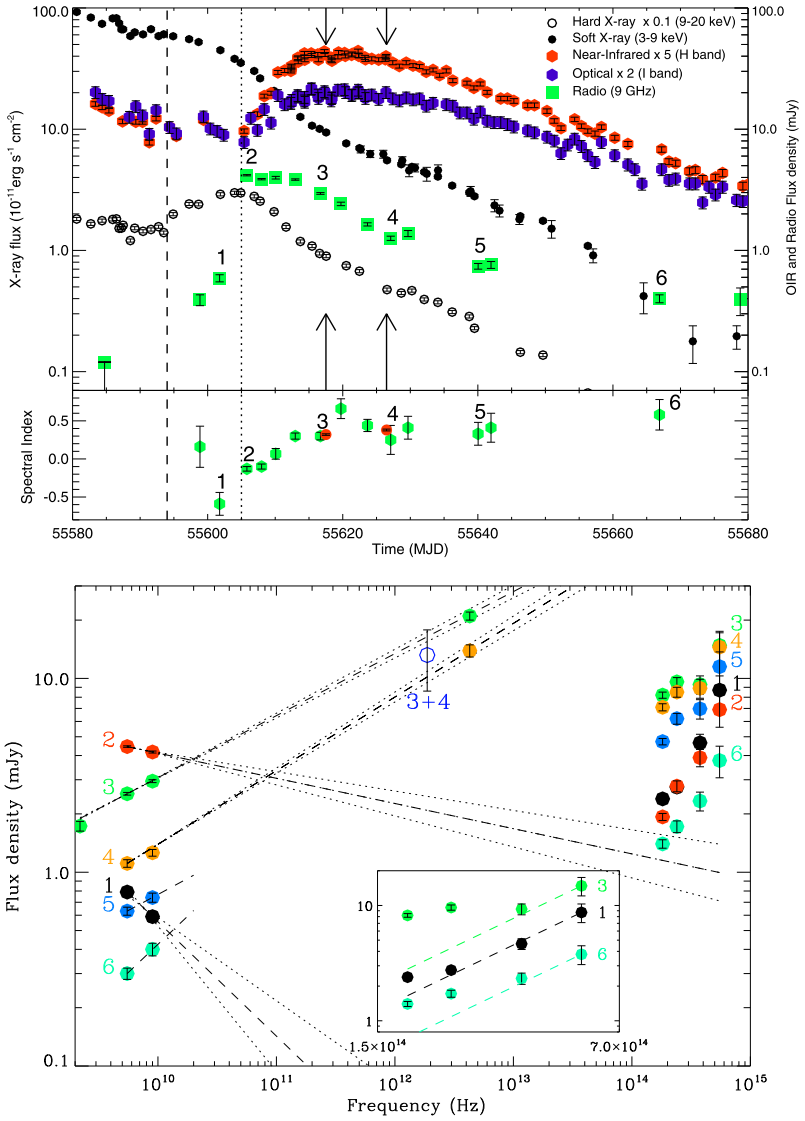

Fig. 7 *Upper panel*: The lightcurves of GX 339–4 during the decay of the 2010–2011 outburst in radio (*green*), NIR (*red*), optical (*blue*), soft X-ray (*filled black circles*) and hard X-ray (*open black circles*). The *bottom sub-panel* shows the evolution of the radio spectral index. The *dashed vertical line* indicates the start of the soft-to-hard state transition, while the *dotted line* marks the start of the OIR flare and the end of the transition (see Fig. 1 in Dinçer et al. 2012). The numbers refer to the individual observations displayed in the *lower plot*. *Lower panel*: Evolution of the radio to OIR spectra of GX 339–4. The *inset* zooms on the OIR spectra, with the *dashed lines* corresponding to power-law with $\alpha = 1.5$ (for an irradiated disc). From Corbel et al. (2013)

Here we only discuss a few representative examples of the recent studies. The broad-band spectrum of GX 339–4 in its hard state (Cadolle Bel et al. 2011, 2013) is shown in Fig. 6. The X-ray spectrum peaking at ∼100 keV is well described by thermal Comptonization. The irradiated disc presumably dominates in the UV band. There is a clear excess in the mid-

and near-IR (Gandhi et al. 2011), but the spectrum becomes harder at longer wavelengths. These data are well explained by the non-thermal synchrotron emission from the hot flow (Veledina et al. 2013a) of about $500R_S$.

Excellent data covering both radio and OIR bands have been collected during the 2010–2011 outburst of GX 339–4 (Cadolle Bel et al. 2011; Dinçer et al. 2012; Corbel et al. 2013, see Fig. 7). A week after the start of the transition to the hard state (marked by the vertical dashed line) the OIR spectrum has a clear soft excess above the reprocessing thermal emission (point 1), while the radio jet optically thin emission can contribute at most 1 % to the OIR. Few days later, when the transition was completed (point 2), the fluxes in the H and I-band show a sharp increase and an obvious IR excess in the OIR spectra is visible, while the radio emission is still soft with $\alpha \sim -0.1$. On a week time scale the radio spectrum transits to the harder, optically thick state with $\alpha \sim 0.5$ (point 3) corresponding to the synchrotron emission from an inhomogeneous source analogously to the extragalactic jets (Blandford and Königl 1979). The radio spectrum stays hard and the IR excess is visible during the following decay. The high flux in the *Herschel* far-IR band lies exactly on the extrapolation of the radio spectra. Because after the break, the jet spectrum must be optically thin and soft, while the OIR spectra are flat (even after subtracting thermal component, as discussed by Dinçer et al. 2012; Buxton et al. 2012; Corbel et al. 2013), the jet does not contribute significantly to the OIR bands. An important conclusion from these data is that there is a rather strong, evolving component in the OIR band which cannot be produced by the jet or reprocessing in the accretion disc at any stage of the outburst. Its appearance in the hard state is, however, consistent with the hot flow interpretation.

The IR excess similar to that seen in GX 339–4 in the hard state appears also in XTE J1550–564 (Jain et al. 2001), 4U 1543–47 (Buxton and Bailyn 2004) and XTE J1752–223 (Russell et al. 2012). The properties of the excess can be studied using the colour-magnitude diagram (see Fig. 8c). During the 2000 outburst of XTE J1550–564 the data in the soft state, soft-to-hard transition and at very low-luminosity hard state can be adequately described by the reddened irradiated disc emission. Both at the rising (filled symbols) and decaying (open symbols) phase of the outburst, we see "flares" during which the spectrum becomes redder. One can interpret these flares as the appearance of the additional red component. Fitting the fluxes at the decaying stage with an exponential plus a constant, one can subtract the contribution from the irradiated disc and obtain a spectrum of the flare component only. We see that the second flare starts with the spectral index $\alpha \sim +0.7$, then becomes softer with $\alpha \sim -0.2$, and then harder again (see green arrows in Fig. 8). (The final points have large errors, because of the uncertainties in the subtraction of the disc.) What is important that the flare starts in I before H, so that the index measured between filters I and H is even larger, $\alpha_{IH} \approx 1.0$. This behaviour rules out immediately the interpretation of the flare in terms of optically thin jet emission.[2] Instead the data are consistent with the inhomogeneous hot accretion flow model of Veledina et al. (2013a). Such indices were also observed in the flare spectrum of XTE J1752–223 (Russell et al. 2012) and GX 339–4 (Dinçer et al. 2012; Buxton et al. 2012). This would mean that all these OIR flares are produced by the hot

[2]Colour-magnitude diagram for the 2000 outburst of XTE J1550–564 was constructed by Russell et al. (2011), who also related the observed colours to the intrinsic spectral indices and claimed very soft spectrum of the flare. Unfortunately, all their formulae are wrong for various reasons and the actual intrinsic spectra are much harder. Furthermore, the exponential fits to the OIR light curves to evaluate the flare spectrum were also flawed, as their fits overestimate the disc contribution in the V and I filters just before the flare (see Fig. 2 in Russell et al. 2010) resulting in over-subtraction of the flux in those filters and in a much too soft spectrum of the flare (compare our $\alpha \sim +0.7$ at the start of the flare with their $\alpha \sim -1.6$).

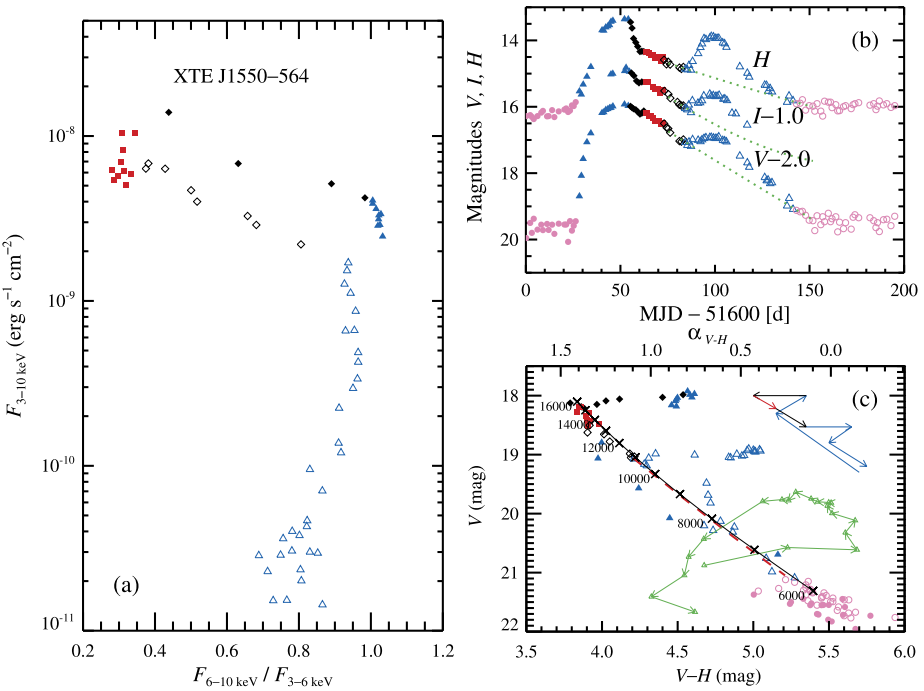

Fig. 8 (**a**) X-rays flux—hardness diagram for XTE J1550–564 during the 2000 outburst. Different colours indicate various stages of the outburst based on their X-ray hardness. The *blue colour* indicate the hard state, the *black colour* is the transition and the *red colour* the soft state. *Open* and *closed symbols* correspond to the rising and decaying outburst stages, respectively. (**b**) The *light curves* in V, I and H-filters of XTE J1550–564 (Jain et al. 2001). The *pink circles* correspond to the quiescent state. The *green dotted curves* show the best-fit model for the decaying disc component. (**c**) The observed V vs $V-H$ colour-magnitude diagram. The *black solid line* represent the relation expected for the black body disc of a characteristic radius 2.7×10^{11} cm inclined at $i=75^{\rm o}$ at distance of 4.38 kpc (Orosz et al. 2011) of different temperatures (marked next to the line). The model magnitudes were reddened following the extinction law of Fitzpatrick (1999) with $A_V=5.0$. Much smaller A_V (that would lead to softer spectrum) is not possible, because the disc temperature would be below hydrogen ionisation temperature needed for the outburst to start. The *blue-black-red arrows* illustrate schematically the time evolution of the source during the outburst. The *green arrows* show the path followed by the flare after MJD 51680 (see the text). The upper x-axes show the intrinsic spectral index $\alpha_{VH}=4.63-0.84\,(V-H)$ computed from the observed colour. We see that the flare component is never softer than $\alpha=-0.2$. From Poutanen et al., in preparation

flow but not the jet. The observed sharp colour change during the flares is related to the collapse/recover of a zone in the hot flow that is responsible for the H-band emission.

The delay of the IR flare peak by about 10 days from the start of the soft-to-hard transition is naturally expected, because the X-ray transition corresponds to the start of the retraction of the cold disc ($R_{\rm tr}\sim10R_{\rm S}$), while the IR flare peaks when the hot flow is large enough ($R_{\rm tr}\gtrsim100R_{\rm S}$) allowing the IR photons to escape (see Fig. 4). At the rising phase of the outburst, just a few day before the hard-to-soft spectral transition, a dip has been observed in the UV light curve of GX 339–4 (Yan and Yu 2012). In Swift J1910.2–0546 a dip first appears in the IR, then optical and finally in the UV (N. Degenaar, priv. comm.). The timing of the dips is consistent with the collapse of the hot flow with increasing accretion rate (see Sect. 2.3).

It is worth noticing that the hard-to-soft and the soft-to-hard spectral transitions occur at different X-ray luminosities (e.g. Zdziarski et al. 2004). This hysteresis is most probably related to the fact that at the same luminosity the cold disc is further away from the central source on the rising phase of the outburst, than on the decline. The hysteresis should be then also reflected in the OIR spectra, namely the fast colour change should occur at a higher X-ray luminosity on the rising phase, than on the decline, as indeed observed.

Some BHBs, however, do show signatures of the jet emission in the OIR band. The most obvious examples is microquasar GRS 1915+105, whose radio light-curve was found to be very similar to the IR one with a few hours delay (Fender et al. 1997) favouring a common origin. It, however, accretes at a nearly Eddington rate and is hardly representative. The OIR spectrum of 4U 1543–47 and MAXI J1836–194 in the hard state is rather soft with $\alpha \sim -0.7$ (Kalemci et al. 2005; Russell et al. 2013), which is consistent with the optically thin synchrotron emission from the jet. Furthermore, the rms spectrum of the IR variability of XTE J1118+480 during the 2005 outburst is close to a power-law with $\alpha \sim -0.8$ (Hynes et al. 2006), implying probably the jet origin. And finally, GX 339–4 in the hard state demonstrated strong correlated IR and X-ray variability with the IR lagging by 0.1 s, which could be interpreted as a signature of propagation delays between the X-ray producing accretion disc and the jet (Casella et al. 2010). It is well possible that three components (the irradiated disc, the hot flow and the jet) contribute to the OIR band and their contribution can vary not only from source to source, but also in the same source from the outburst to the outburst.

3.3 X-Ray Variability

In addition to the spectral properties, the variability in X-rays and longer wavelengths puts strong constraints on the models. In the hard state, the typical power-density spectra (PDS) that describe the X-ray variability can roughly be represented as a doubly-broken power-law with indices 0, -1 and -2 from low to high frequencies. A more accurate description of the PDS is achieved by representing it with the Lorentzians (e.g. Nowak 2000; Axelsson et al. 2005). The main source of the short-term variability in BHs is believed to be fluctuations in the mass accretion rate, propagating through the accretion flow (Lyubarskii 1997).

Often QPOs are observed in the range $\sim$0.1–10 Hz (see reviews by Remillard and McClintock 2006; Done et al. 2007). Their frequencies show correlation with the X-ray flux, amplitude of Compton reflection and anti-correlation with the hardness ratio (see Figs. 5 and 9). The origin of QPOs is often associated with the precession of orbits around the BH due to a misalignment of the BH and the orbital spins, known as Lense-Thirring precession (e.g., Stella and Vietri 1998), or with oscillation modes of the accretion flow itself (e.g., Wagoner et al. 2001). The problem with the Lense-Thirring precession models is that the frequency for test masses is a strong function of radius and the BH spin (see e.g. Schnittman et al. 2006). It is not clear why any specific radius gets selected to produce a QPO. If that radius is defined by the truncation of the cold disc, why the QPOs are then observed in the Comptonization spectrum? However, if the flow is hot and thick, it will precess as a solid body (Fragile et al. 2007) with the frequency mostly depending on its size (which is a function of the accretion rate) and weakly on the BH spin and the flow height-to-radius ratio. In such a case, the precession frequencies lie in the observed range and the model explains well their correlations with other quantities (Ingram et al. 2009; Ingram and Done 2011).

Another way of looking at the variability properties is through the autocorrelation function (ACF, which is related to the PDS via Fourier transform). The ACF becomes narrower at higher X-ray energies (Maccarone et al. 2000, see Fig. 10), which is equivalent to the

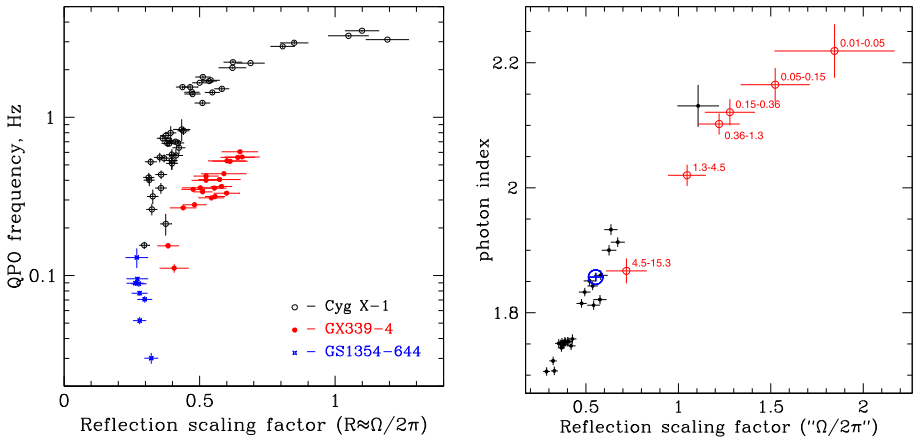

Fig. 9 *Left*: QPO frequency vs reflection correlation. From Gilfanov (2010). *Right*: Photon index–reflection correlation in the average spectra (same as Fig. 5a) and in the Fourier frequency resolved spectra (FFRS) at different frequencies. From Gilfanov et al. (1999)

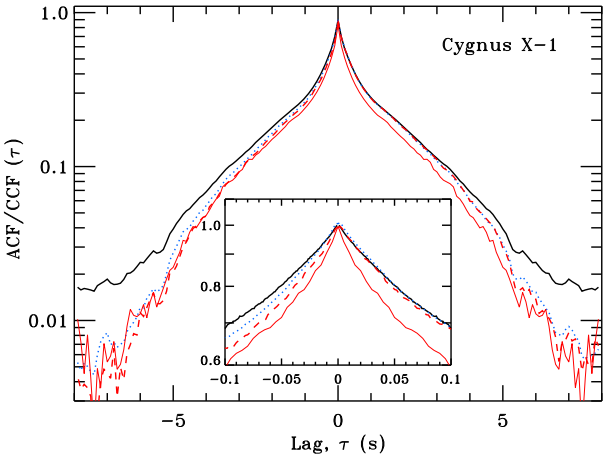

Fig. 10 The ACF and CCFs of Cygnus X-1 observed in December 1997. *Solid curves* show the ACFs for the 2–5 keV energy band (*black solid curves*) and the 24–40 keV band (*red solid curves*). The *blue dotted curve* shows the CCF between the 8–13 keV and the 2–5 keV bands, and the *red dashed curve* represents the CCF for the 24–40 keV vs the 2–5 keV bands. The positive lag corresponds here to the hard photons lagging the soft ones. The CCFs are asymmetric, but the peak do not show any shift from zero lag. From Maccarone et al. (2000)

excess variability at higher frequencies in the PDS at those energies. Moreover, the light curves at different energies are well correlated with each other, but the harder X-rays are delayed with respect to the soft X-rays (Miyamoto and Kitamoto 1989; Nowak et al. 1999a, 1999b, see Fig. 11). This effect is also reflected in the asymmetries of the cross-correlation function (CCF) between the hard and the soft X-ray energy bands (Priedhorsky et al. 1979; Nolan et al. 1981; Maccarone et al. 2000, see Fig. 10).

In order to have a better understanding for these asymmetries, it is useful to look at the time lags Δt between the light-curves at these X-ray energies as a function of the Fourier frequency f. For the hard state of Cygnus X-1 they are shown in Fig. 11a. As a function of energy E, the lags relative to energy E_0 follow the logarithmic law $\propto \ln(E/E_0)$. The rather large lags (exceeding 0.1 s) were first interpreted as produced by Comptonization in a large Compton cloud (Kazanas et al. 1997). For harder photons more scatterings is required, thus they spend more time in the medium before escape and therefore are delayed. Such an interpretation not only causes a problem with the energetics of the cloud (requiring large

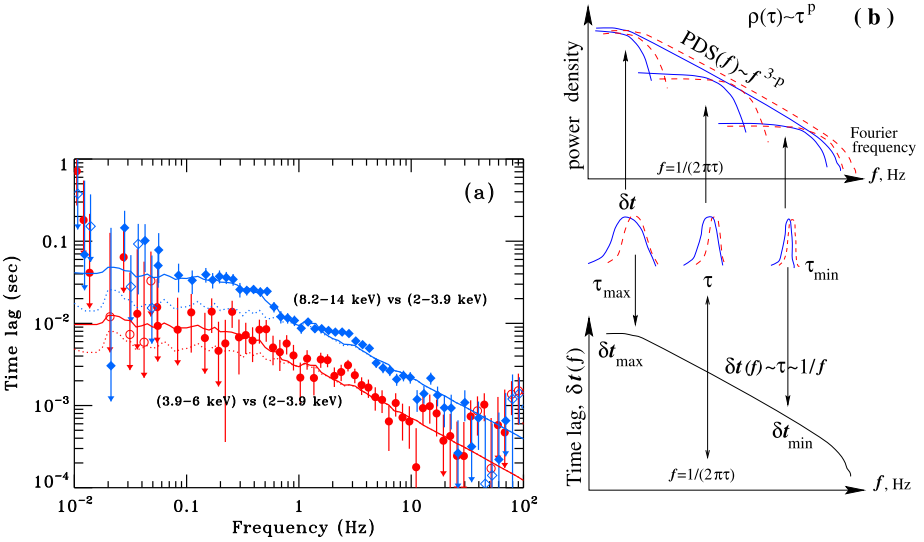

Fig. 11 (**a**) Time lags in Cyg X-1. The data points are from Nowak et al. (1999b). The *dotted curves* represent the model of Poutanen and Fabian (1999), where lags are produces by spectral evolution during flares. The *solid curves* have a contribution at low frequencies from the lags caused by reflection from the outer disc (Poutanen 2002). (**b**) A schematic picture how spectral evolution model produces time lags. The *red dotted curves* represent the flare *light curve* at high photon energies, while the *blue solid curves* represent those at low energies. Spectral hardening during flares produces hard time lags. Here p is the index of the power-law probability distribution of flare duration τ. From Poutanen (2001)

energy release at distances $> 10^4 R_S$), but also contradicts the energy dependence of the ACF width (Maccarone et al. 2000). On the other hand, the large lags, their frequency-dependence f^{-1} and the logarithmic energy dependence can be naturally explained by spectral pivoting of a power-law-like spectrum if the characteristic time-scale of the evolution scales with the duration of shots τ dominating variability at frequency $f \approx 1/(2\pi\tau)$ (see Poutanen and Fabian 1999; Poutanen 2001; Kotov et al. 2001; Körding and Falcke 2004, and Fig. 11b). Among the first physical models explaining the spectral evolution was the flaring magnetic corona model of Poutanen and Fabian (1999). The observed linear relation between the flux and the rms (Uttley and McHardy 2001), however, argues against the independent shots (flares) as the source of variability. In the propagation model of Lyubarskii (1997), spectral evolution can arise when the accretion rate fluctuations propagate towards the BH into the zone with the harder spectra (Miyamoto and Kitamoto 1989; Kotov et al. 2001; Arévalo and Uttley 2006).[3] This is consistent with the multi-zone hot flow model, because a lower flux of soft seed photon from the cold accretion disc as well as a stronger synchrotron self-absorption in the inner part of the flow produce harder Comptonization spectrum (Veledina et al. 2013a).

Additional contribution to the time lags are possible when the intrinsic X-rays from the hot flow are reflected from the distant matter, e.g. outer cold accretion disc (Kotov et al. 2001; Poutanen 2002). Due to the fluorescence and the energy dependence of the photo-electric opacity the contribution of reflection to the total spectrum is energy dependent. Thus the Fe line at 6.4 keV and the Compton reflection bump above 10 keV should show excess

[3]For the time lag production, this model is, however, mathematically identical to the flare evolution model.

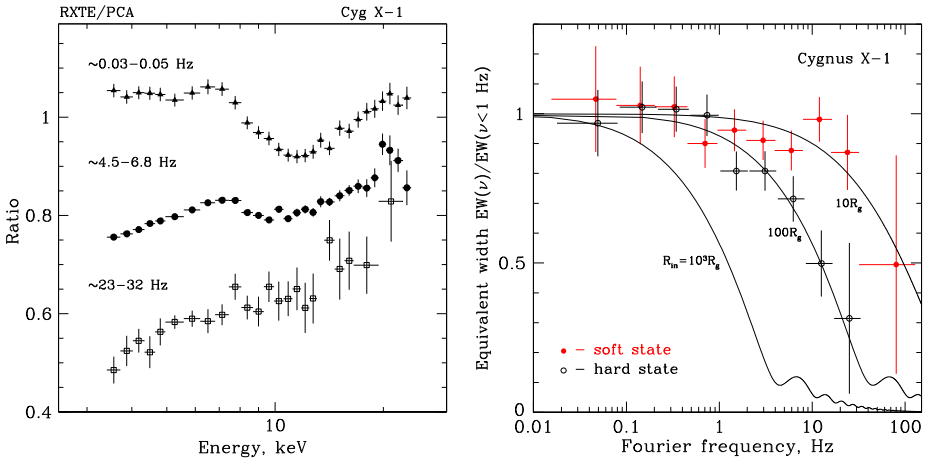

Fig. 12 *Left*: FFRS of Cyg X-1. From Revnivtsev et al. (1999). *Right*: equivalent width of the iron line as a function of Fourier frequency as measured from the FFRS. From Gilfanov et al. (2000)

lags. Surprisingly, the deficit of lags (or "anti-lags") relative to the logarithmic dependence has been observed at these energies (Kotov et al. 2001). Clearly, this deficit cannot be caused by a simple reverberation and the light travel time effect. Instead it could be explained within the hot flow paradigm as follows. The outer parts of the flow which are close to the cold disc have softer spectra and larger reflection amplitude, while the inner flow produces harder spectrum with low or no reflection. Thus in the propagating fluctuation model, the reflection will be *leading* the hard spectrum causing negative delays at photon energies where it contributes (Kotov et al. 2001). Delays due to reprocessing in the inner part of the cold disc are seen at high f in GX 339–4 (Uttley et al. 2011), while at low f the disc photons lead the Comptonized photons, which is consistent with the propagation of fluctuations from the disc to the hot flow.

Further support to the truncated cold disc—hot inner flow scenario comes from the Fourier-frequency-resolved spectra (FFRS; Revnivtsev et al. 1999; Gilfanov et al. 2000), which are softer and have larger reflection amplitude at low Fourier frequencies (see Fig. 9, right and Fig. 12, left). This implies that soft X-rays are mostly produced in the outer zones of the hot flow, closer to the cold reflecting medium, while the hard X-rays are produced in the inner zones that vary at high Fourier frequencies. The reduction of the equivalent width of the 6.4 keV Fe line in the FFRS above 1 Hz (Fig. 12, right) suggests that the cold disc truncation radius in the hard state is about 100 R_S (Revnivtsev et al. 1999; Gilfanov et al. 2000). Even larger truncation radius of the cold disc (300–700 R_S) was measured in the low-extinction BH transient XTE J1118+480 (Chaty et al. 2003; Yuan et al. 2005), where the peak is clearly seen in the UV. In the soft state instead the truncation radius is small ($< 10\ R_S$).

3.4 Optical (IR and UV) Variability and Its Relations to the X-Rays

Data on the fast variability are now available not only in the X-rays, but also at lower energies. The first simultaneous observations in the optical and X-rays were carried out already 30 years ago by Motch et al. (1983) for GX 339–4. Although no confident conclusion could be reached because of the short duration of observations, the optical/X-ray CCF revealed

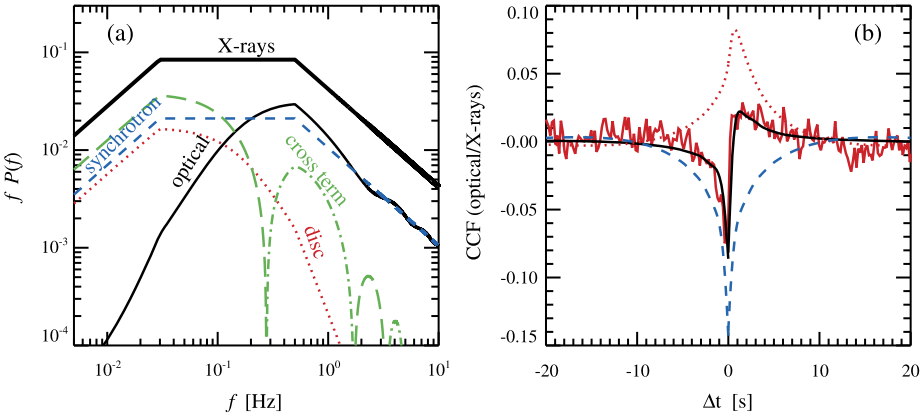

Fig. 13 Two-component model for the optical/X-ray CCF. (**a**) The PDSs of the X-ray (upper double-broken line) and optical light curves (*thin solid line*). Three terms contributing to the optical PDS are also shown: synchrotron (*blue dashed*), reprocessing in the disc (*red dotted*), and the cross term (*green dot-dashed*—positive contribution; *long-dashed*—negative contribution). (**b**) The optical/X-ray CCFs observed from Swift J1753.5–0127 in 2008 (*red noisy curve*, see Fig. A3 in Durant et al. 2011). The model CCF is shown by the *black solid curve*. The smooth lines represent the contributions of the synchrotron emission (*blue dashed*) and the reprocessed emission (*red dotted*). Adapted from Veledina et al. (2011a)

a complicated structure with a precognition dip (i.e. anti-correlation) at negative lags corresponding to optical leading the X-rays and a peak (i.e. correlation) at positive lags (see Fig. 13b). Recently, similar CCFs were obtained from the much longer duration simultaneous observations in three BHBs: XTE J1118+480 (Kanbach et al. 2001; Hynes et al. 2003; Malzac et al. 2003), Swift J1753.5–0127 (Durant et al. 2008, 2009, 2011; Hynes et al. 2009a) and GX 339–4 (Gandhi et al. 2008, 2010). These data provide an important information on the interrelation between various components and give clues to their physical origin.

The observed CCF shape cannot be explained by a simple reprocessing model (Kanbach et al. 2001; Hynes et al. 2003). However, if the optical emission consists of two components, e.g., one coming from the non-thermal synchrotron in the hot flow and another from reprocessed X-ray emission, the complex shape can be reproduced (Veledina et al. 2011a, see Fig. 13b). Increase of the mass accretion rate obviously causes an increase in the X-ray luminosity, but at the same time the optical synchrotron from the hot flow may drop because of higher self-absorption. A higher accretion rate can also lead to a decrease of the truncation radius, collapse of the hot flow at large radii, and the suppression of the OIR emission. Both scenarios leads to anti-correlation between optical and X-rays and to the negative contribution to the CCF, with the shape resembling that of the X-ray ACF. On the other hand, the second, reprocessed component correlates with the X-rays, but is delayed and smeared, giving rise to a positive CCF peaking at positive lags (optical delay). The combined CCF has a complicated shape consistent with the data (Fig. 13b). The PDS of the optical in this model consists of three components: the synchrotron (which has nearly identical shape to the X-ray PDS), the irradiated disc (which has less power at high frequencies because of smearing) and the cross-term of variable sign. The total optical variability is strongly reduced at low frequencies where the synchrotron and the disc vary out of phase (Veledina et al. 2011a, see Fig. 13a). These PDS shapes are very similar to that observed in GX 339–4 (see Fig. 9 in Gandhi et al. 2010).

Further clues on the origin of the optical emission come from the QPOs seen in the light curves of a number of low-mass BHBs (Motch et al. 1983, 1985; Imamura et al. 1990;

Steiman-Cameron et al. 1997; Hynes et al. 2003; Durant et al. 2009; Gandhi et al. 2010). The optical, UV and X-ray QPOs in XTE J1118+480 all have the same frequency, which evolves during the two months of observations (Hynes et al. 2003). There is also a clear connection between the optical and X-ray light curves in the 2007 data on Swift J1753.5–0127 (see Durant et al. 2008; A. Veledina et al. in prep.) seen as a modulation at the optical QPO frequency in the optical/X-ray CCF. Similarly, GX 339–4 shows oscillations at the same frequency in the optical and X-rays (Motch et al. 1983; Gandhi et al. 2010, Fig. 21). The question now arises how it is possible that the X-rays and OIR/UV vary at the same frequency and are phase-connected? This fact finds a simple explanation in the hybrid hot flow model because the hot flow can precess as a solid body (see Sect. 3.3) and therefore the long wavelength emission produced in the outer part of that flow is related to the X-rays produced in the inner part of the same flow (Veledina et al. 2013b).

Recently, periodic eclipses in the optical light curve of BHB Swift J1357.2–093313 were observed (Corral-Santana et al. 2013). If the period is related to the Keplerian frequency of the obscuring region, the sharpness of the eclipses implies that the size of the optical emission region is below 20 000 km (i.e. $< 700 R_{\rm S}$ for a $10 {\rm M}_\odot$ BH). These constraints are easily satisfied in the hot flow scenario.

3.5 Polarisation

Polarisation degree and polarisation angle provide two more observational constraints on the emission models. The only indication of the X-ray polarisation from BHB goes back to the OSO-8 satellite (Weisskopf et al. 1977), which measured 3.1 ± 1.7 % linear polarisation from Cyg X-1 at 2.6 keV. Such a polarisation can be produced by Compton scattering if the geometry of the X-ray emitting region is a flattened disc-like structure ($H/R \sim 0.2$ according to the calculations of Lightman and Shapiro 1976), consistent with the hot flow scenario.

Recently, strong linear polarisation ($\Pi = 67 \pm 30$ %) in the soft γ-rays above 400 keV was detected in Cyg X-1 with the IBIS instrument onboard *INTEGRAL* (Laurent et al. 2011). Similar polarisation ($\Pi = 76 \pm 15$ %) was also observed with the SPI spectrometer (Jourdain et al. 2012b). The polarisation angle of 40°–42° is about 60° away from the radio jet axis at $\approx -20°$ (Jourdain et al. 2012b; Zdziarski et al. 2012). Such a large polarisation degree in the MeV range is extremely difficult to get in any scenario. Synchrotron jet emission from non-thermal electrons in a highly ordered magnetic field can have a large polarisation degree (up to ∼70 per cent) in the optically thin part of the spectrum, and indeed a high polarisation in the radio and the optical bands reaching 30–50 per cent is observed from extragalactic relativistic jets (Impey et al. 1991; Wills et al. 1992; Lister 2001; Marscher et al. 2002; Ikejiri et al. 2011). However, this scenario also needs a very hard electron spectrum as well as an extreme fine-tuning to reproduce the spectral cutoff at a few MeV (Zdziarski et al. 2012). In the hot-flow scenario, the MeV photons are produced by non-thermal Compton scattering of the 100 keV photons by electrons with Lorentz factors $\gamma \sim$2–4. These electrons cannot be isotropic, because no significant polarisation is expected in that case (Poutanen 1994). This then implies that they must have nearly one-dimensional motion, e.g. along the large-scale magnetic field lines threading the flow. The 60° offset of the polarisation vector relative to the jet axis then implies the inclined field lines. If the measured high polarisation degree is indeed real, this would put strong constraints on the physics of particle acceleration in the hot flow and the magnetic field geometry.

In the OIR bands, polarisation is very small and does not exceed a few per cent (Schultz et al. 2004; Shahbaz et al. 2008; Russell and Fender 2008; Chaty et al. 2011). In the hot-flow scenario, polarisation degree of the optically thin synchrotron radiation in the OIR

band is expected to be essentially zero (independently of the magnetic field geometry) because the Faraday rotation angle exceeds 10^5 rad (Veledina et al. 2013a). In the optically thick regime, the intrinsic polarisation (parallel to the magnetic field lines) is not more than about 10 per cent even for the ordered magnetic field (Pacholczyk and Swihart 1967; Ginzburg and Syrovatskii 1969). Faraday rotation in the disc atmosphere can still essentially depolarise that emission. The reprocessed emission from the outer disc can be slightly polarised because magnetic field there is smaller. If the jet were responsible for the OIR emission, one would expect instead a much higher polarisation because its radiation is optically thin, not consistent with the data. The observed small polarisation can also be produced by dust/electron scattering in the source vicinity or by the interstellar dust.

4 Summary

The purely thermal hot-flow model was shown to be consistent with many X-ray characteristics. However, that model fails to account for the MeV tails and a number of OIR properties. Addition of a small, energetically-negligible non-thermal component to the electron distribution dramatically changes the prediction of the model. The hybrid hot-flow model is now successful in explaining the following facts:

1. stability of spectra with photon index $\Gamma \sim 1.6$–1.8 and the cutoff at $\sim$100 keV in the hard state (Poutanen and Vurm 2009; Malzac and Belmont 2009),
2. concave X-ray spectrum (Kotov et al. 2001; Veledina et al. 2013a),
3. low level of the X-ray and OIR polarisation (Veledina et al. 2013a),
4. presence of the MeV tail in the hard state (Poutanen and Vurm 2009; Malzac and Belmont 2009),
5. softening of the X-ray spectrum with decreasing luminosity below $\sim 10^{-2} L_{\rm Edd}$ (Veledina et al. 2011b),
6. weakness of the cold accretion disc component in the hard state,
7. correlation between the spectral index, the reflection amplitude, the width of the iron line and the frequency of the quasi-periodic oscillations,
8. hard X-ray lags with logarithmic energy dependence (Kotov et al. 2001),
9. non-thermal OIR excesses and flat OIR spectra (Veledina et al. 2013a),
10. OIR colours of the flares in the hard state (Poutanen et al., in prep.),
11. strong correlation between OIR and X-ray emission and a complicated CCF shape (Veledina et al. 2011a),
12. quasi-periodic oscillations at the same frequency in the X-ray and optical bands (Veledina et al. 2013b).

The model does not explain the radio points and the soft IR spectra. The jet is obviously a better model for those data. We, however, struggle to find any other observational fact that could be in conflict with the hybrid hot flow—truncated cold disc scenario.

Recently, the jet paradigm became popular and it was claimed that the jets are responsible not only for the radio emission from the BHBs, but also the OIR and even the X-ray emission. Unfortunately, that model is in contradiction with dozens of observed facts (see Veledina et al. 2013a, and references therein), which are usually ignored by the model proponents. When new data appear, they often are rather puzzling and difficult to understand within the available paradigms. However, it would be beneficial for the community when introducing brand new models to check also whether those models satisfy other observational constraints.

In spite of a serious progress in understanding of the viscosity in accretion discs around BHs, there are still many open questions. If non-thermal particles are present in the hot flow, it is now time to understand what is their nature. How are they accelerated: in shocks or in magnetic reconnections events, or maybe via diffusive acceleration by MHD turbulence? How are they related to the magneto-rotational instability that presumably drives the accretion? We hope that the observational advances will soon be reflected in the advance of the theory.

Acknowledgements The work was partially supported by the Academy of Finland grant 268740 (JP) and the Finnish Doctoral Program in Astronomy and Space Physics (AV). We thank Tomaso Belloni, Andrzej Zdziarski, and Feng Yuan for valuable comments and David Russell for the data on XTE J1550–564.

References

V.A. Aref'ev, M.G. Revnivtsev, A.A. Lutovinov, R.A. Sunyaev, Astron. Lett. **30**, 669–674 (2004)
P. Arévalo, P. Uttley, Mon. Not. R. Astron. Soc. **367**, 801–814 (2006)
M. Axelsson, L. Borgonovo, S. Larsson, Astron. Astrophys. **438**, 999–1012 (2005)
R. Belmont, J. Malzac, A. Marcowith, Astron. Astrophys. **491**, 617–631 (2008)
A.M. Beloborodov, in *High Energy Processes in Accreting Black Holes*, ed. by J. Poutanen, R. Svensson. ASP Conf. Ser., vol. 161 (1999a), pp. 295–314
A.M. Beloborodov, Astrophys. J. Lett. **510**, L123–L126 (1999b)
R.D. Blandford, A. Königl, Astrophys. J. **232**, 34–48 (1979)
M.M. Buxton, C.D. Bailyn, Astrophys. J. **615**, 880–886 (2004)
M.M. Buxton, C.D. Bailyn, H.L. Capelo et al., Astron. J. **143**, 130 (2012)
M. Cadolle Bel, M. Ribó, J. Rodriguez et al., Astrophys. J. **659**, 549–560 (2007)
M. Cadolle Bel, J. Rodriguez, P. D'Avanzo et al., Astron. Astrophys. **534**, 119 (2011)
M. Cadolle Bel, S. Corbel, A. Veledina et al., in *IAU Symp*, ed. by C.M. Zhang, T. Belloni, M. Méndez, S.N. Zhang. IAU Symposium, vol. 290 (2013), pp. 17–20
P. Casella, T.J. Maccarone, K. O'Brien et al., Mon. Not. R. Astron. Soc. **404**, 21–25 (2010)
A. Celotti, A.C. Fabian, M.J. Rees, Mon. Not. R. Astron. Soc. **255**, 419–422 (1992)
S. Chaty, C.A. Haswell, J. Malzac et al., Mon. Not. R. Astron. Soc. **346**, 689–703 (2003)
S. Chaty, G. Dubus, A. Raichoor, Astron. Astrophys. **529**, 3 (2011)
C.Y. Chiang, C. Done, M. Still, O. Godet, Mon. Not. R. Astron. Soc. **403**, 1102–1112 (2010)
A. Constantin, P. Green, T. Aldcroft et al., Astrophys. J. **705**, 1336–1355 (2009)
P.S. Coppi, Mon. Not. R. Astron. Soc. **258**, 657–683 (1992)
P.S. Coppi, in *High Energy Processes in Accreting Black Holes*, ed. by J. Poutanen, R. Svensson. ASP Conf. Ser., vol. 161 (1999), pp. 375–403
S. Corbel, H. Aussel, J.W. Broderick et al., Mon. Not. R. Astron. Soc. **431**, 107–111 (2013)
J.M. Corral-Santana, J. Casares, T. Muñoz-Darias et al., Science **339**, 1048–1051 (2013)
C. Cunningham, Astrophys. J. **208**, 534–549 (1976)
S. Das, P.A. Becker, T. Le, Astrophys. J. **702**, 649–659 (2009)
T. Dinçer, E. Kalemci, M.M. Buxton et al., Astrophys. J. **753**, 55 (2012)
J. Ding, F. Yuan, E. Liang, Astrophys. J. **708**, 1545–1550 (2010)
C. Done, in *Accretion Processes in Astrophysics*, ed. by I. González Martínez-País, T. Shahbaz, J. Casares Velázquez (Cambridge University Press, Cambridge, 2013). arXiv:1008.2287
C. Done, M. Gierliński, A. Kubota, Astron. Astrophys. Rev. **15**, 1–66 (2007)
R. Droulans, R. Belmont, J. Malzac, E. Jourdain, Astrophys. J. **717**, 1022–1036 (2010)
M. Durant, P. Gandhi, T. Shahbaz et al., Astrophys. J. Lett. **682**, L45–L48 (2008)
M. Durant, P. Gandhi, T. Shahbaz et al., Mon. Not. R. Astron. Soc. **392**, 309–324 (2009)
M. Durant, T. Shahbaz, P. Gandhi et al., Mon. Not. R. Astron. Soc. **410**, 2329–2338 (2011)
A.A. Esin, J.E. McClintock, R. Narayan, Astrophys. J. **489**, 865–889 (1997)
A.A. Esin, R. Narayan, W. Cui et al., Astrophys. J. **505**, 854–868 (1998)
A.A. Esin, J.E. McClintock, J.J. Drake et al., Astrophys. J. **555**, 483–488 (2001)
R.P. Fender, G.G. Pooley, C. Brocksopp, S.J. Newell, Mon. Not. R. Astron. Soc. **290**, 65–69 (1997)
E.L. Fitzpatrick, Publ. Astron. Soc. Pac. **111**, 63–75 (1999)
P.C. Fragile, O.M. Blaes, Astrophys. J. **687**, 757–766 (2008)
P.C. Fragile, O.M. Blaes, P. Anninos, J.D. Salmonson, Astrophys. J. **668**, 417–429 (2007)

F. Frontera, E. Palazzi, A.A. Zdziarski et al., Astrophys. J. **546**, 1027–1037 (2001)
A.A. Galeev, R. Rosner, G.S. Vaiana, Astrophys. J. **229**, 318–326 (1979)
E. Gallo, S. Migliari, S. Markoff et al., Astrophys. J. **670**, 600–609 (2007)
P. Gandhi, K. Makishima, M. Durant et al., Mon. Not. R. Astron. Soc. **390**, L29–L33 (2008)
P. Gandhi, V.S. Dhillon, M. Durant et al., Mon. Not. R. Astron. Soc. **407**, 2166–2192 (2010)
P. Gandhi, A.W. Blain, D.M. Russell et al., Astrophys. J. Lett. **740**, L13 (2011)
G. Ghisellini, P.W. Guilbert, R. Svensson, Astrophys. J. Lett. **334**, L5–L8 (1988)
G. Ghisellini, F. Haardt, R. Svensson, Mon. Not. R. Astron. Soc. **297**, 348–354 (1998)
M. Gierlinski, A.A. Zdziarski, C. Done et al., Mon. Not. R. Astron. Soc. **288**, 958–964 (1997)
M. Gierliński, A.A. Zdziarski, J. Poutanen et al., Mon. Not. R. Astron. Soc. **309**, 496–512 (1999)
M. Gierliński, C. Done, K. Page, Mon. Not. R. Astron. Soc. **392**, 1106–1114 (2009)
M. Gilfanov, in *The Jet Paradigm*, ed. by T. Belloni. Lecture Notes in Physics, vol. 794 (2010), pp. 17–51
M. Gilfanov, E. Churazov, M. Revnivtsev, Astron. Astrophys. **352**, 182–188 (1999)
M. Gilfanov, E. Churazov, M. Revnivtsev, Mon. Not. R. Astron. Soc. **316**, 923–928 (2000)
V.L. Ginzburg, S.I. Syrovatskii, Annu. Rev. Astron. Astrophys. **7**, 375–420 (1969)
J.E. Grove, W.N. Johnson, R.A. Kroeger et al., Astrophys. J. **500**, 899–908 (1998)
M. Gu, X. Cao, Mon. Not. R. Astron. Soc. **399**, 349–356 (2009)
F. Haardt, L. Maraschi, Astrophys. J. **413**, 507–517 (1993)
F. Haardt, L. Maraschi, G. Ghisellini, Astrophys. J. Lett. **432**, L95–L99 (1994)
K.B. Henisey, O.M. Blaes, P.C. Fragile, Astrophys. J. **761**, 18 (2012)
M. Hoshino, Astrophys. J. **773**, 118 (2013)
R.I. Hynes, K. O'Brien, K. Horne et al., Mon. Not. R. Astron. Soc. **299**, 37–41 (1998)
R.I. Hynes, C.W. Mauche, C.A. Haswell et al., Astrophys. J. Lett. **539**, L37–L40 (2000)
R.I. Hynes, C.A. Haswell, S. Chaty et al., Mon. Not. R. Astron. Soc. **331**, 169–179 (2002)
R.I. Hynes, C.A. Haswell, W. Cui et al., Mon. Not. R. Astron. Soc. **345**, 292–310 (2003)
R.I. Hynes, E.L. Robinson, K.J. Pearson et al., Astrophys. J. **651**, 401–407 (2006)
R.I. Hynes, C.K. Bradley, M. Rupen et al., Mon. Not. R. Astron. Soc. **399**, 2239–2248 (2009b)
R.I. Hynes, K. O'Brien, F. Mullally, T. Ashcraft, Mon. Not. R. Astron. Soc. **399**, 281–286 (2009a)
A. Ibragimov, J. Poutanen, M. Gilfanov et al., Mon. Not. R. Astron. Soc. **362**, 1435–1450 (2005)
S. Ichimaru, Astrophys. J. **214**, 840–855 (1977)
Y. Ikejiri, M. Uemura, M. Sasada et al., Publ. Astron. Soc. Jpn. **63**, 639–675 (2011)
J.N. Imamura, J. Kristian, J. Middleditch, T.Y. Steiman-Cameron, Astrophys. J. **365**, 312–316 (1990)
C.D. Impey, C.R. Lawrence, S. Tapia, Astrophys. J. **375**, 46–68 (1991)
A. Ingram, C. Done, Mon. Not. R. Astron. Soc. **415**, 2323–2335 (2011)
A. Ingram, C. Done, P.C. Fragile, Mon. Not. R. Astron. Soc. **397**, 101–105 (2009)
R.K. Jain, C.D. Bailyn, J.A. Orosz et al., Astrophys. J. Lett. **554**, L181–L184 (2001)
E. Jourdain, J.P. Roques, M. Chauvin, D.J. Clark, Astrophys. J. **761**, 27 (2012b)
E. Jourdain, J.P. Roques, J. Malzac, Astrophys. J. **744**, 64 (2012a)
E. Kalemci, J.A. Tomsick, M.M. Buxton et al., Astrophys. J. **622**, 508–519 (2005)
E. Kalemci, T. Dincer, J.A. Tomsick et al., Astrophys. J. **779**, 95 (2013). doi:10.1088/0004-637X/779/2/95
G. Kanbach, C. Straubmeier, H.C. Spruit, T. Belloni, Nature **414**, 180–182 (2001)
D. Kazanas, X.-M. Hua, L. Titarchuk, Astrophys. J. **480**, 735–740 (1997)
M. Kolehmainen, C. Done, M. Díaz Trigo, Mon. Not. R. Astron. Soc. **437**, 316–326 (2014). doi:10.1093/mnras/stt1886
E. Körding, H. Falcke, Astron. Astrophys. **414**, 795–806 (2004)
O. Kotov, E. Churazov, M. Gilfanov, Mon. Not. R. Astron. Soc. **327**, 799–807 (2001)
J.H. Krolik, Astrophys. J. Lett. **498**, L13–L16 (1998)
P. Laurent, J. Rodriguez, J. Wilms et al., Science **332**, 438 (2011)
A.P. Lightman, S.L. Shapiro, Astrophys. J. **203**, 701–703 (1976)
J.C. Ling, W.A. Wheaton, P. Wallyn et al., Astrophys. J. **484**, 375–382 (1997)
M.L. Lister, Astrophys. J. **562**, 208–232 (2001)
Y.E. Lyubarskii, Mon. Not. R. Astron. Soc. **292**, 679–685 (1997)
T.J. Maccarone, P.S. Coppi, J. Poutanen, Astrophys. J. Lett. **537**, L107–L110 (2000)
R. Mahadevan, Nature **394**, 651–653 (1998)
K. Makishima, H. Takahashi, S. Yamada et al., Publ. Astron. Soc. Jpn. **60**, 585–604 (2008)
J. Malzac, R. Belmont, Mon. Not. R. Astron. Soc. **392**, 570–589 (2009)
J. Malzac, A.M. Beloborodov, J. Poutanen, Mon. Not. R. Astron. Soc. **326**, 417–427 (2001)
J. Malzac, T. Belloni, H.C. Spruit, G. Kanbach, Astron. Astrophys. **407**, 335–345 (2003)
A.P. Marscher, Astrophys. J. **216**, 244–256 (1977)
A.P. Marscher, S.G. Jorstad, J.R. Mattox, A.E. Wehrle, Astrophys. J. **577**, 85–97 (2002)
J.E. McClintock, C.A. Haswell, M.R. Garcia et al., Astrophys. J. **555**, 477–482 (2001)

J.E. McClintock, R. Narayan, J.F. Steiner, Space Sci. Rev. (2013). doi:10.1007/s11214-013-0003-9
M. McConnell, D. Forrest, J. Ryan et al., Astrophys. J. **424**, 933–939 (1994)
M.L. McConnell, A.A. Zdziarski, K. Bennett et al., Astrophys. J. **572**, 984–995 (2002)
S. Miyamoto, S. Kitamoto, Nature **342**, 773 (1989)
C. Motch, M.J. Ricketts, C.G. Page et al., Astron. Astrophys. **119**, 171–176 (1983)
C. Motch, S.A. Ilovaisky, C. Chevalier, P. Angebault, Space Sci. Rev. **40**, 219–224 (1985)
M.P. Muno, J. Mauerhan, Astrophys. J. Lett. **648**, L135–L138 (2006)
R. Narayan, I. Yi, Astrophys. J. Lett. **428**, L13–L16 (1994)
R. Narayan, I. Yi, Astrophys. J. **452**, 710–735 (1995)
R. Narayan, R. Mahadevan, E. Quataert, in *Theory of Black Hole Accretion Disks*, ed. by M.A. Abramowicz, G. Bjornsson, J.E. Pringle (Cambridge University Press, Cambridge, 1998), pp. 148–182
S. Nayakshin, F. Melia, Astrophys. J. Suppl. Ser. **114**, 269–288 (1998)
A. Niedźwiecki, F.-G. Xie, A.A. Zdziarski, Mon. Not. R. Astron. Soc. **420**, 1195–1206 (2012)
P.L. Nolan, D.E. Gruber, J.L. Matteson et al., Astrophys. J. **246**, 494–501 (1981)
D.I. Novikov, K.S. Thorne, in *Black Holes (Les Astres Occlus)*, ed. by C. Dewitt, B.S. Dewitt (Gordon & Breach, New York, 1973), pp. 343–450
M.A. Nowak, Mon. Not. R. Astron. Soc. **318**, 361–367 (2000)
M.A. Nowak, B.A. Vaughan, J. Wilms et al., Astrophys. J. **510**, 874–891 (1999b)
M.A. Nowak, J. Wilms, J.B. Dove, Astrophys. J. **517**, 355–366 (1999a)
K. O'Brien, K. Horne, R.I. Hynes et al., Mon. Not. R. Astron. Soc. **334**, 426–434 (2002)
J.A. Orosz, J.F. Steiner, J.E. McClintock et al., Astrophys. J. **730**, 75 (2011)
F. Özel, D. Psaltis, R. Narayan, Astrophys. J. **541**, 234–249 (2000)
A.G. Pacholczyk, T.L. Swihart, Astrophys. J. **150**, 647–650 (1967)
J. Poutanen, Astrophys. J. Suppl. Ser. **92**, 607–609 (1994)
J. Poutanen, in *Theory of Black Hole Accretion Disks*, ed. by M.A. Abramowicz, G. Björnsson, J.E. Pringle (Cambridge University Press, Cambridge, 1998), pp. 100–122
J. Poutanen, Adv. Space Res. **28**, 267–280 (2001)
J. Poutanen, Mon. Not. R. Astron. Soc. **332**, 257–270 (2002)
J. Poutanen, P.S. Coppi, Phys. Scr. T **77**, 57–60 (1998)
J. Poutanen, A.C. Fabian, Mon. Not. R. Astron. Soc. **306**, L31–L37 (1999)
J. Poutanen, R. Svensson, Astrophys. J. **470**, 249–268 (1996)
J. Poutanen, I. Vurm, Astrophys. J. Lett. **690**, L97–L100 (2009)
J. Poutanen, J.H. Krolik, F. Ryde, Mon. Not. R. Astron. Soc. **292**, L21–L25 (1997)
W. Priedhorsky, G.P. Garmire, R. Rothschild et al., Astrophys. J. **233**, 350–363 (1979)
F. Rahoui, M. Coriat, S. Corbel et al., Mon. Not. R. Astron. Soc. **422**, 2202–2212 (2012)
R.A. Remillard, J.E. McClintock, Annu. Rev. Astron. Astrophys. **44**, 49–92 (2006)
M. Revnivtsev, M. Gilfanov, E. Churazov, Astron. Astrophys. **347**, 23–26 (1999)
M. Revnivtsev, M. Gilfanov, E. Churazov, Astron. Astrophys. **380**, 520–525 (2001)
M.A. Riquelme, E. Quataert, P. Sharma, A. Spitkovsky, Astrophys. J. **755**, 50 (2012)
D.M. Russell, R.P. Fender, Mon. Not. R. Astron. Soc. **387**, 713–723 (2008)
D.M. Russell, D. Maitra, R.J.H. Dunn, S. Markoff, Mon. Not. R. Astron. Soc. **405**, 1759–1769 (2010)
D.M. Russell, D. Maitra, R.J.H. Dunn, R.P. Fender, Mon. Not. R. Astron. Soc. **416**, 2311–2317 (2011)
D.M. Russell, P.A. Curran, T. Muñoz-Darias et al., Mon. Not. R. Astron. Soc. **419**, 1740–1751 (2012)
D.M. Russell, T.D. Russell, J.C.A. Miller-Jones et al., Astrophys. J. Lett. **768**, L35 (2013)
J.D. Schnittman, J. Homan, J.M. Miller, Astrophys. J. **642**, 420–426 (2006)
J. Schultz, P. Hakala, J. Huovelin, Balt. Astron. **13**, 581–595 (2004)
T. Shahbaz, R.P. Fender, C.A. Watson, K. O'Brien, Astrophys. J. **672**, 510–515 (2008)
N.I. Shakura, R.A. Sunyaev, Astron. Astrophys. **24**, 337–355 (1973)
S.L. Shapiro, A.P. Lightman, D.M. Eardley, Astrophys. J. **204**, 187–199 (1976)
M. Shidatsu, Y. Ueda, F. Tazaki et al., Publ. Astron. Soc. Jpn. **63**, 785 (2011)
M.A. Sobolewska, I.E. Papadakis, C. Done, J. Malzac, Mon. Not. R. Astron. Soc. **417**, 280–288 (2011)
T.Y. Steiman-Cameron, J.D. Scargle, J.N. Imamura, J. Middleditch, Astrophys. J. **487**, 396–401 (1997)
L. Stella, M. Vietri, Astrophys. J. Lett. **492**, L59–L62 (1998)
B.E. Stern, M.C. Begelman, M. Sikora, R. Svensson, Mon. Not. R. Astron. Soc. **272**, 291–307 (1995a)
B.E. Stern, J. Poutanen, R. Svensson et al., Astrophys. J. Lett. **449**, L13–L17 (1995b)
P. Uttley, I.M. McHardy, Mon. Not. R. Astron. Soc. **323**, L26–L30 (2001)
P. Uttley, T. Wilkinson, P. Cassatella et al., Mon. Not. R. Astron. Soc. **414**, 60–64 (2011)
A. Veledina, J. Poutanen, I. Vurm, Astrophys. J. Lett. **737**, L17 (2011a)
A. Veledina, I. Vurm, J. Poutanen, Mon. Not. R. Astron. Soc. **414**, 3330–3343 (2011b)
A. Veledina, J. Poutanen, A. Ingram, Astrophys. J. **778**, 165 (2013b)
A. Veledina, J. Poutanen, I. Vurm, Mon. Not. R. Astron. Soc. **430**, 3196–3212 (2013a)

I. Vurm, J. Poutanen, Astrophys. J. **698**, 293–316 (2009)
R.V. Wagoner, A.S. Silbergleit, M. Ortega-Rodríguez, Astrophys. J. Lett. **559**, L25–L28 (2001)
G. Wardziński, A.A. Zdziarski, Mon. Not. R. Astron. Soc. **325**, 963–971 (2001)
M.C. Weisskopf, E.H. Silver, H.L. Kestenbaum et al., Astrophys. J. Lett. **215**, L65–L68 (1977)
B.J. Wills, D. Wills, N.J. Evans II et al., Astrophys. J. **400**, 96–114 (1992)
Q. Wu, M. Gu, Astrophys. J. **682**, 212–217 (2008)
F.-G. Xie, A. Niedźwiecki, A.A. Zdziarski, F. Yuan, Mon. Not. R. Astron. Soc. **403**, 170–178 (2010)
S. Yamada, K. Makishima, C. Done et al., Publ. Astron. Soc. Jpn. **65**, 80 (2013)
Z. Yan, W. Yu, Mon. Not. R. Astron. Soc. **427**, 11–15 (2012)
F. Yuan, R. Narayan, Annu. Rev. Astron. Astrophys. (2014, submitted)
F. Yuan, A.A. Zdziarski, Mon. Not. R. Astron. Soc. **354**, 953–960 (2004)
F. Yuan, E. Quataert, R. Narayan, Astrophys. J. **598**, 301–312 (2003)
F. Yuan, W. Cui, R. Narayan, Astrophys. J. **620**, 905–914 (2005)
F. Yuan, A.A. Zdziarski, Y. Xue, X.-B. Wu, Astrophys. J. **659**, 541–548 (2007)
A.A. Zdziarski, M. Gierliński, Prog. Theor. Phys. Suppl. **155**, 99–119 (2004)
A.A. Zdziarski, W.N. Johnson, J. Poutanen et al., in *ESA SP-382: The Transparent Universe*, ed. by C. Winkler, T.J.-L. Courvoisier, P. Durouchoux (ESA, Noordwijk, 1997), pp. 373–380
A.A. Zdziarski, J. Poutanen, J. Mikolajewska et al., Mon. Not. R. Astron. Soc. **301**, 435–450 (1998)
A.A. Zdziarski, P. Lubinski, D.A. Smith, Mon. Not. R. Astron. Soc. **303**, L11–L15 (1999)
A.A. Zdziarski, J.E. Grove, J. Poutanen, A.R. Rao, S.V. Vadawale, Astrophys. J. Lett. **554**, L45–L48 (2001)
A.A. Zdziarski, P. Lubiński, M. Gilfanov, M. Revnivtsev, Mon. Not. R. Astron. Soc. **342**, 355–372 (2003)
A.A. Zdziarski, M. Gierliński, J. Mikołajewska et al., Mon. Not. R. Astron. Soc. **351**, 791–807 (2004)
A.A. Zdziarski, P. Lubiński, M. Sikora, Mon. Not. R. Astron. Soc. **423**, 663–675 (2012)

Mon. Not. R. Astron. Soc. **000**, 1–16 (2014) Printed 22 August 2014 (MN LATEX style file v2.2)

Spectroscopic evidence for a low-mass black hole in SWIFT J1753.5–0127

Vitaly V. Neustroev[1⋆], Alexandra Veledina[1,2], Juri Poutanen[2,1], Sergey V. Zharikov[3], Sergey S. Tsygankov[4,1,2], George Sjoberg[5,6], Jari J. E. Kajava[7,8,1]

[1]*Astronomy Division, Department of Physics, PO Box 3000, FIN-90014 University of Oulu, Finland*
[2]*Tuorla Observatory, University of Turku, Väisäläntie 20, FIN-21500 Piikkiö, Finland*
[3]*Instituto de Astronomía, Universidad Nacional Autónoma de México, Apdo. Postal 877, Ensenada, 22800 Baja California, México*
[4]*Finnish Centre for Astronomy with ESO (FINCA), University of Turku, Väisäläntie 20, FI-21500 Piikkiö, Finland*
[5]*The George-Elma Observatory, Mayhill, NM, USA*
[6]*American Association of Variable Star Observers, 49 Bay State Road, Cambridge, MA 02138, USA*
[7]*European Space Astronomy Centre (ESA/ESAC), Science Operations Department, 28691 Villanueva de la Cañada, Madrid, Spain*
[8]*Nordic Optical Telescope, Apartado 474, 38700 Santa Cruz de La Palma, Spain*

Submitted to MNRAS on 2014 May 23

ABSTRACT

The black hole (BH) candidate SWIFT J1753.5–0127 has remained active since the onset of its 2005 outburst. Emission lines in the optical spectrum were observed at the very beginning of the outburst, but since then the spectrum has been featureless making a precise BH mass estimation impossible. Here we present results from our optical and UV observations of SWIFT J1753.5–0127 taken in 2012–2013. Our new observations show extremely broad, double-peaked emission lines in the optical and UV spectra. A time-series analysis of these spectral data and our photometric data revealed a possible orbital periodicity of 2.85 h, significantly shorter than the reported 3.2 h periodic signal by Zurita et al. (2008). The observed variability properties argue against a low orbital inclination angle and we present several observational arguments in favour of the BH interpretation. However, the measured velocity semi-amplitude of 382 km s^{-1} and the short orbital period imply that SWIFT J1753.5–0127 has one of the lowest measured mass function for a BH in a low-mass X-ray binary. We show that the compact object mass in excess of 5M$_\odot$ is highly improbable. Thus, SWIFT J1753.5–0127 is a BH binary that has one of the shortest orbital period and hosts probably one of the smallest stellar-mass BH found to date.

Key words: accretion, accretion discs – binaries: close – X-rays: stars – X-rays: binaries – stars: individual (SWIFT J1753.5–0127)

1 INTRODUCTION

X-ray transients are a subset of the low-mass X-ray binaries (LMXBs) which spend most of their lives in a quiescent state, with typical X-ray luminosities below 10^{32} erg s^{-1}. Occasionally they exhibit bright X-ray and optical outbursts, which occur irregularly with intervals from a few years to decades or even longer. During the outbursts, the X-ray luminosity increases by a factor of up to $10^6 - 10^7$ in a few days and then decays back to quiescence in a few months.

SWIFT J1753.5–0127 is an X-ray transient discovered by the *Swift* Burst Alert Telescope (BAT) on 2005 May 30 as a bright variable X-ray source (Palmer et al. 2005). Although the mass of the primary has not been dynamically measured, the system displays a number of characteristics that suggests the binary hosts a black hole (BH). Firstly, the hard X-ray spectrum at the outburst peak had a maximum (in νF_ν) at ∼150 keV (Cadolle Bel et al. 2007), while the corresponding peaks in neutron star (NS) binaries do not exceed 50 keV (Barret et al. 2000; Poutanen & Gierliński 2003; Gierliński & Poutanen 2005; Lin et al. 2007, 2010; Ibragimov & Poutanen 2009). Secondly, the X-ray spectrum of SWIFT J1753.5–0127 has significantly hardened during the decline phase, with the photon spectral index reaching values as low as $\Gamma = 1.65$ (Chiang et al. 2010), which is typical for hard state BHs, but is much smaller than that in binaries hosting a NS (Zdziarski et al. 1998; Zdziarski & Gierliński 2004; Gilfanov 2010). Thirdly, the X-ray power density spectrum of SWIFT J1753.5–0127 reveals a strong power suppression at frequencies above ∼10 Hz (Durant et al. 2009; Soleri et al. 2013), unlike in NS binaries, which show significant power above ∼500 Hz (Sunyaev & Revnivtsev 2000). Moreover, temporal analysis of the *RXTE* data (Morgan et al. 2005) revealed the presence of the low-frequency quasi-periodic oscillations (QPOs) with a shape

⋆ vitaly@neustroev.net

typically seen in the BH candidates (type C QPO, see Belloni et al. 2011). Neither X-ray bursts, nor pulsations were detected since the initial outburst further hinting towards the BH nature of the central source in the binary.

It is intriguing that 9 years after the beginning of the outburst, SWIFT J1753.5–0127 has not yet returned to the quiescent state. This unusual behaviour has triggered an interest in the binary. Among other properties, a challenging task was to measure system parameters. Neither the mass M_1 of the primary nor even the orbital period $P_{\rm orb}$ are reliably measured at the moment. The optical photometry conducted by Zurita et al. (2008) and Durant et al. (2009) revealed a light curve with a complex non-sinusoidal morphology. The detected $\sim$3.24 h modulations were attributed to the superhump period, which is known to be slightly longer than the orbital period $P_{\rm orb}$ (Patterson et al. 2005). This makes SWIFT J1753.5–0127 one of the shortest orbital period BH systems.

The most direct method of estimating the system parameters of the binary system involves optical spectroscopy, which can give the orbital radial velocity curve of the donor star and of the accretion disc around the primary compact object. A precise determination of the radial velocity amplitude of the secondary in a LMXB is of the highest importance as it allows us to set an absolute lower limit for the mass of the compact object. These measurements are usually done through the analysis of absorption spectra of the secondary. The most appropriate time to study the nature and dynamical properties of the secondary star in X-ray transients is quiescence, during which light from the star contributes significantly to the visible spectrum. Unfortunately, for the case of SWIFT J1753.5–0127 it will be a complicated task owing to the faintness of the source during a quiescent state. It is not visible in archival images and can be as faint as $V\sim$21 mag (Cadolle Bel et al. 2007).

However, some dynamical information about the secondary star can potentially be derived even during outburst. For example, Steeghs & Casares (2002) detected a large number of very narrow emission line features from the irradiated secondary star in the persistent X-ray binary Sco X-1. Furthermore, the discovery of sharp emission components of the Bowen blend in Sco X-1 and the X-ray transient GX 339–4 caught in an outburst state allowed the determination of the primary masses (Steeghs & Casares 2002; Casares et al. 2003; Hynes et al. 2003; Muñoz-Darias et al. 2008).

No time-resolved spectroscopic studies for SWIFT J1753.5–0127 were reported to date, even though a few spectra were presented in the past. The observations near the outburst peak revealed the presence of the double-peaked Hα and He II λ4686 lines (Torres et al. 2005), which seemed to disappear a month later (Cadolle Bel et al. 2007). After that the object showed a rather featureless spectrum (Durant et al. 2009). Our photometric monitoring of SWIFT J1753.5–0127 revealed that in 2012 the binary has weakened by at least $\sim$0.3–0.4 mag in comparison with the previous spectroscopic observations. This gave us grounds to suspect that the lines might have become more apparent. This motivated us to perform time-resolved spectroscopy of SWIFT J1753.5–0127 in order to attempt detection of these lines and to estimate the system parameters. Here we present a study of SWIFT J1753.5–0127 based on our optical and UV spectroscopic observations, supported by the optical photometric monitoring.

2 OBSERVATIONS AND DATA REDUCTION

2.1 *HST* Ultraviolet Observations

We observed SWIFT J1753.5–0127 with the Cosmic Origins Spectrograph (COS) aboard *HST* on 2012 October 8 (PID 12919). The FUV spectra were collected using the low-resolution grating G140L in the 1280 Å setting. This grating covers 1260–2400 Å and 200–1170 Å on the A and B segments of the detector, respectively, with a spectral resolution of $\sim$0.75 Å. The total exposure time of the observations was 1.36 h acquired over a 2.2 h time period (2 orbits).

The data were analyzed using PyRAF routines from STSDAS package *hstcos* (version 3.16). The data from each of the four exposures were summed to produce a single spectrum. Due to very low instrument sensitivity at shorter and longer wavelengths and the relatively low flux of the object ($f_\lambda \lesssim 2\times10^{-15}$erg s^{-1}cm^{-2}Å^{-1}), we cut out the B segment of the spectrum at 1080–1170 Å and the A segment at 1260–2000 Å.

We also used another data set of the COS observations of SWIFT J1753.5–0127 retrieved from the Multi-Mission Archive at STScI (MAST) and reduced in a similar way to that above. These data (PID 12039) taken in both the FUV and NUV channels, were obtained six days before our observations during 5 *HST* orbits, on 2012 October 2. The FUV spectra in this data set were taken with the high-resolution gratings G130M and G160M. The reduced spectra closely resemble our spectrum but are much noisier. Therefore, we did not use them for the following analysis. In the NUV region, the low-resolution grating G230L in the 2950 Å and 3360 Å settings was used, with the exposure time of $\sim$0.4 h in each setting. Four NUV segments were covered (1690–2090 Å, 2120–2515 Å, 2790–3180 Å and 3205–3600 Å) providing a spectral resolution of $\sim$0.8 Å. The G230L data for wavelengths longwards of 3200 Å can be strongly contaminated by second order light and the flux calibration applied by *calcos* at these wavelengths is unreliable (Massa et al. 2010). For this reason we excluded from our analysis the segment covering the wavelength range 3205–3600 Å.

2.2 Optical time-resolved observations

The optical spectra of SWIFT J1753.5–0127 were obtained during four consecutive nights of 2013 August 6–9 at the Observatorio Astronomico Nacional (OAN SPM) in Mexico on the 2.1-m telescope. The observations were conducted with the Boller & Chivens spectrograph, equipped with a 13.5 μm (2174 $\times$ 2048) Marconi E2V-4240 CCD chip. A total of 54 spectra were obtained in the wavelength range of 3600–7000 Å, in the first order of a 400 line mm^{-1} grating with corresponding spectral resolution of $\sim$4.5 Å measured from the night-sky lines. During the first night of observations 600 s individual exposures were taken (12 spectra), while the rest of the spectra were obtained using 900 s individual exposures. The total exposure time was 750 min that allowed us to achieve a signal-to-noise ratio (SNR) in the averaged spectrum of $\sim$160 at 5200 Å.

All the nights of observations were photometric with exception for the first half of the second night (August 7) when cirrus clouds could have affected the flux level of the output spectra. The seeing ranged from 1 to 2 arcsec. The slit width of 2.5 arcsec was chosen to avoid slit losses due to possible imperfect pointing of the telescope. In order to apply an accurate flux correction, three standard spectrophotometric stars were observed every night. They were selected from Feige 110, HZ 44, BD+33 2642

Table 1. Log of optical time-resolved observations of SWIFT J1753.5–0127.

Date	HJD Start 2450000+	Telescope / Instrument	Filter / λ range (Å)	Exp.Time (s)	Number of exps.	Duration (h)
2013-Aug-06	6510.808	2.1 m / B&Ch	3600–7000	600	12	1.97
2013-Aug-07	6511.688	1.5 m / RATIR	V, i	80	140	3.78
	6511.718	2.1 m / B&Ch	3600–7000	900	12	3.66
2013-Aug-08	6512.660	2.1 m / B&Ch	3600–7000	900	18	5.15
	6512.684	1.5 m / RATIR	V, i	80	140	3.62
2013-Aug-09	6513.712	2.1 m / B&Ch	3600–7000	900	12	3.84

Table 2. Log of photometric observations of SWIFT J1753.5–0127.

Date	HJD start 2450000+	Exp. Time (s)	Duration (h)	Average Magnitudes B	V	R	I
2012-Sep-21	6191.687	300	1.33	17.30±0.04	16.90±0.03	16.63±0.02	16.16±0.02
2012-Oct-03	6203.630	420	1.40	...	16.88±0.03	16.62±0.02	16.19±0.02
2012-Oct-08	6208.632	300	1.67	...	...	16.58±0.01	...
2012-Oct-09	6209.589	300	0.67	17.18±0.05	16.85±0.04	16.66±0.03	16.15±0.03
2013-Apr-12	6394.903	300	1.33	17.30±0.04	16.89±0.03	16.63±0.02	16.10±0.02
2013-Apr-16	6398.926	300	1.33	17.28±0.04	16.91±0.03	16.64±0.02	16.19±0.02
2013-Jun-19	6462.728	300	3.33	17.24±0.05	16.93±0.02	16.62±0.03	16.19±0.03
2013-Aug-09	6513.631	300	3.67	17.33±0.05	16.93±0.02	16.63±0.03	16.15±0.03
2013-Aug-10	6514.627	300	3.33	17.33±0.05	16.91±0.02	16.67±0.03	16.17±0.03
2013-Aug-11	6515.543	300	3.33	17.31±0.05	16.89±0.03	16.65±0.03	16.12±0.03
Mean				17.28±0.05	16.90±0.02	16.63±0.03	16.16±0.03

and BD+28 4211 (Oke 1990). Comparison spectra of Cu-He-Ne-Ar lamp were used for the wavelength calibration. The data reduction was performed using the IRAF environment.

During the nights of August 7 and 8, the spectroscopic observations were accompanied by photometric time-resolved observations on the Harold L. Johnson 1.5 m telescope at the same site. The observations were performed simultaneously in the Johnson V and SDSS i bands with the use of a multi-channel imager RATIR (Butler et al. 2012; Watson et al. 2012). The exposure times were 80 s. The V magnitudes of the object were determined using the calibration stars reported by Zurita et al. (2008). Due to the lack of observations of photometric standard stars in the SDSS i filter, we used an arbitrary zero-point for the i measurements. Table 1 provides the journal of the optical time-resolved observations of SWIFT J1753.5–0127.

2.3 Optical and UV photometric monitoring

In order to investigate the long-term photometric behaviour and to check for the current state of the object during our spectroscopic observations, we additionally obtained several sets of multi-colour photometric data. These observations were performed from September 2012 to August 2013 at New Mexico Skies in Mayhill, New Mexico with the 0.35-m Celestron C14 robotic telescope and an SBIG ST-10XME CCD camera with Johnson-Cousins $BV(RI)_C$ Astrodon Photometric filters. The images were usually taken in a sequence B-V-R-I with exposure times of 300 s for each filter. In order to establish nightly averaged fluxes, we observed the object for several hours per night. The data reduction was performed using the IRAF environment and the software AIP4Win v. 2.4.0 (Berry & Burnell 2005). In order to improve the confidence of our measurements we aligned and summed all the nightly images for each filter and then measured the average magnitudes. We used the secondary standards found in Zurita et al. (2008) to establish the zero points. Table 2 provides a journal of the photometric observations with the measured magnitudes. We note that the VRI magnitudes obtained on 2012 October 3 are very close to the values of Froning et al. (2014) obtained a day before.

We also performed a ToO observation of SWIFT J1753.5–0127 in $uvw2$ filter with the UV-Optical Telescope (UVOT) onboard the *Swift* X-ray satellite (Gehrels et al. 2004) on 2012 September 19. Furthermore, we used the *Swift*/UVOT data obtained during the entire 2012 year. These observations were analyzed with the Swift Release 3.7 software[1] together with the most recent version of the Calibration Database. The UVOT observations were reduced following the procedure described in Poole et al. (2008).

3 DATA ANALYSIS AND RESULTS

3.1 UV spectrum

The UV spectrum of SWIFT J1753.5–0127 is shown in Fig. 1 (left panel). The spectrum is uncorrected for the interstellar reddening, which manifests itself in a deep absorption feature centered at 2175 Å. We also show the UVOT measurements in UV filters (*uvw1*, *uvm2*, *uvw2*). Only the *uvw2* measurements were obtained near the time of the *HST* observations, the fluxes in other UVOT filters are the average of the measurements obtained during the year 2012. The UVOT fluxes are very similar to those derived from the spectroscopy.

[1] http://swift.gsfc.nasa.gov/docs/software/lheasoft/

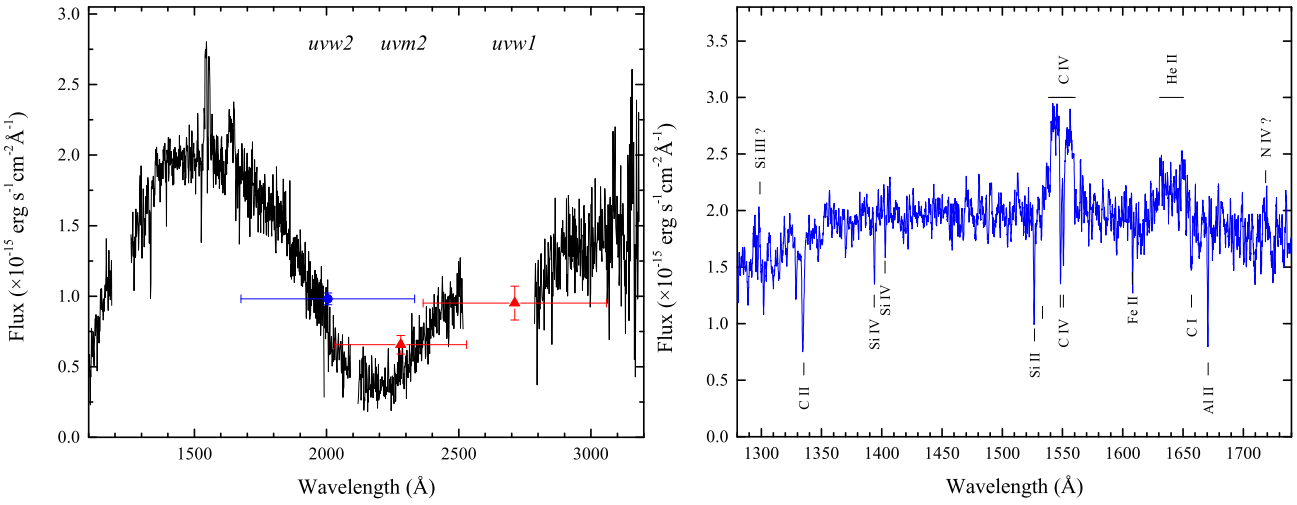

Figure 1. Left: The UV spectrum of SWIFT J1753.5–0127 uncorrected for interstellar reddening. The data have been binned to ∼2.5 Å spectral resolution. The blue circle and red triangles show the Swift/UVOT measurements. Right: A part of the FUV spectrum containing the strongest lines and smoothed with a 20 point running boxcar to show the weaker lines.

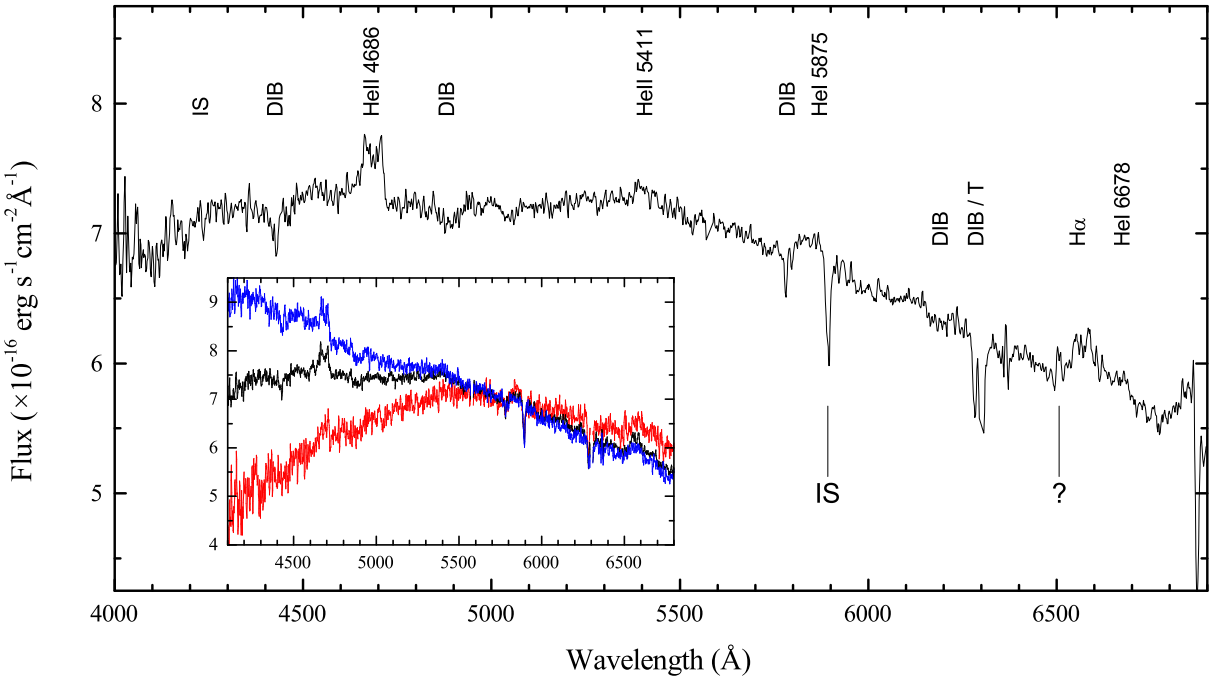

Figure 2. The averaged optical spectrum of SWIFT J1753.5–0127. The inset shows the extreme shapes of the variable continuum.

The UV spectrum is dominated by broad and double-peaked emission lines of C IV λ1550 and He II λ1640 with no P Cyg absorption components. There is also a hint of other weaker emission lines of Si III λ1298 and N IV λ1718. The absorption spectrum is rich in features, but all these absorption lines are very narrow and are not shifted with respect to the rest wavelength being consistent with the interstellar origin. The strongest lines are C I λ1657, C II λ1335, C IV (λ1548.2, λ1550.7), Si II (λ1527, λ1533), Si IV (λ1393.8, λ1402.7), Fe II λ1608, Al II λ1671. In the NUV spectrum we were unable to identify any spectral lines. A part of the FUV smoothed spectrum containing the strongest lines is shown in Fig. 1 (right panel).

3.2 Optical spectrum

The averaged optical spectrum of SWIFT J1753.5–0127 is shown in Fig. 2. It exhibits very broad double-peaked emission lines of He II λ4686 and Hα. There are also hints of He II λ5411 and He I emission lines (5875 Å, 6678 Å) and of the Bowen blend. We also note the presence of a narrow, unidentified emission line at ∼6507 Å. This feature seems to be real and not an artefact of the data reduction because it is present in all our subsets of observations of SWIFT J1753.5–0127, but is not seen in spectra of any other targets observed the same nights. To the best of our knowledge, the detection of a similarly weak emission line in this wavelength region was reported only for the X-ray transient GX 339–4.

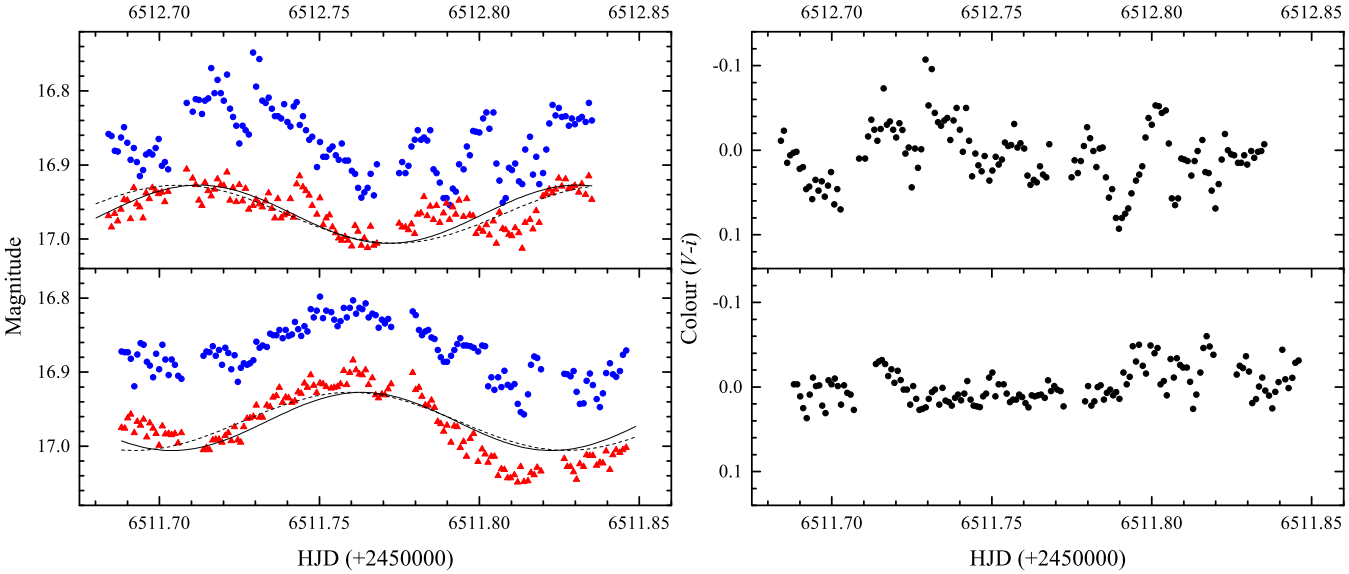

Figure 3. Left: The V (blue circles) and SDSS i-band (red triangles) light curves of SWIFT J1753.5–0127. Due to the lack of observations of photometric standard stars in the SDSS i filter, an arbitrary zero-point was used for the i-band measurements. The solid and dashed lines are sinusoidal fits to the i-band data with the period constrained to ∼2.85 h and ∼3.24 h, respectively. Right: The corresponding $V - i$ colour (with the linear trend subtracted for each night of observations).

Soria, Wu, & Johnston (1999) identified this line with N II λ6505. However, we doubt this identification as no other N II lines are observed in either SWIFT J1753.5–0127 or GX 339–4.

Several diffuse interstellar bands (DIB), interstellar (IS) and telluric absorption lines (T) are apparent in the spectrum. Besides them, no other absorption lines which might be identified with the secondary star are seen in this averaged spectrum. However, the time-resolved spectra reveal a few narrow absorption and emission features which show significant sinusoidal Doppler shifts. We discuss these features in Section 3.4.

The continuum in the averaged spectrum has a broken-line shape with a knee around 5400 Å, somewhat similar to the WHT/ISIS spectrum obtained in 2006 June 17 (Durant et al. 2009), but in contrast to most of other spectra from early observations which could be reasonably well represented by a straight line (Cadolle Bel et al. 2007; Durant et al. 2009). A visual inspection of individual spectra has shown that the continuum shape exhibits strong variability. The slope of the shorter wavelength segment significantly varies, while the longer wavelength segment is much more stable (see the inset in Fig. 2). We checked if these variations could be caused by wavelength dependent slit losses and found no correlation with seeing and airmass. Moreover, the spectra of other variable and standard stars taken during the same nights with the same telescope/instrument did not reveal such variability of the continuum shape. Thus, the detected variability is real and is not an artefact of the flux calibration.

In order to study the time dependence of this variability, we calculated the ratio F_{4300}/F_{6250}, where F_{4300} and F_{6250} are the fluxes averaged across the wavelength bands centered at 4300 Å and 6250 Å with the widths of 600 Å and 500 Å, respectively. This ratio is analogous to the colour $B - R$. In Section 3.3, we show that F_{4300}/F_{6250} displays a notable variability with the orbital period. In addition, there are signs in our RATIR data of another, shorter time-scale variability associated with varying continuum shape, which is stronger in the V-band than in the i-band. The corresponding peak-to-peak amplitude of the $V - i$ colour index variability is as large as ∼0.15 mag, which is similar to the amplitude of the orbital modulation (Fig. 3). Because of the shortness of these RATIR observations we are unable to reach a firm conclusion on the periodicity of the detected variability, but the data hint towards the period of ∼ 33 min. Longer multicolour observations with high enough time resolution preferably in the B and R filters should shade more light on this phenomenon. In conclusion, we note that the nightly averaged magnitudes are very stable in all the filters except for B (Table 2, see also Froning et al. 2014). The latter shows the relatively large observed scatter in magnitudes. It can naturally be explained by the optical continuum variability if it is also present on the longer time scales.

3.3 Orbital period

SWIFT J1753.5–0127 is known to show relatively strong modulations as seen in its optical light curve (Zurita et al. 2008; Durant et al. 2009), however the precise orbital period of the system is still unknown. Zurita et al. (2008) reported a determination of the modulation period to be ∼3.24 h which they attributed to a superhump period. During our observations, a similar modulation is also clearly visible in both V and i filters (Fig. 3). There also is an apparent colour variability that is in contrast to the observations of Durant et al. (2009), during which the colours varied very little. The Lomb-Scargle periodograms for the V and i RATIR photometric data show the strongest peaks at a frequency of ∼8.4 cycle day^{-1} (Fig. 4), which is close to the one-day alias of the period found by Zurita et al. (2008).

Besides the analysis of photometric variability, we also performed a time series analysis of our optical spectroscopic data. In addition to the colour index F_{4300}/F_{6250} introduced in Section 3.2, we also calculated additional quantities. The quantity LF (normalised Line Flux) is closely related to the equivalent width of He II λ4686 and defined as the flux integrated over the wavelength range λλ4645–4726 Å divided by the averaged flux in the wavelength ranges λλ4512–4612 Å and λλ4727–4827 Å. We also

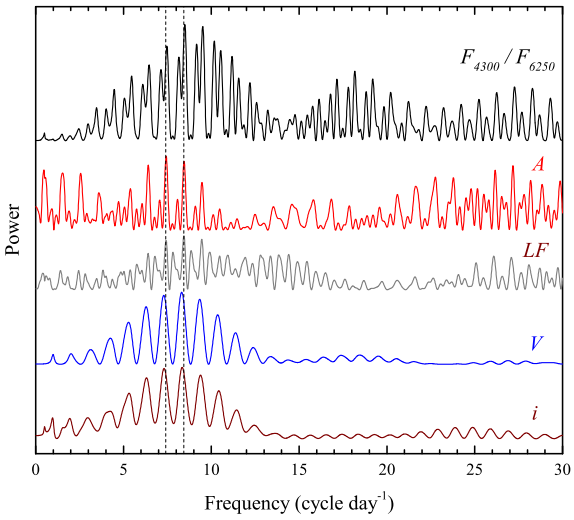

Figure 4. Power spectra of different quantities calculated from the optical photometric and spectroscopic data (see text for explanation). The vertical dashed lines mark the adopted orbital frequency of 8.41 cycle day^{-1} and the previously proposed 3.24 h period (7.41 cycle day^{-1}).

introduce the asymmetry parameter A as the ratio of the equivalent widths of the He II λ4686 line on each side of the rest wavelength. This parameter is sensitive to the variations of both the radial velocity and the shape of the He II λ4686 line profile.

The power spectra of F_{4300}/F_{6250}, A and LF are also shown in Fig. 4. Most of them are dominated by a peak at the same frequency of $\sim$8.4 cycle day^{-1}, with its averaged value being 8.41 ± 0.04 cycle day^{-1} (2.85$\pm$0.01 h). The existence of the variability with the same period in both the photometric and spectroscopic data indicates that this is the true orbital period.

3.4 The radial velocity of the secondary star

In outburst, the optical flux from the binary system is dominated by emission from the luminous accretion disc, making the photospheric absorption lines of the donor virtually undetectable. However, closer inspection of the trailed spectrum of SWIFT J1753.5–0127 revealed hints of several narrow absorption and emission features that showed radial velocity variations with a large amplitude and in phase with each other. These weak features are more or less clearly seen only in the wavelength region with the highest SNR ($\sim$5100–5400 Å). A few other absorption lines may also be presented in other spectral regions, though their detection is less reliable. The strongest detected lines are located at $\sim$5193.0 Å, 5279.0 Å and 5356.1 Å and marked by the dashed lines in Fig. 5 (top panel). Surprisingly, their identification is unclear. This spectral region of late K- and M-type stars contains a wealth of absorption lines. Some of them can be matched with the features detected in the spectrum of SWIFT J1753.5–0127, but the absence of other expected lines stalls the identification (Fig. 5, bottom panel).

Nevertheless, the presence in the spectrum of an ensemble of spectral features with nearly synchronous and significant Doppler motions indicates their common origin which we tentatively associate with the secondary star.

In order to characterize these velocity variations, we firstly phased the individual spectra with the orbital period of 2.85 h and then co-added the spectra into 20 separate phase bins. We placed orbital phase zero at HJD 2 456 510.8081 – the time of inferior con-

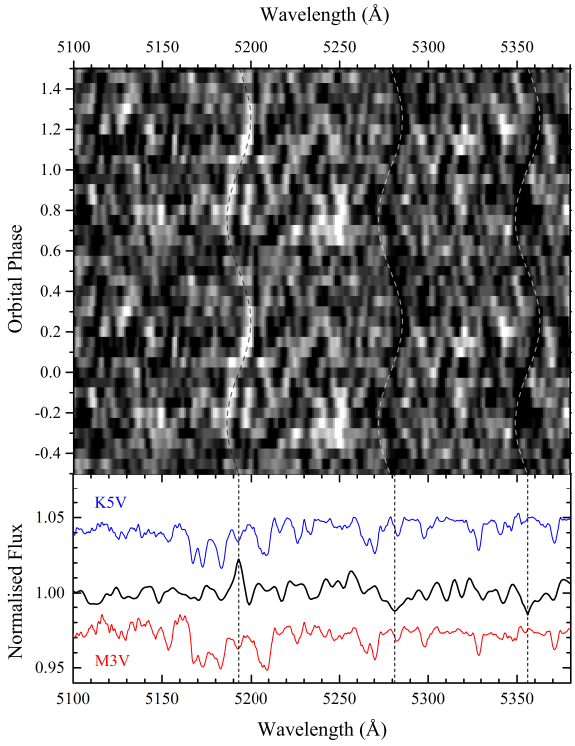

Figure 5. Top: A part of the trailed spectrum of SWIFT J1753.5–0127 showing sinusoidal trails of absorption and emission features, marked by the dashed lines. White indicates emission. Two cycles are shown for clarity. Bottom: The averaged and normalized spectrum of SWIFT J1753.5–0127, compared with two spectral standards. The spectrum of SWIFT J1753.5–0127 have been corrected for orbital motion of the secondary star.

junction of the secondary star (derived later in this section). The resulted phase-folded spectra have relatively high SNR of $\sim$50–70 (at 5200 Å).

The radial velocity measurements of the donor star in LMXBs are usually obtained through cross-correlation of the absorption lines with stellar templates of similar spectral type. This method works even if the spectral features of the secondary star are not obvious in the spectrum. However, the mismatch between spectral lines of SWIFT J1753.5–0127 and the standard stars requires to use another template. Following the iterative approach described in Neustroev & Zharikov (2008), we created the cross-correlation template spectrum from the observed spectra of the system. This approach maximises the similarity between the template and the individual spectra to be cross-correlated.

The first step was to measure the radial velocity variations of the strongest observed lines λ5193 Å and λ5356. The velocities were independently measured by fitting each line profile in the phase-folded spectra with a single Gaussian. The resulting radial velocity curves were then fitted with a sinusoid of the form

$$V(\phi) = \gamma - K_{2,\mathrm{o}} \sin\left[2\pi\left(\phi - \phi_0\right)\right]. \qquad (1)$$

We obtained the observed radial velocity semi-amplitude $K_{2,\mathrm{o}}$ to be 383 ± 13 km s^{-1} for the emission line λ5193 Å and 349 ± 20 km s^{-1} for the absorption line λ5356 Å, whereas the difference between the phase zero-points ϕ_0 for these lines was found to be $\sim$0.01 (Fig. 6). Using these preliminary values of $K_{2,\mathrm{o}}$ and ϕ_0, each individual spectrum was then shifted to correct for the orbital motion of the donor star. The cross-correlation template was then obtained by averaging shifted individual spectra.

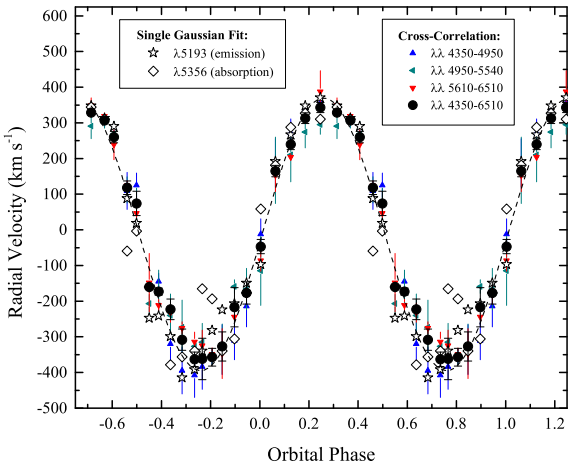

Figure 6. Radial velocities of the secondary star folded on the ephemeris from Table 4. The measurements are obtained using the cross-correlation in different wavelength ranges. It also shows the radial velocities of the lines λ5193 Å (in emission) and λ5336 Å (in absorption) obtained with a single Gaussian fit. Two cycles are shown for clarity.

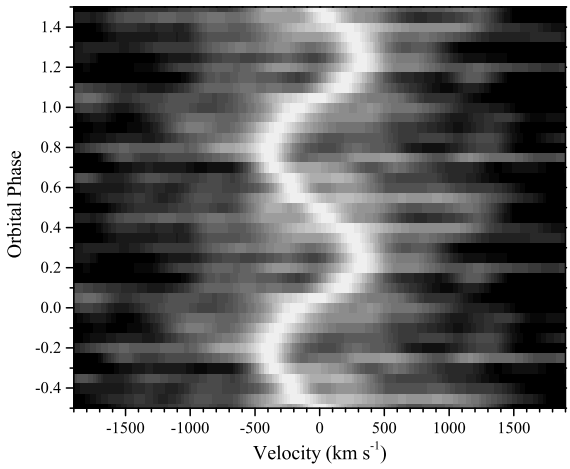

Figure 7. Two-dimensional representation of the cross-correlation function obtained over the wavelength interval of $\lambda\lambda$4350–6510 Å. Two cycles are shown for clarity.

In the next step, the phase-folded spectra of SWIFT J1753.5–0127 were cross-correlated with the template. Prior to the cross-correlation, the target and template spectra were normalised by dividing by the result of fitting a low-order spline to the continuum. In a case of noise-dominated spectra, its cross-correlation with any template may produce spurious peaks in the cross-correlation function (CCF) and the correspondingly measured radial velocities would not follow a common sine curve. Therefore, in order to test for reliability in the derived parameters, the cross-correlation was carried out in three separate wavelength regions $\lambda\lambda$4350–4950 Å, $\lambda\lambda$4950–5550 Å and $\lambda\lambda$5610–6510 Å. To avoid the influence of the emission and the night-sky lines, the portions of the spectra around these spectral features were masked. We found that all the corresponding CCFs show strong and distinct peaks (Fig. 7). The radial velocity and its accuracy were then determined by fitting the strongest peak of each CCF with a Gaussian and a linear background. Our solutions obtained by fitting the measured radial velocities with the sinusoid (1) are very similar for all three wavelength ranges and they are close to the measurements obtained for the visually detected lines.

In the final step, these solutions were used to create a new cross-correlation template. The cross-correlation analysis was then performed over the full wavelength interval of $\lambda\lambda$4350–6510 Å giving the best-fitting results $K_{2,\mathrm{o}} = 382 \pm 8$ km s^{-1}and the phase zero-point of inferior conjunction of the secondary star ($\phi_0 = 0$) corresponding to T_0=HJD 2 456 510.8081±0.0005. In Fig. 6 we show the measured radial velocities together with their sinusoidal fit.

The similarity of the solutions in different wavelength regions leaves no doubts in the reality of the radial velocity variability. The presented analysis also strongly indicates that in addition to the visible spectral lines, there must exist other emission or absorption features in all parts of the spectrum, which are undetectable by eye, but distinguishable by cross-correlation. Using the final cross-correlation template, which essentially is the spectrum of SWIFT J1753.5–0127 corrected for orbital motion of the secondary star, we made another attempt to identify the spectral features of a late-type star, but were again unsuccessful.

A possible reason for our failure may be the extreme conditions under which the donor star existed at the time of our observations. During the outburst stage the secondary should be significantly heated by its companion. Theoretical studies show that a dramatic temperature inversion is expected in the atmosphere of an irradiated M dwarf star. As a result, the emergent spectrum will be significantly different from that of an isolated M dwarf (Barman, Hauschildt, & Allard 2004). Depending on the power of the incident flux and the temperature, pressure, and chemical composition of the secondary's atmosphere, the resulting spectrum can have complex mixtures of emission and absorption lines. The identification of such a spectrum would be a very complicated task.

3.5 Disc emission lines

We compared the emission lines between the UV and optical data sets and show mean profiles in Fig. 8. In contrast to the UV lines, the optical lines are much weaker (for example, the peak normalised fluxes of He II λ1640 and λ4686 are 1.37 and 1.08, respectively), nevertheless their profiles are very similar in shape and width.

The lines are very wide, and the higher excitation lines are much wider than Hα. This property and the double-peaked appearance of the emission lines suggest their origin in an accretion disc (Smak 1981; Horne & Marsh 1986). Table 3 outlines different parameters of the major emission lines measured from the averaged spectra.

3.5.1 Accretion disc parameters from modelling of the emission line profiles

Despite the similarity of the emission line profiles in SWIFT J1753.5–0127 with those typically observed in other LMXBs, the steepness of the profile wings of high excitation lines (He II and C IV) in SWIFT J1753.5–0127 is quite unusual. It is well known that the shape of the double-peaked profile wings is controlled by the surface radial emissivity profile (Smak 1981; Horne & Marsh 1986). This profile is commonly assumed to follow a power-law model of the form $f(r) \propto r^{-b}$, where r is the radial distance from the compact object. The mechanism powering the emission lines in quiescent accretion discs is discussed in Horne & Saar (1991). Observations of cataclysmic variables (CVs)

and BH binaries show that b is usually in range of 1–2, rarely being less than 1.5 (Johnston et al. 1989; Orosz et al. 1994, 2002).

In order to estimate b and other parameters of the accretion disc of SWIFT J1753.5–0127, we fitted the symmetrical double-peaked emission line profiles using a simple model of a uniform flat axisymmetric Keplerian geometrically thin disc (Smak 1981). To calculate the line profiles we used the method of Horne & Marsh (1986). Examples of the application of this technique to the real data are given in Johnston et al. (1989); Orosz et al. (1994, 2002); Neustroev (1998); Neustroev et al. (2002). The three primary free parameters of the model are

(i) $V_{\rm out}$, the velocity of the outer rim of the accretion disc,
(ii) b, the power-law index of the line emissivity profile $f(r)$.
(iii) $r_{\rm in}/r_{\rm out}$, the ratio of the inner to the outer radii of the disc,

Fig. 8 shows four optical and UV emission line profiles together with the corresponding model fits. Parts of the profiles affected by other spectral features (such as deep interstellar absorptions in the centre of C IV and a strong emission feature in the centre of Hα) were excluded from the fit. The best-fitting model parameters are listed in Table 3 and the errors were estimated with a Monte Carlo approach described in Borisov & Neustroev (1998). The best-fitting power-law index for Hα line was $b = 1.58$, which is very close to the values of b found for many other LMXBs. However, the model fits for He II and C IV lines give $b{\approx}0$ and even negative values that suggests an unusually flat (or even inverted) radial distribution of the emission-line flux from the accretion disc of SWIFT J1753.5–0127. Because of the lack of data, it is not clear whether such a behaviour is common for BH binaries. However, Marsh & Horne (1990) found that in the dwarf nova IP Peg during an outburst stage, the He II λ4686 radial emissivity profile is also remarkably flat compared to the Balmer emission ($b \approx 0.1$ and ≈ 2, respectively). Marsh & Horne showed that such a behaviour is not in agreement with the predictions of line emission from optically thin discs. They concluded that photoionization by the soft X-rays and UV photons generated in the centre of the accretion disc should be taken into account. We suggest that a similar mechanism may explain the observed properties of the emission lines of SWIFT J1753.5–0127.

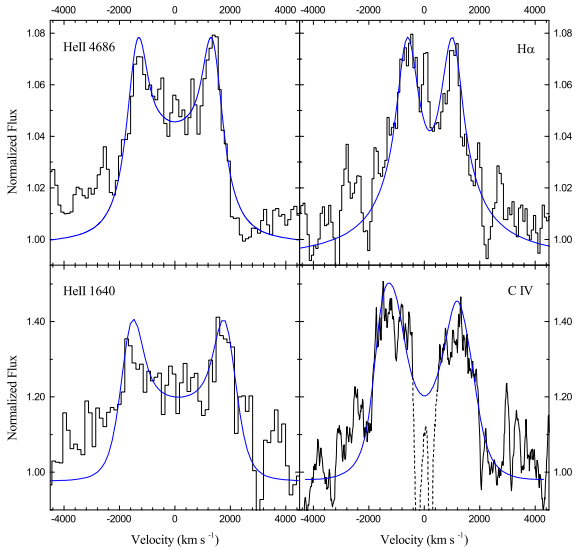

Figure 8. The profiles of the emission lines observed in the optical and UV spectra of SWIFT J1753.5–0127 together with the corresponding model fits.

3.5.2 *Orbital variability of the optical emission lines, the equivalent widths and Doppler tomography*

A visual inspection of the optical spectra has shown orbital variations in the line profiles. This is better seen in trailed spectra as variations of the relative intensity of the two peaks in the double-peaked profiles (see top left panels of Fig. 9). We measured the equivalent widths (EW) of the emission lines in the phase-folded spectra using the IRAF task *splot* (Fig. 10). The 1σ errors were estimated from the noise fluctuations in the continuum. Though the obtained EWs exhibit rather significant dispersion, none the less we see that they are modulated with the amplitudes of about $\pm 25\%$ of the mean value.

The observed EW minima could be due to an increase in the continuum luminosity when the region of enhanced emission crosses the line-of-sight. There is, however, an apparent shift between the EW curves and optical light curves (see the phase-binned i-band light curve in Fig. 10). The maximum of the optical flux occurs close to the inferior conjunction of the secondary star at phase 0, whereas the EW minima are observed around phase 0.2.

The orbital variation of the emission line profiles indicates the presence of a non-uniform structure in the accretion disc. In order to study it in more detail, we used Doppler tomography. Technical details and examples of the application of Doppler tomography to real data are given by Marsh & Horne (1988) and Marsh (2001). The Doppler maps of the He II λ4686 and Hα emission lines were computed using the code developed by Spruit (1998). The resulting tomograms are presented in the bottom panels of Fig. 9, whereas the observed and reconstructed emission line profiles are shown in the top panels. To help in interpreting the Doppler maps, additional symbols are inserted, which mark the positions of the compact object (lower cross), the centre of mass of the binary (middle cross) and the Roche lobe of the secondary star (upper bubble with the cross). The circle of radius 600 km s^{-1} around the center of mass corresponds to the projected velocity of the outer part of the largest accretion disc restricted by tidal forces. The Roche lobe of the secondary has been plotted using the system parameters: M_1=3M$_\odot$, M_2=0.2M$_\odot$, i=40°(see Section 4).

The observed sharp asymmetric double-peaked profiles of the emission lines produced the azimuthally asymmetric annuli of emission. The radii of the annuli are different for He II and Hα, reflecting the different peak-to-peak velocity separation in these lines. However, the overall appearance of the tomograms is rather similar. They both display the enhanced emission region in the upper-right quadrant. The origin of this structure is unclear. It is located far from the region of interaction between the stream and the disc, which is situated to the left of the secondary star bubble. The data neither show the emission from the donor which is often observed in the CVs during outbursts.

We also note that the Hα data display the low-velocity component which produces a compact spot of emission located around the centre of mass of the binary in the corresponding Doppler map. The source of this feature is not clear. It might be a result of poor subtraction of the geocoronal Hα night sky line. However, the phase dependence of this line raise a doubt.

Table 3. Parameters of the major emission lines in the averaged spectrum of SWIFT J1753.5–0127.

Spectral line	Flux ($\times 10^{-14}$ erg s^{-1}cm^{-2})	EW (Å)	Relative flux	FWHM (km s^{-1})	Peak-to-peak (km s^{-1})	Model parameters $V_{\rm out}$ (km s^{-1})	b	$r_{\rm in}/r_{\rm out}$
Hα	0.223	3.6	1.07	2450	1650	798±10	1.58±0.05	0.02±0.01
He II λ4686	0.329	4.3	1.08	4200	2690	1370±6	−0.80±0.11	0.06±0.05
He II λ1640	1.21	7.1	1.37	4020	3400	1677±7	−0.85±0.11	0.14±0.06
C IV λ1548.2	1.33	7.1	1.45	3820	2440	1348±8	0.05±0.12	0.14±0.06
C IV λ1550.8						1352±9	0.02±0.15	0.10±0.04

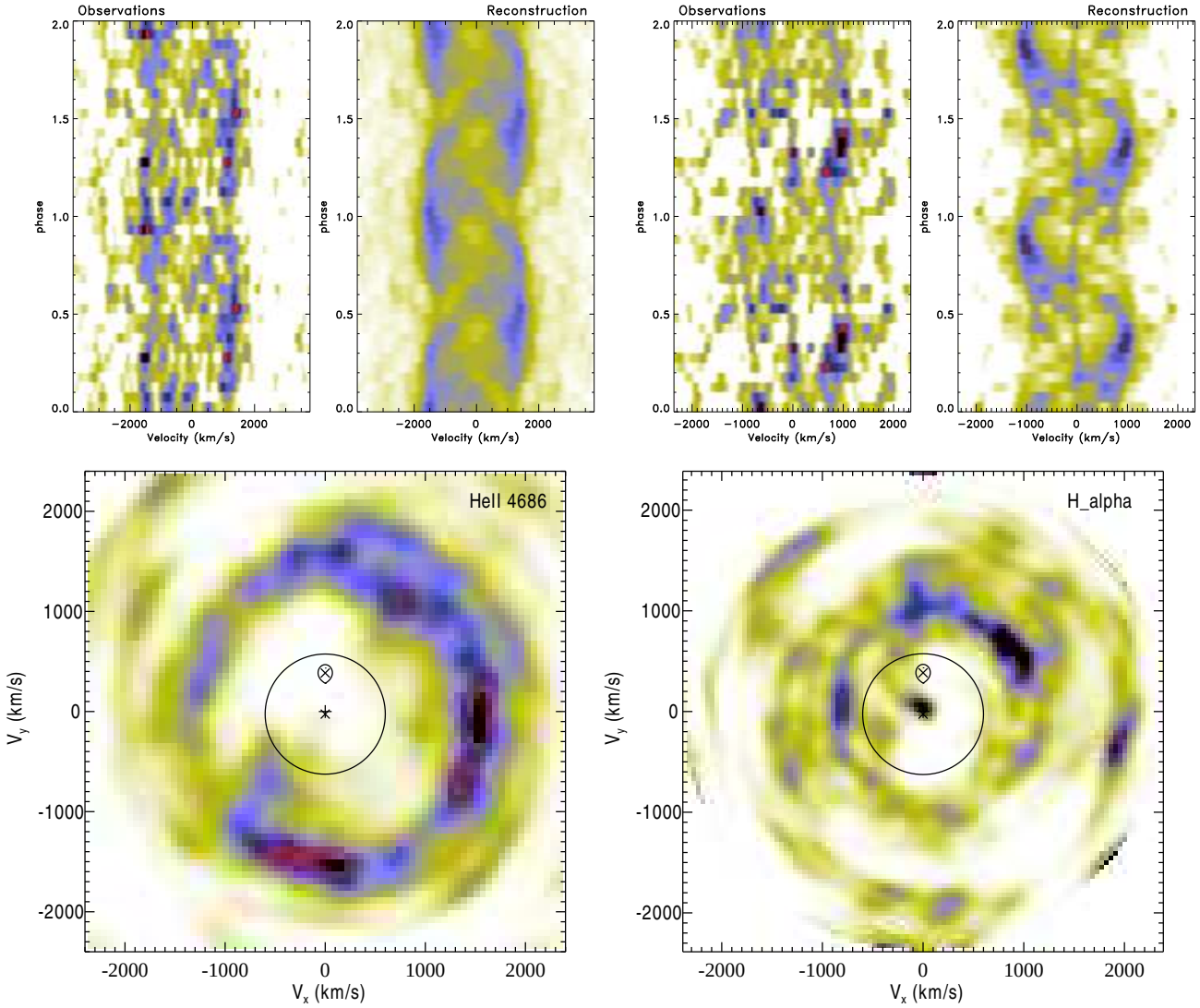

Figure 9. Doppler tomography for the He II λ4686 and Hα emission lines. The top panels show the observed (left) and reconstructed (right) line profiles folded on the orbital period. The corresponding Doppler maps are shown in the bottom panels.

3.5.3 Radial velocity analysis

We attempted to derive the radial velocity curve of the compact object in SWIFT J1753.5–0127 using the double-Gaussian method (Schneider & Young 1980; Shafter 1983), but results were implausible. This is not a surprise, as the method uses the extreme wings of the emission line profile which are very noisy even in the phase-folded spectra of the object because of their steepness. Instead, the radial velocities were measured by fitting the modelled double-peaked profile (see details in Section 3.5.1) to the observed phase-binned profiles. All the primary parameters of the model ($V_{\rm out}$, b and $r_{\rm in}/r_{\rm out}$) were frozen to the averaged values listed in Table 3, but the model profile was allowed to shift along wavelengths. We used only the He II λ4686 line for this analysis as it has more clear and symmetric profiles than Hα and also because it is presumably

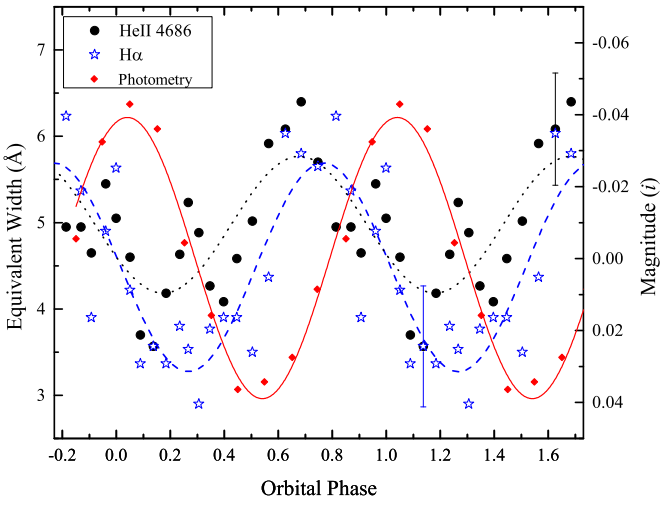

Figure 10. The variation of the EWs of He II λ4686 (filled circles) and Hα (open stars) with the orbital period. Also shown the phase-binned i-band light curve (red diamonds, the right axis). Two periods are shown for clarity.

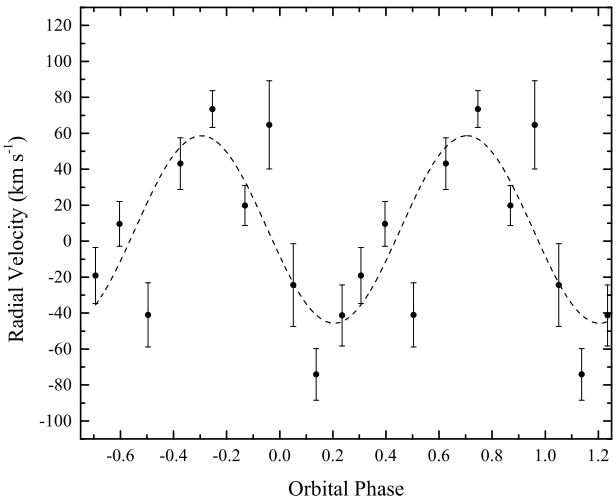

Figure 11. Radial velocities of the He II λ4686 emission line folded on the ephemeris from Table 4. Two cycles are shown for clarity.

formed in the inner parts of the accretion disc. Therefore, it should represent the motion of the central star with a higher reliability.

The results are shown in Fig. 11 (right panel). The errors are the formal model fitting errors estimated with a Monte Carlo approach. We made a non-linear least-square fit of the derived velocities to a sinusoid of the form (1), where K_2 was replaced by K_1. This fit gives the semi-amplitude $K_1 = 52 \pm 10$ km s^{-1}, the systemic velocity $\gamma = 6 \pm 6$ km s^{-1} and $\phi_0 = 0.45 \pm 0.03$. The difference between the phase zero-points obtained from the emission and absorption lines is close to 0.5, as expected if the derived velocities from those lines trace the motion of the two components. However, it is well known that the parameters obtained with this method are affected by systematic errors, because the emission lines arising from the accretion disc may have severe asymmetric distortions (see, for example, discussion in Orosz et al. 1994). Thus, the obtained value of K_1 should be used with great caution.

4 THE BINARY SYSTEM PARAMETERS

4.1 The K-correction

The observed values of $K_{2,\rm o}$ are often known to suffer from non-uniform distribution of absorption or emission spectral features on the donor star surface due to the heating effect by irradiation from the X-ray source. The noncoincidence of the centre-of-mass and the centre-of-light of the donor can result in systematic errors in the determined velocity amplitude $K_{2,\rm o}$. A mixture of emission and absorption lines in the spectrum of SWIFT J1753.5–0127 strongly suggests that irradiation of the secondary plays a significant role. Moreover, the flux at 5000 Å from a low-mass star with temperature of 3000 K and radius of 2×10^{10} cm at 2 kpc is expected to be considerably smaller than the observed one ($F_\lambda \approx 2.5\times10^{-19}$ and 7×10^{-16} erg s^{-1}cm^{-2}Å^{-1}, respectively). Thus, no lines from the dark side of the star should be visible in the observed spectrum. This suggests that the cross-correlation signal likely originates in the irradiated surface of the secondary. Therefore, in order to obtain the true value of K_2, a 'K-correction' should be applied.

The K-correction generally depends on the mass ratio and the distribution of spectral line emission or absorption over the surface of the secondary star and can be expressed as (Wade & Horne 1988; see also equation 2.77 in Warner 1995):

$$\frac{K_{2,\rm o}}{K_2} \approx 1 - 0.462 q^{1/3} (1+q)^{2/3} \frac{\Delta R_2}{R_2}, \qquad (2)$$

where q is the mass ratio M_2/M_1, R_2 is the radius of the secondary and ΔR_2 is the displacement of the centre-of-light from the centre of mass of the secondary star. It is difficult to quantify the correction without the knowledge of these parameters. In order to estimate its reliable extreme value, we adopted the realistic values of $q = 0.04 - 0.12$ (see Section 4.5) and assumed $\Delta R_2/R_2$ to be $\sim$0.5 that roughly corresponds to the extreme case where the spectral lines come only from the hemisphere closest to the primary. Within these assumptions $K_{2,\rm o}/K_2$ is in the range 0.88–0.92, therefore in the following analysis we use $K_{2,\rm o}/K_2 = 0.9$ as an illustration for a possible K-correction.

In theory, the correction can be larger if emission is tightly concentrated near the L_1-point. However, this is not supported by observations. Such a compact emission source should be luminous enough to produce a visible structure in the Hα Doppler map. Moreover, in a realistic situation, the accretion disc's outer rim casts a broad shadow onto the donor star, and only relatively small areas near the poles of the donor's facing hemisphere can be directly irradiated by the central X-ray source. In order for the secondary star to be illuminated, indirect irradiation via scattered X-rays should be taken into account, or there should exist another source of irradiation, located outside the equatorial plane. Both these scenarios imply that sufficiently extended regions on the donor star will be irradiated (for a detailed discussion, see Dubus et al. 1999 and Ritter 2008).

4.2 Mass function and constraints on the compact object mass from the double-peaked emission lines

The semi-amplitude K_2 of the secondary's radial velocity curve and the orbital period $P_{\rm orb}$ give the mass function which sets an absolute lower limit for the mass of the compact object:

$$f(M) = \frac{K_2^3 P_{\rm orb}}{2\pi G} = \frac{M_1^3 \sin^3 i}{(M_1+M_2)^2}, \qquad (3)$$

where M_1 is the mass of the compact object , M_2 is the mass of the secondary star and i is the binary inclination. From the observed velocity $K_{2,\rm o} = 382$ km s^{-1} we can calculate the "observed" mass function $f_{\rm o}(M) = 0.69 \pm 0.04$ M$_\odot$. Applying the K-correction, we obtain the mass function $f(M) \lesssim 0.95$ M$_\odot$, which is one of the smallest mass function for a BH LMXB (Casares & Jonker 2014).

Another independent approach to constrain the compact object mass is to measure the outer disc velocity. Smak (1981) has shown that assuming the Keplerian velocity in the accretion disc

$$V_{\rm K} = \sqrt{\frac{GM_1}{r}}\,, \tag{4}$$

the double-peaked profiles can be used to determine the projected velocity $V_{\rm out}$ of the outer rim of the accretion disc, which, in turn, depends on the mass M_1 of the accreting star and the radius of the disc. The largest radius of the accretion disc, should it be determined from observations, can further constrain the system parameters.

We measured $V_{\rm out} \approx 800$ km s^{-1} through the modelling of the Hα emission line, which originates in the outermost part of the accretion disc (see Section 3.5.1 and Table 3). We note, however, that during our observations both Hα and He II λ4686 lines were much wider than they were at the beginning of the outburst, when the peak-to-peak separation for Hα was 1200–1300 km s^{-1} (Torres et al. 2005).

This implies that the accretion disc of SWIFT J1753.5–0127 has shrunk by about 45 per cent compared to the early phase of the outburst, similar to what was observed in other LMXBs (Calvelo et al. 2009) and in CVs (Warner 1995). In this context we note that the outer parts of a large accretion disc are under the gravitational influence of the secondary star, which prevents the disc from growing above the tidal truncation radius $r_{\rm max}$, where the tidal and viscous stresses are comparable (Warner 1995 and references therein). It can be estimated as (see equation 2.61 in Warner 1995):

$$r_{\rm max} = a\frac{0.6}{1+q}\,, \tag{5}$$

where a is the binary separation. Combining Kepler's third law with equations (4) and (5), we obtain the relation:

$$(M_1 + M_2)\,\sin^3 i = \frac{0.074\,P_{\rm orb}V_{\rm K,max}^3}{G}\,, \tag{6}$$

where $V_{\rm K,max}$ is the projected Keplerian velocity of the accretion disc at the tidal radius. Adopting Torres et al.'s value for $V_{\rm out}$ of 600 km s^{-1} as an estimate of $V_{\rm K,max}$ we get $(M_1 + M_2)\,\sin^3 i = 1.2M_\odot$. Using the realistic value of 0.2M$_\odot$ for the secondary mass (see Section 4.3), we find that the solutions for M_1 for any inclination are in good agreement with the solutions obtained from the mass function with the K-correction applied (Fig. 12).

4.3 Constraints on the secondary mass

It is clear that the secondary is a low-mass star, otherwise its absorption lines would be much more apparent in the spectrum of SWIFT J1753.5–0127. In order to be transferring matter onto the compact component, the secondary star must fill its Roche lobe. The relative size of the donor star is therefore constrained by the Roche geometry and the donor must obey the period-density relation for the Roche lobe filling objects (Warner 1995). If the secondary is a main sequence star, one immediately gets an estimate for the mass. The empirical and theoretical mass-period relations for a 2.85 h orbital period binary yields the mass of the secondary star in the range 0.17–0.25 M$_\odot$ (Warner 1995; Smith & Dhillon 1998; Patterson et al. 2005). If the donor is an evolved star, it is likely somewhat inflated relative to isolated main-sequence stars of the same mass, thus the mass inferred from such relation can be considered as an upper limit (Kolb et al. 2001; Knigge 2012). The recently calculated evolutionary sequences for NS binaries with a 3 h period obtain the secondary masses in the range 0.1–0.3M$_\odot$(Podsiadlowski et al. 2002; Lin et al. 2011). We conservatively assume this mass range for the secondary in SWIFT J1753.5–0127.

4.4 Constraints on the inclination

It is clear from the discussion above that the companion mass is rather low, and therefore the BH mass mostly depends on the unknown inclination of the system and the possible K-correction. Even though the BH mass can be rather large for small i, there are additional observational reasons which argue against a very low orbital inclination angle.

- The UV spectrum of SWIFT J1753.5–0127 is dominated by relatively strong emission lines C IV and He II without P Cyg absorption components, and no other absorption lines are detected. From studies of CVs with high accretion mass rates (nova-like stars and dwarf novae in outbursts) it is known that the appearance of their UV spectra strongly depends on orbital inclination: low inclination systems show mainly absorption features in spectra, intermediate-to-low inclination systems exhibit P Cyg profiles and/or blue-shifted deep absorptions, whereas high inclination systems show strong emission lines (La Dous 1989; Puebla et al. 2007, 2011). It is not clear if these results can be applied to LMXBs whose accretion discs are strongly irradiated by the X-rays from the inner region. Published UV spectra of LMXBs show relatively strong emission lines. However, to the best of our knowledge, no UV observations of any low or intermediate-to-low inclination systems are available in the literature. Thus, based on the results of the numerical simulations of CVs (La Dous 1989; Puebla et al. 2011), we can put a lower limit of $i \gtrsim 40^\circ$.
- The time-resolution optical light curves of SWIFT J1753.5–0127 obtained during our observations, display prominent orbital variations with the amplitude of 0.10–0.15 mag in V (Fig. 3), whose nature is not yet clear. The source of orbital modulation cannot be the varying aspect of the irradiated secondary star because the maximum of light is observed around phase 0.0, i.e. inferior conjunction of the secondary star. This also can hardly be a bright spot or bulge on the outer edge of the disc formed by the impact of the gas stream. SWIFT J1753.5–0127 is still in outburst, thus its accretion disc is in the hot, ionized state. The observations of CVs and LMXBs show that the bright spot is barely seen during the outburst stage. Most likely, this orbital modulation is due to some sub-structures in the non-uniform or/and non-axisymmetric accretion disc (i.e., spiral waves, warps or tidally thickened regions). The detection of the enhanced emission regions in the Doppler maps and of the EW variability supports this idea. It is quite obvious that a low-inclination binary system is unable to produce a relatively large amplitude EW variability and orbital modulation in the light curve. Our simulations have shown (see Appendix A) that for more or less realistic parameters of the bright area in the accretion disc it is virtually impossible to obtain the orbital variability with the required amplitude for the orbital inclination $i \lesssim 40^\circ$.

On the other hand, large inclinations are ruled out too, because both ours and the published photometry and spectroscopy

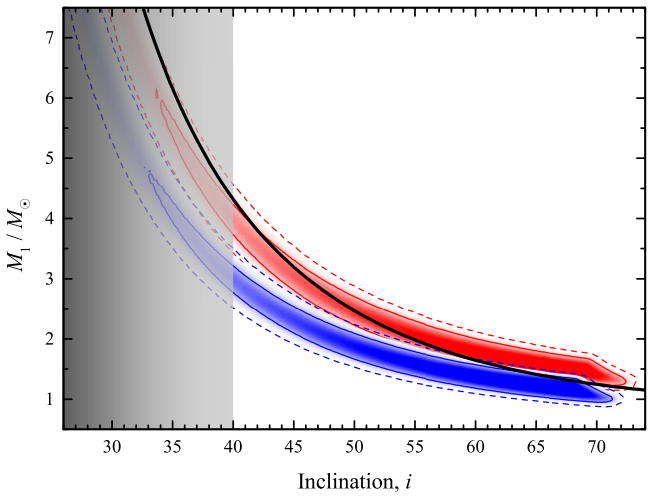

Figure 12. Constraints on the black hole mass M_1 in SWIFT J1753.5–0127 obtained using a Monte Carlo simulation of the observed parameters. The blue area corresponds to the observed semi-amplitude $K_{2,\rm o}$, whereas the red data are calculated for the K-correction $K_{2,\rm o}/K_2 = 0.9$. Denser colours represent higher probability. The solid and dashed lines are the 68 per cent and 95 per cent confidence levels, respectively. The black line shows the BH mass as set by the relation (6) for M_2 =0.2M$_\odot$. The shaded area marks the improbable solutions because of the observed strong photometric and spectroscopic orbital variability (see the text for explanation).

of SWIFT J1753.5–0127 are extensive enough to rule out any significant eclipse. The maximal possible inclination in absence of eclipses generally depends on the mass ratio and can be estimated as

$$\cos i \gtrsim \frac{R_2/a}{1 - r_{\rm d}/a}, \tag{7}$$

where $r_{\rm d}$ is the disc size, which we assume to be equal to 60 per cent of the maximal tidally-allowed size $r_{\rm max}$ (see Section 4.2), and the nominator is computed from the Eggleton (1983) formula:

$$\frac{R_2}{a} = \frac{0.49q^{2/3}}{0.6q^{2/3} + \ln(1+q^{1/3})}. \tag{8}$$

4.5 Observational and Monte-Carlo constraints on the binary system parameters

From the above analysis we can put a conservative lower limit for the orbital inclination to be $i\gtrsim$40°, constrain its upper limit using Equation (7), and consequently restrict the BH mass M_1 to the ranges 1.0–3.1M$_\odot$ for the observed $K_{2,\rm o}$ and 1.3–4.1M$_\odot$ with the K-correction applied.

In order to illustrate the cumulative effect of uncertainty in input parameters, we also applied a Monte-Carlo approach using 10^8 trials for gaussian distribution of K_2 (with σ = 8 km s^{-1}), a top-hat distribution of secondary mass in the limits of 0.1–0.3M$_\odot$and a uniform distribution of $\cos i$. The simulations were performed for the observed $K_{2,\rm o}$ and with the K-correction applied ($K_2 = K_{2,\rm o}/0.9$). For any set (M_2, i, $K_{2,\rm o}$) we calculate M_1 from the mass function, and the parameters are accepted if there are no eclipses (Equation 7).

Fig. 12 shows the results of the Monte-Carlo simulations with the formal 68 and 95 per cent confidence levels[2]. Denser colours represent higher probability reflecting a strong tendency for lower masses. In the figure we also show the BH mass as set by the relation (6) based on constraints obtained from the double-peaked emission lines. These calculations show that the compact object mass in excess of 5M$_\odot$ is rather improbable, because it requires an extremely large K-correction or a lower inclination angle, which is also unlikely because of the observed strong photometric and spectroscopic orbital variability.

We note that even with the lowest possible upper limit on the inclination and the large K-correction, the solution allows for the compact object mass to be below 1.3M$_\odot$, that would correspond to a low-mass NS. Nevertheless, X-ray properties of SWIFT J1753.5–0127 are typical for a BH binary and argue strongly in favour of a BH accretor in the system. This fact can be used to impose an additional restriction on the solution by requiring that the BH has a mass greater than some specified limit, e.g. the maximum possible NS mass. Following the modern theoretical calculations, which give the maximum NS mass $\lesssim$2.4M$_\odot$ (Lattimer 2012), this limit can be put at 2.5M$_\odot$. Nevertheless, admitting that the value of this limit is not well defined, we leave this discussion for the interested reader to complete.

The values of the measured and constrained system parameters are summarised in Table 4. In Fig. 13 we show a schematic representation of the suggested geometry for SWIFT J1753.5–0127, plotted using the system parameters: M_1=3M$_\odot$, M_2=0.2M$_\odot$, i=40°.

The presented BH mass calculations were done with the orbital period of 2.85 h. However, even if the previous value ∼3.2 h found by Zurita et al. (2008) appears to be the correct orbital period, the results will not change significantly due to the relatively weak dependence of the mass function on the period and a large uncertainty in other parameters.

Table 4. Orbital and system parameters for SWIFT J1753.5–0127.

Parameter	Value
Observed	
$P_{\rm orb}$ (h)	2.85±0.01
T_0 (+2450000)	6510.8081±0.0005
K_1 (km s^{-1})	52±10
$K_{2,\rm o}$ (km s^{-1})	382±8
γ (km s^{-1})	6±6
$f_{\rm o}(M)$/M$_\odot$	0.69±0.04
Constrained	
i^a	$\gtrsim$40°
M_1/M$_\odot$	$\lesssim$3.1 (4.1)^a
M_2/M$_\odot$	0.1–0.3
$q = M_2/M_1$	$\gtrsim$0.04 (0.03)
$a/R_\odot$	$\lesssim$1.53 (1.67)

[a]The numbers in parentheses correspond to the solutions with the K-correction applied.

[2] The simulations were performed without additional limitations which should be applied but which values are not well defined (e.g., the minimal orbital inclination). This biases the Monte-Carlo tests and may affect the confidence levels.

5 DISCUSSION

5.1 The BH mass

According to the current convention, the black holes are compact objects, whose measured masses exceed the limit of $3M_\odot$. To date, many BH binaries were identified according to the high measured mass function $f(M)$ $>3M_\odot$, which puts an absolute lower limit for the primary mass (Casares & Jonker 2014). In a number of other systems, additional constraints were required to obtain the mass of the compact object in excess of this limit. The inferred masses of BHs used to be well above the value $3M_\odot$, while the measured NS masses tend to cluster at $\sim$1.4–$1.5M_\odot$ (Remillard & McClintock 2006; Lattimer 2012). The observed distribution of compact objects thus seems to have a double-peak structure at $\sim1.5M_\odot$ and $\sim7M_\odot$ for NSs and BHs, correspondingly (Bailyn et al. 1998; Özel et al. 2010), with a gap in the mass range 2–$5M_\odot$. Investigations of the minimal possible black hole mass (Farr et al. 2011) gave $M_{\rm BH,min}$ $\sim4.3M_\odot$, significantly above the maximum NS mass, further supporting the existence of a gap. Theoretical interpretation of the observed mass distribution was given in the context of different supernova mechanisms (Belczynski et al. 2012): the gap appeared in the simulations with rapidly developing explosions (launched within $\sim$0.2 s after the core bounce), while the delayed explosions (developing on timescales $\sim$0.5–1 s) result in continuous mass distribution. The obtained range of masses for SWIFT J1753.5–0127 put the binary right into the 2–$5M_\odot$ gap, suggesting that the object might be formed in the delayed explosion scenario. Alternatively, the primary mass, initially below $2M_\odot$, could have been enhanced as a result of the accretion processes on the Hubble timescale, to reach the maximum possible mass of a stable NS and then collapsed into a BH. Such effects of binary evolution were considered in Belczynski et al. (2012), who showed that this results in the small additional number of objects with the masses in the range 2–$3M_\odot$.

On the other hand, investigations of Kreidberg et al. (2012), suggest that the gap is an artefact of systematic uncertainties in mass measurements. They conclude that the BH masses in two objects, GRO J0422+32 and 4U 1543–47, plausibly lie within the mass gap. Other 'outliers' include the binary 4U 1700–37, $M = 2.44 \pm 0.27M_\odot$ (Clark et al. 2002), for a long time being classified as a NS (Reynolds et al. 1999), but again returning to the originally proposed (e.g., Brown et al. 1996) BH class by the discovery of the very low-frequency quasi-periodic oscillations (Dolan 2011). The compact object in the classical BH candidate Cyg X-3 was recently estimated to have $M = 2.4^{+2.1}_{-1.1}M_\odot$ (Zdziarski et al. 2013), again right in the middle of the mass gap. Our estimates for SWIFT J1753.5–0127 further support the existence of compact objects with masses in the range 2–$5M_\odot$. A re-analysis of the full set of data is probably required to conclude whether the mass gap still exists.

Masses of BHs used to be comfortably above the limit of $3M_\odot$. However, a growing amount of measurements suggest that there exist a population of compact objects very close to this limit. They can be formed either in the processes of the delayed supernova explosion (such as in simulations of Belczynski et al. 2012) or by the accretion-induced collapse of the NS (initially formed in the supernova explosion) during the common-envelope phase or by accretion from the companion on the Hubble time. It becomes evident that the firm classification based on the compact object mass estimate alone is becoming less and less reliable, and other diagnostic method should be agreed on to serve a criterion to distinguish between BHs and NSs. Such a technique will likely be based on the difference of observational appearance of objects with and without solid surface. The most promising methods are based on the X-ray colour evolution as a function of flux (Done & Gierliński 2003) and on the properties of the broadband noise (Sunyaev & Revnivtsev 2000).

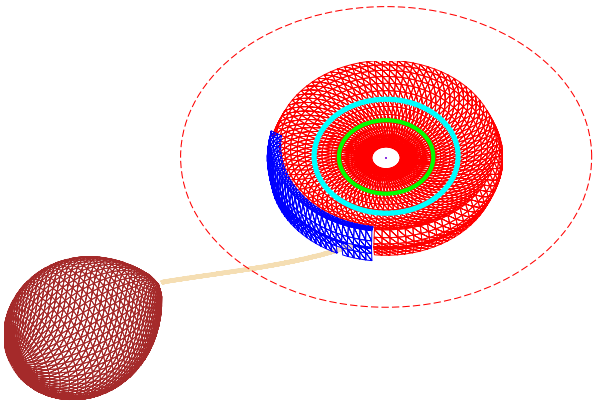

Figure 13. A schematic representation of the suggested geometry for SWIFT J1753.5–0127 plotted using the system parameters: M_1=$3M_\odot$, M_2=$0.2M_\odot$, i=40°. The red thick dashed circle shows the largest radius of the accretion disc determined by tidal limitations. We suggest that it was the accretion disc outer radius during the observations of Torres et al. (2005). At the time of our optical observations the disc (shown as a red disc) has shrunk by about 45 per cent compared to Torres et al.'s observations. The cyan and green rings represent the disc outer radii in which emission lines with higher excitation energies than Hα were originated at the time of observations (cyan: He II λ4686 and C IV, green: He II λ1640). The blue segment located at the outer rim of the accretion disc in front of the secondary shows the bright area which position is assigned according to the relative phasing of the photometric and radial velocity modulations.

5.2 Orbital period

Both our photometric and spectroscopic data suggest the orbital period of SWIFT J1753.5–0127 2.85 h. This puts the system right into the so-called period gap between about 2.15 and 3.18 h (according to results of Knigge 2006). The gap marks the dearth of active CVs in this period range, which appear to have smaller radii compared to the Roche lobe size. The traditional explanation of the period gap involves a thermal bloating of the secondary at periods above $\sim$3 h due to enhanced mass transfer rates (due to magnetic braking mechanism) over those driven by the gravitational radiation losses alone (Howell et al. 2001; Knigge et al. 2011). The magnetic braking abruptly stops at this upper limit when the secondary becomes fully convective (Spruit & Ritter 1983), leading to a reduction of the mass-loss rate and, as a result, its contraction. The binary continues to evolve towards shorter periods as detached system, and eventually the Roche lobe becomes small enough to resume the mass transfer. The fact that SWIFT J1753.5–0127 displays an outburst whilst having the period in the middle of the gap supports our suggestion that the secondary is a slightly evolved star, whose radius is larger than that of a main-sequence star of the same mass. The same conclusion was reached for the LMXB MAXI J1659–152 (2.4 h, Kuulkers et al. 2013) and can also be applied to SWIFT J1357.2–0933 (2.8 h, Corral-Santana et al. 2013).

6 SUMMARY

Despite of the long history of study, system parameters of SWIFT J1753.5–0127 apart from the orbital period were not investigated. The system exhibits X-ray properties typical for the BH binary and has always been considered in the context of the BH primary. Its mass, however, was not dynamically measured, and the assumed values in some cases reached $12M_{\odot}$ (Zurita et al. 2008; Froning et al. 2014). For the first time, we performed the analysis of spectroscopic data to determine the system parameters. Our main result is that the primary in SWIFT J1753.5–0127 is not at all so massive – its mass in excess of $5M_{\odot}$ is highly improbable. This result not only affects the modelling of spectral properties, but also supports the possibility of existence of compact objects in the range $2–5M_{\odot}$, the so-called mass gap. The later conclusion greatly limits the formation scenarios. For instance, in the rapid supernova explosion mechanisms, it is not possible to produce the compact objects with masses $3–5M_{\odot}$, even accounting for the binary evolution effects. We suggest that the primary in SWIFT J1753.5–0127 can either be produced in the delayed explosion or be the result of the accretion-induced collapse of a NS.

We also performed time-series analysis of our photometric and spectroscopic data and confirm that SWIFT J1753.5–0127 is one of the shortest-period X-ray binaries, as initially proposed by Zurita et al. (2008). Our data, however, is better described by the orbital period of 2.85 h, in contrast to $\sim$3.24 h found by them. This finding puts the system into the well-known period gap, in which the main-sequence companions do not fill their Roche lobes. The fact that SWIFT J1753.5–0127 is still in outburst suggests that the mass transfer proceeds, therefore, the companion has a radius larger than that of a main sequence star of the same mass. This is naturally explained if the secondary is somewhat nuclearly evolved.

ACKNOWLEDGMENTS

This work was supported by the Finnish Doctoral Program in Astronomy and Space Physics (AV) and the Academy of Finland grant 268740 (JP). SZ acknowledges PAPIIT grants IN-100614 and CONACyT grant 151858 for resources provided toward this research. JJEK acknowledges partial financial support from the Emil Aaltonen Foundation and the Väisälä Foundation. Our research was partially based on UV observations by NASA missions HST and Swift which we acknowledge. We thank Neil Gehrels for approving the Target of Opportunity observation with Swift and the Swift team for executing the observation. This research has made use of data obtained through the High Energy Astrophysics Science Archive Research Center Online Service, provided by the NASA/Goddard Space Flight Center. We would like to acknowledge the anonymous referee whose comments have significantly improved this paper.

REFERENCES

Bailyn C. D., Jain R. K., Coppi P., Orosz J. A., 1998, ApJ, 499, 367
Barman T. S., Hauschildt P. H., Allard F., 2004, ApJ, 614, 338
Barret D., Olive J. F., Boirin L., Done C., Skinner G. K., Grindlay J. E., 2000, ApJ, 533, 329
Belczynski K., Wiktorowicz G., Fryer C. L., Holz D. E., Kalogera V., 2012, ApJ, 757, 91
Belloni T. M., Motta S. E., Muñoz-Darias T., 2011, Bull. Astr. Soc. India, 39, 409
Berry R., Burnell J., 2005, The handbook of astronomical image processing, 2nd ed. Willmann-Bell, Richmond, VA
Borisov N. V., Neustroev V. V., 1998, Bull. Spec. Astrophys. Obs., 44, 110 (astro-ph/9806159)
Brown G. E., Weingartner J. C., Wijers R. A. M. J., 1996, ApJ, 463, 297
Butler N. et al., 2012, SPIE, 844610
Cadolle Bel M. et al., 2007, ApJ, 659, 549
Calvelo D. E., Vrtilek S. D., Steeghs D., Torres M. A. P., Neilsen J., Filippenko A. V., González Hernández J. I., 2009, MNRAS, 399, 539
Casares J., Jonker P. G., 2014, SSRv, in press (arXiv:1311.5118)
Casares J., Steeghs D., Hynes R. I., Charles P. A., O'Brien K., 2003, ApJ, 590, 1041
Chiang C. Y., Done C., Still M., Godet O., 2010, MNRAS, 403, 1102
Clark J. S., Goodwin S. P., Crowther P. A., Kaper L., Fairbairn M., Langer N., Brocksopp C., 2002, A&A, 392, 909
Corral-Santana J. M., Casares J., Muñoz-Darias T., Rodríguez-Gil P., Shahbaz T., Torres M. A. P., Zurita C., Tyndall A. A., 2013, Sci, 339, 1048
Cowley A. P., Schmidtke P. C., Hutchings J. B., Crampton D., 2002, AJ, 123, 1741
Dolan J. F., 2011, arXiv:1107.1537
Done C., Gierliński M., 2003, MNRAS, 342, 1041
Dubus G., Lasota J.-P., Hameury J.-M., Charles P., 1999, MNRAS, 303, 139
Durant M., Gandhi P., Shahbaz T., Peralta H. H., Dhillon V. S., 2009, MNRAS, 392, 309
Eggleton P. P., 1983, ApJ, 268, 368
Farr W. M., Sravan N., Cantrell A., Kreidberg L., Bailyn C. D., Mandel I., Kalogera V., 2011, ApJ, 741, 103
Froning C. S., Maccarone T. J., France K., Winter L., Robinson E. L., Hynes R. I., Lewis F., 2014, ApJ, 780, 48
Gehrels N. et al., 2004, ApJ, 611, 1005
Gierliński M., Poutanen J., 2005, MNRAS, 359, 1261
Gilfanov M., 2010, in T. Belloni, ed., Lecture Notes in Physics Vol. 794, The Jet Paradigm. Springer-Verlag, Berlin, p. 17
Horne K., Marsh T. R., 1986, MNRAS, 218, 761
Horne K., Saar S. H., 1991, ApJL, 374, L55
Howell S. B., Nelson L. A., Rappaport S., 2001, ApJ, 550, 897
Hynes R. I., Steeghs D., Casares J., Charles P. A., O'Brien K., 2003, ApJL, 583, L95
Ibragimov A., Poutanen J., 2009, MNRAS, 400, 492
Johnston H. M., Kulkarni S. R., Oke J. B., 1989, ApJ, 345, 492
Knigge C., 2006, MNRAS, 373, 484
Knigge C., 2012, MmSAI, 83, 549
Knigge C., Baraffe I., Patterson J., 2011, ApJS, 194, 28
Kolb U., King A. R., Baraffe I., 2001, MNRAS, 321, 544
Kreidberg L., Bailyn C. D., Farr W. M., Kalogera V., 2012, ApJ, 757, 36
Kuulkers E. et al., 2013, A&A, 552, A32
La Dous C., 1989, A&A, 211, 131
Lattimer J. M., 2012, ARNPS, 62, 485
Lin D., Remillard R. A., Homan J., 2007, ApJ, 667, 1073
Lin D., Remillard R. A., Homan J., 2010, ApJ, 719, 1350
Lin J., Rappaport S., Podsiadlowski P., Nelson L., Paxton B., Todorov P., 2011, ApJ, 732, 70
Marsh T. R., 2001, in Boffin H. M. J., Steeghs D., Cuypers J., eds, Lecture Notes in Physics Vol. 573, Astrotomography, Indirect

Imaging Methods in Observational Astronomy. Springer-Verlag, Berlin, p.1
Marsh T. R., Horne K., 1988, MNRAS, 235, 269
Marsh T. R., Horne K., 1990, ApJ, 349, 593
Massa D., Aloisi A., Keyes C., Bohlin R., Froning C., 2010, Instrument Science Report COS 2010-01(v1). Space Telescope Science Institute
Morgan E., Swank J., Markwardt C., Gehrels N., 2005, ATel, 550
Muñoz-Darias T., Casares J., Martínez-Pais I. G., 2008, MNRAS, 385, 2205
Neustroev V. V., 1998, Astr. Rep., 42, 748
Neustroev V. V., Borisov N. V., Barwig H., Bobinger A., Mantel K. H., Šimić D., Wolf S., 2002, A&A, 393, 239
Neustroev V. V., Zharikov S., 2008, MNRAS, 386, 1366
Oke J. B., 1990, AJ, 99, 1621
Orosz J. A., Bailyn C. D., Remillard R. A., McClintock J. E., Foltz C. B., 1994, ApJ, 436, 848
Orosz J. A. et al., 2002, ApJ, 568, 845
Özel F., Psaltis D., Narayan R., McClintock J. E., 2010, ApJ, 725, 1918
Palmer D. M., Barthelmey S. D., Cummings J. R., Gehrels N., Krimm H. A., Markwardt C. B., Sakamoto T., Tueller J., 2005, ATel, 546
Patterson J. et al., 2005, PASP, 117, 1204
Podsiadlowski P., Rappaport S., Pfahl E. D., 2002, ApJ, 565, 1107
Poole T. S. et al., 2008, MNRAS, 383, 627
Poutanen J., Gierliński M., 2003, MNRAS, 343, 1301
Puebla R. E., Diaz M. P., Hillier D. J., Hubeny I., 2011, ApJ, 736, 17
Puebla R. E., Diaz M. P., Hubeny I., 2007, AJ, 134, 1923
Remillard R. A., McClintock J. E., 2006, ARA&A, 44, 49
Reynolds A. P., Owens A., Kaper L., Parmar A. N., Segreto A., 1999, A&A, 349, 873
Ritter H., 2008, NewAR, 51, 869
Schneider D. P., Young P., 1980, ApJ, 238, 946
Shafter A. W., 1983, ApJ, 267, 222
Smak J., 1981, AcA, 31, 395
Smith D. A., Dhillon V. S., 1998, MNRAS, 301, 767
Soleri P. et al., 2013, MNRAS, 429, 1244
Soria R., Wu K., Johnston H. M., 1999, MNRAS, 310, 71
Spruit H. C., 1998, preprint (astro-ph/9806141)
Spruit H. C., Ritter H., 1983, A&A, 124, 267
Steeghs D., Casares J., 2002, ApJ, 568, 273
Sunyaev R., Revnivtsev M., 2000, A&A, 358, 617
Torres M. A. P. et al., 2005, ATel, 566
Tovmassian G., Hernandez S. M., González-Buitrago D., Zharikov S., García-Díaz M. T., 2014, AJ, 147, 68
Wade R. A., Horne K., 1988, ApJ, 324, 411
Warner B., 1995, Cataclysmic variable stars, Cambridge Astrophysics Series, No. 28. Cambridge University Press, Cambridge
Watson A. M. et al., 2012, SPIE, 84445L
Zdziarski A. A., Gierliński M., 2004, Prog. Theor. Phys. Suppl., 155, 99
Zdziarski A. A., Mikolajewska J., Belczyński K., 2013, MNRAS, 429, L104
Zdziarski A. A., Poutanen J., Mikolajewska J., Gierlinski M., Ebisawa K., Johnson W. N., 1998, MNRAS, 301, 435
Zharikov S., Tovmassian G., Aviles A., Michel R., Gonzalez-Buitrago D., García-Díaz M. T., 2013, A&A, 549, A77
Zurita C., Durant M., Torres M. A. P., Shahbaz T., Casares J., Steeghs D., 2008, ApJ, 681, 1458

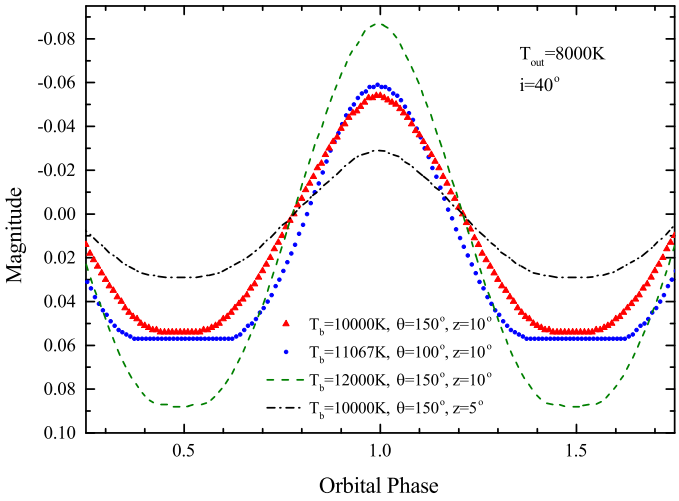

Figure A1. Light curves calculated for different bright area parameters.

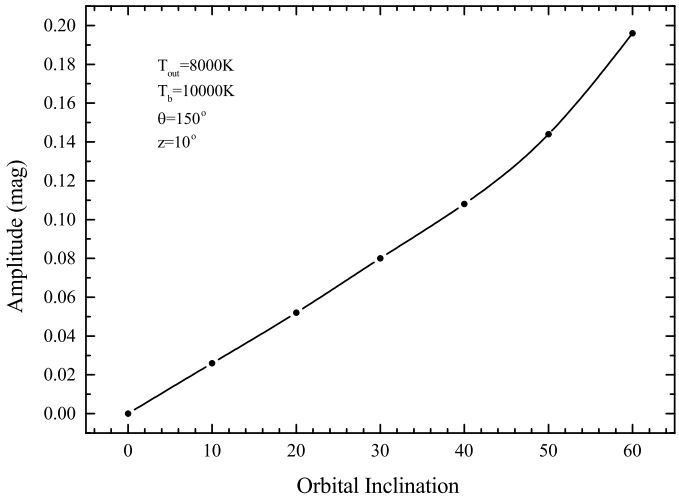

Figure A2. The dependence of the full amplitude of orbital modulation on the orbital inclination.

APPENDIX A: BRIEF DESCRIPTION OF THE LIGHT CURVE SIMULATIONS

The detailed fitting of the light curve of SWIFT J1753.5–0127 requires to make certain assumptions on the accretion disc structure which we do not know. In order to reproduce the observed light curve of SWIFT J1753.5–0127 in terms of shape and amplitude, we adopted the modelling technique from Zharikov et al. (2013) and Tovmassian et al. (2014). A simple geometrical model of SWIFT J1753.5–0127, presented in Fig. 13 is comprised of a concave accretion disc, a secondary red dwarf star, a stream from the inner Lagrangian point, and a bright area located at the outer rim of the accretion disc in front of the secondary.

We assume that the steady-state, optically thick, viscous accretion disc radiates as a blackbody at the local temperature which radial distribution across the disc is given by $T(r) = T_{\rm out}\,(r/r_{\rm out})^{-3/4}$, where $T_{\rm out}$ is the temperature at the outer edge of the disc. The bright area is characterized by the azimuthal extension θ and the temperature $T_{\rm b}$. The vertical extension of the bright area is equal to the thickness of the concave accretion disc at the outer edge and characterized by the opening angle z as seen from

the BH. The donor star fills its Roche lobe. Emission from the accretion stream is not taken into account. The surface of each component of the system is divided in a series of triangles as shown in Fig. 13, each triangle emits as a blackbody with corresponding temperature. The total flux from the binary is obtained by integrating the emission from all the elements lying in a sight of view and then folded with the response of the V filter.

The fixed parameters for the model are set as follows:

- The mass of the primary is $3\mathrm{M}_{\odot}$;
- the mass of the donor star is $0.2\mathrm{M}_{\odot}$;
- the temperature of the donor star is 3000K;
- the outer and inner radii of the disc are imposed by the parameters $V_{\rm out} = 800$ km s^{-1} and $r_{\rm in}/r_{\rm out} = 0.02$ estimated for the Hα emission line (see Section 3.5.1 and Table 3);
- the temperature at the outer edge of the disc is $T_{\rm out}$=8 000K.

We calculated a variety of models using different bright area parameters. We found that the shape of the light curve mostly depends on the azimuthal extension θ whereas the amplitude of variability relies on the orbital inclination i, the opening angle of the disc z, and the ratio of temperatures of the bright area and the disc $T_{\rm b}/T_{\rm out}$ (Figure A1). The amplitude of light curve decreases quickly with decreasing i (Figure A2). Our simulations show that for the orbital inclination of 30° the bright area with $T_{\rm b}$=10 000K, θ=150° and z=10° and the accretion disc with the above parameters creates the modulation with the total amplitude of only 0.08 mag, less than the observed amplitude. Here we claim that these parameters of the bright area are *unrealistic*. They correspond to the blackbody luminosity of the bright area which is twice as large as the total luminosity of the visible half of the accretion disc rim that is not observed in LMXBs or CVs in outbursts. Furthermore, the decrease of the geometrical parameters of the bright area will require to increase this discrepancy further in order to keep the same amplitude of the orbital modulation.

Thus, we conclude that with the use of more or less realistic parameters for the bright area it is nearly impossible to obtain the required orbital variability with the amplitude of at least 0.10 mag for the orbital inclination $i \lesssim 40°$. Only extraordinarily bright and extended area can produce such variability.